ABSTRACT

Title of Document: DEVELOPMENT OF VARIABLE TUBE GEOMETRY HEAT EXCHANGERS USING ADJOINT METHOD WITH PERFORMANCE EVALUATION OF AN ADDITIVELY MANUFACTURED PROTOTYPE

Ellery W. Klein, Doctor of Philosophy, 2023

Directed By: Reinhard Radermacher, Professor
Yunho Hwang, Research Professor
Vikrant Aute, Research Professor

Air-to-refrigerant heat exchangers are a key component for heating, ventilation, air conditioning, and refrigeration (HVAC&R) systems. The performance of these heat exchangers is limited by their air-side thermal resistance. Finless non-round bare tube designs have the potential to improve the air-side thermal-hydraulic performance over their finned counterparts and consequently improve the coefficient of performance (COP) of air-conditioning systems. Previous researchers have used heuristic methods such as multi-objective genetic algorithms (MOGA) with approximation-assisted optimization (AAO) methods utilizing computational fluid dynamics (CFD) based metamodels to shape and topology optimize non-round bare tube heat exchangers. A rather unexplored optimization technique used for heat exchanger optimizations is the gradient based adjoint method. CFD solvers utilizing discrete adjoint methods can be used to shape optimize bare tube heat exchangers and can reveal unintuitive, organic, and potentially superior designs. Additionally, additive manufacturing technology has the capability of building these previously unrealizable heat exchanger designs.

The objectives of this dissertation are to experimentally evaluate the performance of shape and topology optimized compact bare tube heat exchangers with non-round bare tubes on a 1) component level, and 2) system level integrated into an air conditioner. Plus, 3) develop new shape optimized variable geometry compact bare tube heat exchangers using discrete adjoint methods for HVAC&R applications.

First, a comprehensive experimental investigation of multiple shape and topology optimized compact non-round bare tube heat exchangers was conducted under dry and wet evaporator, condenser, and radiator conditions. For all heat exchangers, air-side pressure drop and heat transfer capacity were predicted within 37% and 15%, respectively. Next, an experimental test facility capable of evaluating the system level performance of a 7.03-8.79 kW commercial packaged air conditioning unit was designed and constructed. The performance of the air conditioning unit was evaluated before and after its conventional tube-fin evaporator was replaced with a shape and topology optimized bare tube evaporator. Results are presented and discussed. Lastly, an ε-constraint and penalty method optimization scheme was implemented which utilizes a commercial CFD software with a built-in discrete adjoint solver to perform multi-objective shape optimizations of 2D bare tube heat exchangers. Critical solver/mesh set-up to best optimize heat exchangers with 0.5-10.0 mm diameter bare tubes were identified and established. The optimized designs can achieve a 40-50% reduction in air-side pressure drop with at least the same heat transfer capacity compared to the initial circular bare tube geometry. An adjoint shape optimized 500 W bare tube radiator was additively manufactured in polymer and experimentally tested. Air-side pressure drop and heat transfer capacity were predicted within 15% and 10%, respectively. The experimental performance confirms the adjoint method shape optimized designs improve the thermal-hydraulic performance over the initial circular bare tube geometry.

DEVELOPMENT OF VARIABLE TUBE GEOMETRY HEAT EXCHANGERS USING ADJOINT METHOD WITH PERFORMANCE EVALUATION OF AN ADDITIVELY MANUFACTURED PROTOTYPE

By

Ellery W. Klein

Dissertation submitted to the Faculty of the Graduate School of the
University of Maryland, College Park, in partial fulfillment
of the requirements for the degree of
Doctor of Philosophy
2023

Advisory Committee:

Professor Reinhard Radermacher (Chair)
Professor Hosam Fathy
Professor James Baeder (Representative of Dean)
Professor Peter Sunderland
Research Professor Vikrant Aute
Research Professor Yunho Hwang

Dedication

To my family and friends.

Acknowledgments

The journey of achieving a Ph.D. is a long and winding one and so many people have had a positive impact on me during that time. It makes it impossible to acknowledge all those who deserve it in this short of a section. To those who are not explicitly mentioned, you still had a profound impact on me, and I am forever in your debt. I first would like to thank Professor Reinhard Radermacher. He provided the initial opportunity to start my career here at CEEE, and I thank you for your support and understanding while I pursued my dreams and grew professionally and intellectually. I would like to thank Dr. Vikrant Aute for his modeling and optimization expertise and lessons and Dr. Yunho Hwang for his experimental thermal engineering advice and guidance. My dissertation would not have been possible without all their assistance. I would also like to express my deepest appreciation to all my other committee members: Dr. Peter Sunderland, Dr. Hosam Fathy, and Dr. James Baeder. Thank you for your insights on my dissertation. I would also like to thank the Clark Doctoral Fellowship for their support throughout the program.

I would like to thank Jan Muehlbauer for teaching me by example experimental research skills in the lab and helping with any questions or troubleshooting when stuck. Students would not be nearly as successful with their experimental work without your guidance in lab. I'd like to thank Dr. Jiazhen Ling for his guidance on the HPRC-HX project and always kind and positive words. I am grateful for the modeling and optimization guidance from my colleague Dr. James Tancabel and enjoyed working with you on the HPRC-HX project.

I started my graduate program at the same time as Joe Baker and Nehemiah Emaikwu and it was a pleasure trudging through the program together. I always looked up to my elder lab mates, David Catalini and Yiyuan Qiao, when I started and thank them for guidance and aspired to their

level of work. To my current lab mates, Jango Yang and Cheng-Yi Lee, thank you for your support and always being able to share a laugh together.

To all my friends from high school, undergraduate and graduate school thank you for always being supportive, uplifting, and making me laugh. I wish I could list all your names out, but you goofballs know who you are.

Lastly, I cannot thank my family enough for their support during my time here. You all truly lifted me up during my darkest and toughest times and I would not have been able to complete my studies without your help. To my sister Savannah, you inspired me as you completed your Ph. D in Biology and will always be my best friend. To my Mother, your kindness, generosity, and love are unbounding and have molded me into the person I am today. To my Father and Step-Mother, your love, support, and guidance were always a pillar to lean on and helped me navigate through the most difficult parts of life. I would not be the same person today without you two.

Table of Contents

List of Tables

List of Figures

Nomenclature

A	Area or Surface Area	[m^2]
b	Systematic Uncertainty	
c	CFD control variables	
c_p	Specific heat	[kJ/kg-K]
D	Diameter	[m],[mm]
D_h	Hydraulic diameter	[mm]
EB	Energy balance	[%]
f	Friction factor	[-]
F	Correction Factor	[-]
G	Mass Flux	[kg/m^2s]
Gr	Graetz Number	[-]
h	Avg. heat transfer coefficient or	[W/m^2-K]
	Specific enthalpy	[kJ/kg]
j	Colburn j factor	[-]
J	Observable of Interest	
L	Length or Tube Length	[m]
L	Lagrangian	
m	Mass	[kg]
$\dot{m}$	Mass flow rate	[g/s],[kg/s]
N	Number of Samples	
Nu	Nusselt Number	[-]
P	Pressure or	[Pa],[kPa],[psi]
	Power	[w],[kW]
ΔP	Pressure drop	[Pa],[kPa],[psi],[in.H_2O]
Pr	Prandtl Number	[-]
Q	Heat Transfer	[W],[kW]
R	Result	
Re	Reynolds number	[-]
s	Random Standard Uncertainty	
T	Temperature	[°C],[K]
u	Velocity	[m/s]
U	Error Estimate or	
	Overall heat transfer Coefficient	[W/m^2-K]
V	Volume or	[cm^3]
	Velocity	[m/s]
$\dot{V}$	Volumetric Flow Rate	[m^3/s],[CFM]
w	CFD Flow Solution	
W	Width	[m],[cm]
x	Quality	[-]
$\bar{X}$	Mean Value	

Subscripts

a,air	Air
amb	Ambient
avg	Average
c	Condenser
dry	Dry Conditions
e	Evaporator or Envelope
fg	Vaporization
g	Gravity
h	Hydraulic
hl	Heat Loss
hts	Heat Transfer Surface
hx	Heat Exchanger
l	Latent
m	Mean
max	Maximum
min	Minimum
norm	Normalized
o	Out, or Overall
r	Refrigerant
rad	Radiator Conditions
s	Sensible
t	Total
w	Water
wet	Wet Conditions
$\bar{x}$	of Mean

Greek Symbols

α	Thermal Diffusivity
ε	Epsilon
η	Surface Efficiency
θ	Sensitivity
μ	Dynamic Viscosity
ρ	Density
σ	Contraction Ratio
Δ	Delta/Change In
ω	humidity Ratio
Ψ	Lagrange Multiplier

Abbreviations

2D	Two Dimensional
3D	Three Dimensional
AAO	Approximation Assisted Optimization
AHRI	Air-Conditioning, Heating, and Refrigeration Institute

AM	Additive Manufacturing
AOHX	Adjoint Optimized Heat Exchanger
AOHX-D15	Adjoint Optimized Heat Exchanger – Design 15
ASHRAE	American Society of Heating Refrigeration and Air-Conditioning Engineers
CAD	Computer Aided Design
CFD	Computational Fluid Dynamics
CGDS	Cold Gas Dynamic Spray
CNTHX1	Copper NURBS Tube Heat Exchanger 1
CNTHX-FS	Copper NURBS Tube Heat Exchanger Full Size
COP	Coefficient of Performance
DAQ	Data Acquisition System
DMLS	Direct Metal Laser Sintering
DP	Differential Pressure
ENTHX	Expanded NURBS Tube Heat Exchanger
ESP	External Static Pressure
FDM	Fused Deposition Modeling
GWP	Global Warming Potential
HDT	Heat Deflection Temperature
HTC	Heat Transfer Coefficient
HTS	Heat Transfer Surface
HVAC&R	Heating, Ventilation, Air-Conditioning and Refrigeration
HX	Heat Exchanger
LCM	Lithography Based Ceramic Manufacturing
LIGA	Lithography
LMTD	Log Mean Temperature Difference
L-PBF	Laser-Powder Bed Fusion
LPW	Laser Polymer Welding
MOGA	Multi-Objective Genetic Algorithm
NPT	National Pipe Taper
NSGA	Non-Dominated Sorting Genetic Algorithm
NURBS	Non-Uniform Rational B-Spline
NTHX1	NURBS Tube Heat Exchanger 1
NTU	Number Transfer Units
OD	Outer Diameter
PDE	Partial Differential Equation
PMMA	Polymethyl Methacrylate
PNTHX	Polymer NURBS Tube Heat Exchanger
PPCFD	Parallel parameterized Computational Fluid Dynamics
RH	Relative Humidity
RTD	Resistance Temperature Detector
RT	Refrigeration Ton
SEER	Seasonal Energy Efficiency Ratio
SLM	Selective Laser Melting
SLS	Selective Laser Sintering
TC	Thermocouple
TXV	Thermostatic Expansion Val

Chapter 1: Introduction and Literature Review

1.1 Motivation

Commercial and residential buildings composed approximately 30-40% of total U.S. energy consumption (EIA, 2022; LLNL, 2021). Of this category, space heating and cooling makes up approximately 50% for residential buildings and 39% for commercial buildings (EIA, 2012, 2018). Energy use for air conditioning will increase more than any other end use in commercial and residential buildings by approximately 0.6 QBTU (Sugawara and Nikaido, 2019). In addition, developing countries, such as China and India, are rapidly developing and improving the quality of life for their citizens. Part of this improvement includes space heating and cooling. Worldwide, air conditioning energy consumption will increase over 2010 levels of approximately 4.5 times for developing countries and 1.3 times for developed countries by 2050 (Goetzler et al., 2016). The Paris Climate Accords set carbon dioxide emission goals for all participating countries to mitigate climate change. Developing and developed countries will continue to increase their air conditioning and space heating usage as it vastly improves people's quality of life. To meet the Paris Climate accords' emission goals, it is not feasible nor is it ethical to prevent additional installation and usage of space conditioning. It is apparent that to help achieve these emission goals, the efficiency of air conditioning systems needs to be improved to reduce overall energy consumption.

The U.S. is increasing the efficiency standard of air conditioning units for residential and commercial units. All new residential air-conditioning systems must meet a minimum Seasonal Energy Efficiency Ratio (SEER) (EIA, 2019b). Specifically, the SEER must be at least 15 in the

Southeast and Southwest and at least 14 in the rest of the U.S. There are many ways to improve the SEER of residential air conditioners. A keystone component of air conditioners is the air-to-refrigerant heat exchanger. There is typically a condenser and evaporator heat exchanger in all systems. By improving the performance of these heat exchangers, the overall efficiency, or Coefficient of Performance (COP), of the air conditioning unit can also be improved.

1.2 Compact Heat Exchanger Design

The challenge with respect to air-to-refrigerant heat exchangers is finding new ways to improve the heat transfer performance in the same (or less) amount of space (envelope volume) without significantly increasing the air-side or refrigerant-side pressure drop. Table 1 shows the general design goals for an air-to-refrigerant heat exchanger.

Table 1: Air-to-Refrigerant Heat Exchanger Design Goals

↑	Air-Side HTC
↓	Air-Side ΔP
↓	Refrigerant-Side ΔP
↓	Envelope Volume
↓	Weight/Material Volume
↓	Refrigerant Charge/Internal Volume

This is a very general formulation, and the design challenge is highly dependent on the heat exchangers' operating conditions. i.e. the optimal geometry and topology will be different for different air inlet temperature, velocity, humidity, refrigerant side conditions, etc.. Typically, for residential HVAC&R applications cross-flow air-to-refrigerant heat exchangers are used. Two of the most common refrigerants used are R-410A and R-134a. However, these are slowly being

phased out due to their high global warming potential (GWP) in favor of lower GWP A2L refrigerants. Table 2 shows various ways to define the performance evaluation of compact heat exchangers.

Table 2: Heat Exchanger Performance Evaluation Figures

Key Figure	Definition	Units
Energy Efficiency (Fugmann et al., 2019)	$\frac{\eta h_a A_{HTS}}{\Delta P \dot{V}_a}$	$\frac{1}{K}$
Volume Efficiency (Fugmann et al., 2019)	$\frac{\eta h_{air} A_o}{V_e}$	$\frac{W}{m^3 K}$
Mass Efficiency (Fugmann et al., 2019)	$\frac{\eta h_a A_o}{m}$	$\frac{W}{kgK}$
Compactness (R. K. Shah and Sekulic, 2003)	$\frac{A_o}{V_e}$	$\frac{m^2}{m^3}$
Colburn j-Factor (R. K. Shah and Sekulic, 2003)	$\frac{h_a}{\rho V_{max} c_p} Pr^{2/3}$	*[-]*
Friction (f)-Factor (R. K. Shah and Sekulic, 2003)	$\frac{A_{min}}{A_o}\frac{\rho_m}{\rho_{in}}[\frac{2\Delta P \rho_{in}}{G_{max}{}^2} - (1+\sigma^2)(\frac{\rho_{in}}{\rho_{out}} - 1)]$	*[-]*

The most significant limitation of air-to-refrigerant compact heat exchangers is the air-side thermal resistance. The air-side thermal resistance can make up approximately 80% of the total thermal resistance. Hence, it is also where the most improvements can be made. Most commonly, extended surfaces, such as fins, are used to overcome the high air-side thermal resistance and improve heat transfer performance. Fins achieve this by drastically increasing the air-side active surface area. Even though the air-side heat transfer coefficient limits the heat transfer, there is significant enough surface area to overcome this.

Many types of extended surfaces have been employed to improve the design of heat exchangers and have been exhaustively studied experimentally and numerically. As well as other single phase

convection enhancement methods. There are extensive literature review summaries of cross-flow air-to-refrigerant heat exchangers with finned/extended surfaces as well as other single phase heat transfer enhancement methods, such as vortex generators (Alam and Kim, 2018; Awais and Bhuiyan, 2018; Kumar et al., 2015; Maji and Choubey, 2020; Strobel and Mortean, 2022). Table 3 lists a select number of the most common air heat transfer enhancement techniques found in literature.

Table 3: Common Air Heat Transfer Enhancement Techniques

Type	References
Plain Fin	N. H. Kim and Youn, 1999; Sarpotdar et al., 2016; C.-C. Wang et al., 2000; Chi Chuan Wang et al., 2015
Slit Fin	Kong et al., 2016; Chi Chuan Wang et al., 2001; Yun et al., 2009
Louver Fin	Čarija et al., 2014; Chang and Wang, 1997; Ryu and Lee, 2015; Sarpotdar et al., 2016; C. C. Wang et al., 1998; Chi Chuan Wang et al., 2015
Wavy Fin	Bacellar et al., 2014; Chi Chuan Wang et al., 1998, 2001, 2002
Perforated Fin	Chaudhari et al., 2022; Liu et al., 2020
Microchannel	Hassan et al., 2004; M. H. Kim and Bullard, 2002; Yadav and Singh, 2023
Vortex Generators	Menéndez Pérez et al., 2022; Saini et al., 2023; Sinha et al., 2016; Syaiful et al., 2021

While these passive heat transfer enhancement methods improve the air-side thermal performance, innovation and magnitude of improvement have begun to stagnate in this conventional size range of tubes (hydraulic diameter greater than approximately 6 mm). More compact heat exchanger designs are needed to improve the air-side heat transfer performance. Compact heat exchangers are defined as having a hydraulic diameter of less than 6 mm and are characterized as having a smaller envelope volume and weight for the same amount of active heat transfer area or a surface area density of greater than 700 m^2/m^3 (R. K. Shah and Sekulic, 2003). When looking at compact air-to-refrigerant crossflow compact heat exchangers the use of extended surfaces begins to become less advantageous. To begin with, there are already disadvantages using extended surfaces

at tube hydraulic diameters above 6 mm. This includes, additional viscous resistance, larger weight and external volume, unwanted temperature gradients, reduced air mixing, and extra frosting under evaporator conditions (Bacellar et al., 2017). Both computational and experimental works in recent literature have shown that finless compact heat exchangers can have a superior air-side thermal-hydraulic performance when compared to their finned counterpart when using tubes with a hydraulic diameter approximately less than 3 mm (Bacellar et al., 2014, 2017; Bacellar, Aute, and Radermacher, 2016; Lim et al., 2020; Radermacher et al., 2017; Shikazono et al., 2007). Bacellar et al. showed the cost (flow resistance) of improving the air-side heat transfer coefficient for finned versus bare tubes for a given case (Bacellar et al., 2017). As the hydraulic diameter decreases, the bare tubes begin to outperform the finned designs around a hydraulic diameter of 1-2.5 mm for that particular set-up. For the same air-side pressure drop penalty, or pumping power, a higher air-side heat transfer coefficient can be achieved with finless bare tube designs in this tube diameter range (Bacellar et al., 2017). On top of that, bare tubes with non-circular cross-sectional shapes can further improve the air-side thermal-hydraulic performance over circular designs. There have been numerous numerical and experimental studies demonstrating this (Alnakeeb et al., 2021; Bacellar et al., 2017; Z. Huang et al., 2018, 2020; Kang et al., 2021; Li et al., 2019; Mirabdolah Lavasani and Bayat, 2016; Radermacher et al., 2017; Ranut et al., 2014).

Air-to-refrigerant bare tube compact heat exchangers with non-round cross-sectional shapes have the potential to have improved thermal-hydraulic performance when compared to conventional finned heat exchangers when moving towards tubes with outer diameters less than approximately 3 mm. The next question is how these potential improved thermal-hydraulic performance heat exchangers facilitate higher system level COP of air-conditioning systems. An increase in air-side heat transfer coefficient can facilitate an increase in the overall air-conditioning system COP. This

can be explained with the following rationale. Let's take an evaporator that provides active cooling as an example. Evaporator 1 is the exact same as evaporator 2 except evaporator 1 has a higher air-side heat transfer coefficient. Both have the same amount of active air-side surface area, so to achieve the same heat transfer capacity, heat exchanger 1 will need less of a temperature difference between the refrigerant and air; again, assuming all other factors are exactly the same, like refrigerant mass flow rate, air-side and refrigerant-side pressure drop, etc. Assuming the inlet air is the same temperature/humidity and mass flow rate in both situations, the compressor will need to provide a lower temperature lift and will have lower power consumption. Lower compressor power consumption increases the COP of the overall system. A similar thought-process occurs for improved condenser designs with higher air-side HTC. Less temperature difference is needed between the air and refrigerant for the same condenser capacity and the compressor will expend less energy at a lower temperature lift. Obviously, there are significantly more factors to take into consideration such as air-side and refrigerant-side pressure drop, refrigerant charge, etc. Multiple studies have found (while taking into account many of these other factors) that approximately doubling the air-side heat transfer coefficient, the overall COP can increase by approximately 15-20% (Beshr et al., 2016; Radermacher et al., 2017; Westphalen et al., 2006).

1.3 Compact Heat Exchanger Modeling and Optimization

The previous section discussed that compact finless bare tube heat exchangers with non-round cross-sectional shapes have the potential to improve the thermal-hydraulic performance of air-to-refrigerant heat exchangers and consequentially improve the COP of air conditioning systems. The next question posed is how to accurately model, design, and optimize the heat exchangers within a reasonable amount of computational power.

Computational Fluid Dynamics (CFD) has become an essential tool towards simulating and predicting the performance of heat exchangers. By solving approximated Navier-Stokes equations (finite volume), one can predict the pressure, velocity, and temperature fields in a given flow formulation. Commercial or in-house developed CFD software/code discretize the mass, momentum, and energy conservation equations typically using a finite volume method. The mass, momentum, and energy conservation equations are shown in the Equations below.

$$\nabla \cdot \vec{u} = 0 \qquad \text{Eq. 1}$$

$$\rho(\vec{u} \cdot \nabla)\vec{u} = -\nabla \mathrm{P} + \mu \nabla^2 \vec{u} \qquad \text{Eq. 2}$$

$$\vec{u} \cdot \nabla \mathrm{T} = \alpha \nabla^2 \mathrm{T} \qquad \text{Eq. 3}$$

CFD has the capability to predict the air-side thermal-hydraulic performance (pressure drop and heat transfer coefficient) of air flow over bare tubes less than 6mm within 30% (Bacellar et al., 2017). Additionally, advances in PPCFD have allowed for automated and faster simulations (Abdelaziz, 2009; Abdelaziz et al., 2010).

Various optimization techniques are used with CFD to design air-to-refrigerant heat exchangers. Table 4 shows a summary of optimization techniques for heat exchangers in HVAC&R applications.

Table 4: Summary of Optimization Techniques*

Methodology	Expertise	Relative Computational Cost
Exhaustive Search	Low	10,000,000
Random Search	Low	1,000,000
Parametric Search	Low	100,000
Gradient-Based Methods	Medium	10,000
Heuristic Methods (e.g. MOGA, NSGA, etc.)	Medium	10,000
Approximation Assisted Optimization (Offline)	High	100-1,000
Approximation Assisted Optimization (Online)	High	100

*(L. Huang et al., 2015)

A literature review by Tancabel et al. provides a comprehensive summary of shape and topology optimization used for air-to-refrigerant heat exchangers (Tancabel et al., 2018). Additionally, Kang et al. identified a variety of heat exchangers optimized via design/optimization methods including parametric studies and MOGA with metamodeling for bare tube heat exchangers in HVAC&R applications (Kang et al., 2021). Parametric studies and approximation assisted optimization using heuristic methods such as MOGA are the more common methods used to optimize heat exchangers in the HVAC&R field.

In general, the more computationally expensive a technique is the less experience/skill is needed to implement it while computationally inexpensive techniques require significantly less expertise/skill. Exhaustive search, random search, and parametric search are the most computationally expensive. Of the three, parametric search is the most common for tube shape and topology optimizations for HVAC&R applications. A finite number of design variables are varied over a set range to observe the effect on the objective function. Parametric study capabilities are readily available with many commercial CFD software such as ANSYS Fluent (ANSYS Inc.,

2016) and COMSOL Multiphysics (COMSOL, 2022) and somewhat straightforward to implement.

Heuristic methods such as MOGA can be used with approximation assisted optimization (AAO) methods with CFD based metamodels. These methods require less computational expense, but to successfully implement requires significantly more expertise and time to set up the framework. There are MOGA and AAO toolboxes (such as Kriging) in commercial software like MATLAB (MathWorks, 2022), but the process of efficiently and successfully creating AAO metamodels via CFD and then feeding these metamodels to heuristic models (MOGA) is an involved and intricate process.

A successful utilization of such a framework using an approximation assisted metamodeling via CFD and MOGA is shown in the following works (Bacellar, Aute, Huang, et al., 2016b; Bacellar et al., 2017; Radermacher et al., 2017; Tancabel et al., 2022). This framework has developed many finless non round bare tube compact heat exchangers. These studies utilize a comprehensive multi-scale analysis and shape optimization approach for exploring potential improvements in heat exchanger designs by leveraging automated CFD simulations and AAO metamodeling techniques. The overarching optimization framework is shown in Figure 1.

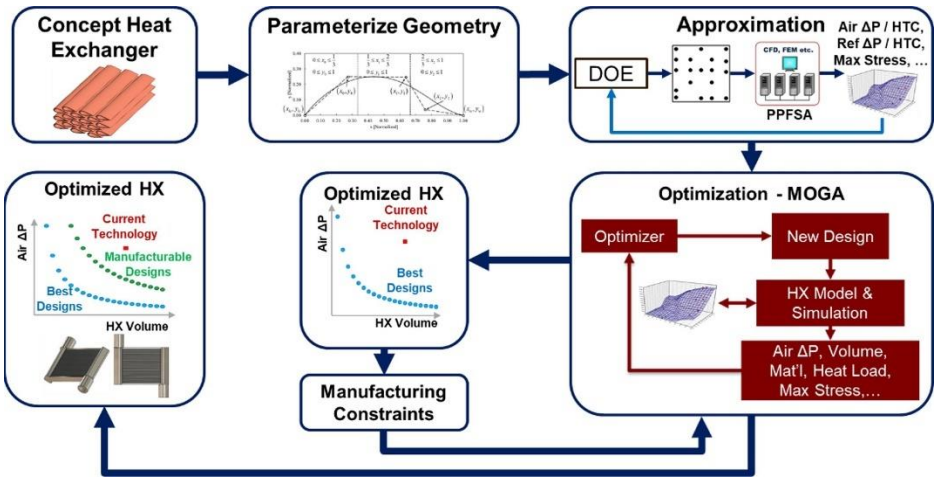

Figure 1: Shape and Topology Optimization Framework (Tancabel et al., 2022)

This framework utilizes non-uniform rational B-Splines (NURBS) to parameterize the geometry of the tubes. The shape and topology of the geometry using NURBS led to non-circular shapes, such as those shown in Figure 2.

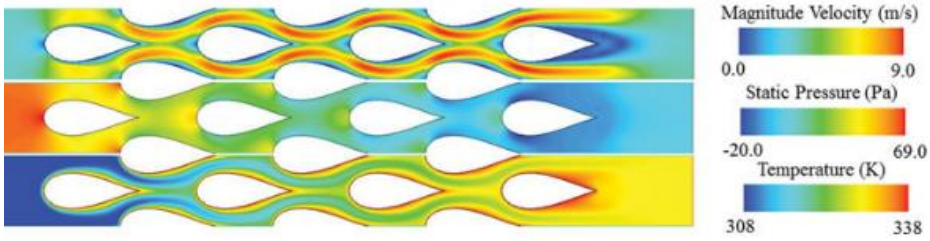

Figure 2: 2D CFD Simulation of Shape and Topology Optimized NURBS Tube Heat Exchanger (NTHX) (Bacellar et al., 2017)

The heat exchanger prototype, NTHX1, was optimized using this framework and was previously successfully experimentally validated as a radiator, with its air-side pressure drop and heat transfer capacity being predicted within 15% and 5%, respectively (Bacellar et al., 2017). This was the first experimental validation of a compact finless bare tube heat exchanger with non-round cross-sectional geometry using this multi-scale analysis and optimization framework. All heat

exchangers experimentally evaluated in Chapter 2 of this dissertation were designed and optimized using the same/similar framework via the respective authors indicated in Table 16.

Moving on to the last category in Table 4, gradient based optimization methods. One specific gradient based technique is the adjoint method. Adjoint solvers can be used to obtain shape/design sensitivities with respect to many design variables as a guide for gradient based optimization methods for little additional computational cost and can reveal unintuitive, organic, and potentially superior designs. The computational cost to obtain these sensitivities does not increase as the number of design variables increases. Adjoint method is not a new mathematical method and one of the first applications to an aerodynamic optimization problems was in 1974 (Pironneau, 1974). Pironneau derived the change in energy dissipation due to a small hump on a body in uniform, steady, laminar flow. Since then, adjoint method has been applied to numerous fluid mechanics and heat transfer problems. Jameson mathematically developed the adjoint method for compressible Euler equations (Jameson, 1988) and applied adjoint method on viscous and inviscid compressible flow (Jameson et al., 1998). Adjoint method has been utilized with RANS turbulence models such as k-ε (C. S. Kim et al., 2001). Some of the first works using adjoint method for heat transfer applications were used towards solving inverse heat transfer problems for different scenarios (Jarny et al., 1991; Subasi, 2002).

Adjoint method can be classified into two major categories, continuous or discrete approach adjoint method. With the continuous adjoint approach, the objective function is augmented using the Navier-Stokes and energy flow equations in their continuous form (PDEs, prior to their discretization) and the resulting adjoint equations are in the form of PDEs, to be discretized and numerically solved in order to compute the adjoint variables (Papoutsis-Kiachagias and Giannakoglou, 2016). With the discrete approach, the objective function is augmented using the

discretized residuals of the primal equations. After differentiating the augmented objective function and rearranging, the adjoint variables are computed by numerically solving the resulting, already discretized, system of adjoint equations (Papoutsis-Kiachagias and Giannakoglou, 2016). Recently with improvement in CFD solvers and in computer computational power, the discrete method has become more frequently used to optimized thermal-fluid problems.

There are studies in recent literature using gradient based adjoint method optimization to improve the thermal hydraulic performance of heat exchanger and heat sink designs. Vidya et al. performed multi-objective optimizations of a pin fin heat exchangers in cross flow with Re ranging from 10-100. Authors achieved a design with 11% increase and 11% decrease in heat transfer and air-side pressure drop, respectively (Vidya et al., 2018). Ghasemi and Elham conducted 2D shape and topology multi-objective optimizations on a series of pin-fin heat exchangers (Ghasemi and Elham, 2021). The optimized topologies demonstrated superior cooling performances at lower costs of pressure losses compared to conventional (circular) in-line and staggered fins. Vidya et al. also performed multi-objective shape optimization of a single 3D cylinder in cross flow at Re of 10. The final tube design achieved 1.9% increase of heat transfer and -2.4% decrease of drag force compared to initial circular tube (Vidya et al., 2019). Other studies conducted adjoint-based heat exchanger design with applications ranging from finned heat sinks to fluid-to-fluid heat exchangers. Table 5 summarizes these studies that have used adjoint method to shape and or topology optimize heat exchangers/heat sinks.

Table 5: Heat Exchanger/Heat Sink Optimized using Adjoint-Method Studies Summary

Study Title	Summary/Key Takeaway(s)
Multi-objective topology optimization of pin-fin heat exchangers using spectral and finite-element methods (Ghasemi and Elham, 2021)	The optimized topologies demonstrated superior cooling performances at lower costs of pressure losses compared to conventional (circular) in-line and staggered fins, and confirmed the supremacy of topology over pure sizing optimization.
Topology optimization of a heat sink with an axially uniform cross-section cooled by forced convection (Lee et al., 2021)	A heat sink is optimized in a physical domain and simplified for manufacturability. The topology-optimized heat sink has a 31% lower total thermal resistance, as well as 9% reduced weight compared to the commercial heat sink.
Three-dimensional multi-objective shape optimization of a cylinder in a cross-flow using discrete adjoint method (Vidya et al., 2019)	A cylinder in a cross-flow is modeled and optimized using the discrete adjoint method. The area close to the front and rear stagnation points do not undergo a significant change, while the area around the 45° and 135° angle of the cylinder are gradually deformed. the optimized cylinder can achieve 1.9% increase of heat transfer and -2.4% decrease of drag force.
Application of adjoint solver to optimization of fin heat exchanger (C. Wang et al., 2015)	Improved the design of a generic fin heat exchanger, using novel discrete adjoint solver tools in the computational fluid dynamics (CFD) software FLUENT. The combined objective, heat transfer and drag, was improved by approximately 50%, compared to the initial design.
Optimization of air cooling system using adjoint solver technique (Czerwiński and Wołoszyn, 2021)	Optimized the shape of the heat sink geometric model using adjoint solver technique. The temperature reduction behind the heat sink by as much as 25 °C, with minor changes in heat source temperature, has been achieved.
Topology optimization of two fluid heat exchangers (Høghøj et al., 2020)	A method for density-based topology optimization of heat exchangers with two fluids is proposed. The optimized designs for both cases show an improved heat transfer compared to the baseline designs. For the shell-and-tube case, the full freedom topology optimization approach is shown to yield performance improvements of up to 113% under the same pressure drop.
Multi-objective optimization of a heat exchanger using the discrete adjoint method (Vidya et al., 2018)	2D staggered cylinders in cross-flow were optimized using ANSYS Fluent's discrete adjoint solver. Multi-objective optimizations were conducted and increased heat transfer by 11% and reduced pressure drop by 11%.
A new framework for design and validation of complex heat transfer surfaces based on adjoint optimization and rapid prototyping technologies (Kametani et al., 2020)	Adjoint shape optimization conducted on two different pin fin arrays to maximize objective function of ratio of heat transfer to air-side pumping power. The pin fin arrays were additively manufactured and thermal-hydraulic performance evaluated. Objective function increased 39-54%.
Synergistic use of adjoint-based topology and shape optimization for the design of bi-fluid heat exchangers (Galanos et al., 2022)	A method that combines topology and shape optimization for the design of bi-fluid heat exchangers is presented. Both are based on continuous adjoint to compute the gradient of objective and constraint functions.
Optimal shape design of compact heat exchangers based on adjoint analysis of momentum and heat transfer (Morimoto et al., 2010)	An adjoint-based shape optimization method of heat exchangers, which takes into account the heat transfer performance with the pressure loss penalty, is proposed. When applied to a modeled heat-exchanger passage with a pair of oblique wavy walls the j/f factor is further increased by 4% from the best value of the initial obliquely wavy duct.
Multi-physics topology optimization for thermal-flow problems applied to additively manufactured heat exchangers (Tang et al., 2021)	A thermal-flow topology optimization workflow was developed for heat exchanger applications. Adjoint sensitivity was computed with an adjoint solver based on a defined objective function. The thermal flow topology optimization was extended for dual flow topology optimization problem to enable simultaneous optimization of two fluid domains with different material properties for heat exchanger applications.
Optimal design and thermal modelling for liquid-cooled heat sink based on multi-objective topology optimization: An experimental and numerical study (H. Li et al., 2019a)	Developed a design method for liquid-cooled heat sink based on topology optimization where adjoint variable method is applied to conduct the sensitivity analysis. Optimized cooling channel can achieve a lower thermal resistance and a higher Nusselt number in comparison to the conventional parallel channel. Both traditional parallel and topology optimized channel were manufactured and performance experimentally validated.
3D topology optimization of heat sinks for liquid cooling (Sun et al., 2020)	Conducted topology optimization of three-dimensional heat sinks for liquid cooling. A set of consistent adjoint equations are derived from the weak forms of the state equations in order to obtain the sensitivity. Parallel plate fin heat sink could consume up to 450% more pumping power than the topology optimization design while achieving the same thermal performance.
Topology optimization of turbulent forced convective heat sinks using a multi-layer thermofluid model (Zhao et al., 2021)	Topology optimizations of a heat sink for coil-cooling are carried out to reduce the average temperature rise of the heat source under a maximum volume fraction constraint. The adjoint method is employed to determine the analytical sensitivity of the objective/constraint functions. Topology-optimized heat sinks exhibit better thermal performance and provide up to a 32.39% reduction of the average temperature rise, compared with the reference designs.
Topology optimization of conductive heat transfer devices: An experimental investigation (Subramaniam et al., 2018)	Presented an experimental thermal management investigation of tree-like structures obtained by topology optimization. The gradient information of the objective function is computed using the adjoint method.
Thermal design of microchannel heat sinks using a contour extraction based on topology optimization method (Zhou et al., 2022)	Performed topology optimization on microchannel heat sink. Adjoint method is used to find the sensitivities of the objective function and volume constraint with respect to the design variables. Experimental thermal-hydraulic performance agreed well with simulated performance.

Many of these studies focus on a very limited geometry or very specific case to optimize. There are minimal studies which investigate multi-objective optimizations of cross-flow heat exchangers for condenser, evaporator, and radiator conditions (Air-to-fluid). The most similar studies to this being by Vidya et al., Ghasemi and Elham, and Kametani et al. (Ghasemi & Elham, 2021; Kametani et al., 2020; Vidya et al., 2018). Experimental validation of adjoint optimized heat exchangers is limited. Four of the sixteen studies in Table 5 have experimental validation (Kametani et al., 2020; H. Li et al., 2019a; Subramaniam et al., 2018; Zhou et al., 2022).

Adjoint based shape optimization of finless bare tube heat exchangers has the potential to greatly improve the thermal-hydraulic performance. It is important in this context to determine in this design space (bare tubes <10 mm), how well can adjoint based shape optimizations design bare tube heat exchangers when compared to other optimization methods such as the shape and topology framework Figure 1 used to design the NTHXs (Bacellar et al., 2017; Tancabel et al., 2022).

Figure 3 shows the shape change of a single tube in cross flow using adjoint method as a simple demonstration example. In this example, the objective is to increase the outlet air-temperature by changing the shape of the bare tube, i.e. changing the shape of the mesh. The shape sensitivities are used as a guide to determine how the tube shape should change to improve the objective function. Once the tube shape is changed and mesh morphed accordingly, the adjoint solver runs again to find the new shape sensitivities with the new morphed geometry. The objective function improves each iteration until a local optimum is reached and the solution converges.

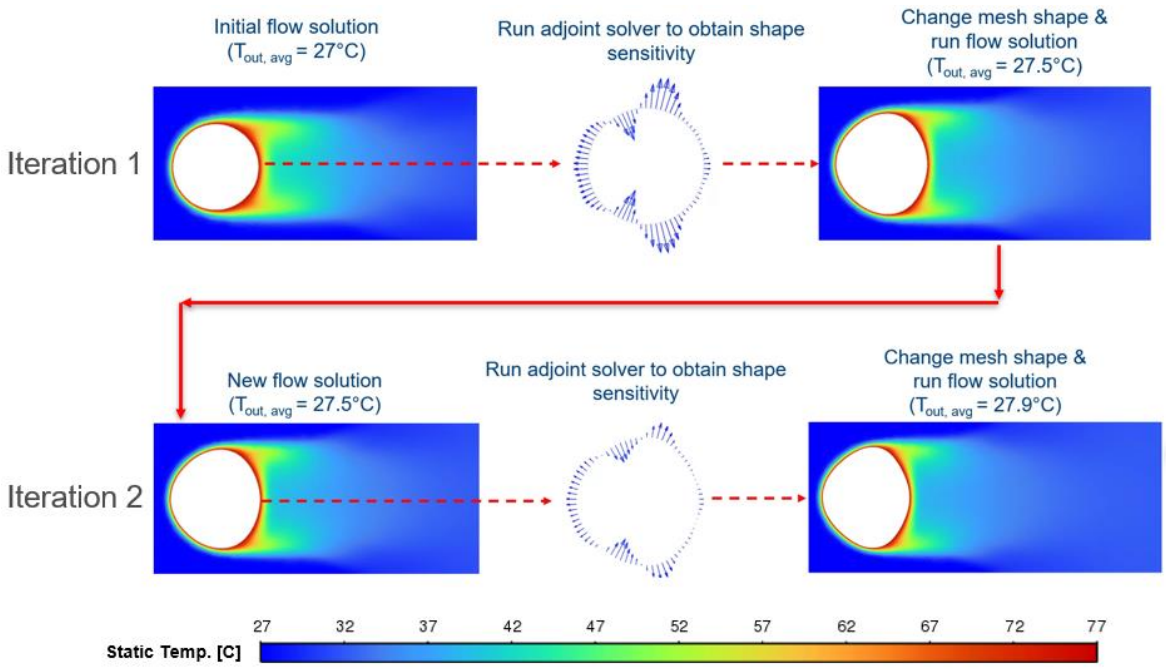

Figure 3: Shape Optimization of 2D Bare Tube in Air Cross-Flow using Adjoint Method

The final optimized design will more than likely change depending on the initial starting geometry, and it is most likely that these optimized designs are not globally optimal. This is in contrast with the heuristic methods discussed previously, such as MOGAs, which have a much higher chance of finding global optimums. Though, the optimized adjoint designs have more possible complex shapes since there can be a significantly larger number of design variables. I.e. the geometry, such as a bare tube shape, can be discretized into a large number of segments, with the location of each segment being a design variable. This can lead to very complex designs difficult for MOGA and AAO optimization algorithms to reach.

1.4 Additively Manufactured Heat Exchangers Literature Review

Compact bare tube heat exchangers with non-circular/uniform cross sections can be designed and optimized within a reasonable amount of computational power, but the manufacturing methods need to exist to build them. Many of these adjoint method optimized designs have unconventional shapes and vary throughout the entire heat exchanger. Additive Manufacturing (AM) has the potential to facilitate great innovation for the next generation of more efficient heat exchangers as it can manufacture many of these unique designs. Heat exchangers have previously, and still do today, rely on traditional manufacturing methods such as milling, die-casting, alignment, brazing/welding, or a combination of processes to mass produce cost efficient products (Matthew Wong et al., 2009). Typical compact heat exchangers, such as microchannel heat exchangers, use fins to augment heat transfer and are manufactured using stamping or folding techniques (M. A. Arie et al., 2016). These methods limit the types of geometries and size and thickness of features, such as tube walls, that can be fabricated. AM could mitigate these limitations. AM is the creation of three-dimensional objects by joining materials together, usually layer-by-layer. Typically, a 3D Computer Aided Design (CAD) model is created and then fed to splicing software, which divides the model into thin horizontal slices. These slices act as instructions for the 3D printer which creates each individual layer one at a time. AM is not limited to just using traditional plastics, but also can create parts composed of metal alloys, ceramics, composites, and even biological materials (Y. Huang et al., 2015). Manufacturers are beginning to take advantage of the new technology. Since parts are built by adding successive layers, complex internal geometries can be built with one monolithic build. This coupled with the fact that different types of materials can be used, facilitates the production of heat exchangers that use less material, have lower volume, and have increased thermal performance and reliability. Considering AM allows for rapid low-cost

prototyping, researchers can design, fabricate, and test novel heat exchangers within a short period of time. One of the earliest examples of researchers taking advantage of metal AM to produce and test a heat exchanger was done in 2006 (Tsopanos et al., 2006). Two micro-scale heat exchangers and three meso-scale heat sinks were rapidly manufactured using Selective Laser Melting (SLM) and the thermal performance experimentally determined. This literature review found the number of researchers using AM to create new cutting-edge heat exchangers and heat sinks has rapidly increased over the past five to ten years.

Surface Roughness

The effect of surface roughness on heat transfer ability is still an active area of research, especially for mini-channel and microchannel heat exchangers. AM processes typically produce parts that have a higher surface roughness compared to the raw material. The common AM technique Selective Layer Sintering (SLS) has been reported to produce parts with a surface roughness of 5-35 μm (Kumbhar and Mulay, 2018). Surface roughness is highly dependent on the AM process, machine parameters, and build direction. Surface roughness has been shown to increase heat transfer. For the simple case of convective heat transfer over a cylinder, in the trans critical flow regime, surface roughening increased the heat transfer by a factor of approximately 2.5 (Achenbach, 1977). If the roughness element height is of the same order of magnitude as the laminar sublayer thickness in turbulent flow, the roughness element tends to break up the laminar sublayer, thereby, increasing the wall shear stress and heat transfer (R. Shah and Sekulic, 2003). Multiple studies have been performed to study the effects of additively manufactured surface roughness on heat transfer. Researchers experimentally studied pressure drop and heat transfer performance through small channels manufactured using DMLS (Stimpson et al., 2016). With decreasing hydraulic diameter, the friction factor increased due to higher roughness-to-hydraulic

diameter ratios. The friction and heat transfer augmentation of the additively manufactured channels were compared to channels with grooves, which have been reported to have enhanced thermal performance. The thermal performance of the additively manufactured channels had comparable heat transfer performance to the grooved channels. Another study investigated the potential of the artificial roughness in manufacturing flat and finned heat sinks for electronics cooling (Ventola et al., 2014). The convective heat transfer was enhanced, on average, by 63% for flat surfaces and 35% for finned surfaces. As researchers and manufacturers use AM to create channels, more quantitative information is needed to help predict the heat transfer and fluid flow through these channels. With regard to correlations and quantification of flow and heat transfer of additively manufactured channels, researchers conducted a thorough study on the effect of DMLS caused channel roughness on channels of various hydraulic length scales (Stimpson et al., 2017). They developed necessary tools for designers that use AM for building parts. A correlation was presented that correlates the relative arithmetic mean roughness with the relative equivalent sand grain roughness for use of estimating the friction factor of flow through a DMLS rough channel. This can be used to predict the Nusselt number of the flow. A downfall of the increased surface roughness is the increased pressure drop which can decrease the performance of the heat exchanger. This can be explained by the increased friction factor (Stimpson et al., 2016). However, new geometries can facilitate lower pressure drop if designed correctly. There is a clear tradeoff between the ability to create new geometries and the increase in pressure drop on the performance of the heat exchanger. Three major characteristics of these additively manufactured heat exchangers that affect the overall design and performance are the surface roughness, material porosity, and the potential smallest feature thickness that can be successfully manufactured.

Material Porosity

There are numerous AM processes that produce parts with internal porosity which is considered a very common defect. Porosity in SLM created parts are a result of shrinkage, gas entrapment during solidification, and adhesion of partially molten particles to surfaces between layers (Aqida et al., 2004; Bauereiß et al., 2014; Tapia et al., 2016). The porosity affects the performance of heat exchangers in two major ways; they include the thermal conductivity of the material and the tensile and fatigue strength. Processed material that is less dense (more porous) than the pure material curtails the thermal conductivity and can negatively affect the performance of the heat exchanger. Researchers used 6061 Aluminum with a bulk conductivity of 170 $\frac{W}{m-K}$ to create multiple heat sinks with different geometries using the AM process SLM (M. Wong et al., 2009a). However, the effective thermal conductivity of the produced part was only reported to be 70 $\frac{W}{m-K}$ partly because the solids produced were 90% dense. It is also well established that excessive porosity can contribute to a reduction in tensile strength, ductility, and fatigue properties (Tapia et al., 2016). This poses an issue for the design and reliability of heat exchanger design. Undesirable porosity could contribute to the mechanical failure of these heat exchangers. Furthermore, the layer thickness, which can limit the feature size, affects the porosity (Zhang et al., 2020).

Minimum Feature Thickness

As the accuracy of AM increases, the possibility to design and manufacture extremely thin features arises. These extremely thin features facilitate the creation of new geometries, increased complexity at smaller scales, and most importantly the reduction of tube wall thickness. As the wall thickness becomes smaller, the overall thermal resistance decreases and hence the effectiveness of the heat exchanger increases as well. Thus, smaller and more compact heat exchangers can be designed and manufactured. The minimum feature thickness obtainable is

dependent on the AM process and material used. Table 6 provides a summary of some of the smallest features manufactured for metal, polymer, and ceramic AM found in the literature. This provides a rough estimate of what the current technological limit is. A study by (M. A. Arie et al., 2016) suggests with current DMLS AM technology, the safe manufacturing limit of metal fin thickness is 0.3mm, the technological limit is 0.15mm, and the future technological projection is 0.05mm. Note that this is for fins, not tube or plate walls which have to hold a certain amount of pressure and separate the two active fluids.

Table 6: Summary of Smallest Feature Thickness Attainable using AM for Varying Materials

Material	AM Process	Wall Thickness
Metal (M. A. Arie et al., 2016)	Direct Metal Laser Sintering (DMLS)	~150 μm
Polymer (Rua et al., 2015)	Polyjet	~32-100 μm
Ceramic (Scheithauer et al., 2018)	Lithography-based Ceramic Manufacturing (LCM)	~100 μm

Additively Manufactured Heat Exchanger Literature Review Summary

Table 7, Table 8, and Table 9 summarize all studies which used additive manufacturing to produce a heat exchanger in metal, polymer, and ceramic, respectively

Table 7: Summary of Metal Additively Manufactured Heat Exchanger Studies

Researchers	AM Process	Summary/Major Findings
Tsopanos et al., 2006	SLM	• Micro scale heat exchangers and meso scale heat sinks were manufactured. • Micro scale heat exchangers demonstrated consistent performance with those considered in previous research. • Meso scale heat sinks did not perform as well as existing pin-fin designs.
Matthew Wong et al., 2007	SLM	• Heat transfer and pressure loss characteristics of four heat sinks experimentally studied. • Aluminum 6061 proven to as a viable material to be used with SLM.
M. Wong et al., 2009	SLM	• Five heat sink geometries manufactured using Aluminum 6061. • Lattice-structure heat sink demonstrates that increasing surface area alone does not necessarily improve the overall heat transfer performance.
Matthew Wong et al., 2009	SLM	• Three novel finned structures manufactured using Aluminum 6061 and Stainless Steel 316L. • Heat sinks produced showed superior performance to the conventional heat sinks. • New geometries incurred lower pressure drop.
Yan et al., 2014	DMLS	• Evaluates the manufacturability and performance of AlSi10Mg periodic cellular lattice structures. • DMLS can be used with this new alloy to produce porous lattice structures.

Ventola et al., 2014	DMLS	• When compared to smooth surfaces, rough flat surfaces and finned surfaces produced with DMLS respectively experienced on average 63% and 35% better convective heat transfer.
Pakkanen et al., 2016	SLM	• Cylindrical geometry for internal channels built at different angles using AlSi10Mg and Ti6Al4V and internal surfaces analyzed. • Surface roughness of internal channels evolve depending on building angle.
M. A. Arie et al., 2016	DMLS	• Implementation of DMLS was studied on a manifold-microchannel heat exchanger. • Manifold-microchannel geometry using DMLS offers significant improvement over state-of-the art advanced fin technologies.
M. Arie et al., 2016	DMLS	• Fabricated and experimentally tested a high-performance titanium alloy air-water heat exchanger that utilizes manifold-microchannel design. • Demonstrated a 45-100% increase in base conductance and 15-50% increase in heat transfer coefficient for the same pressure drop compared with wavy-fin surfaces.
Stimpson et al., 2016	DMLS	• With decreasing hydraulic diameters, the friction factors increased as a consequence of higher roughness-to-hydraulic diameter ratios. • Channels made with DMLS have relatively comparable thermal performance to channels with grooves.
Kirsch and Thole, 2017	DMLS	• Three wavy channel coupons, each containing channels of varying wavelength, were designed and additively manufactured to evaluate pressure loss and heat transfer performance of the channels.
Snyder et al., 2016	DMLS	• Cylindrical-shaped channels built in three different orientations, while teardrop and diamond shaped channels built horizontally. • Vertically built channels had the lowest friction factor, while the diagonally built coupons had the highest friction factor.
Stimpson et al., 2017	DMLS	• Developed correlations that relate the physical roughness measurements to the effect the roughness has on the flow friction and heat transfer. • Heat transfer correlation is presented which predicts Nusselt number of flow through DMLS microchannels using predictions or measurement of friction factor.
Bernardin et al., 2017	DMLS	• Presented a process to improve the thermal performance of a twisted shell-and-tube heat exchanger by leveraging CFD -modeling and expanded fabrication space of AM. • Modeled to have a 40% increase in heat transfer coefficient.
Bacellar et al., 2017	LPBF	• A new bare tube heat exchanger was designed and additively manufactured using laser powder bed fusion. • Achieved ~20%reduction in size, ~20% reduction in air pressure, ~40% reduction in material volume, and ~2% reduction in face area compared to a microchannel heat exchanger.
Ibrahim et al., 2017	LPBF	• L-PBF used to fabricate a multi-layered, Ti-6Al-4V oscillating heat pipe(ML-OHP) • Characterized the ML-OHP thermal performance.
Garde, 2017	SLM	• Additively manufactured oil cooler was designed and manufactured using SLM • Design is projected to transfer heat at 15kW at the design conditions
Gerstler and Erno, 2017	DMLS	• Novel heat exchanger designed to meet the heat transfer and fluid pressure drop requirements of a turbine engine fuel cooled oil cooler. • Mass and volume of the heat exchanger is 66% and 50% lower than the legacy fuel cooled oil cooler with similar performance.
Korinko et al., 2017	SLM	• Type 316 Stainless Steel printed tubing has a higher mechanical strength and lower ductility than annealed Type 316L Stainless Steel.
M. A. Arie et al., 2018	DMLS	• Three prototype heat exchangers were fabricated out of stainless-steel, titanium alloy, and aluminum alloy for power plant air-water heat exchangers. • Improvement in gravimetric heat transfer density compared to wavy fin heat exchanger.
Hathaway et al., 2018	SLM	• Commercial -scale tube bank oil cooler fabricated. • Unique features include, lenticular tubes with offset strip fins, and angled plate-fins.
Jazi et al., 2009	Wire-Arc Spraying	• Dense, alloy 625 deposited on the surface of 10 pores per inch (PPI) and 20 PPI nickel foam sheets to fabricate compact heat exchangers. 20 PPI foam showed higher resistance to flow and greater heat transfer than the 10 PPI foam because of its smaller pore size and larger internal surface area.
Cormier et al., 2013	CGDS	• Pyramidal fin array produced with CGDS outperformed traditional straight cut fins at the same fin density and hydraulic diameter due to fluid mixing increasing the convective heat transfer coefficient.
Cormier et al., 2014	CGDS	• Investigated the effect of varying the fin height and the fin density of pyramidal pin fins. • Increasing either fin height or fin density also increases the total thermal conductivity at the expense of a higher-pressure loss.
Dupuis et al., 2014	CGDS	• Two new geometric pin fin arrays manufactured; pyramidal and trapezoidal fin arrays. • Two new geometries have better heat transfer performance than traditional plain rectangular fins, but larger pressure loss.
Farjam et al., 2015	CGDS	• Pyramidal fin arrays with different volume fractions of aluminum-alumina were produced. • Use of Aluminum-Aluminum feedstock powder as an alternative to pure aluminum prevents the use of costly polymer nozzles that wear out quickly.

Cormier et al., 2016	CGDS	• Near-net-shaped pyramidal fin arrays of various materials were manufactured; including aluminum, nickel, and grade 34 stainless steel. • The aluminum powder outperformed the other materials.
Dupuis, Cormier, Fenech, Corbeil, et al., 2016	CGDS	• Pyramidal pin fins fabricated using CGDS. • Classic double recirculation structures, and flow bypass structures observed in wake regions of fins.
Dupuis, Cormier, Fenech, and Jodoin, 2016	CGDS	• Pressure losses and the convective coefficients of square base, round base and diamond base tapered pin fins. • Staggered configurations produce higher convective coefficients and higher-pressure losses.

Table 8: Summary of Polymer Additively Manufactured Heat Exchanger Studies

Researchers	AM Process	Summary/Major Findings
Harris et al., 2000	LIGA	• Cross-flow micro heat exchanger was developed to provide function similar to a car radiator. • Micro heat exchanger demonstrated good heat transfer rate/volume ratio.
Deisenroth and Bar-cohen, 2016	LPW	• Provides a thorough review of polymer heat exchangers. • Case study presented of an air-to-water heat exchanger constructed using Laser Polymer Welding. • Polymer heat exchanger required 85% less mass, but 35% more volume than a metallic wavy fin heat exchanger of the same capacity. COP also increased by 27%.
Rua et al., 2015	Polyjet	• Aimed to quantify the limitations of the AM process when used for printing microfluidic channels in heat exchanger fins. • .032mm-.1mm walls were possible to clean with care, but deformed slightly under pressure.
M. A. Arie et al., 2017	LPW	• LPW or layer-by-layer line welding by laser was used to fabricate an air-to-water heat exchanger. • Extremely thin walls (150 μm) reduced the thermal resistance of the wall to only 3% of the total thermal resistance.
Felber et al., 2016	FDM	• Prototype air-to-water heat exchanger designed and printed using FDM. • Improving the thermal conductivity for the printed polymer directly affects the heat exchanger performance, but this is a non-linear relationship.
Cevallos, 2014	FDM	• Novel polymer composite heat exchanger, called a webbed-tube heat exchanger. • Design shown to have similar performance to a plate-fin heat exchanger but used less material volume.

Table 9: Summary of Ceramic Additively Manufactured Heat Exchanger Studies

Researchers	AM Process	Summary/Major Findings
Liu et al., 2020	Mould Shape Deposition	• Fabricated micro heat exchanger with four and 40 channels out of silicon carbide.
Shulman and Nicole, 2015	LOM	• Demonstrated complex ceramic heat exchangers can be built using LOM processes. • Ceramic heat exchanger could be manufactured at a reasonable cost.
Schwarzer et al., 2017	LCM	• Demonstrated the creation of complex designs using LCM. • Components with densities after sintering higher than 99% were achieved.
Scheithauer et al., 2018	LCM	• LCM allowed the production of alumina and zirconia components. • A heat transfer surface of more than 3500mm^2 and holes with a diameter if 0.2mm can be realized.

1.5 Research Gaps and Objectives

Research Gaps

Based on the current literature review, the research gaps are as follows:

- Airside thermal-hydraulic performance of cross-flow air-to-refrigerant heat exchangers has potential to be improved. While compact heat exchangers with extended surfaces have been thoroughly investigated, non-circular bare tube heat exchangers with a hydraulic diameter below 6 mm have the potential to increase the air-side heat transfer coefficient and reduce the air-side pressure drop and have not been thoroughly investigated. There is a need for more experimental performance evaluation of finless non-round bare tube compact air-to-refrigerant heat exchangers under radiator, wet and dry evaporator, and condenser conditions (hydraulic diameter less than 6 mm). This includes the performance on a component level and with system level integration.

- The use of additive manufacturing to construct heat exchangers has rapidly expanded in the past decade as it is able to realize previously impossible to manufacture heat exchanger designs. However, the consequences of using said technology for heat transfer devices are not yet fully understood. There lacks experimental evaluation of additively manufactured heat exchangers.

- Gradient-based adjoint optimizations using CFD has the ability to design unintuitive, organic, and potentially superior heat exchanger designs. There are few numerical investigations of using adjoint method based optimization to design compact bare tube heat

exchangers for HVAC&R applications. Moreover, there are few reported experimental investigations of heat exchangers for HVAC&R applications designed and optimized using adjoint based methods based on the literature review conducted.

Objectives

The overarching goal is to expand knowledge and improve the design of compact bare tube air-to-fluid heat exchangers with complex non-circular bare tube geometry. There are three main objectives to accomplish this.

Objective 1: Provide a comprehensive experimental investigation of shape and topology optimized compact heat exchangers with non-round finless bare tubes under evaporator (dry and wet), condenser, and radiator conditions. Heat exchangers were optimized using heuristic methods (MOGA) used with approximation assisted optimization (AAO) utilizing CFD based metamodels (Bacellar, Aute, Huang, et al., 2016b; Bacellar et al., 2017; Radermacher et al., 2017; Tancabel et al., 2022). Refrigerants include R-410A and R-134a.

Objective 2: Design and construct an experimental test facility capable of evaluating the system level performance of a 2.0-2.5 RT (7.03-8.79 kW) commercial packaged air conditioning unit under AHRI 210/240 conditions. Experimentally investigate the system level performance of the packaged unit first, with a traditional fin-tube heat exchangers ("out-of-box"). Then, replace the conventional evaporator with a new compact finless non-round bare tube evaporator. The packaged unit's performance is evaluated at the same AHRI 210/240 conditions. This provides experimental evaluation of how the performance of an air-conditioning unit is affected with the new finless bare-tube heat exchanger design.

Objective 3:

Part A) Develop new shape optimized variable geometry compact bare tube heat exchangers using discrete adjoint method for HVAC&R applications. Develop a custom multi-objective optimization scheme utilizing a discrete adjoint solver to determine the potential improvement of finless bare tube heat exchangers with hydraulic diameters ranging from 0.5-10.0 mm. Compare these designs' thermal-hydraulic performance to heat exchangers developed using heuristic methods (MOGA) used with approximation assisted optimization (AAO).

Part B) Lastly, experimentally confirm the adjoint method shape optimized designs improve the thermal-hydraulic performance over the initial circular bare tube geometry. Design, additively manufacture, and experimentally validate a single 500 W finless non-circular bare tube radiator which is optimized using adjoint shape optimization.

Table 10 breaks down each objective by their heat exchanger design space, design and optimization method, and manufacturing method(s) used to produce prototypes.

Table 10: Objectives Information Summary/Breakdown

Objective	**Bare Tube Design Space / Size Range**	**Optimization Method**	**Performance Level**	**Applied HX Manufacturing Method(s)**
Objective 1	2–3 mm OD Finless Bare Tubes	MOGA with AAO Metamodels Shape and Topology Optimization	HX Component	Additive and Conventional Manufacturing Methods
Objective 2	2–3 mm OD Finless Bare Tubes	MOGA with AAO Metamodels Shape and Topology Optimization	A/C System	Conventional Manufacturing Methods
Objective 3: Part A	0.5–10 mm OD Finless Bare Tubes	Discrete Adjoint Method Shape Optimization	HX Component	n/a
Objective 3: Part B	5–8 mm OD Finless Bare Tubes	Discrete Adjoint Method Shape Optimization	HX Component	Additive Manufacturing

Dissertation Organization

Chapter 1 presents the research motivation, literature review of compact heat exchangers, their design/optimization methods, and additive manufacturing methods, and lastly the objectives of this dissertation.

Chapter 2 presents the results of objective 1; a comprehensive experimental investigation of shape and topology optimized compact heat exchangers with non-round finless bare tubes under evaporator (dry and wet), condenser, and radiator conditions.

- First the heat exchanger test facility used is shown with data reduction methodology.
- All NTHX heat exchangers' experimental results are presented and summarized.

Chapter 3 presents the results of objective 2.

- First, the design and construction of an experimental test facility capable of evaluating the system level performance of a 2.0-2.5 RT (7.03-8.79 kW) commercial packaged air conditioning unit under AHRI 210/240 is shown.
- Experimental results of the baseline packaged unit with a tube-fin heat exchanger and then with the Copper NURBS Tube Heat Exchanger-Full Size (CNTHX-FS) are presented and discussed.

Chapter 4 presents the results of objective 3 (Part A and B).

- ANSYS Fluent's adjoint solver is selected to conduct the shape optimizations of finless bare tube heat exchangers and a validation study is conducted of the CFD model used. An

ε-constraint and penalty method optimization scheme was used which utilized ANSYS Fluent's adjoint solver to perform multi-objective shape optimizations of 2D bare tube heat exchangers.

- Critical adjoint solver settings and 2D mesh set-up used are presented and discussed.
- Optimization results are presented of finless bare tube heat exchangers with hydraulic diameters ranging from 0.5-10.0 mm using adjoint method shape optimization.
- A 500 W heat exchanger is optimized using the developed framework, additively manufactured, and experimentally tested as a radiator.
- Lastly, multi-objective optimizations were conducted on a previously shape and topology optimized NTHX design as the starting geometry instead of circular bare tubes at an inlet air velocity of 3 m/s.

Chapter 5 draws main conclusions and summarizes the main contributions and publications completed with this work. Future work and recommendations are discussed.

Chapter 2: NTHX Experimental Testing

2.1 Heat Exchanger Test Facility

A dedicated heat exchanger testing facility was used to experimentally test compact heat exchangers under air-to-refrigerant, R-410A and R-134a, and air-to-water conditions. This testing facility facilitates the testing of heat exchangers on a component level; meaning the thermal-hydraulic characteristics on the air-side and refrigerant-side are measured with no system level integration in mind. The heat exchanger testing facility consists of three major testing set-ups, an AHSRAE standard closed loop wind tunnel, a pumped refrigerant loop, and a pumped water loop. The closed loop wind tunnel controls the inlet air conditions to the test heat exchanger. This includes the inlet air mass flow rate, temperature, and relative humidity. The refrigerant pumped loop controls the inlet refrigerant conditions to the test heat exchanger as a condenser or an evaporator with R-410A or R-134a. This includes the heat exchanger inlet refrigerant mass flow rate, temperature, pressure, and/or quality. Lastly, the pumped water loop controls the inlet water conditions to the test heat exchanger. This includes the heat exchanger inlet water mass flow rate and temperature. The following sub-sections details each test set-up.

2.1.1 Closed Loop Wind Tunnel

The ASHRAE standard closed loop wind tunnel's design is based on ASHRAE standard 41.2 (ASHRAE, 1987) and 33 (ASHRAE, 2000) and is capable of testing air-to-water/refrigerant heat exchangers between a capacity of 500 W to 10 kW with an uncertainty less than +/- 5% (Z. Huang, 2017). Figure 4 shows the closed loop wind tunnel. A picture of the full closed loop and schematic of the wind tunnel are shown in Figure 4 and Figure 5, respectively. There are two test sections; test section 1 is for smaller capacity heat exchangers between approximately 500 W to 4 kW and

test section 2 is for larger capacity heat exchangers between 4 kW to 10 kW. Test section 1 has a cross-sectional area of 0.33 x 0.33 m. Test section 2 has a cross-sectional area of 0.66 x 0.66 m. The length of each test section is 2.5 meters, and both test sections are made of the 9.5 mm thick polypropylene plates. It has a modular design, in that heat exchangers can be easily installed and uninstalled. When one test section is in use the other is blocked. Figure 6 shows a simplified schematic of the wind tunnel when in use.

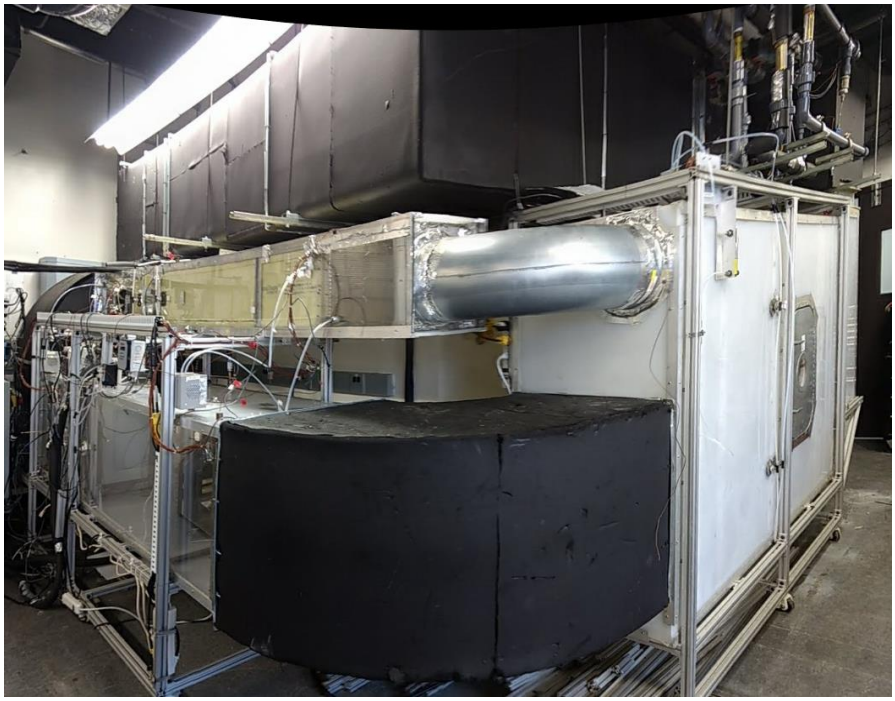

Figure 4: Heat Exchanger Test Facility, Closed Loop Wind Tunnel

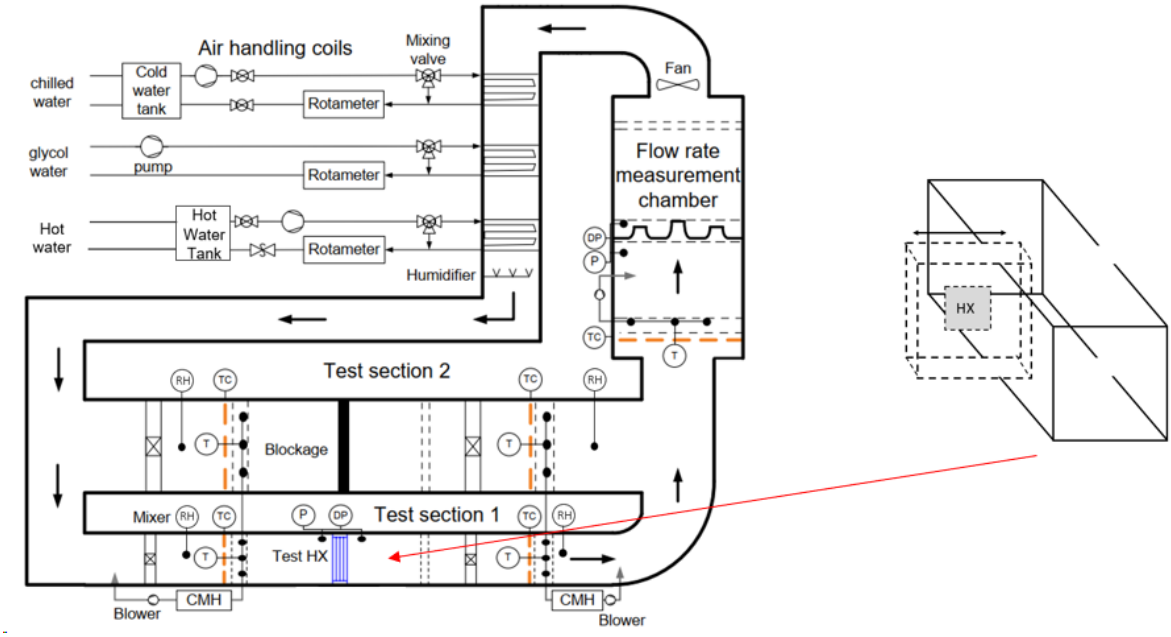

Figure 5: Heat Exchanger Test Facility, Closed Loop Wind Tunnel Schematic (Z. Huang, 2017)

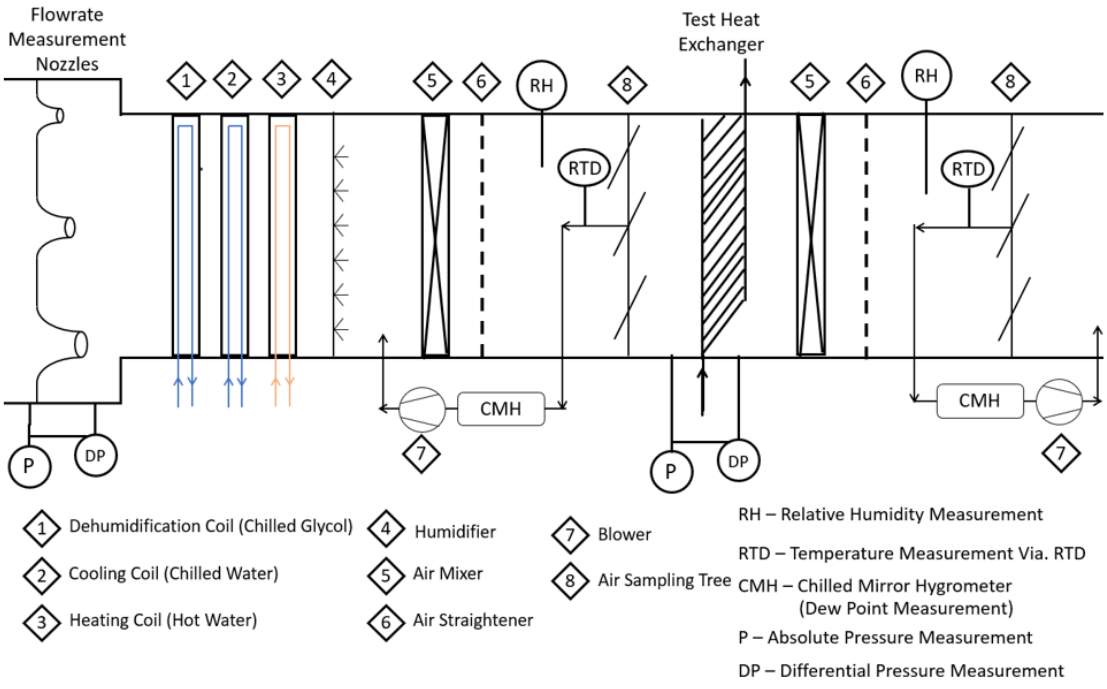

Figure 6: Simplified Wind Tunnel Schematic for Heat Exchanger Testing (Not to scale)

Starting in the section labeled, “flow rate measurement chamber” in Figure 5, there is an array of ASHRAE standard nozzles. The airside mass flow rate was measured using a nozzle grid of seven ASHRAE standard nozzles based on ASHRAE standard 41.2 (ASHRAE, 1987) and (Bohanon, 1975). This array is shown in Figure 7. During testing the applicable nozzle was opened and the others were blocked. A series of pressure taps measure the static pressure drop across the nozzles (eight before and after) and this is correlated to VFR (Bohanon, 1975). An air volumetric flow rate of between 70-1800 CFM (0.033 – 0.850 m^3/s) can be measured. Table 11 shows all nozzle sizes with applicable volumetric flow rates. A variable speed centrifugal fan (after the nozzles is used to generate airflow.

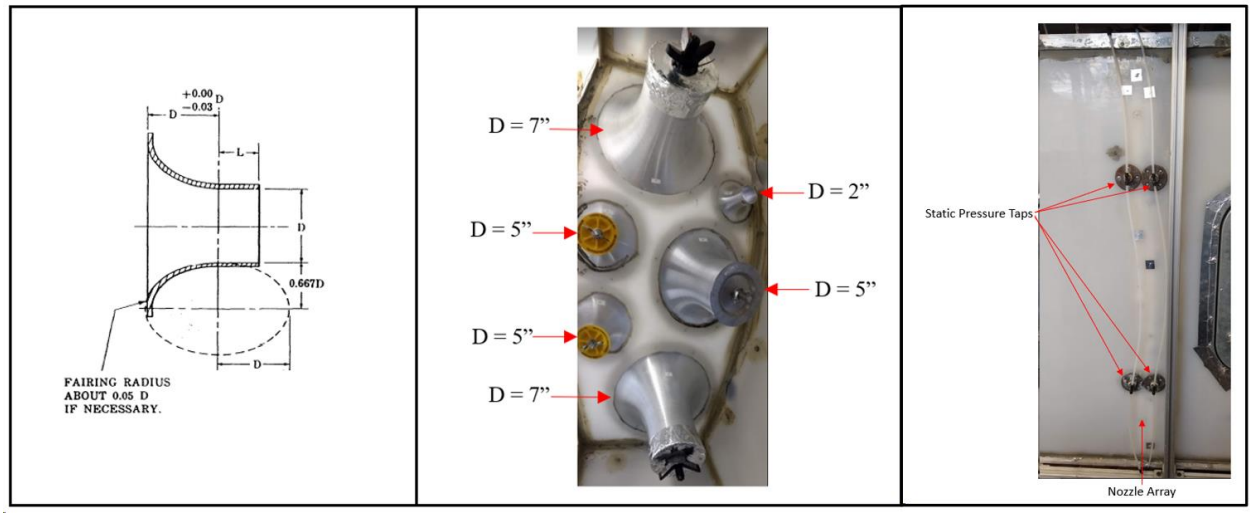

Figure 7: Left: Standard Nozzle Cross-Section Geometry 2 (ASHRAE, 1987); Middle: Nozzle Grid Chamber in Closed Loop Wind Tunnel; Right: Static Pressure Drop Measurement across Nozzle(s)

Table 11: Nozzle Quantities with Applicable air VFR

Nozzle Diameter Size [mm , Inch]	Quantity	Applicable Air Mass Flow Rate [m^3/s , CFM]
50.8mm , 2in	1	0.033-0.071 , 70-150
76.2mm , 3in	2	0.071-0.156 , 150-330
127.0mm , 5in	1	0.212-0.425 , 450-900
177.8mm , 7in	2	0.401-0.850 , 850-1800

Settling means straighten the flow directly before the nozzle. A relative humidity sensor, evenly distributed array of thermocouples, and barometric pressure transducer determine the humidity, air temperature, and absolute pressure, respectively. Eq. 4 is used to calculate the airside mass flow rate.

$$\dot{m}_{Air} = \dot{V}_{air}\rho_{air} \qquad \text{Eq. 4}$$

Figure 8 shows the instrumentation and equipment set-up for the heat exchanger test sections. Air sampling trees with an in-line 1/10 DIN RTD and chilled mirror hygrometer are located before and after the test heat exchanger to obtain dry bulb temperature and dew point temperature. Mixers and settling means ensure uniform flow and temperature at the plane of the air sampling tree. Relative humidity sensors are located at each measuring plane as an extra humidity measurement. Additionally, a grid of thermocouples is located at each measuring plane to confirm an even temperature distribution across the air profile; six thermocouples per plane in the smaller test section 1 and nine per plane in the larger test section 2. Air-side pressure drop is measured across the test heat exchanger using a differential pressure transducer with static pressure taps (four before and after) directly before and after the heat exchanger.

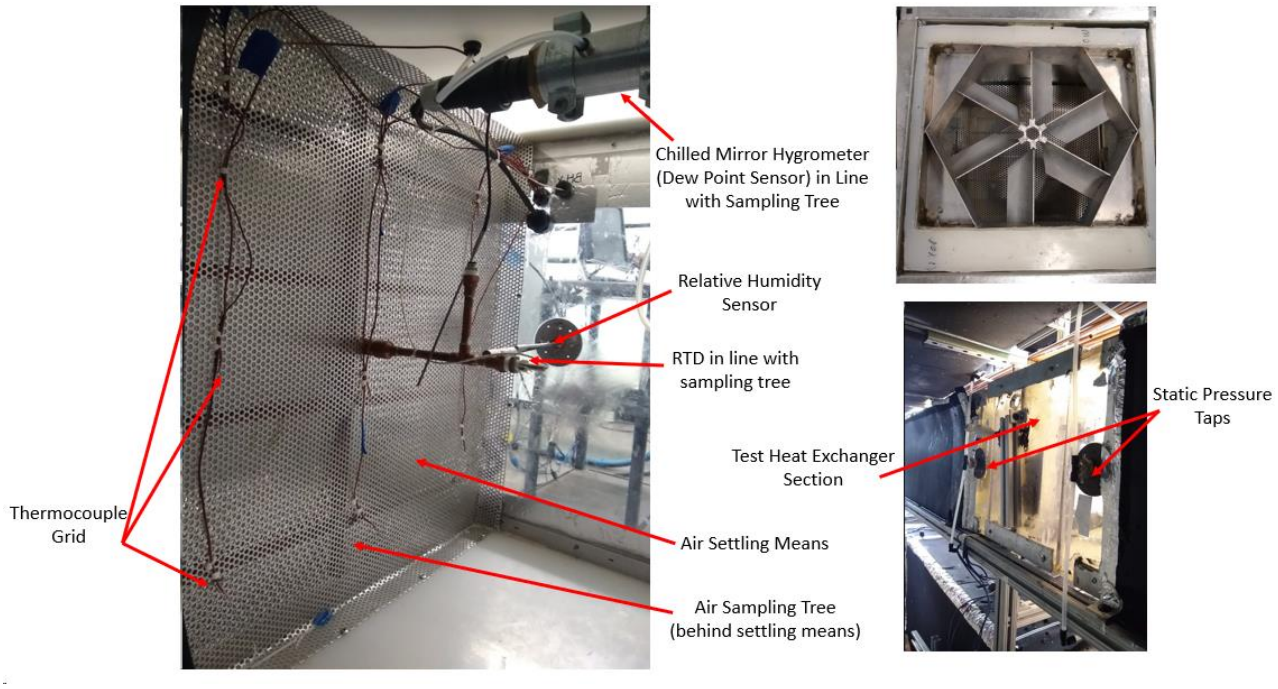

Figure 8: (Left) Measuring Plane Set-Up (before and after test heat exchanger); (Top-Right) Air-Mixer; (Bottom-Right) Static Pressure Taps across Test Exchanger

A cooling coil, heating coil, dehumidification coil, and humidifier condition the air to the desired air inlet temperature and humidity. A water skid distributes hot and chilled water to the coils and rejects heat to an outdoor chiller via a chilled glycol line. Figure 9 shows the water skid, conditioning coils, and steam humidifier.

Figure 9: (Left) Hot and Cold Water Distribution Skid; (Top-Right) Honeywell Humidifier; (Bottom-Right) Water and Glycol Distribution Lines into Air-Loop's Conditioning Coils

While the nozzle pressure drop correlates well with air volumetric flow rate as dictated by (Bohanon, 1975). Extra air mass flow rate calibrations were conducted before heat exchanger testing to ensure accuracy and that no significant air leaks are present in the closed loop. Figure 10 shows a simplified schematic of the air mass flow rate calibration set-up and installed resistance heater.

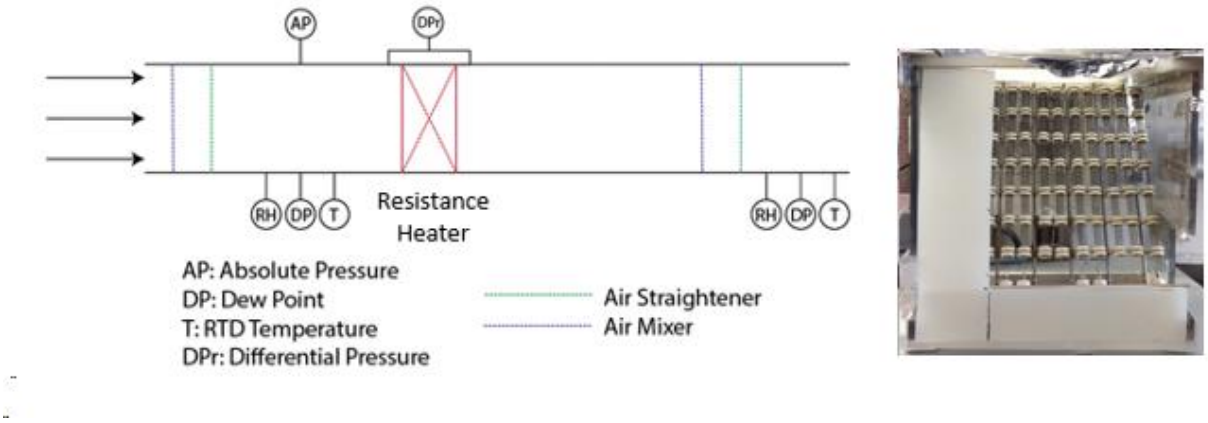

Figure 10: (Left) Air Mass Flow Rate Calibration Schematic (Right) Resistance Heater Installed into Test Section

A resistance heater was installed where the heat exchanger would be tested (test section 1 or 2). Air-flow was established through the test section and 208VAC was applied across the resistance heater to create greater than 10 K air temperature change, and a watt-meter was used to measure the power dissipation of the resistance heater. Eq. 5 was used to calculate the air mass flow rate through the test section.

$$\dot{m}_{\text{Air}} = \frac{PWR_{Heater}}{C_{p,Air}\Delta T_{Air}} \qquad \text{Eq. 5}$$

Air-side pressure drop across the nozzle array, Figure 7 ,was also used to calculate the air mass flow rate as described by (Bohanon, 1975). The air mass flow rate was then varied over the desired

range. The air mass flow rate calculated via the resistance heater and the pressure drop across the nozzles were compared. The difference between the two was never more than 5% difference for testing to continue. If the difference between the two calculated values was greater than 5%, then this indicated air leaks formed within the closed loop and needed to be resealed or sensors needed to be re-calibrated. Twice over the course of five years significant leaks formed where the ducts needed to be resealed. Table 12 shows a summary of the closed loop wind tunnel's instrumentation and respective uncertainties.

Table 12: Closed Loop Wind Tunnel Instrumentation and Uncertainty

Instrument	**Type**	**Range**	**Systematic Uncertainty**
RTD	1/10 DIN	-200 to 800 °C	± 0.03 to 0.07 °C
Thermocouple	T	-250 to 350 °C	± 0.5 °C
Barometric Pressure	Strain	60 to 110 kPa	± 150 Pa
HX Differential Pressure	Strain	0 to 248.8 Pa	± 0.62 Pa
Nozzle Differential Pressure	Strain	0 to 1244.2 Pa	± 3.11 Pa
Dew Point Sensor	Chilled Mirror Hygrometer	-40 to 60 °C	± 0.2 °C
Relative Humidity	Capacitive	0 to 100 %	± 1.0 %
Watt Meter	Hall Effect	0 to 4 kW	± 20 W

2.1.2 Pumped Refrigerant Loop

To achieve the desired refrigerant inlet conditions for air-to-refrigerant heat exchangers, an oilless pumped refrigerant loop was designed and constructed. Figure 11 and Figure 12 show a picture of the completed pumped refrigerant loop and its schematic, respectively. The pumped loop can circulate refrigerants such as R410A and R134a and achieve steady state condenser or evaporator conditions for the heat exchanger of interest. The pressure limit for the system is 500 psia.

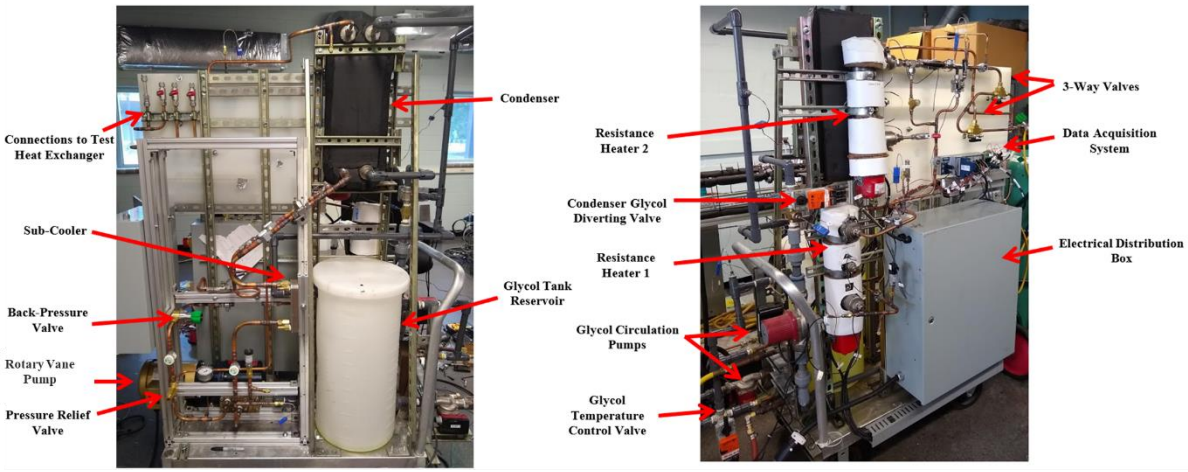

Figure 11: Pumped Refrigerant Loop Completed Set-Up

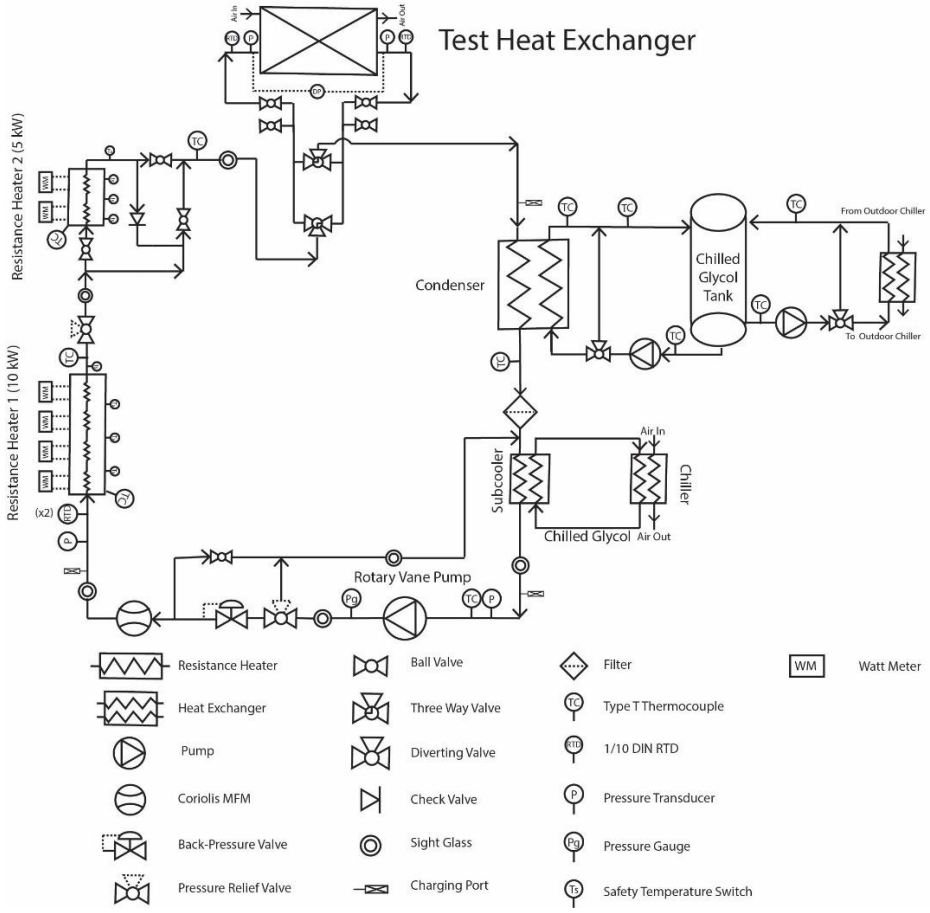

Figure 12: Pumped Refrigerant Loop Schematic

Starting with the return refrigerant flow from the test heat exchanger to the condenser (plate heat exchanger), heat is rejected to a chilled glycol line. A diverting valve controls the mass flow rate of the glycol to the condenser and a separate control/heat rejection loop controls the temperature of the chilled glycol. By varying the temperature and mass flow rate of the chilled glycol entering the condenser, the condensing pressure of the refrigerant is controlled. Consequentially, the condensing temperature then controls the refrigerant pressure of the test heat exchanger. After exiting the condenser, a liquid column of refrigerant is produced using a low-capacity plate heat exchanger (subcooler). A variable speed rotary vane pump controls the refrigerant mass flow rate and is measured using a Coriolis mass flow meter. Absolute pressure and temperature are measured directly before a series of resistance heaters to determine the thermodynamic state of the subcooled liquid. The resistance heaters dissipate enough heat to achieve the test heat exchangers desired refrigerant inlet thermodynamic state. For evaporator testing the outlet refrigerant of the heater is typically two-phase, and its enthalpy is determined by Eq. 6.

$$h_{r,heater,o} = \frac{PWR_{Heater}}{\dot{m}_{ref}} + h_{ref,heater,} \qquad \text{Eq. 6}$$

Hence, the enthalpy and evaporation pressure/temperature to the inlet of the evaporator are known. The refrigerant exits the evaporator as a superheater vapor and the pressure and temperature are measured. For condenser testing the outlet refrigerant of the heaters is typically superheated vapor. The pressure and temperature measurement at the inlet of the test heat exchanger is used to calculate thermodynamic state. The condenser outlet of the test heat exchanger is a subcooled liquid and its temperature and pressure are also measured. For condenser testing an expansion

valve is installed directly after the test heat exchanger to achieve higher pressures. Table 13 shows a summary of the pumped refrigerant loop's instrumentation and respective uncertainties. Appendix A shows the electrical schematics constructed for this system.

Table 13: Pumped Refrigerant Loop Instrumentation and Uncertainty

Instrument	Type	Range	Systematic Uncertainty
Mass Flow Meter	Coriolis	0 to 500 g/s	± 0.1% of reading
RTD	1/10 DIN	-200 to 800 °C	± 0.03 to 0.07 °C
Thermocouple	T	-250 to 350 °C	± 0.5 °C
Absolute Pressure	Strain	0 to 3447 kPa	± 5.2 kPa
Differential Pressure	Strain	0 to 34.5 kPa	± 0.03 kPa
Watt Meter (s)	Hall Effect	0 to 4 kW	± 20 W

2.1.3 Water Loop Facility

Figure 13 shows the schematic of the water loop used for air-to-water testing and Figure 14 shows the water loop experimental set-up.

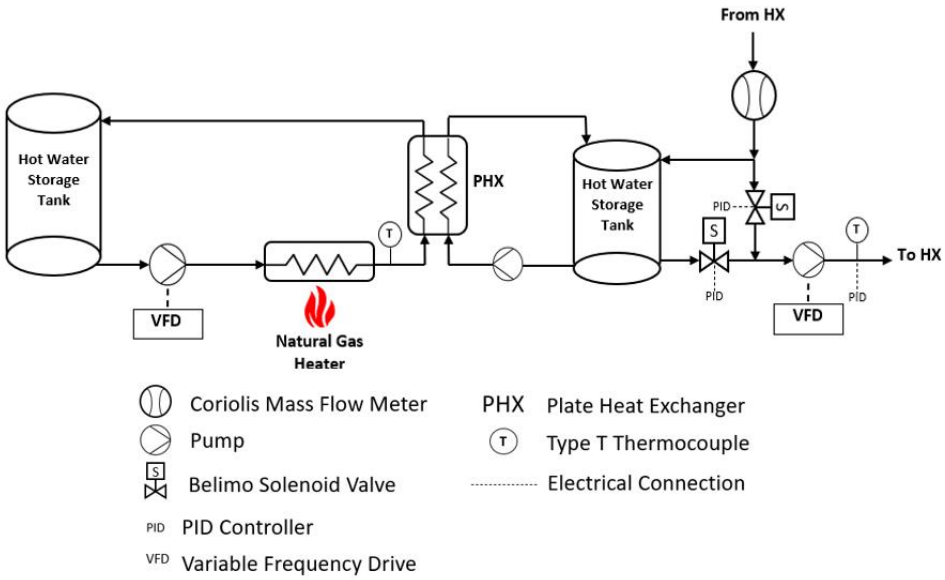

Figure 13: Pumped Water Loop Schematic

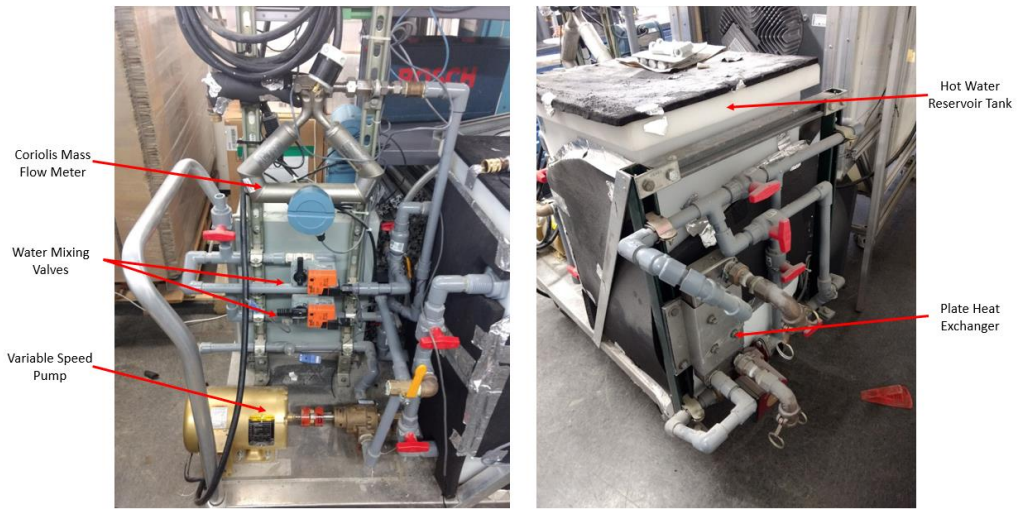

Figure 14: Pumped Water Loop Experimental Rig

Hot water up to 80 °C is produced using a gas water heater. A variable speed pump controls the mass flow rate of water to the test heat exchanger and is measured using a Coriolis mass flow meter. Two diverting valves control the amount of return water from the test heat exchanger and water from the hot water storage tank to control the inlet water temperature to the test heat exchanger. Figure 15 shows a schematic of the water-side test heat exchanger's instrumentation during radiator testing and an example of one the many test heat exchangers tested installed in the section of the duct. Three in stream water-side RTDs measure the inlet and outlet water temperature. Absolute pressure transducers measure the water's absolute pressure, and a differential pressure transducer measures the water side pressure drop through the heat exchanger.

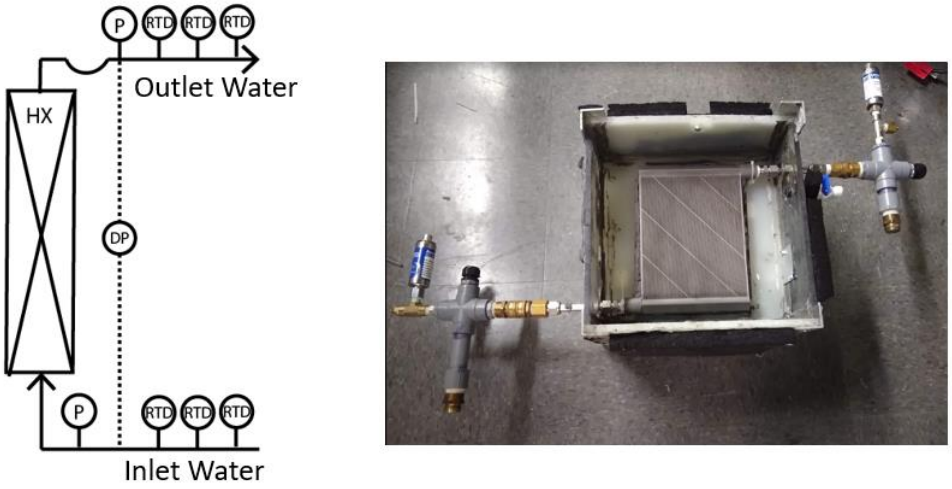

Figure 15: (Left) Waterside Instrumentation during Radiator Testing (Right) Installed Heat Exchanger in Duct Section

Table 14 shows a summary of the pumped refrigerant loop's instrumentation and respective uncertainties.

Table 14: Water Loop Instrumentation and Uncertainty

Instrument	Type	Range	Systematic Uncertainty
Mass Flow Meter	Coriolis	0 to 500 g/s	± 0.1% of reading
RTD	1/10 DIN	-200 to 800 °C	± 0.03 to 0.07 °C
Thermocouple	T	-250 to 350 °C	± 0.5 °C
Absolute Pressure	Strain	0 to 1378.95 kPa	± 1.72 kPa
Differential Pressure	Strain	0 to 34.5 kPa	± 0.03 kPa

2.1.4 Experimental Data Acquisition and Controls

National Instruments' (NI) compact data acquisition (DAQ) modules with the software LabVIEW were used for data collection. An example of the DAQ module set-up is shown in Figure 16. The DAQ modules have built in cold junction compensation for all thermocouples. To achieve steady state testing conditions an autotuning PID with long response time algorithm was implemented

into LabVIEW. Details on the PID autotuning program can be found at (NationalInstruments, 2023).

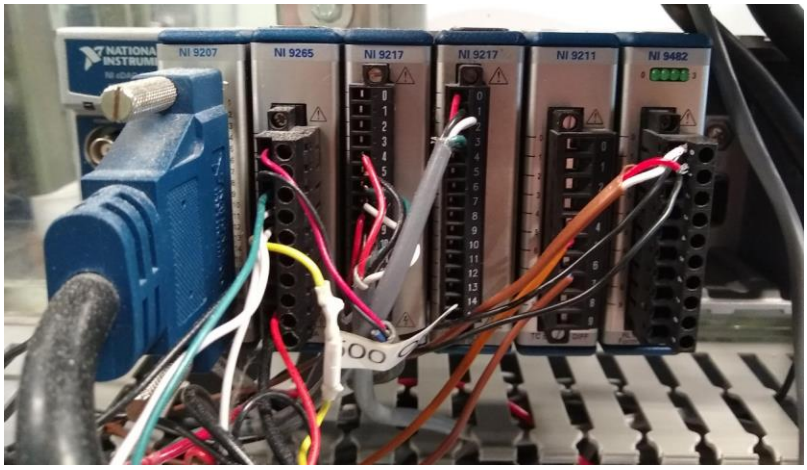

Figure 16: National Instruments Compact Data Acquisition System

2.1.5 Experimental Uncertainty Analysis

All uncertainty analysis followed ASME PTC 19.1 (ASME, 2013). For a given measurement, there is a mean value $\overline{X}$ measured over the course of steady state testing and an estimate of error $U_{\bar{X}}$ with a given confidence level (Eq. 7).

$$\overline{X} \pm U_{\bar{X}} \qquad \text{Eq. 7}$$

The uncertainty estimate of a measurement is composed of two elements, the systematic ($b_{\bar{X}}$) and random ($s_{\bar{X}}$) standard uncertainty. Instrumentation systematic uncertainty is typically reported by the manufacturer and includes hysteresis, linearity, and repeatability. Random uncertainty, $s_{\bar{X}}$, of a measurement is calculated over the course of a steady state test. Where N is the total number of samples measured. The combined expanded uncertainty with a 95% confidence level ($U_{\bar{X}}$) is calculated in Eq. 9.

$$s_{\bar{X}} = \frac{\sqrt{\sum_{j=1}^{N} \frac{(X_j - \bar{X})^2}{N-1}}}{\sqrt{N}} \quad \text{Eq. 8}$$

$$U_{\bar{X}} = 2\sqrt{{s_{\bar{X}}}^2 + {b_{\bar{X}}}^2} \quad \text{Eq. 9}$$

Error propagation of a calculated result, whether that be analytically through a mathematically defined set of equations or numerically. Define a calculated result, R, as dependent on $\bar{X}$ number of parameters, $R = f(\bar{X}_1, \bar{X}_{2,} \bar{X}_3, \ldots \bar{X}_i)$. To analytically find the sensitivity take the partial derivative of R with respect to each parameter. To numerically find the sensitivity finite increments in the parameter can be used.

$$\theta_{i,Analytic} = \frac{\partial R}{\partial \bar{X}_i} \quad or \quad \theta_{i,Numerical} = \frac{\Delta R}{\Delta \bar{X}_i} \quad \text{Eq. 10}$$

Once all the sensitivities are found with respect to the result. The absolute systematic standard uncertainty of the result, R, is.

$$b_R = [\sum_{i=1}^{I} \theta_i b_{\bar{X},i}]^{1/2} \quad \text{Eq. 11}$$

The random standard uncertainty of a results, R, is.

$$s_R = \frac{\sqrt{\sum_{j=1}^{N} \frac{(R_j - \bar{R})^2}{N-1}}}{\sqrt{N}} \quad \text{Eq. 12}$$

The expanded uncertainty of a result at approximately 95% confidence is then given by.

$$U_{\bar{R}} = 2\sqrt{{s_R}^2 + {b_R}^2} \quad \text{Eq. 13}$$

All error-bars on all figures have approximately a 95% confidence level. Appendix B shows an applicable error propagation example for reference. More details on the uncertainty analysis can be found in the standard's documentation (ASME, 2013).

Table 15 shows a summary of the relative systematic uncertainty range for final measured parameters for radiator, condenser, evaporator, and system level testing.

Table 15: Final Measured Parameters' Systematic Uncertainty Range

Final Parameter	**Relative Systematic Uncertainty Range**
Average Capacity (Sensible Evaporator, Radiator, Condenser) [W]	< ±5%
Average Capacity Wet Evaporator [W]	< ±10%
Sensible Heat Ratio [-]	< ±6%
Air Mass Flow Rate [g/s]	< ±3%
Refrigerant Mass Flow Rate [g/s]	< ±0.1%
Power Consumption (A/C System Level) [W]	< ±2%
COP (A/C System Level) [-]	< ±6%

2.2 Data Reduction Methodology

The following section details the data reduction methodology for the testing of individual heat exchangers contained in Chapter 2. This includes radiator, condenser, and dry and wet evaporator testing. For all thermodynamic property evaluations, the commercial software XProps was used (Optimized Thermal Systems, 2023). This includes the refrigerants R410A, R134a, and water, as well as moist air.

2.2.1 Air-Side Data Reduction

Values of the air's specific heat, c_p, and density, ρ, are calculated as an evenly weighted average between the heat exchanger inlet and outlet unless otherwise specified.

Air-Side Pressure Drop and Inlet Velocity

Pressure drop across the heat exchanger of interest is an important parameter to quantify the heat exchanger's hydraulic characteristics. Often the heat exchanger does not have the same face area (smaller) as the closed loop wind tunnel. When this is the case, the air-side pressure drop across the heat exchanger test section will be due to the pressure drop through the heat exchanger and the contraction through the smaller face area cross section. This is shown in Figure 17. To estimate air-side pressure drop of the heat exchanger alone, air-side pressure drop without the heat exchanger installed (open orifice) is measured before testing. The difference in pressure drop with and without the heat exchanger installed at the same air volumetric flow rate is estimated as the pressure drop of the heat exchanger alone without the contraction as shown in Eq. 14. Where ΔP_t is the total pressure drop across the test section with the heat exchanger installed during the experiment, ΔP_e is the pressure drop across the test section without a heat exchanger, and ΔP_{HX} is the estimated pressure drop of the heat exchanger alone. ΔP_{HX} is the value reported for all conditions, radiator, condenser, and evaporator (wet and dry).

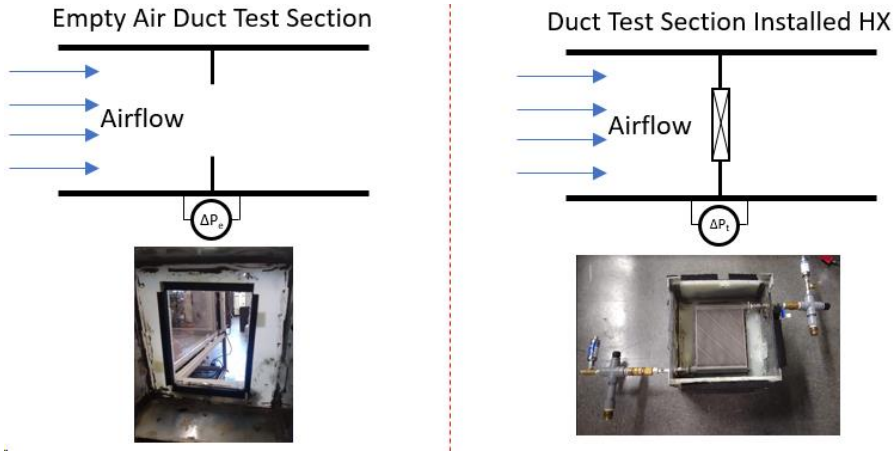

Figure 17: Heat Exchanger Air-Side Pressure Drop Measurement across Test Section

$$\Delta P_{HX,a} = \Delta P_{t,a} - \Delta P_{e,a} \qquad \text{Eq. 14}$$

The heat exchanger inlet air velocity is assumed to be uniform across the inlet face area. Eq. 15 shows how the inlet air velocity is calculated.

$$V_{in} = \frac{VFR}{(L\ x\ w)} \qquad \text{Eq. 15}$$

Some heat exchange prototypes' headers protrude into the tube bundle, effectively changing length used in Eq. 15 as the air flows through. This is shown in Figure 18 . When calculating the inlet air velocity, the length used is the one at cross-section C.

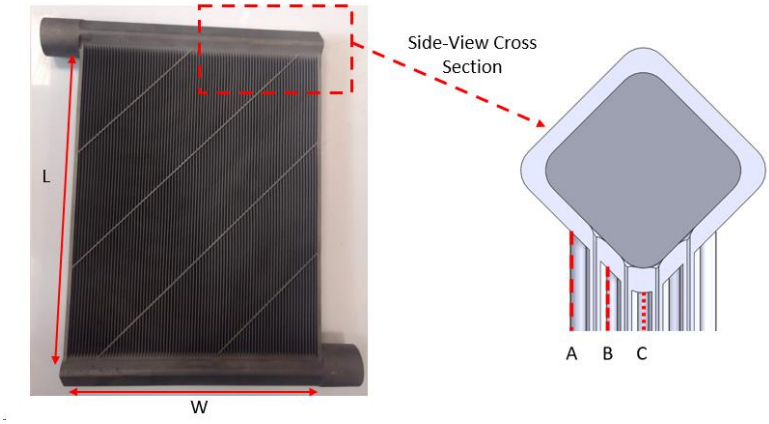

Figure 18: Heat Exchanger Air-Side Inlet Air Velocity Cross Section

Heat Transfer Capacity

Condenser and radiator total air-side heat transfer capacity is simply the sensible heat transfer capacity as shown in Eq. 16 . The latent load is assumed to be zero.

$$Q_{c,a} = Q_{rad,a} = \dot{m}_a c_{p,avg}(T_{a,o} - T_{a,i}) \qquad \text{Eq. 16}$$

Dry evaporator (low inlet relative humidity) total air-side heat transfer capacity is also assumed to be all sensible, Eq. 17. It was visually confirmed during testing that no condensate was forming.

$$Q_{e,dry} = \dot{m}_a c_{p,avg}(T_{a,i} - T_{a,o}) \qquad \text{Eq. 17}$$

Wet evaporator total capacity is comprised of both sensible and latent load and is calculated by Eq. 18. The outlet air's temperature is used to determine condensate enthalpy of vaporization, h_{fg}.

$$Q_{e,wet,t} = Q_s + Q_l = \dot{m}_a c_{p,avg}\left(T_{a,i} - T_{a,o}\right) + \dot{m}_a h_{w,fg}(w_{a,i} - w_{a,o}) \quad \text{Eq. 18}$$

The wet evaporator sensible heat ratio is defined by Eq. 19. This quantity is important for determining the proportion of sensible to latent cooling.

$$SHR_e = \frac{Q_s}{Q_s + Q_l} \quad \text{Eq. 19}$$

Heat Loss Calibration

Air-side heat loss calibration was conducted before experimental testing. There is a minimum duct length needed before and after the heat exchanger needed for proper air mixing to accurately measure the air temperature and humidity at the measuring planes. Hence, there is a large amount of duct surface area for heat loss and affects the measured air-side heat transfer capacity. If there is too much heat loss it can cause a poor energy balance and inaccurate results. Insulation was installed to minimize heat loss. Ambient temperature around the air duct was measured and the desired air-side flow rate and temperature was achieved. The set-up for heat loss calibration is shown in Figure 19. Six type T thermocouples are spread evenly in the ambient air surrounding the test section where heat loss/gain occurs.

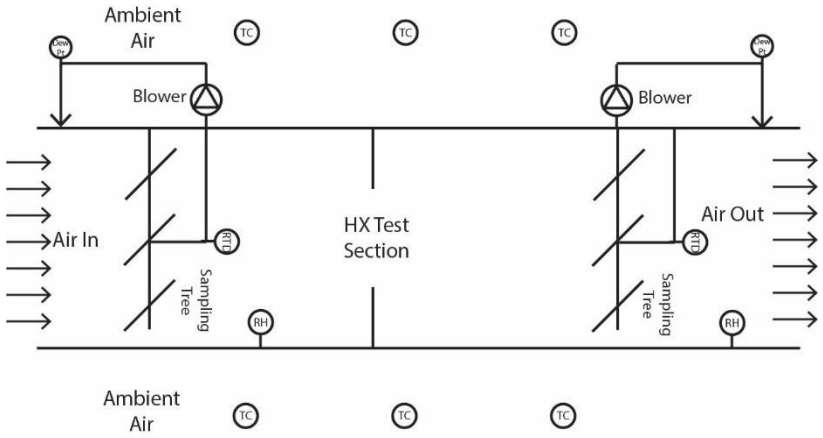

Figure 19: Wind Tunnel Heat Loss Calibration Experimental Set-Up

The test section is empty (no heat exchanger) and the inlet air's temperature is varied while ambient air's temperature is kept constant. Heat loss is determined as a function of temperature difference between ambient and the test section, Eq. 20.

$$\Delta T_{amb-duct,avg} \propto Q_{hl} = \dot{m}_a c_{p,avg}\left(T_{a,in} - T_{a,out}\right) \qquad \text{Eq. 20}$$

During actual heat exchanger testing the difference between ambient air and average duct temperature is used to estimate heat loss and Eq. 21 calculates the corrected sensible heat transfer. This applies to evaporator, radiator, and condenser testing and is the value reported for all results. It was assumed all heat loss/gain was sensible and latent load was not affected.

$$Q_{s,corrected} = Q_s + Q_{hl} \qquad \text{Eq. 21}$$

2.2.2 Refrigerant-Side Data Reduction

Heat Transfer Capacity

For radiator testing, water-side capacity is calculated as shown in Eq. 22. The inlet and outlet water temperature are each an averaged value of three RTDs to reduce uncertainty. This is shown in Figure 15.

$$Q_{rad,w} = \dot{m}_w c_{p,avg}(T_{w,i} - T_{w,o}) \quad \text{Eq. 22}$$

For condenser testing, the inlet refrigerant is a superheated vapor and its enthalpy is determined by the measured temperature and absolute pressure. Outlet refrigerant is a subcooled liquid with its enthalpy also determined using the measured temperature and absolute pressure. Typically, greater than two degrees of subcooling was achieved to ensure no refrigerant is two-phase. Refrigerant-side capacity during condenser testing is calculated as shown in Eq. 23.

$$Q_{c,r} = \dot{m}_r(h_{r,i} - h_{r,o}) \quad \text{Eq. 23}$$

For evaporator testing (dry and wet), the inlet refrigerant is in the two-phase region with a quality typically between 0.10 to 0.30. Inlet refrigerant absolute pressure and temperature are measured. However, this is not enough to fully define the thermodynamic state since it is two-phase. Eq. 6 calculates the refrigerant enthalpy at the inlet of the heat exchanger. Using the inlet refrigerant's enthalpy and temperature or absolute pressure the quality can then be determined. The outlet refrigerant is a superheated vapor and its enthalpy is determined using the measured temperature and absolute pressure. Typically, greater than two degrees of superheat was achieved to ensure no refrigerant is two-phase at the outlet. Refrigerant-side capacity during evaporator testing is thus calculated as shown in Eq. 24.

$$Q_{e,r} = \dot{m}_r(h_{r,o} - h_{r,i}) \quad \text{Eq. 24}$$

Pressure Drop

Refrigerant-side pressure drop was measured across the heat exchangers using strain pressure differential transducers. The following elements contribute to the total pressure drop measurement; port fittings, headers, core, and gravity as shown in Eq. 25. All refrigerant (R410A, R134a, and water) pressure drop values reported are total.

$$\Delta P_{r,tot} = \Delta P_{ports} + \Delta P_{headers} + \Delta P_{core} + \Delta P_g \quad \text{Eq. 25}$$

2.2.3 Overall Parameters

An important quantity to confirm the accuracy of the experimental results is the energy balance between the measured air-side and refrigerant-side heat transfer capacity (ASHRAE, 2000). Energy balance was generally maintained between -5.0 to 5.0 % during all heat exchanger testing. If the energy balance was outside this range, it indicated that there was an error during the data reduction or re-calibration was needed.

$$Energy\ Balance = 2 * 100 * \frac{(Q_{ref,tot} - Q_{a,tot})}{(Q_{ref,tot} + Q_{a,tot})} \quad \text{Eq. 26}$$

Average or nominal heat exchanger heat transfer capacity is frequently reported and is simply the average between the refrigerant-side and air-side capacity. This is the heat transfer value used when compared to the simulation values.

$$Q_{avg} = \frac{(Q_{ref,tot} + Q_{a,tot})}{2} \quad \text{Eq. 27}$$

2.2.4 Colburn j and f factor

The air-side hydraulic diameter for these heat exchangers is shown in Eq. 28 (Kays and London, 1984). Where A_{min} is the minimum flow-cross sectional area, L_{HX} is the depth of the heat exchanger core (direction of airflow), and A_o is the total active air-side surface area.

$$D_h = \frac{4A_{min}L_{HX}}{A_o} \quad \text{Eq. 28}$$

Air-side Reynolds number is calculated as shown in Eq. 29, where V_{max} is the velocity at the minimum free-flow cross section, A_{min}.

$$Re = \frac{\rho V_{max} D_h}{\mu} \quad \text{Eq. 29}$$

The friction factor, f, is then calculated, where σ is the contraction ratio, A_{min}/A_{in}, ratio of the minimum flow area to frontal area. $V_{max} = V_{in}/\sigma$. G_{max} is the mass flux at the minimum cross-section area.

$$f = \frac{A_{min}}{A_o}\frac{\rho_m}{\rho_{in}}\left[\frac{2\Delta P \rho_{in}}{G_{max}{}^2} - (1+\sigma^2)\left(\frac{\rho_{in}}{\rho_{out}} - 1\right)\right] \quad \text{Eq. 30}$$

Eq. 31 calculates the Colburn J factor.

$$j = \frac{h_{a,avg}}{\rho_m V_{max} c_{p,m}} Pr^{2/3} \quad \text{Eq. 31}$$

To calculate the average air-side heat transfer coefficient during radiator testing the following process was used. Nominal heat transfer capacity is defined with Eq. 32.

$$Q_{avg} = UA * F * (LMTD) \quad \text{Eq. 32}$$

Where Log Mean Temperature Difference (LMTD) is for counter-flow configuration, F is a correction factor for different configuration (in this case cross-flow), and UA is the overall heat transfer coefficient. UA can be further broken down into individual thermal resistances; wall conduction, refrigerant-side convection, and air-side convection. Wall thermal resistance can be readily calculated, and the appropriate water-side average Nusselt number correlation can be used to find the average water-side HTC. Based on this knowledge, the air-side average HTC can then be calculated.

2.3 NURBS Tube Heat Exchangers (NTHX) Component Level Experimental Testing

A comprehensive experimental investigation was conducted for five novel compact bare tube heat exchangers.

2.3.1 NTHX Background

Two important performance factors for finless bare tube heat exchanger designs are the air-side heat transfer coefficient and pressure drop, which should be maximized and minimized, respectively. Both the air-side heat transfer coefficient and pressure drop are inversely proportional to the hydraulic diameter of the finless tubes. Both computational and experimental works in recent literature have shown that finless compact heat exchangers have a superior air-side thermal-hydraulic performance when compared to their finned counterpart (Bacellar et al., 2014, 2017). For the same air-side pressure drop penalty, or pumping power, a higher air-side heat transfer coefficient can be achieved (Bacellar et al., 2017). Hence, heat exchanger designs with smaller hydraulic diameters are desirable for the improved thermal-hydraulic performance for air-to-refrigerant heat exchanger applications. The question posed is how to successfully design, optimize, and manufacture air-to-refrigerant heat exchangers small diameter bare tubes with non-round shapes and different topologies. With regards to design and optimization; First, advances in PPCFD have allowed for automated and faster simulations (Abdelaziz, 2009; Abdelaziz et al., 2010). Additionally, recent progress in optimization techniques such as multi-objective genetic algorithms (MOGA) and approximation-assisted optimizations (AAO) further reduce the computational expense and allow for both shape and topology optimization of heat exchangers (Abdelaziz, 2009; Abdelaziz et al., 2010; Aute et al., 2013; Bacellar et al., 2017; Gharbi et al.,

2015; Hilbert et al., 2006; Ranut et al., 2014; Saleh et al., 2010; Tancabel et al., 2022). Then, concerning the manufacturing of these heat exchangers; recent advances in additive manufacturing have allowed for the manufacturing of these heat exchangers in one single monolithic build (Klein et al., 2018).

Bacellar et al. created a multi-scale analysis and shape and topology optimization framework for novel bare tube heat exchangers (Bacellar et al., 2017). A metal heat exchanger prototype was additively manufactured and experimentally validated under radiator and chilled water conditions (Bacellar et al., 2017; Z. Huang et al., 2020). Building upon this work, Tancabel et al. incorporated structural analysis to this shape and topology optimization framework using finite element analysis (FEA). Figure 20 shows the framework of the optimization method. The framework uses approximation-assisted optimization (AAO) (Simpson et al., 2001) utilizing CFD (Abdelaziz et al., 2010) and FEA, kriging metamodeling (Jones et al., 1998), and a MOGA scheme (Deb, 2001).

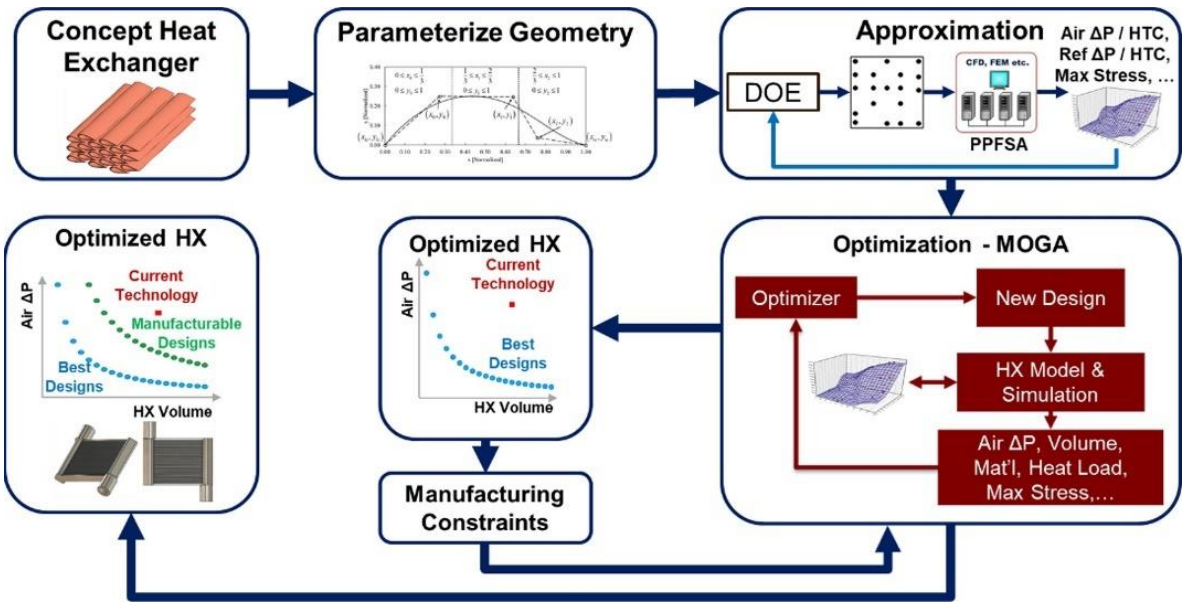

Figure 20: Shape and Topology Optimization Framework (Tancabel et al., 2022)

Both optimization frameworks utilized by both Tancabel et al. and Bacellar et al. use Non-Uniform Rational B-Splines (NURBS) to parameterize the geometry of the heat exchanger cross sectional shape. Hence, many of the heat exchangers named here are termed NURBS Tube Heat Exchanger NTHX. Table 16 lists all NTHX heat exchangers experimentally tested with heat exchanger dimensions, respective authors who optimized the heat exchanger design with respective references, and experimental conditions tested in this document. All optimizations were conducted by the Modeling and Optimization Consortium (MOC) group at CEEE and work conducted in this chapter is only experimental.

Table 16: NTHX Prototypes Overview

Heat Exchanger	**Picture**	**Core Dimensions (LxWxD) [mm]**	**Experimental Testing Conditions**	**References/ Comments**
NURBS Tube Heat Exchanger (NTHX1)	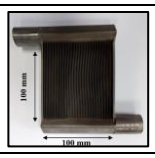	100x100x17	- Radiator - Dry Evaporator - Condenser	Bacellar et al., 2017; Z. Huang et al., 2020; Radermacher et al., 2017
Expanded NURBS Tube Heat Exchanger (ENTHX1)	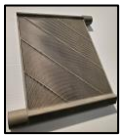	213x180x17	- Radiator	Same optimization framework as Bacellar et al., 2017
Copper NURBS Tube Heat Exchanger (CNTHX1)	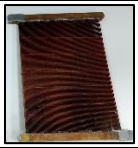	329x246x12.5	- Dry and Wet Evaporator	Tancabel et al., 2022
Copper NURBS Tube Heat Exchanger-Full Size (CNTHX-FS)		564x580x29	- Dry Evaporator	Same optimization framework as Tancabel et al., 2022
Polymer NURBS Tube Heat Exchanger (PNTHX)		208x107x43	- Radiator	Same optimization framework as Tancabel et al., 2022

The five novel heat exchangers in Table 16 were experimentally tested under a variety of different experimental conditions. All of these heat exchangers' cores are comprised of hundreds to thousands of bare tubes. Any fin-like structures in the core are there for structural support or assist in the construction process. Figure 21 shows a sample CAD rendered cross section of a NTHX prototype's core.

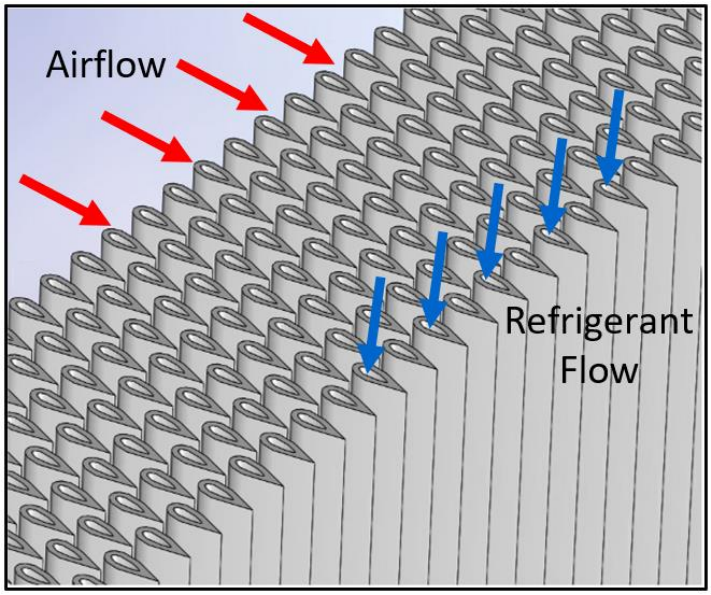

Figure 21: CAD Rendering of NTHX Cross Section

All of the heat exchangers listed in Table 16 have a similar teardrop shaped cross section. The following sections will present all the heat exchangers' experimental performance. At every measured steady state test point presented in this section, the capacity performance of each heat exchanger was predicted using CoilDesigner®, which is a finite volume heat exchanger model utilizing ε-NTU solver (Jiang et al., 2006). Air-side pressure drop predicted values are from 2D CFD simulations (Bacellar et al., 2017; Tancabel et al., 2022).

2.3.2 NTHX1 Experimental Performance

The first prototype, named "NTHX1", was fabricated using state-of-the-art metal additive manufacturing techniques (Bacellar et al., 2017; Z. Huang et al., 2020; Radermacher et al., 2017). A Laser-Powder Bed Fusion (L-PBF) printer was used. The final printed heat exchanger can be seen in Figure 22. NTHX1 is made of Grade 5 Titanium and has a designed capacity of 1 kW as a radiator. Grade 5 Titanium was chosen for reliability and to achieve the smallest feature thickness possible, i.e. tube wall thickness. Table 17 shows a summary of NTHX's characteristics and physical properties.

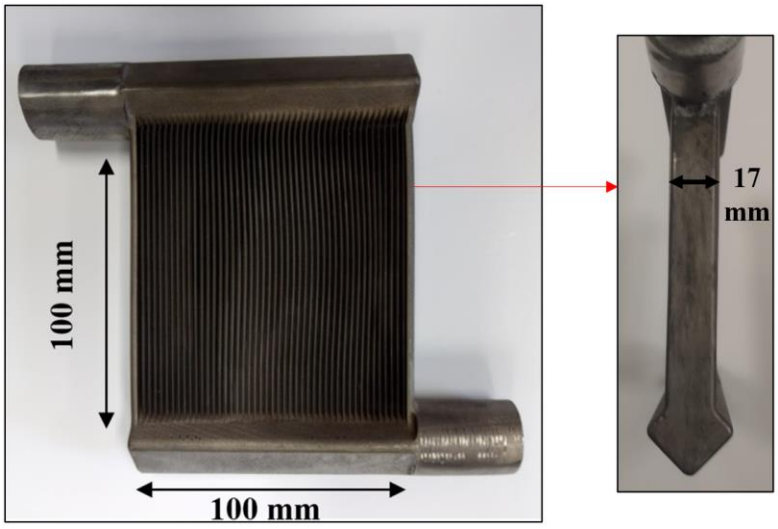

Figure 22: Additively Manufactured Titanium NTHX1

Table 17: NTHX1 Prototype Summary

Parameter	Units	Value
Core Dimensions (LxWxD)	[mm]	100 x 100 x 17
Envelope Volume (w/ headers)	[cm^2]	818.4
Core Volume (no headers)	[cm^2]	170.0
Frontal Area	[m^2]	0.01
Weight	[kg]	0.952
Material	-	Grade 5 Titanium
Manufacturing Process	-	Additive Manufacturing, L-PBF
No. Fluid Passes	-	1
No. Tubes	-	314
No. Banks	-	7
Tube Hydraulic Diameter (Air-Side)	[mm]	2-3

Before testing began, two preliminary tests were completed; these include a pressure test and a flow distribution (blockage) test. In a safe area, NTHX1 was pressurized to approximately 3000 kPa. A defect was found in the manifold port and was leaking at this pressure. Most likely the leak was due to increased material porosity at this location. The leak was sealed using a steel reinforced epoxy. Thermal imaging was taken of NTHX1 as cold fluid was flowed through the core to check if there are any tube blockages. More details on the repair and blockage thermal imaging can be found in Appendix C. NTHX1 was experimentally tested as a radiator, condenser (R134a), and a dry evaporator (R410A).

NTHX1 Radiator Testing

Prototype NTHX1 was experimentally tested under radiator conditions. Table 18 shows a condensed testing conditions summary. The water mass flow rate was varied between 30 to 70 grams per second and the air inlet velocity was varied between 3.6 to 7.0 m/s. In total, there were 15 steady state tests performed with each test lasting 30 minutes. Air-side and water-side capacity and pressure-drop were measured. Figure 23 shows the NTHX1 mounted inside the wind tunnel's test section and how water flows through the tubes from top to bottom against gravity.

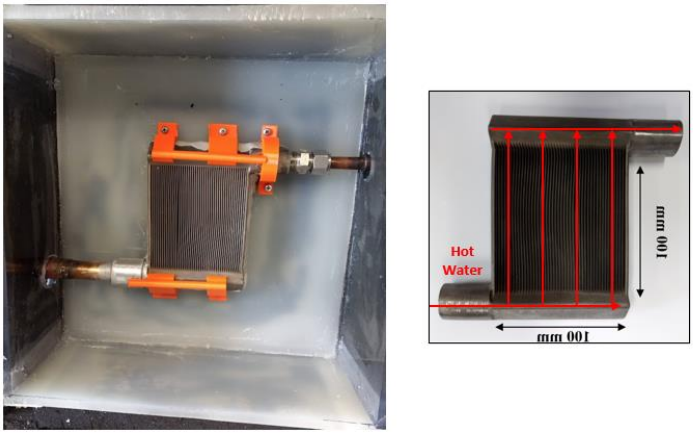

Figure 23: NTHX1 Mounted inside Wind-Tunnel for Radiator Testing and Hot Water's Flow Path

Table 18: NTHX1 Radiator Experimental Testing Summary

Parameter		Units	Value(s)
Water-Side	Mass Flow Rate	[g/s]	30 – 70
	Inlet Temperature	[°C]	60
Air-Side	Inlet Temperature	[°C]	35
	Inlet Velocity	[m/s]	3.2 – 7.0
	Inlet RH	[%]	< 20
	VFR	[m^3/s , CFM]	0.0326-0.070 , 69 – 148
Measured Performance	Air-Side Pressure Drop	[Pa]	62 - 205
	Water-Side Pressure Drop	[kPa]	2.2 – 4.6
	Nominal Capacity	[W]	496 - 855
	Energy balance	[%]	-5.0 – 2.4

Figure 24 shows the measured energy balance for all points and the measured water-side capacity versus the measured air-side capacity. The energy balance was below 5% for all 15 data points; indicating good agreement between the water-side and air-side capacity.

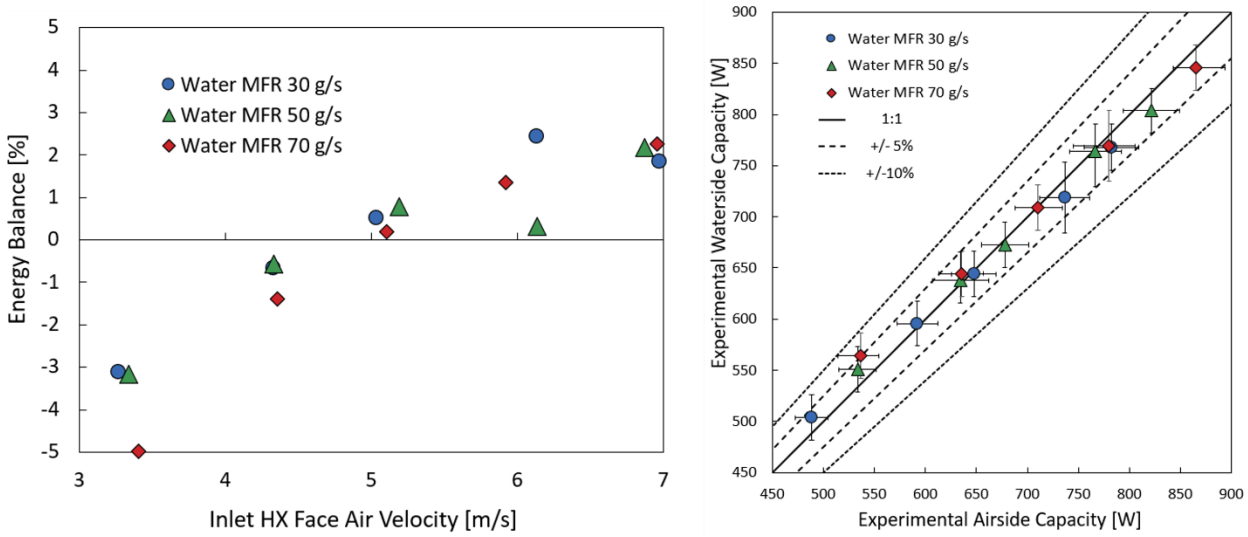

Figure 24: (Left) NTHX1 Radiator Energy Balance (Right) NTHX1 Radiator Experimental Water-Side versus Air-Side Capacity

Figure 25 shows the measured average nominal capacity as the air inlet velocity is varied. As inlet air velocity increases the heat exchanger capacity increases as well. This is because the average air-side heat transfer coefficient increases as the inlet air velocity increases. Since this is the lowest heat transfer coefficient it will have the most effect on changing the overall thermal resistance. The capacity increases with water mass flow rate as well, but the effect is less apparent.

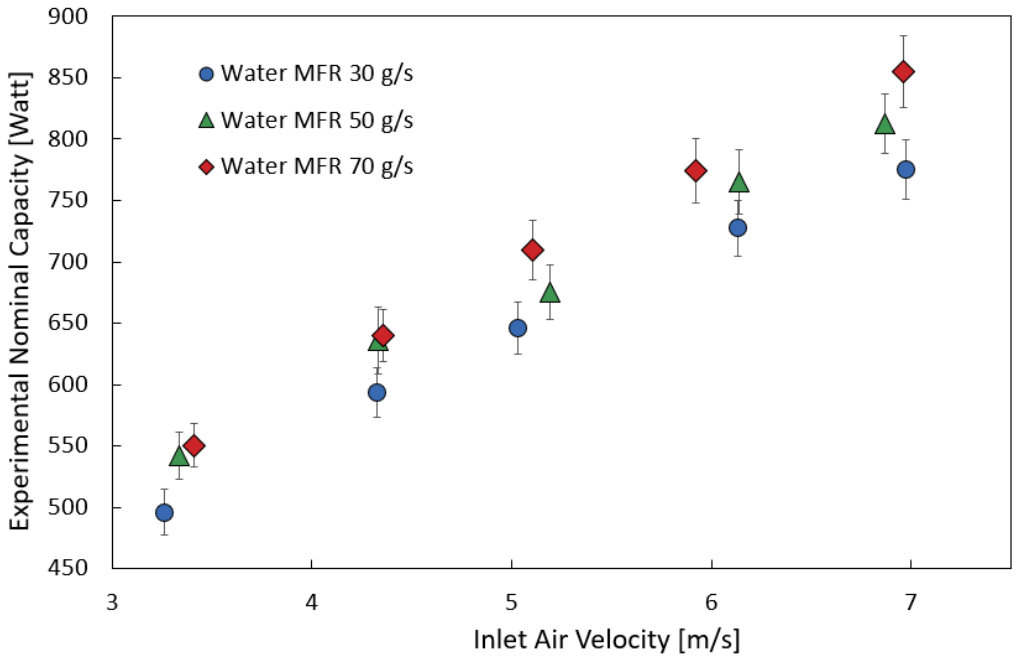

Figure 25: NTHX1 Radiator Nominal Capacity versus Inlet Air Velocity

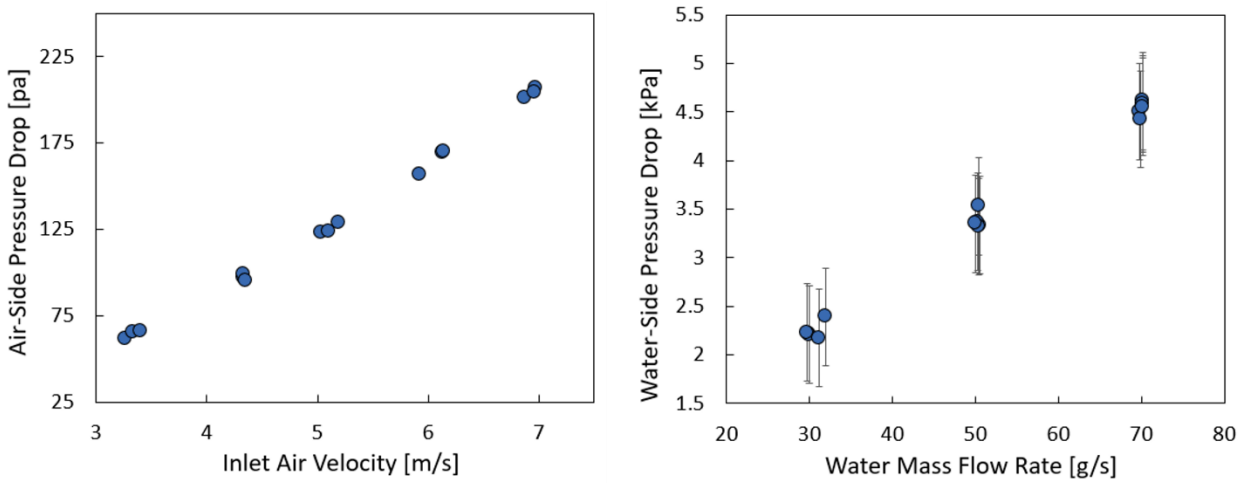

Figure 26: (Left) NTHX1 Air-Side Pressure Drop versus Inlet Air Velocity (Right) NTHX1 Water-side Pressure Drop versus Water Mass Flow Rate

Figure 26 shows the measured air-side and water-side pressure drop. Air-side experimental pressure drop uncertainty for all points was between 1.23-1.25 Pa.

Using Eq. 32, NTHX1's average air-side HTC was calculated. Inlet and outlet temperatures were used to estimate the correction factor F (Bowman et al., 1940). Water-side Re ranged from 225 to 530. Hence, it is in the laminar regime and the water-side average HTC was estimated using Eq. 33 (Baehr and Stephan, 2006), where Gz is the Graetz number, $Gz=(Dh_w/L_{tube})Re_wPr_w$. Air-side average HTC, j and f factors are shown in Figure *27*.

$$\overline{Nu}_{D_h,w} = \frac{\frac{3.66}{\tanh[2.264Gz^{-1/3}+1.7Gz^{-2/3}]}+0.0499Gz\tanh Gz^{-1}}{\tanh 2.432Pr^{1/6}Gz^{-1/6}} \qquad \text{Eq. 33}$$

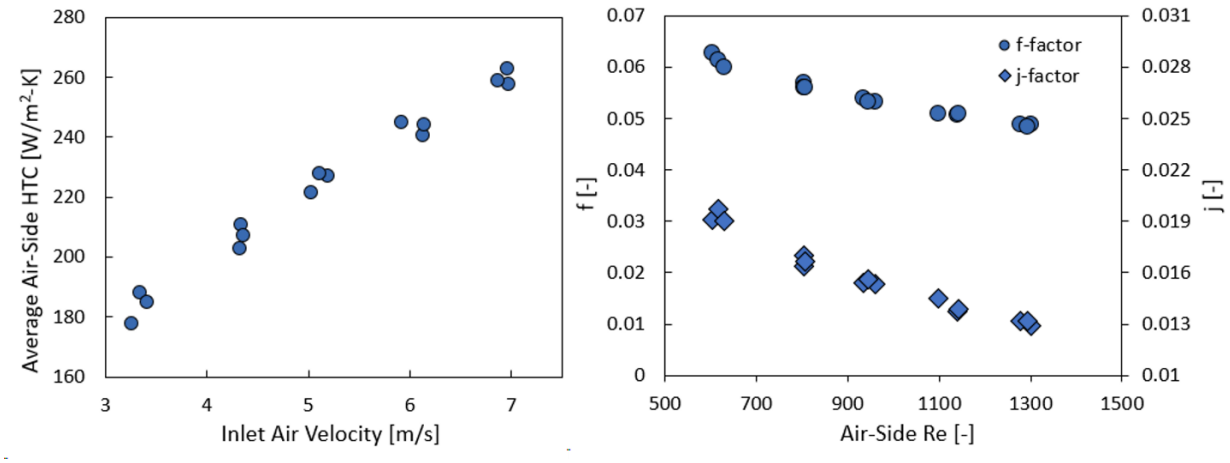

Figure 27: (Left) NTHX1 Average Air-Side HTC versus Inlet Air Velocity (Right) NTHX1 Air-Side f and j Factors versus Re Number

The air-side pressure-drop and heat transfer coefficients used in this simulation are based on CFD based correlations during the design and optimization of NTHX1. Figure 28 shows the comparison between the simulated and experimental capacity and pressure drop.

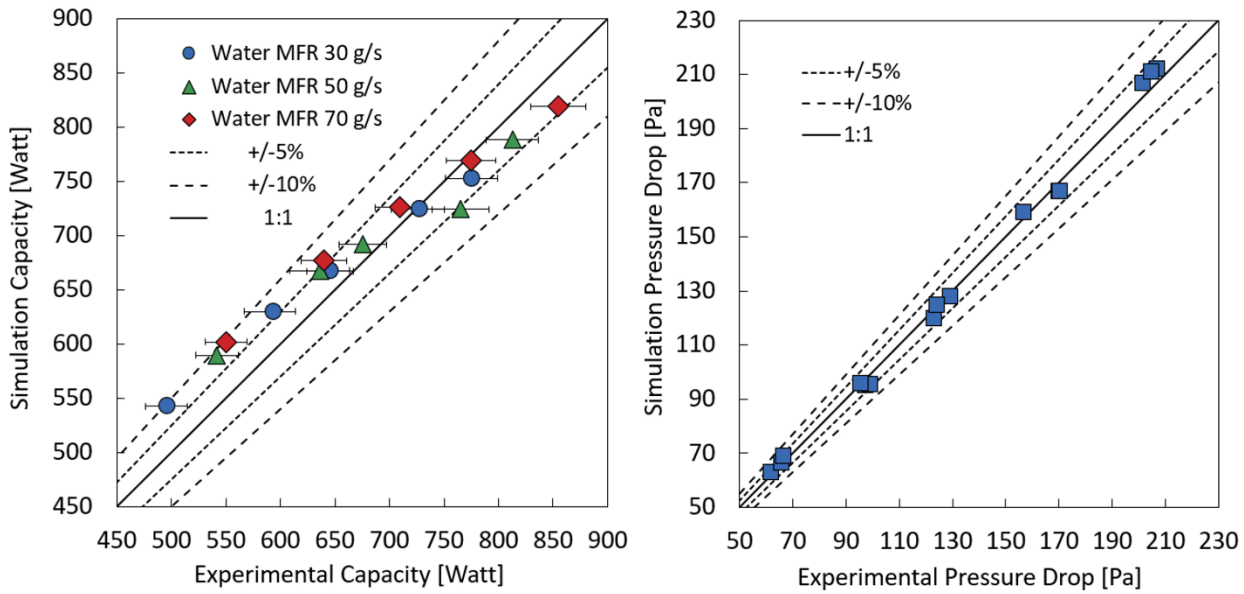

Figure 28: NTHX1 Radiator Testing Simulated versus Experimental (Left) Heat Transfer Capacity (Right) Air-Side Pressure Drop

For both airside pressure-drop and capacity, the simulated and experimental results are within 10% of one another. Showing excellent agreement between the simulated and experimental results. At lower capacity levels (~<700 W), the simulation tends to overpredict the performance and at higher capacity levels (~>700 W) it underpredicts. The highest deviation occurs at the lower capacities, 500-550 W. There is no clear trend with over/under prediction with air-side pressure drop. The highest deviation in air-side pressure drop occurs at the lowest values (60-70 Pa).

NTHX1 R-134a Condenser Testing

NTHX1 was tested under condenser conditions with R-134a. The air inlet temperature was 22 °C, and the R-134a condensing temperature was 42 °C. The refrigerant pumped loop at the time of this condenser testing was not able to achieve low enough R-134a mass flow rate to allow for complete condensation from superheated vapor to sub-cooled liquid. I.e., the air-side limits the total capacity and at a high refrigerant mass flow rate complete condensation from superheated vapor cannot be

achieved. So, the inlet refrigerant state to NTHX1 was two-phase with a quality varied between 0.15 – 0.36, and sub-cooling was maintained between 1-3 K to ensure no two-phase refrigerant was present at the outlet. The air mass flowrate was varied between 40 - 80 g/s, and the refrigerant mass flow rate was varied between 12, 17, and 24 g/s. A total of 15 steady state points were measured for 30 minutes each. NTHX1 was mounted in the wind tunnel similarly as shown in Figure 23, except the direction of refrigerant flow was reversed. R134a entered at the top right and flowed down with the force of gravity. Sub-cooled liquid builds up in the bottom header and flows out the bottom left port.

Table 19 shows a condensed testing conditions summary.

Table 19: NTHX1 Condenser Experimental Testing Summary

Parameter		Units	Value(s)
R-134a	Mass Flow Rate	[g/s]	11.8 – 24.1
	Condensing Temperature	[°C]	41.7 – 43.4
	Inlet Quality	[-]	0.11 – 0.35
	Sub-Cooling	[K]	1.1 – 3.1
Air	Inlet Temperature	[°C]	21.7
	Inlet Velocity	[m/s]	3.4 – 6.9
	Inlet RH	[%]	40 – 50
	VFR	[m^3/s CFM]	0.0335-0.069, 71 – 146
Measured Performance	Air-Side Pressure Drop	[Pa]	67 – 206
	Nominal Capacity	[W]	476 – 746
	Energy balance	[%]	-5.0 – 3.1

Figure 29 shows the energy balance for all 15 points and the measured R134a versus air-side capacity. Figure 30 shows the measured air-side capacity and pressure drop. Figure 31 shows the predicted versus measured air-side thermal-hydraulic performance.

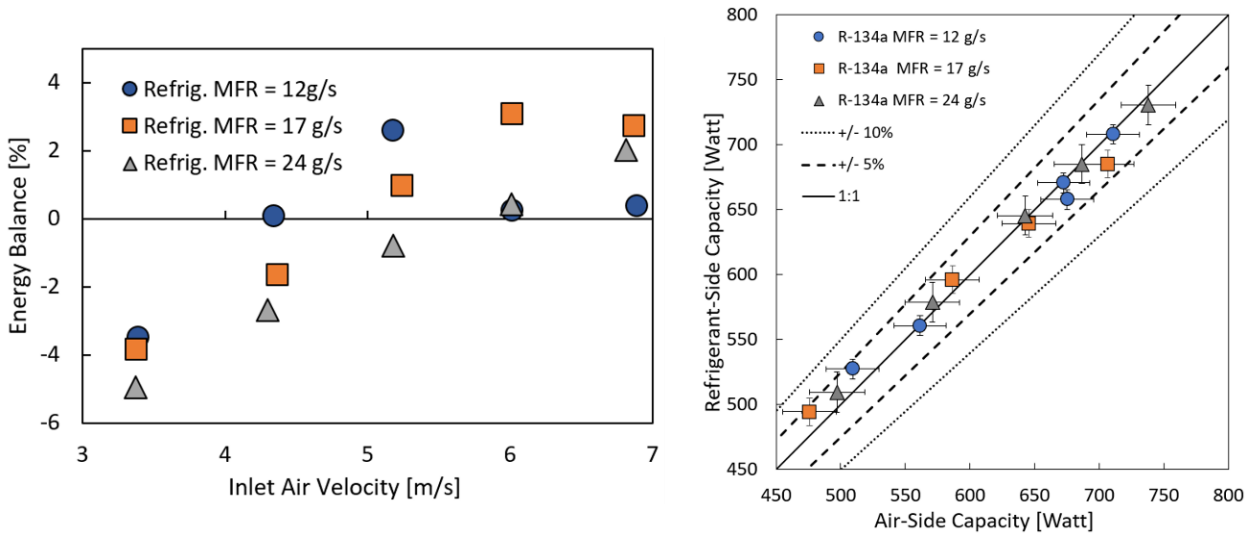

Figure 29: (Left) NTHX1 R134a Condenser Energy Balance (Right) NTHX1 Condenser Experimental Refrigerant-Side versus Air-Side Capacity

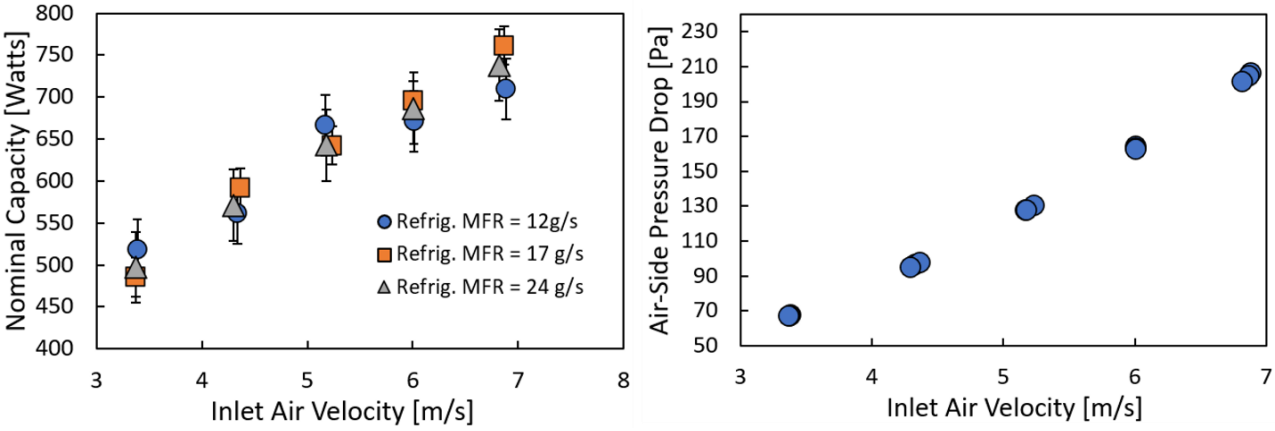

Figure 30: NTHX1 Condenser Measured (Left) Nominal Capacity (Right) Air-Side Pressure Drop

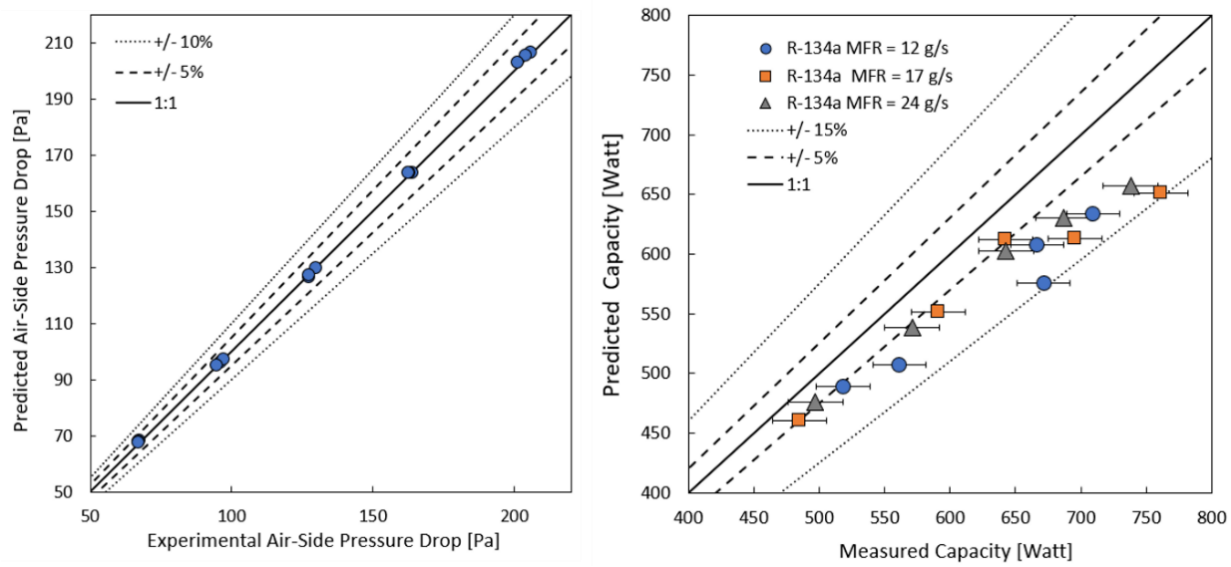

Figure 31: NTHX1 Condenser Testing Simulated versus Experimental (Left) Heat Transfer Capacity (Right) Air-Side Pressure Drop

The air-side pressure-drop and nominal capacity were predicted within 5% and 15%, respectively. Showing excellent agreement between the simulated and experimental results. The simulation consistently underpredicted the capacity. There is no clear trend with over/under prediction with air-side pressure drop. The highest deviation in air-side pressure drop occurs at the lowest values (~60-70 Pa).

NTHX1 R-410A Evaporator Testing

NTHX1 was tested under dry evaporator conditions with R-410A. The test conditions were based by AHRI standard 210/240 (AHRI, 2023). The inlet air relative humidity was always kept below 20% to avoid any latent load and, at least 1K superheat was required to ensure no two-phase refrigerant was present at the outlet of the heat exchanger where the state of the refrigerant was measured. Three different evaporation temperatures were measured, 10, 14, and 16 °C. Only one data point was measured for 14°C and 16°C, each with an inlet air velocity of 3.7 m/s. The

objective was to demonstrate the capability of NTHX1 as a sensible evaporator at different evaporation temperatures. At an evaporation temperature of 10°C, nine data points were measured with inlet air velocity ranging from 4.5 to 6.4 m/s and R410A mass flow rate between 3.0 – 4.6 g/s. All 12 steady state points were for a minimum of 20 minutes. NTHX1 was mounted in the wind tunnel similarly as shown in Figure 23. R-410A two-phase entered the bottom header and then flowed upward during the evaporation process, and superheated vapor built up in the top header. Table 20 shows a condensed testing conditions summary.

Table 20: NTHX1 Evaporator Experimental Testing Summary

	Parameter	Units	Value(s)
R410A	Mass Flow Rate	[g/s]	3.0 – 4.6
	Evaporation Temperature	[°C]	10 – 16
	Inlet Quality	[-]	0.30 – 0.33
	Superheat	[K]	1.2 – 7.4
Air	Inlet Temperature	[°C]	30 – 34
	Inlet Velocity	[m/s]	3.7 – 6.4
	Inlet RH	[%]	< 20
	VFR	[m^3/s, CFM]	0.036 – 0.063, 76 – 134
Measured Performance	Air-Side Pressure Drop	[Pa]	68 – 190
	Nominal Capacity	[W]	411 – 704
	Energy balance	[%]	-4.7 – 1.4

The energy balance between the measured air-side and water-side capacity for all twenty points were within ±5.0% and is shown in Figure 32. The measured capacity and air-side pressure drop are shown in Figure 33 and Figure 34, respectively. Lastly, the comparison between the predicted and measured capacity and between the predicted and measured air-side pressure drop are shown in Figure 36.

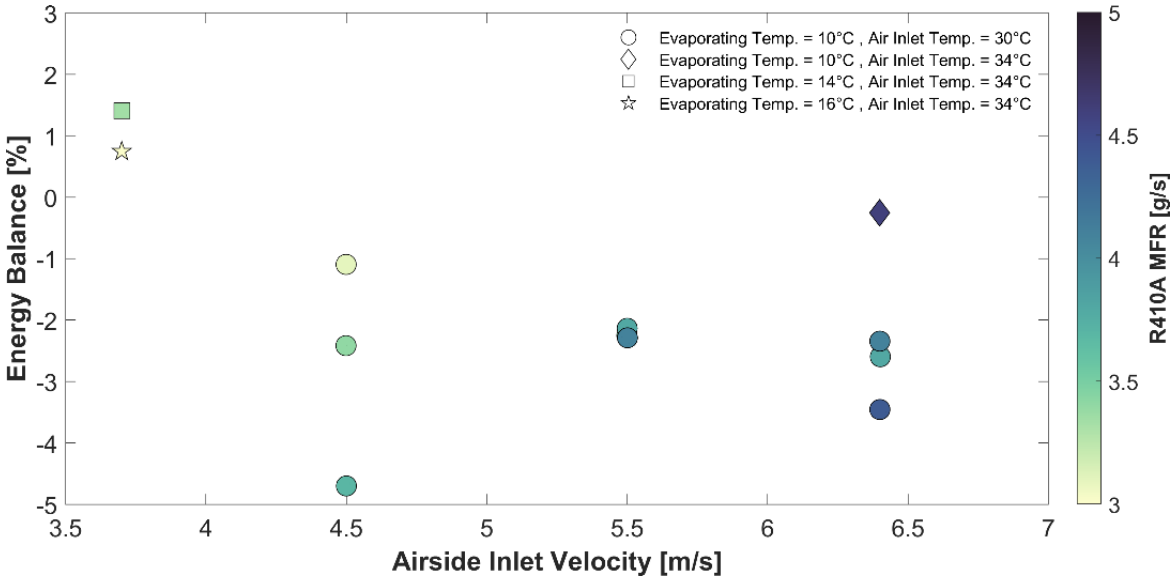

Figure 32: NTHX1 Energy Balance between Measured Refrigerant-Side and Air-Side Capacity

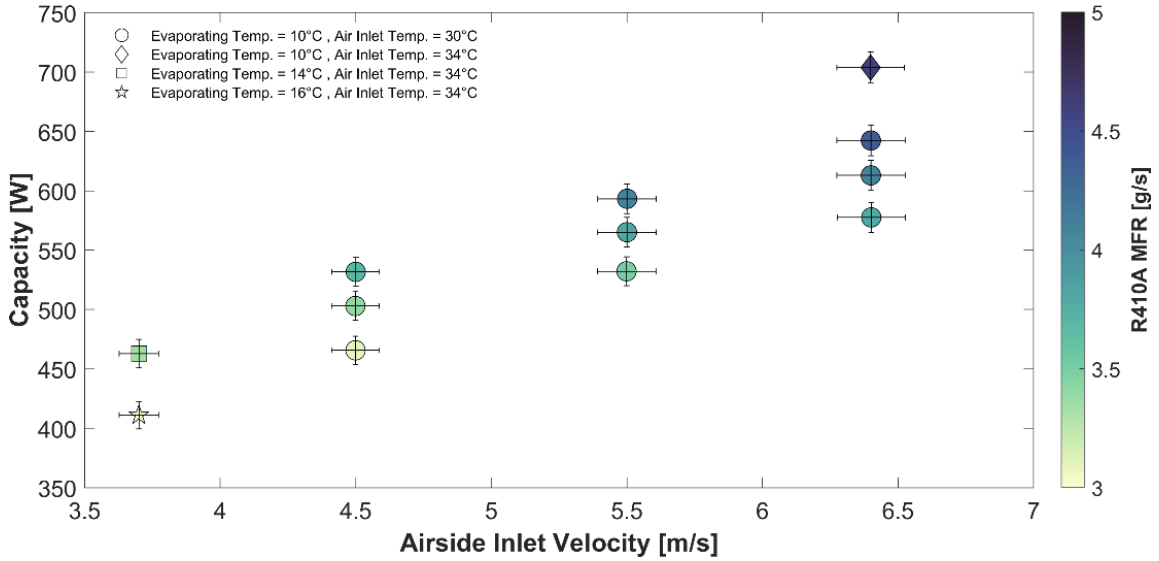

Figure 33: NTHX1 Measured Capacity under Dry Evaporator Conditions

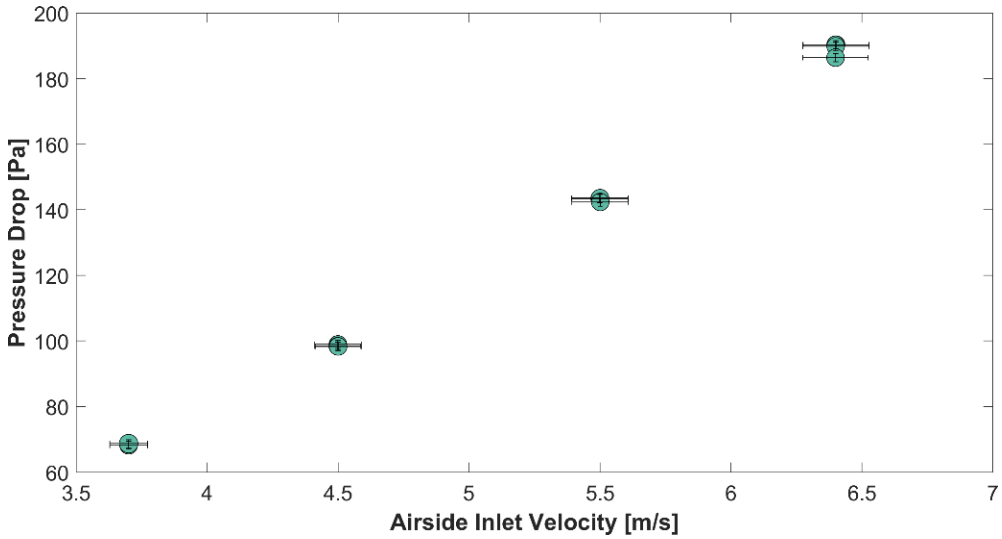

Figure 34: NTHX1 Measured Air-Side Pressure Drop under Dry Evaporator Conditions

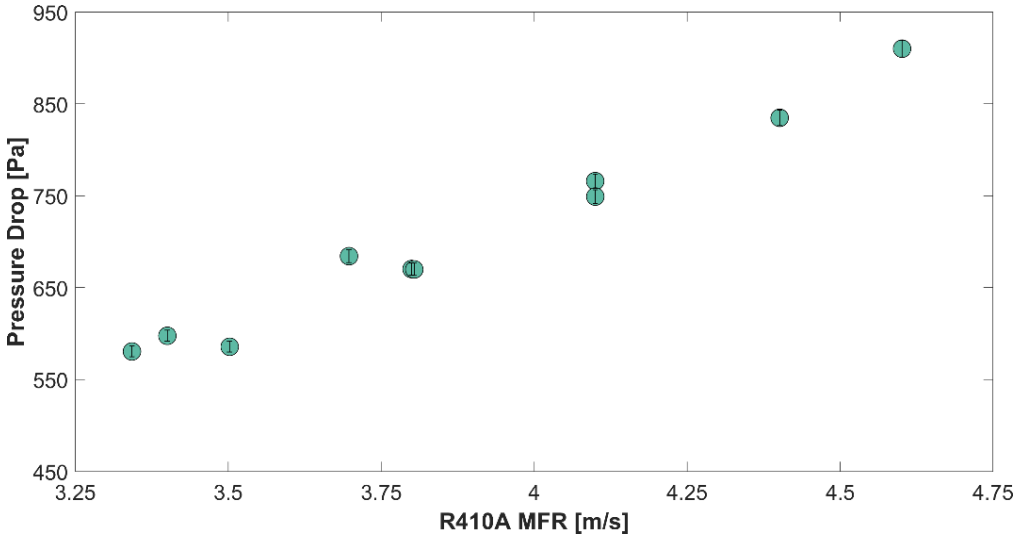

Figure 35: NTHX1 R410A Pressure Drop versus Mass Flow Rate

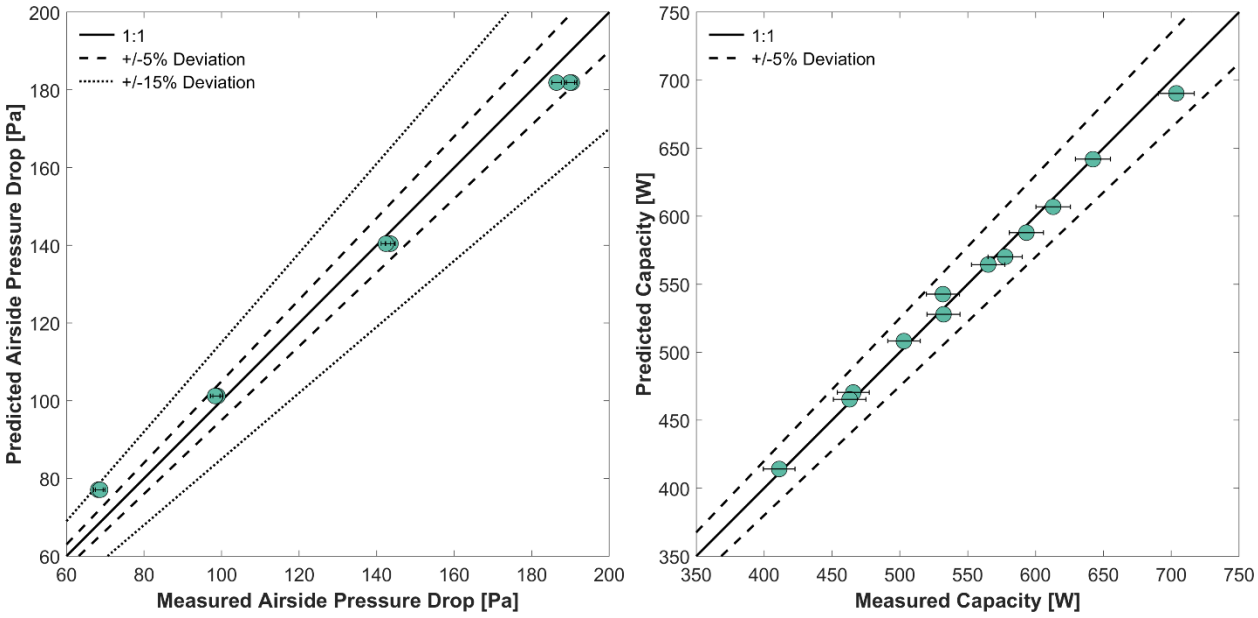

Figure 36: (Left) NTHX1 Evaporator Air-Side Pressure Drop Validation Plot (Right) NTHX1 Capacity Validation Plot

The nominal capacity was predicted within ±5% of the measured values, and air-side pressure drop was predicted within ±15% of the measured value. Showing excellent agreement between the simulated and experimental results. There is no clear trend with over/under prediction of capacity. The simulation overpredicts the air-side pressure drop at the lower inlet air velocities and underpredicts at higher inlet air velocities. The highest deviation in air-side pressure drop occurs at the lowest values (60-70 Pa).

NTHX1 Experimental Testing Summary

NTHX1 was experimentally tested as a radiator, condenser (R-134a), and dry evaporator (R-410A). Energy balance for all testing was within +/-5%. The comprehensive testing of NTHX1 demonstrates the capability of additive manufacturing to build functional heat exchangers that perform well under a variety of HVAC applications. NTHX1's heat transfer capacity and air-side pressure drop under all testing conditions is shown in Figure 37 and Figure 38, respectively.

Capacity and air-side pressure drop were predicted within +/- 15%; indicating excellent agreement between the simulated and experimental performance.

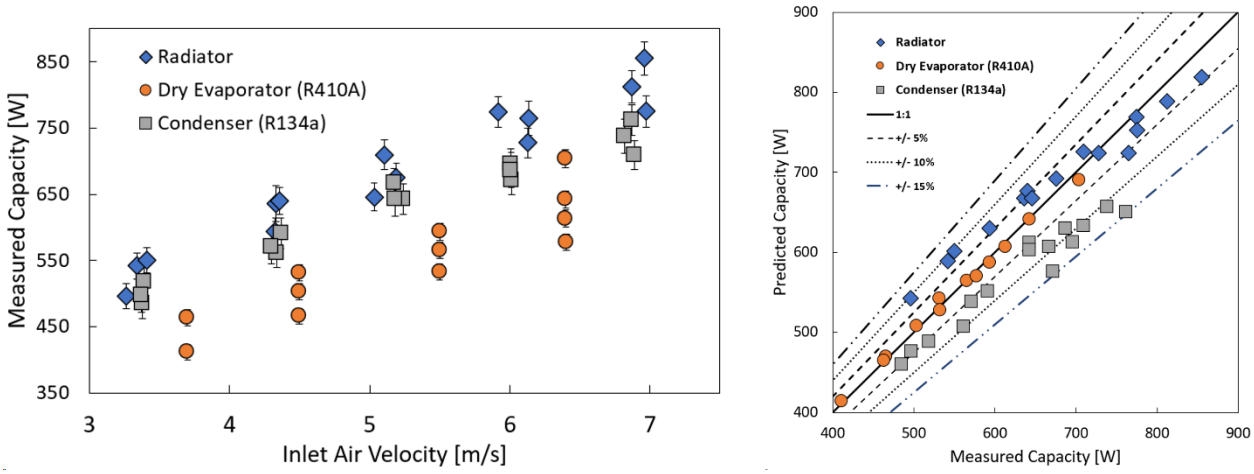

Figure 37: (Left) NTHX1 Compiled Measured Capacity under all Testing Conditions (Right) NTHX1 Compiled Capacity Validation Plot

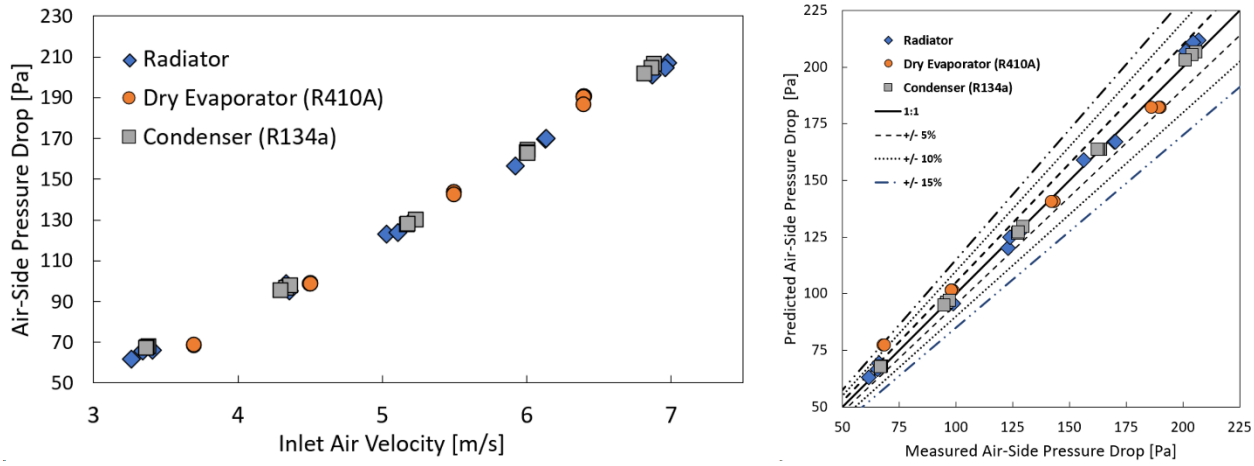

Figure 38: (Left) NTHX1 Compiled Measured Air-Side Pressure Drop under all Testing Conditions (Right) NTHX1 Compiled Air-Side Pressure Drop Validation Plot

2.3.3 ENTHX1 Experimental Performance

The prototype termed, Expanded-NTHX-1 (ENTHX1), was designed as a 2-3 kW radiator. Its lower capacity predecessor, NTHX1, has a capacity of 1 kW and a face area of 0.01 m^2. NTHX1's performance was measured under radiator, evaporator, and condenser conditions, but the lowest inlet air velocity reached during testing was 3.2 m/s at a volumetric flow rate of 0.032 m^3/s. This volumetric flow rate was the lowest measurable with the wind tunnel used for testing. However, many heat exchangers used for residential applications have an inlet air velocity lower than 3.2 m/s. It was desired to measure this heat exchanger design's performance at lower inlet air velocities. The solution was to additively manufacture a heat exchanger with a larger face area so at the same air-side volumetric flow rate of 0.032 m^3/s, lower inlet air velocities would be achieved. The heat exchanger was manufactured using L-PBF through the direct manufacturing services of Sintavia LLC (Sintavia LLC, 2023). This new heat exchanger is termed ENTHX1 and has the same bare tube shape and topology as NTHX1 but a larger face area. The only other major difference is the addition of diagonal supports to reduce the risk of damaging the tubes due to bending or vibrations. Figure 39 shows a comparison between the two prototypes and Figure 40 shows the 3D printed prototype.

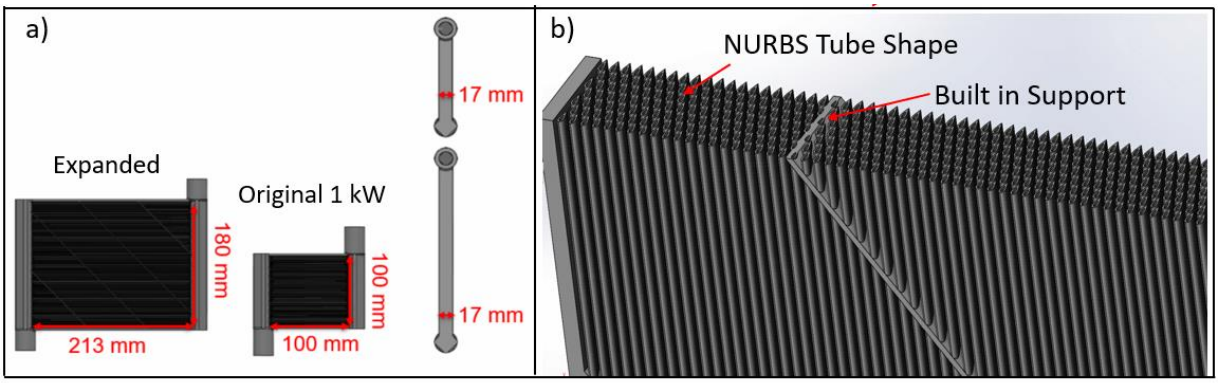

Figure 39: (Left) Dimensions of NTHX1 and ENTHX1 (Right) CAD Rendering Cross-Section of ENTHX1

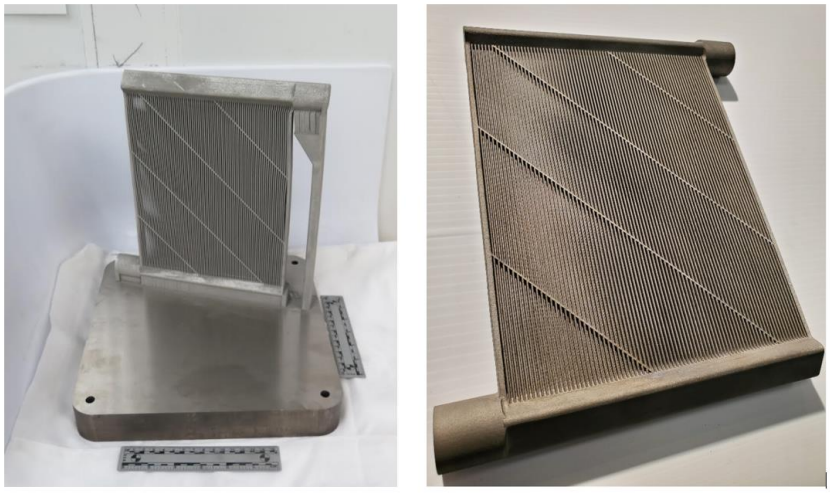

Figure 40: (Left) ENTHX1 Immediately after being Printed (Right) ENTHX1 Finished Product

Table 21 shows a summary of ENTHX's characteristics and physical properties and Figure 41 shows its overall dimensions.

Table 21: ENTHX1 Prototype Summary

Parameter	Units	Value
Core Dimensions (LxWxD)	[mm]	213 x 180 x 17
Envelope Volume (w/ headers)	[cm^3]	1631
Core Volume	[cm^3]	651.8
Frontal Area	[m^2]	0.038
Weight	[kg]	1.84
Material	-	Grade 5 Titanium
Manufacturing Process	-	Additive Manufacturing, L-PBF
No. Fluid Passes	-	1
No. Tubes	-	567
No. Banks	-	7
Tube Hydraulic Diameter (Air-Side)	[mm]	2-3

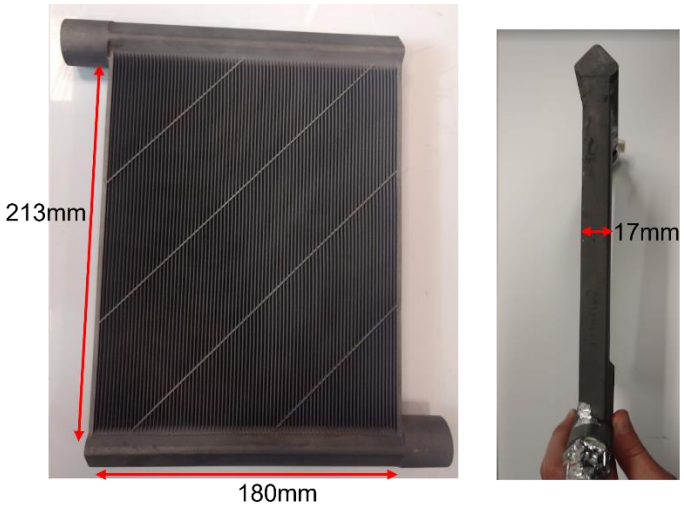

Figure 41: Additively Manufactured Titanium ENTHX1

Before testing began, a flow distribution (blockage) test was conducted. Thermal images were taken of ENTHX1 with a FLIR ONE Pro infrared camera as cold water was flowed through the core to check if there are any tube blockages. No blockages were found and ENTHX1 was deemed ready for experimental radiator testing. Additionally, ENTHX1 was pressurized to 50 kPa with no leaks found.

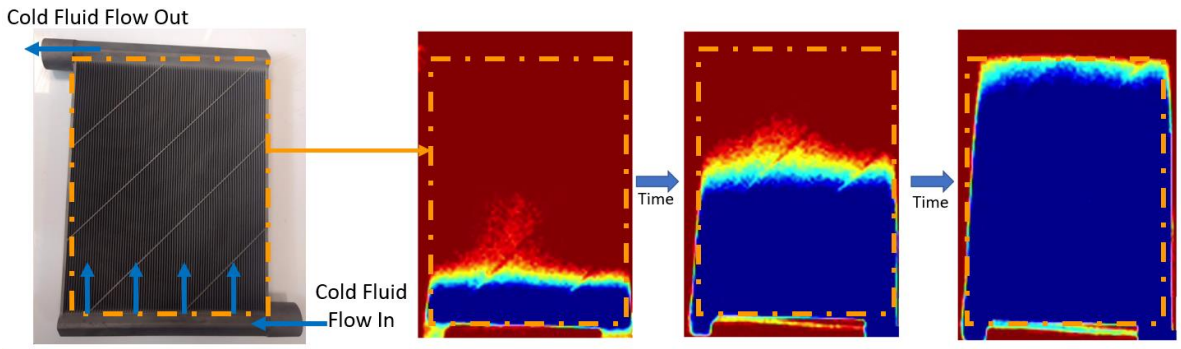

Figure 42: ENTHX1 Thermal Image Blockage Test

ENTHX1 was experimentally tested under radiator conditions (air-to-water). Figure 43 shows ENTHX1 mounted in the wind tunnel section. Hot water flows into the bottom header, flows up the tubes against gravity, and then the chilled water exits the top header.

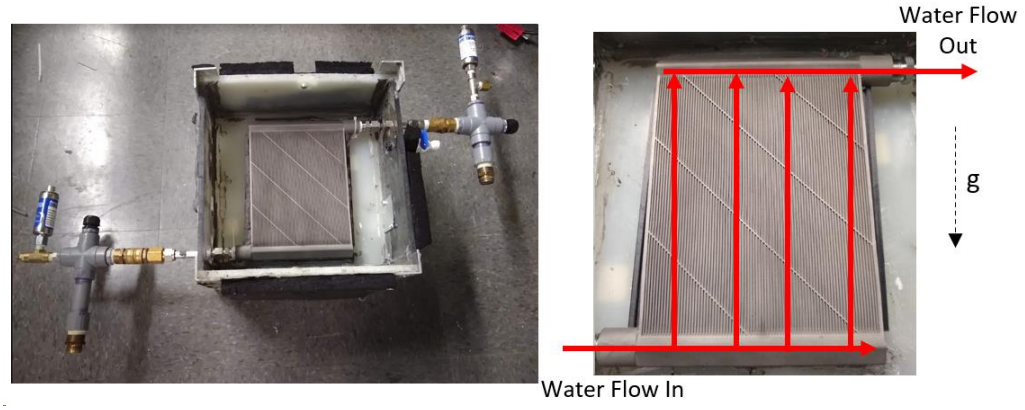

Figure 43: ENTHX1 Mounted in Wind Tunnel Test Section for Radiator Testing

Table 22: ENTHX1 Radiator Experimental Testing Summary

Parameter		Units	Value(s)
Water-Side	Mass Flow Rate	[g/s]	40 – 100
	Inlet Temperature	[°C]	60
Air-Side	Inlet Temperature	[°C]	35
	Inlet Velocity	[m/s]	1.0 – 5.0
	Inlet RH	[%]	< 20
	VFR	[m^3/s, CFM]	0.040-0.196, 84 – 415
Measured Performance	Air-Side Pressure Drop	[Pa]	22.7 – 212.8
	Water-Side Pressure Drop	[kPa]	0.91 – 3.06
	Nominal Capacity	[W]	940 – 2828
	Energy balance	[%]	-4.7 – 0.9

Twenty steady state points were measured; each over a time period of at least 20 minutes. Air inlet air velocity varied from 1-5 m/s. At each air inlet velocity water mass flow rate was varied between

40-100 g/s. The energy balance for all twenty points was within ±5.0% and is shown in Figure 44; indicating excellent agreement between the measured water-side and air-side capacity. The measured capacity versus inlet air velocity is shown in Figure 45. Air-side and water-side pressure drop is shown in Figure 46. Lastly, the comparison between the predicted and measured capacity and between the predicted and measured air-side pressure drop are shown in Figure 47.

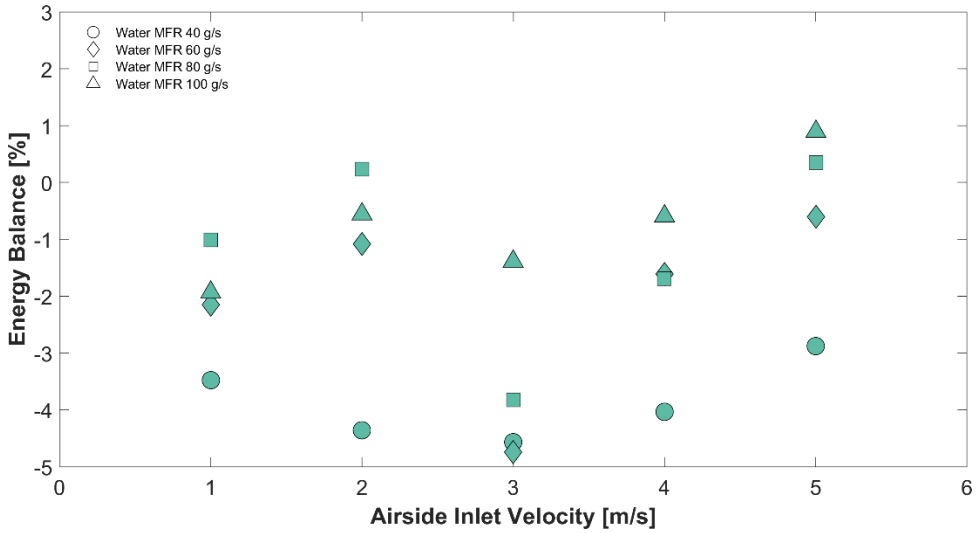

Figure 44: ENTHX1 Energy Balance between Measured Water-Side and Air-Side Capacity

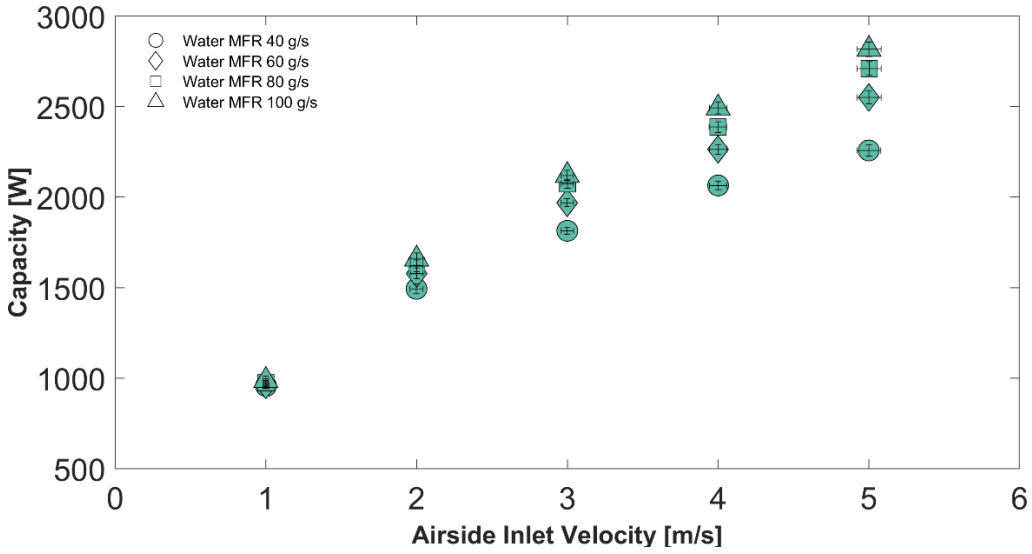

Figure 45: ENTHX1 Radiator Measured Nominal Heat Transfer Capacity

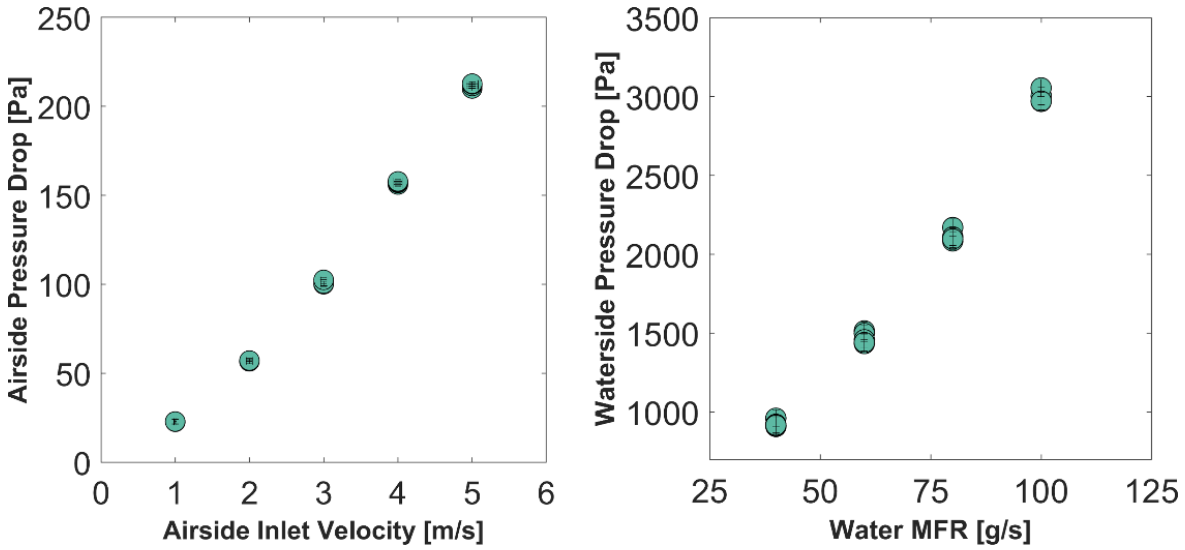

Figure 46: (Left) ENTHX1 Air-Side Pressure Drop versus Inlet Air Velocity (Right) ENTHX1 Water-side Pressure Drop versus Water Mass Flow Rate

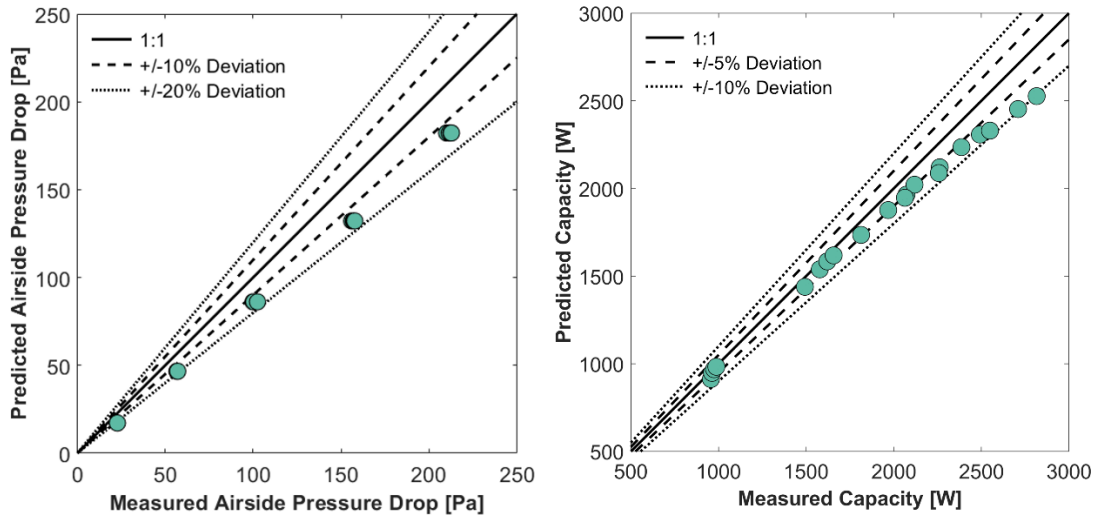

Figure 47: (Left) ENTHX1 Air-Side Pressure Drop Validation Plot (Right) ENTHX1 Capacity Validation Plot

The capacity was predicted within ±10% of the measured values, and air-side pressure drop was predicted within ±20% of the measured values. Note, the only difference between ENTHX1 and NTHX1 is the total face area. They have the same tube shape and topology and core depth of

17mm. Hence, at the same inlet air velocity the air-side pressure drop should be equal. However, ENTHX1's air-side pressure drop is significantly higher than NTHX1, Figure 48.

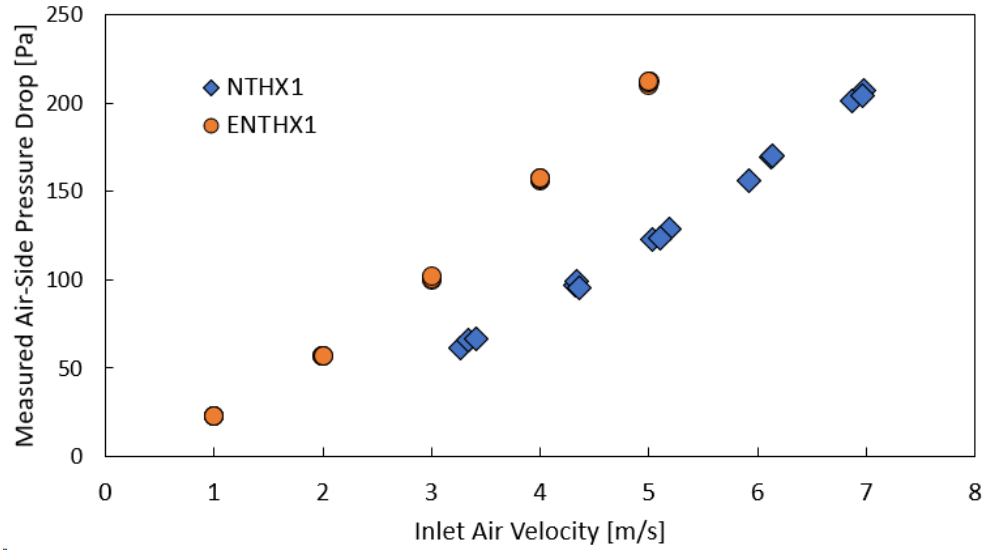

Figure 48: Comparison of ENTHX1 and NTHX1 Air-Side Pressure Drop at Similar Air Velocities

ENTHX1 has 60-70% higher airside pressure drop when compared to NTHX1 at similar air inlet velocity. ENTHX1's higher air-side pressure drop values are attributed to the significantly higher surface roughness and addition of the diagonal supports. ENTHX1's surface roughness is estimated to be ~ 6.35-10.2 µm. The original NTHX1 prototype is considerably smoother than ENTHX1 with an estimated surface roughness of ~3.8 - 6.1 µm. Figure 47 predicted CFD air-side pressure drop assumed a surface roughness of ~10.2 µm for ENTHX1. A takeaway from all this is that when designing compact air-to-refrigerant heat exchangers, one must take into consideration the final surface roughness of the printed material as it could drastically increase the air-side pressure drop.

Using Eq. 32 ENTHX's average air-side HTC was calculated. Inlet and outlet temperatures were used to estimate the correction factor F (Bowman et al., 1940). Water-side Re ranged from 160 to 425. Hence, it is in the laminar regime and the water-side average HTC was estimated using Eq. 33 (Baehr and Stephan, 2006), where Gz is the Graetz number, $Gz=(Dh_w/L_{tube})Re_wPr_w$. Air-side average HTC, j and f factors are shown in Figure 49.

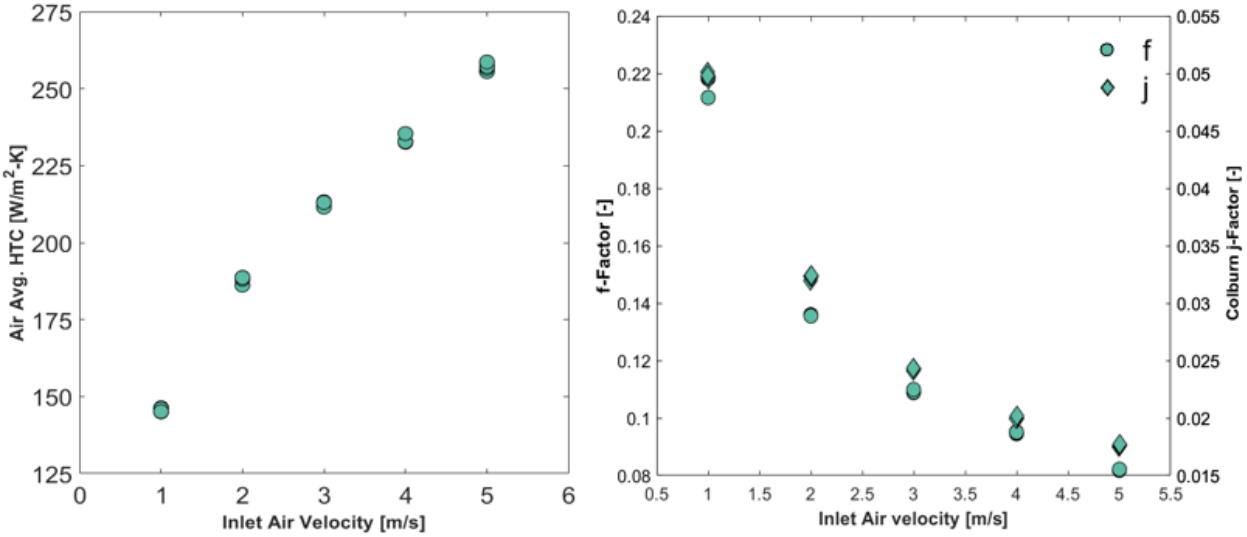

Figure 49: (Left) ENTHX1 Air-Side Average Heat Transfer Coefficient (Right) Air-Side f-Factor and Colburn j-Factor

Additionally, thermal images were taken during steady state testing to investigate the water-side flow and temperature distribution. Four thermal images were taken in total at an inlet air velocity of 2 m/s at a water-side mass flow rate of 40, 60, 80, and 100 g/s. The camera view is of the air outlet side. The images show relatively uniform temperature distribution as the water flows upwards through the bare tubes. Indicating low water-side and air-side flow maldistribution. Note there is some distortion in the thermal image on the top left corner and some debris at the very bottom causing a cold spot reading.

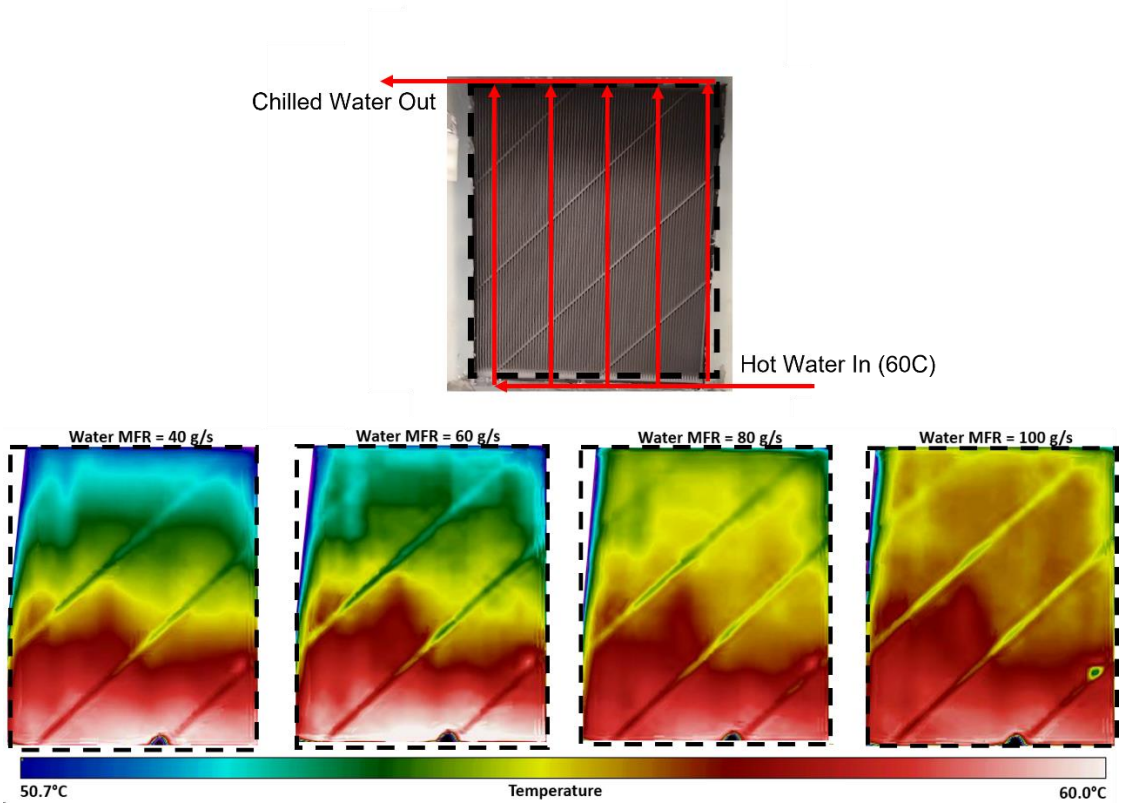

Figure 50: ENTHX1 Thermal Imaging of Outlet Air Face at Inlet Air Velocity of 2 m/s

2.3.4 CNTHX1 Experimental Performance

A finless 1-2 kW Copper crossflow air-to-refrigerant (R-410A) heat exchanger, termed "Copper NURBS Tube Heat Exchanger-1" (CNTHX1), was fabricated by Heat Transfer Technologies LLC using conventional manufacturing methods without the aid of any AM. The tubes were created using an extrusion method and then assembled to the headers using a soldering process. No additive manufacturing was used during the creation of this heat exchanger. CNTHX1 was designed and optimized for air-to-refrigerant (R-410A) two-phase applications. When compared to a state-of-the-art tube-fin air-to-refrigerant heat exchanger, it was designed to have 20% reduction in envelope volume, 20% reduction in air-side pressure drop, and 30% reduction of

internal volume with equal to or greater capacity and the same airside pressure drop (Tancabel et al., 2022). Figure 51 shows the completed heat exchanger. The core of the heat exchanger has a twist but was straightened when mounted in the wind tunnel for testing. Spacers are evenly distributed throughout the core and were used to assist during the construction process; they are not intended to act as an extended heat transfer surface. Table 23 shows a summary of CNTHX1's characteristics and physical properties.

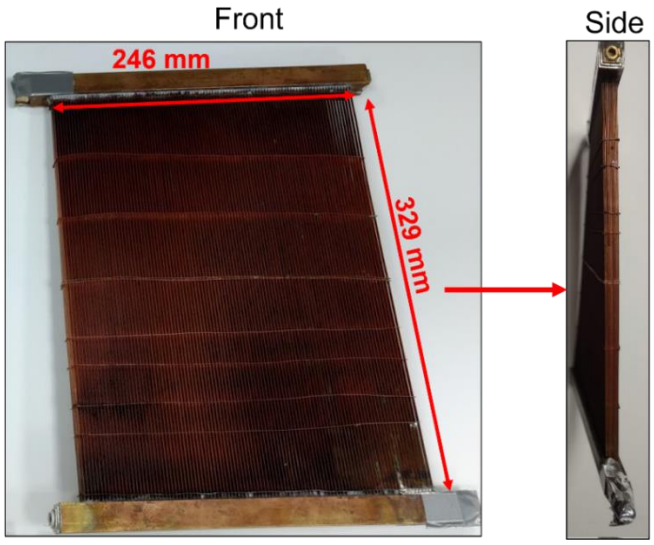

Figure 51: 1-2 kW CNTHX1, Manufactured using Conventional Methods

Table 23: CNTHX1 Prototype Summary

Parameter	Units	Value
Core Dimensions (LxWxD)	[mm]	329 x 246 x 12.5
Envelope Volume (w/ headers)	[cm^3]	1943.5
Core Envelope Volume	[cm^3]	1011.7
Frontal Area	[m^2]	0.081
Weight	[kg]	2.17
Material	-	Copper
Manufacturing Process	-	Tube Extrusions + Solder Connections
No. Fluid Passes	-	1
No. Tubes	-	515
No. Banks	-	5
Tube Hydraulic Diameter (Air-Side)	[mm]	2-3

Before testing began, two preliminary tests were completed; these include a pressure test and a flow distribution (blockage) test. In a safe area, CNTHX1 was pressurized to an absolute pressure of 2850 kPa and it successfully held this pressure for 48 hours. Next, thermal imaging was conducted while chilled isopropyl alcohol flowed through the heat exchanger to check for major tube blockages. Thermal imaging showed an even distribution of chilled Isopropyl Alcohol as it filled CNTHX1; indicating there are no tube blockages.

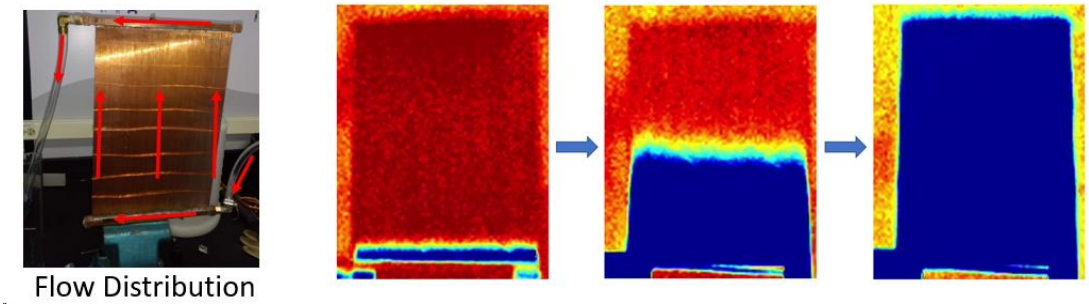

Figure 52: CNTHX1 Thermal Image Blockage Test

CNTHX1 Dry Evaporator Testing

Heat exchanger prototype CNTHX1 was first tested under air-to-refrigerant (R-410A) dry evaporator conditions. The test conditions were based on AHRI Standard 210/140 Test C (AHRI, 2023). A total of 12 steady states points were obtained. The air inlet velocity and R410A mass flow rate were varied, and the R410A inlet quality of 0.19 was kept constant. Superheat greater than 6.0 K was obtained for all tests to ensure no two-phase refrigerant exits the heat exchanger. Table 24 shows a condensed testing summary.

Table 24: CNTHX1 Dry Evaporator Experimental Testing Summary

Parameter		Units	Value(s)
R-410A	Mass Flow Rate	[g/s]	5.0 - 9.5
	Evaporation Temperature	[°C]	10.0
	Inlet Quality	[-]	0.19
	Superheat	[K]	6.3 – 12.9
Air	Inlet Temperature	[°C]	26.7
	Inlet Velocity	[m/s]	1.0 – 2.5
	Inlet RH	[%]	< 22
	VFR	[m^3/s , CFM]	0.081-0.202 , 172 – 429
Measured Performance	Air-Side Pressure Drop	[Pa]	6.4 – 24.6
	Nominal Capacity	[W]	874 – 1675
	Energy balance	[%]	-5.1 – -0.1

Figure 53 shows CNTHX1 set-up in the wind tunnel and the flow distribution. R410A flows into the bottom header as two-phase and then flows upwards against the force of gravity. Superheated vapor collects in the top header and then flows out.

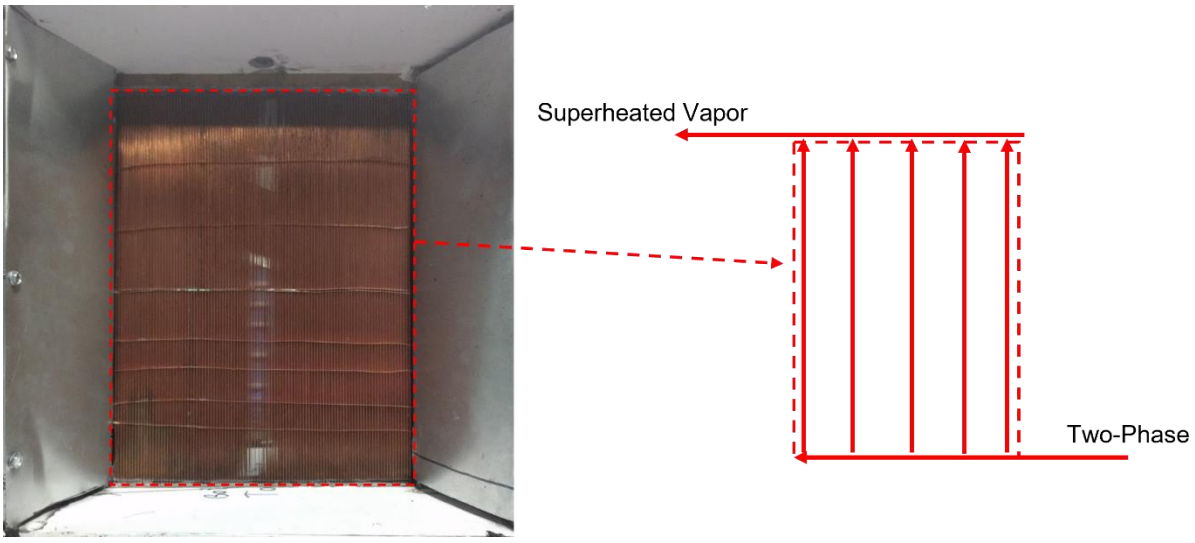

Figure 53: CNTHX1 Mounted in Wind Tunnel Test Section and Flow Distribution

Figure 54 shows the energy balance for all 12 points. They are all between -5.1% and -0.1%; indicating good agreement between the capacity measured on the refrigerant-side and the air-side. Figure 55 and Figure 56 show the measured nominal capacity and air-side pressure drop, respectively. Figure 57 shows the measured refrigerant-side pressure drop, respectively. Lastly, the comparison between the predicted and measured capacity and between the predicted and measured air-side pressure drop are shown in Figure 58.

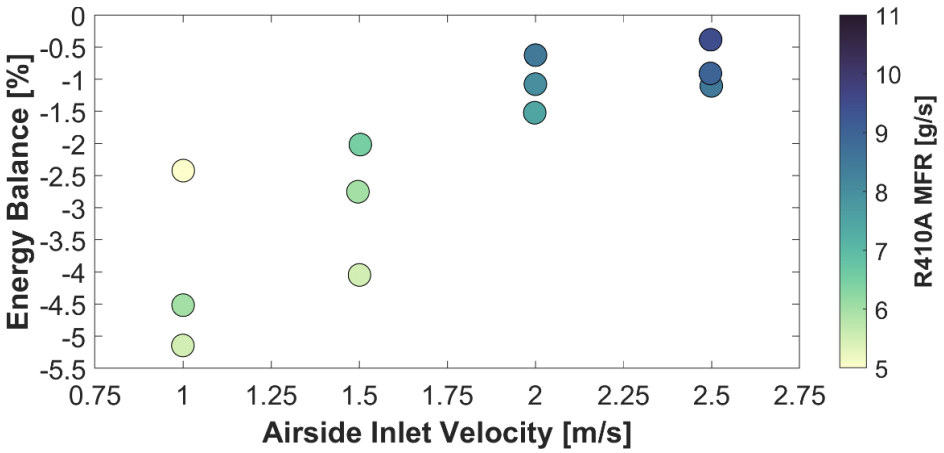

Figure 54: CNTHX1 Dry Evaporator Energy Balance

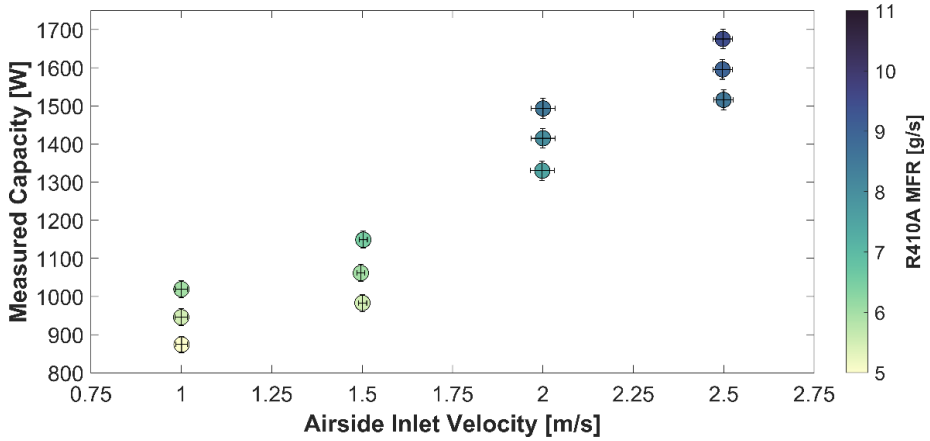

Figure 55: CNTHX1 Dry Evaporator Measured Nominal Capacity

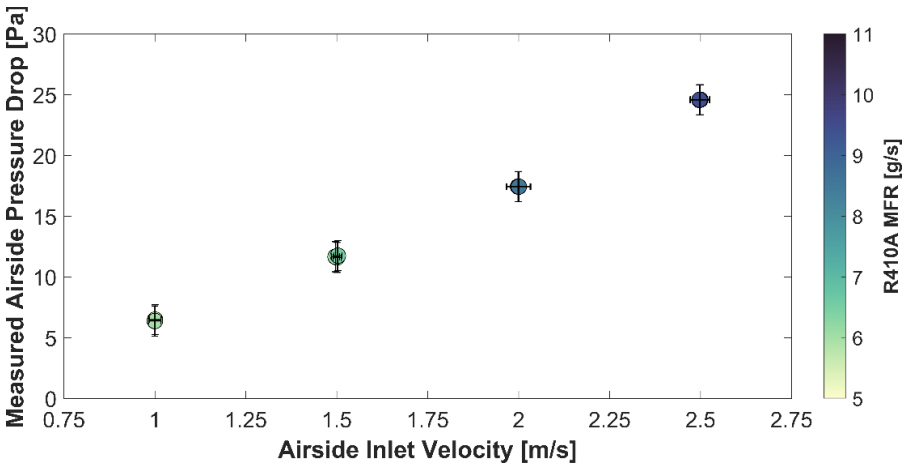

Figure 56: CNTHX1 Dry Evaporator Measured Air-Side Pressure Drop

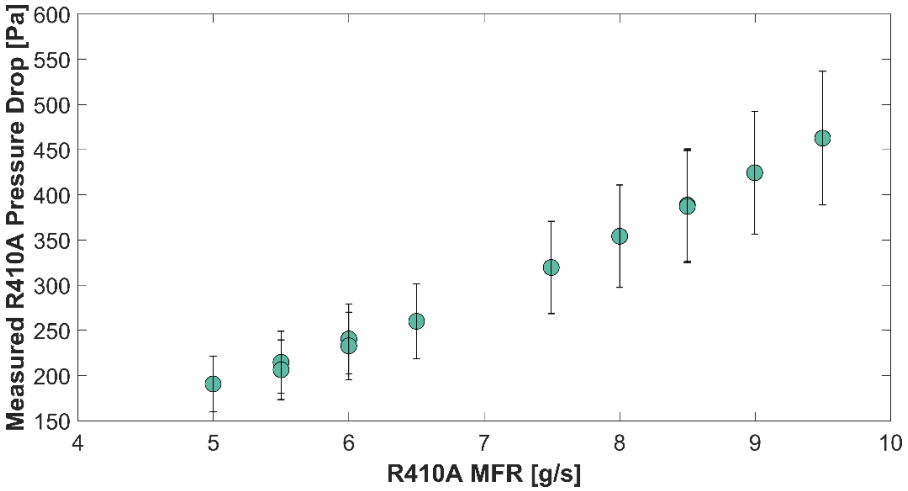

Figure 57: CNTHX1 Dry Evaporator Measured R410A Pressure Drop

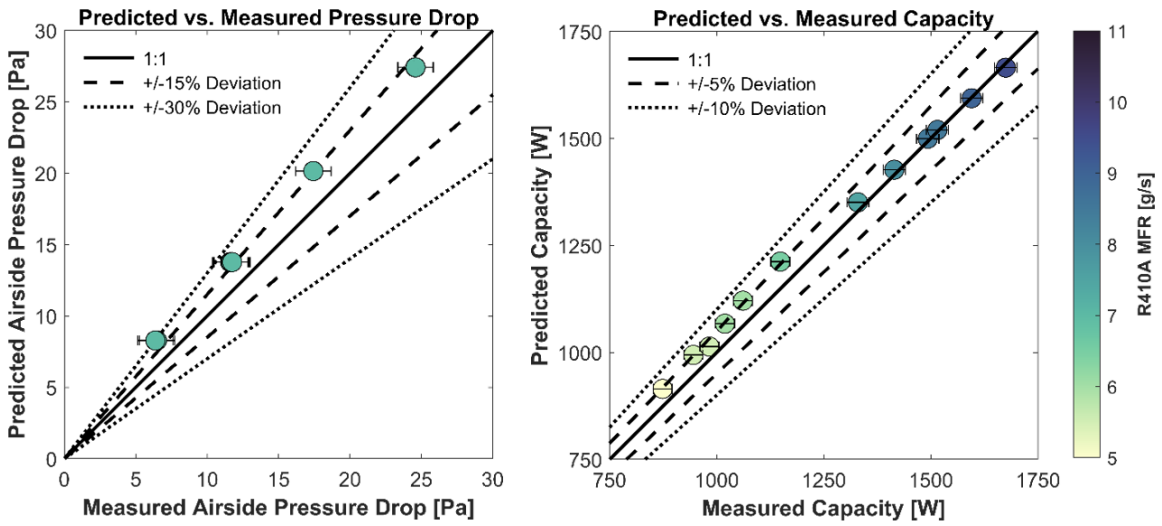

Figure 58: (Left) CNTHX1 Air-Side Pressure Drop Validation Plot (Right) CNTHX1 Capacity Validation Plot

The airside pressure drop and capacity were predicted within ±30% and ±10%, respectively. The measured air-side pressure drop was lower than the predicted CFD values for all 12 points, while the measured capacity was slightly lower or nearly identical to the predicted value; indicating that CNTHX1 has slightly better thermal-hydraulic performance than expected as a sensible evaporator. Additionally, thermal images were taken with a FLIR ONE Pro infrared camera during steady state testing to investigate the refrigerant flow distribution and location of superheated vapor versus two-phase refrigerant. The camera view is of the air outlet side. Note, in the very center there is a horizontal line which is a colder temperature than its surroundings. This is an epoxy material in one of the spacers that has a different emissivity than copper. There is a higher refrigerant flow on the right side of the heat exchanger, indicated by less superheat at the top. There appears to be some two-phase fluid at the top right. Potentially, there is two-phase entering the top header from one of the other tube banks. Since this is the air outlet side, the air mass flow distribution could also be causing the maldistribution in refrigerant superheat and flow. The

maldistribution was not severe enough to degrade the performance significantly below what was predicted.

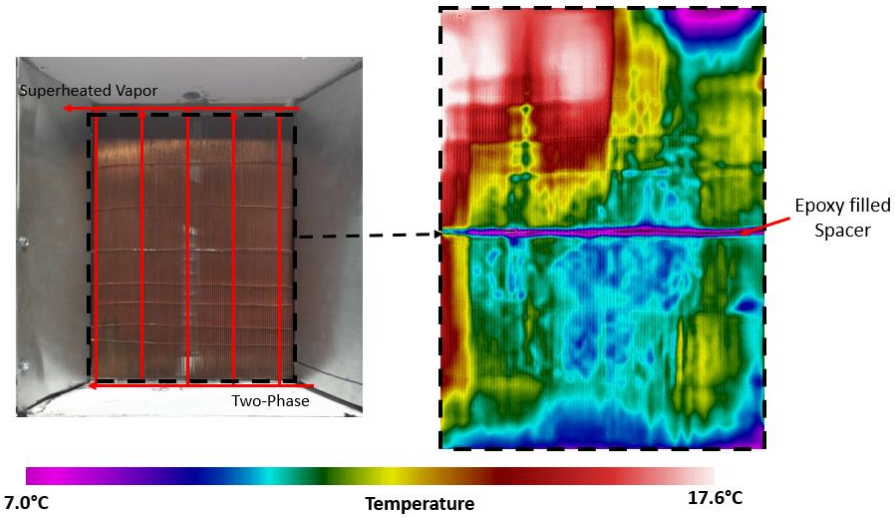

Figure 59: CNTHX1 Thermal Imaging of Outlet Air Face at Inlet Air Velocity of 2 m/s and R410A MFR of 8 g/s

CNTHX1 R410A Wet Evaporator Testing

Heat exchanger prototype CNTHX1 was also tested under air-to-refrigerant (R410A) wet evaporator conditions. Table 25 contains a data summary for the wet evaporator test matrix. A total of 11 steady states points were obtained. The air inlet velocity and R410A mass flow rate were varied, and the inlet R410A inlet quality of 0.20 was kept constant. Superheat greater than 6.8 K was obtained for all tests to ensure no two-phase refrigerant exits the heat exchanger. Nominal capacity of CNTHX1 is calculated as the average of the refrigerant-side and total (sensible + latent) airside capacity. The experimental set-up is the same as shown in Figure 53, with refrigerant flowing from the bottom header up against gravity and out the top header. A condensate pan was added to catch and collect condensate during testing.

Table 25: CNTHX1 Wet Evaporator Experimental Testing Summary

Parameter		Units	Value(s)
R-410A	Mass Flow Rate	[g/s]	5.0 - 9.5
	Evaporation Temperature	[°C]	10.0
	Inlet Quality	[-]	0.19
	Superheat	[K]	6.8 – 10.9
Air	Inlet Temperature	[°C]	26.7
	Inlet Velocity	[m/s]	1.0 – 2.5
	Inlet RH	[%]	52.0
	VFR	[m^3/s, CFM]	0.081-0.202, 172 – 429
Measured Performance	Air-Side Pressure Drop	[Pa]	16 – 62.6
	Nominal Total Capacity	[W]	1218 - 2097
	Sensible Capacity	[W]	875-1650
	Latent Capacity	[W]	300 - 525
	Sensible Heat Ratio	[-]	0.70 – 0.74
	Energy balance	[%]	-2.5 – 4.7

Figure 60 shows the energy balance for all 11 points. All 11 points are between -2.5% and 4.8%; indicating good agreement between the air-side and R-410A side.

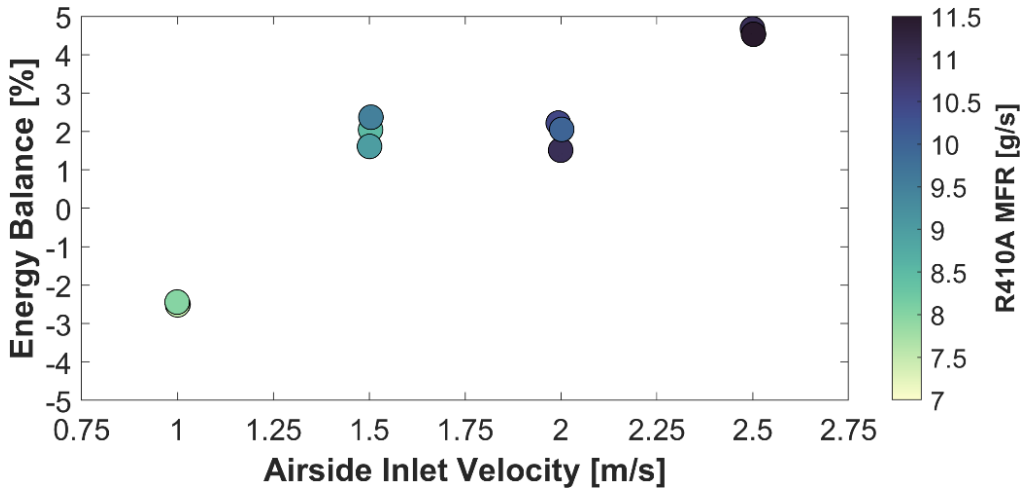

Figure 60: CNTHX1 Wet Evaporator Energy Balance

Figure 61 shows the measured total capacity and Figure 62 breaks down the total capacity into its sensible and latent components. Figure 63 shows the measured air-side and R410A pressure drop.

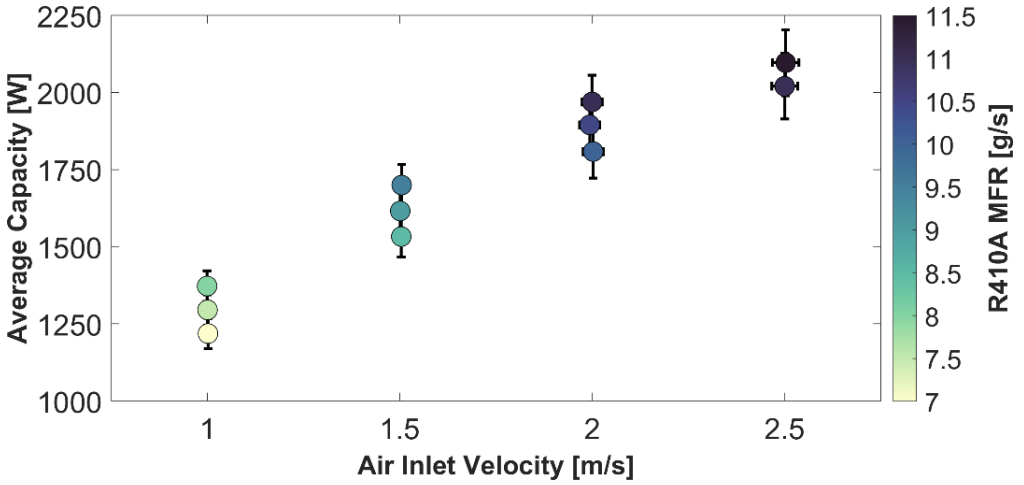

Figure 61: CNTHX1 Wet Evaporator Measured Nominal Total Capacity

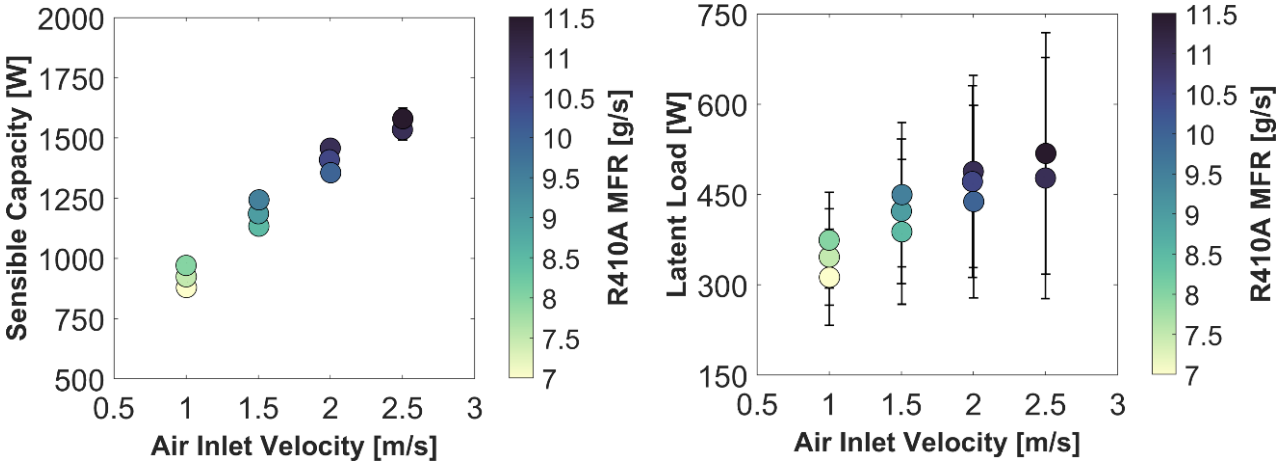

Figure 62: (Left) CNTHX1 Measured Sensible Capacity (Right) CNTHX1 Measured Latent Capacity

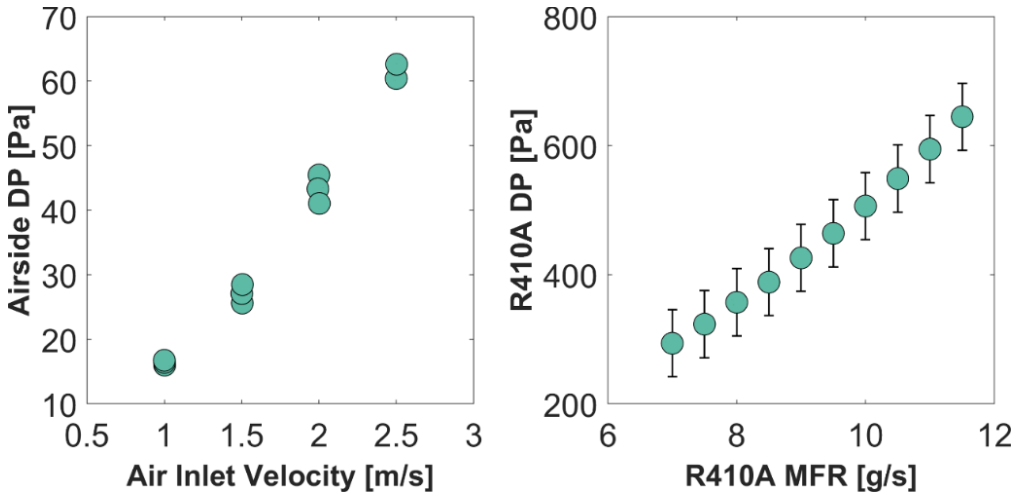

Figure 63: (Left) CNTHX1 Measured Air-Side Pressure Drop (Right) CNTHX1 R410A Pressure Drop

The predicted versus measured sensible load and the predicted versus measured latent load is shown in Figure 64. Figure 65 shows the predicted versus measured sensible heat ratio and the predicted versus measured total capacity. The sensible load and latent load were predicted within ±10% and ±20%, respectively. The sensible heat ratio and total capacity were both predicted within ±5%; indicating excellent agreement between the predicted and experimental values.

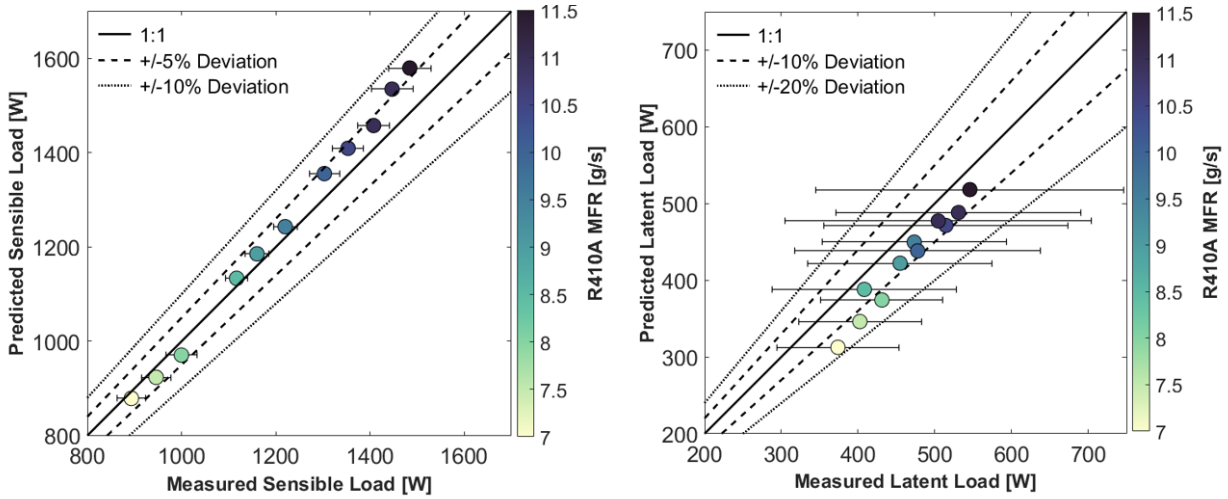

Figure 64: (Left) CNTHX1 Sensible Capacity Validation Plot (Right) CNTHX1 Latent Capacity Validation Plot

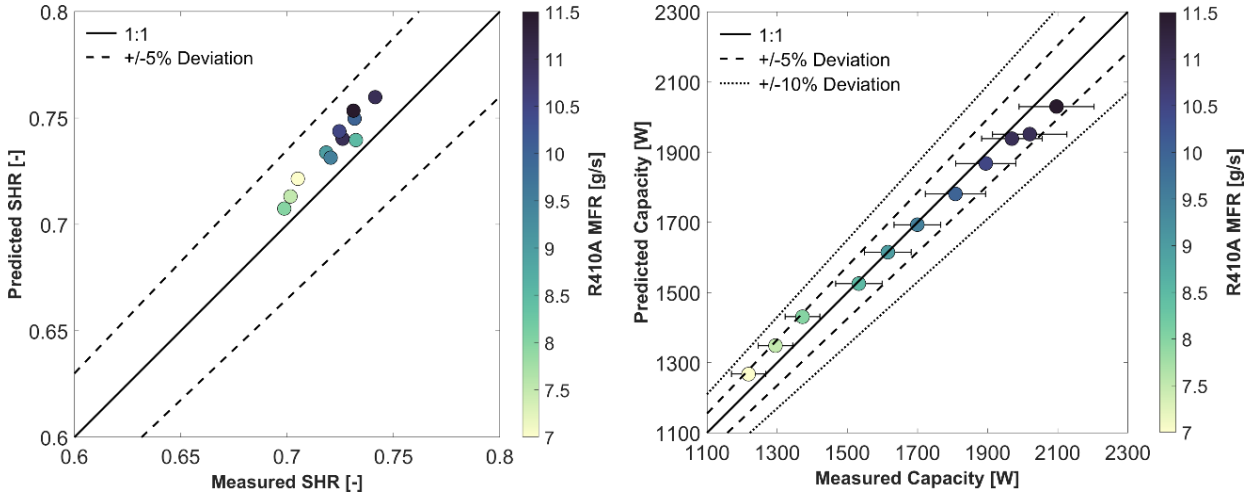

Figure 65: (Left) CNTHX1 Sensible Heat Ratio Validation Plot (Right) CNTHX1 Nominal Total Capacity Validation Plot

Figure 66 shows the airside pressure drop for both the dry evaporator and wet evaporator conditions. The airside pressure drop under wet evaporator conditions is significantly higher than the dry conditions due to condensate formation. Air-side pressure drop increased 111–160% at the same inlet air velocity when under wet conditions when compared to dry conditions (Figure 66).

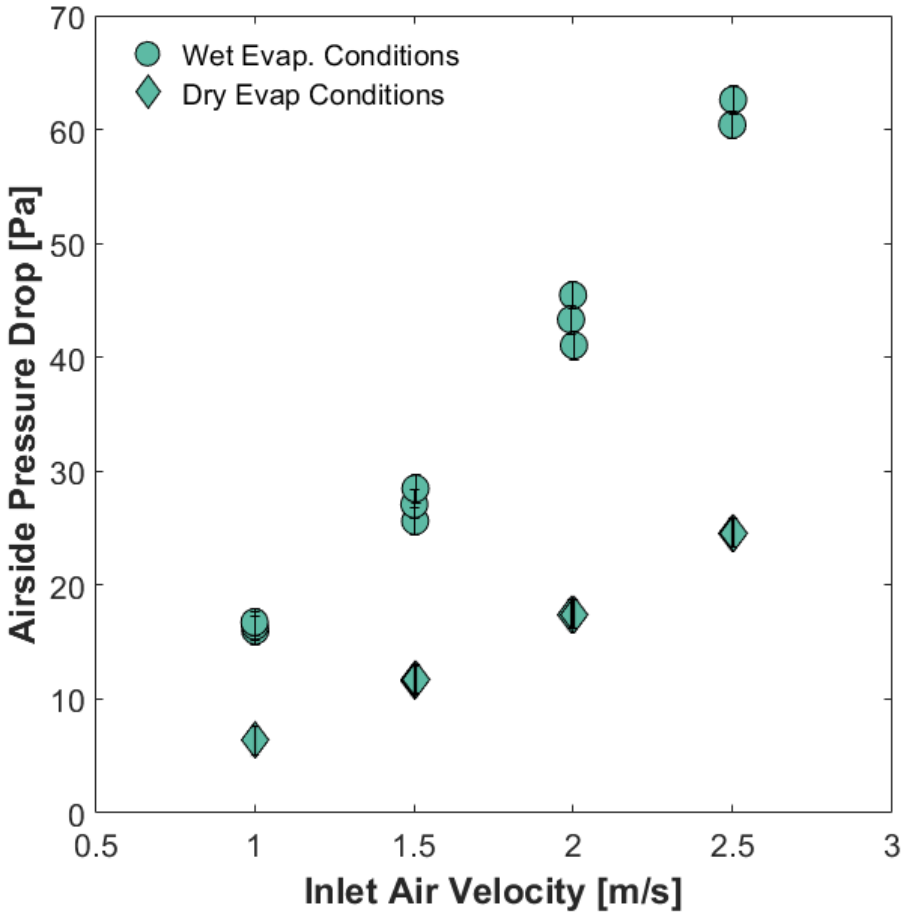

Figure 66: CNTHX1 Air-side Pressure Drop under Dry and Wet Conditions

CNTHX1 Dehumidification Performance Discussion

Figure 67 shows a picture of the condensate on CNTHX1 during evaporator testing at the air outlet side. Note, this photo was taken in an area of R410A superheated vapor.

Figure 67: CNTHX1 Condensate Bridging during Wet Evaporator Testing

Condensate formed and collected on the bare tubes during wet evaporator testing. When droplets became large enough, they bridge between tubes, and begin to slide down due to gravity. Generally, droplets would only begin to slide down when they were bridged between tubes; indicating that the size/weight of the droplet when it overcomes adhesion to the tubes is larger than the distance between the bare tubes. Spacers, as shown in Figure 67, were used along the length of CNTHX1 to help with the manufacturing process. Condensate collected on the spacers as well, reducing the drainage rate. Condensate bridged between tubes and impeded air-flow. This increased the air-side hydraulic resistance. The condensate bridging and build-up in the core of the heat exchanger was more severe than anticipated.

Table 26 shows a summary of reviewed experimental studies which report the wet versus dry air-side hydraulic performance of common tube-fin heat exchangers.

Table 26: Literature Review of Hydraulic Performance Comparison of Tube-Fin Heat Exchanger Wet versus Dry Conditions

Study Name and Authors	Air Velocity Range [m/s]	Extended Surface Type	Fin Spacing [mm]	Percent Increase over dry Conditions [%]	Reported Air-Side Parameter
Condensate retention effects on the air-side heat transfer performance of plain and wavy-louvered heat exchangers (Yin & Jacobi, 2000)	(V_{in}) 0.5 – 2.0	Plain-Fin	2.12	45%	f-factor
			1.27	70%	
		Wavy-Louvered Fin	2.12	30%	
			1.27	30%	
Performance of plate finned tube heat exchangers under dehumidifying conditions (Chi Chuan Wang et al., 1997)	(V_{in}) 0.3-4.5	Plain-Fin	1.82-3.2	60-120%	f-factor
Condensate retention and shedding effects on air-side heat exchanger performance (Korte & Jacobi, 1997)	(V_{max}) 1.2-9.9	Plain-Fin	6.35	0%	f-factor
			2.97	0-10%	
			2.29	5-32%	
			1.92	11-35%	
Air-side performance of brazed aluminum heat exchangers under dehumidifying conditions (M. H. Kim & Bullard, 2002a)	(V_{in}) 1.0	Louvered-Fin	1.0-1.4	3-30%	Pressure Drop
Thermal-hydraulic experimental study of louvered fin-and-flat-tube heat exchanger under wet conditions with variation of inlet humidity ratio (Ayad et al., 2021)	(V_{in}) 1.1-4.5	Louvered-Fin	1.1	15-43%	f-factor

The increase in air-side pressure drop is highly dependent on fin pitch and geometry. For example, if the fin pitch is large enough, condensation does not significantly increase air-side pressure drop. Korte and Jacobi reported no increase in air-side pressure drop between dry and wet conditions of plain fin-tube heat exchangers with a fin pitch of 6.35 mm (Korte & Jacobi, 1997). While an increase of 11-35% was reported for a fin pitch of 1.92 mm (Korte & Jacobi, 1997). The fin

geometry can impact the increase in air-side pressure drop at wet conditions as well. Yin and Jacobi reported that for the same fin pitch wavy-louvered fin tube heat exchangers had a lower pressure drop increase at wet conditions over plain-fin tube heat exchanger (Yin & Jacobi, 2000).

CNTHX1's increase in air-side pressure drop penalty under wet conditions (111-160% increase) is more severe than all but one of the studies in Table 26. The highest reported hydraulic resistance increase in Table 26 were using plain-fin-tube heat exchangers with 1.27 mm fin pitch (Yin & Jacobi, 2000) and 1.82 mm (Chi Chuan Wang et al., 1997). These studies measured an increase in air-side friction factor of 70% and 120%, respectively.

CNTHX1's latent load and sensible heat ratio were both predicted within 20% and 5%, respectively. Indicating the extra condensate retention in core of the heat exchanger was not detrimental to the heat transfer performance. Section 3.1.4 shows testing of a packaged air conditioning unit with a plain fin-tube evaporator with fin pitch of 1.8 mm showed the evaporator had a sensible heat ratio of 0.74 – 0.78 with R410A at similar inlet air dry bulb and wet bulb temperature (Table 38). CNTHX1's sensible heat ratio was measured to be 0.70-0.74. The sensible heat ratio was slightly lower or equal with measured values of 0.74 – 0.78 from the fin-tube heat exchanger. This indicates this new type of heat exchanger is able to handle the latent load under these air-side conditions with approximately equal to 10% lower sensible heat ratio.

It is recommended in the future to further investigate the performance of this new type of compact heat exchanger under wet evaporator conditions and further quantify fundamental heat and mass transfer principles under de-humidifying conditions. This could be quantified by Lewis number correlations. Additionally, it is recommended to investigate how the tube orientation with respect to gravity (vertical versus horizontal) affects condensate retention, air-side pressure drop, heat transfer capacity, and sensible heat ratio.

2.3.5 Copper NTHX Full-Size Experimental Performance

The largest capacity heat exchanger tested was the Copper NTHX Full-Size (CNTHX-FS). CNTHX-FS was fabricated by Heat Transfer Technologies LLC using conventional manufacturing methods without the aid of any AM. The tubes were created using an extrusion method and then assembled to the headers using a soldering process. This is the same extrusion process as CNTHX1's tubes. No additive manufacturing was used during the manufacturing of this heat exchanger. It was designed and optimized for air-to-refrigerant (R410A) two-phase evaporator applications with a capacity of 5.28 kW. Figure 68 shows the completed heat exchanger. Spacers are evenly distributed throughout the core and were used to assist during the construction process; they are not intended to act as an extended heat transfer surface. Table 27 shows a summary of characteristics and physical properties.

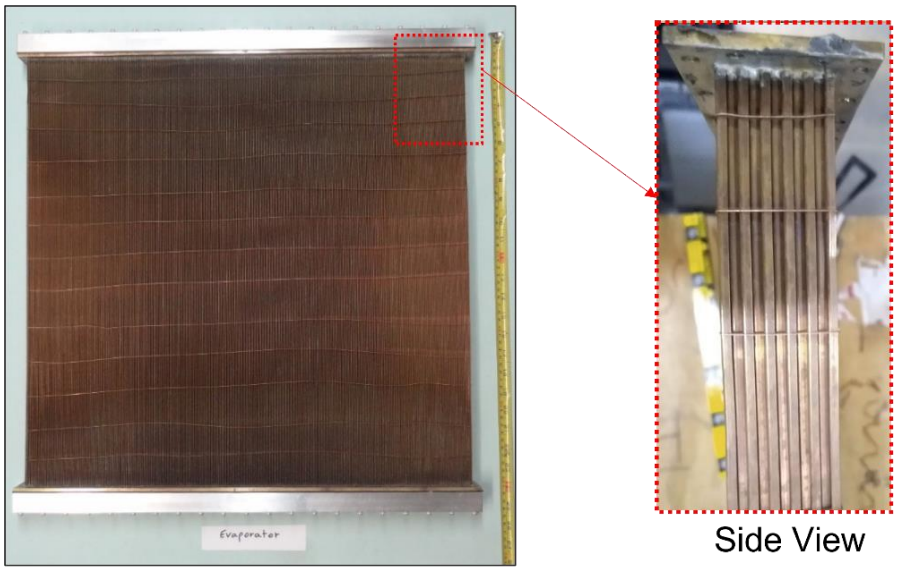

Figure 68: 5.28 kW CNTHX-FS, Manufactured using Conventional Methods

Table 27: CNTHX-FS Prototype Summary

Parameter	Units	Value
Core Dimensions (LxWxD)	[mm]	564 x 580 x 29
Envelope Volume (w/ headers)	[cm^3]	19,403.7
Envelope Volume Core	[cm^3]	9,486.5
Frontal Area	[m^2]	0.3271
Weight	[kg]	15.4
Tube Material	-	Copper
Manufacturing Process	-	Tube Extrusions + Solder Connections
No. Fluid Passes	-	1
No. Tubes	-	2,123
No. Banks	-	11
Tube Hydraulic Diameter (Air-Side)	[mm]	2-3

Before testing began, two preliminary tests were completed; these include a pressure test and a flow distribution (blockage) test. In a safe area, CNTHX-FS was pressurized to an absolute pressure of 1813 kPa and it successfully held this pressure for 48 hours. Next, thermal imaging was conducted while chilled isopropyl alcohol flowed through the heat exchanger to check for major tube blockages. Thermal imaging showed an even distribution of chilled Isopropyl Alcohol as it filled CNTHX-FS; indicating there are no tube blockages. This process was repeated on the opposite air-side with the exact same results.

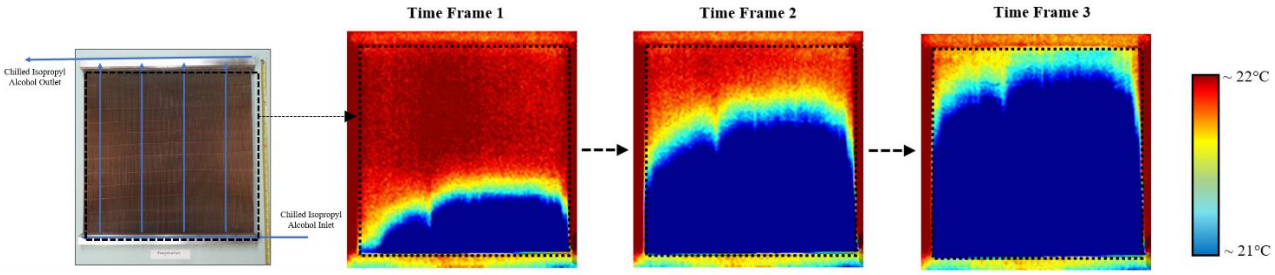

Figure 69: CNTHX-FS Thermal Image Blockage Test

CNTHX-FS R410A Dry Evaporator Testing

CNTHX-FS was tested under R-410A dry evaporator conditions for two steady-state points. These two points are shown in Table 28. The heat exchanger's core is larger than the wind tunnel's dimensions. Hence, a small section of the heat exchanger core was not exposed to the wind-tunnel's air flow. Approximately 60 mm of the heat exchanger core (~10% of frontal area) is sticking outside the wind tunnel and will get minimal airflow.

Table 28: Full-Size Evaporator Steady State Experimental Testing w/ R410A

Category	Measurand	Units	Test 1	Test 2
R410A	Mass Flow Rate	g/s	8.2	9.3
	Inlet Quality	-	0.30	0.30
	Evaporation Temperature	°C	13.0	13.0
	Abs. Pressure Inlet	kPa	1205.9	1207.2
	Superheat	K	11.9	10.7
	Pressure Drop	kPa	2.24	3.36
Air	Temp. Inlet	°C	26.6	26.3
	Temp. Outlet	°C	20.3	19.2
	RH Inlet	%	33.2	33.0
	Pressure Drop	Pa	1.75	1.76
	Mass Flow Rate	g/s	180.2	180.2
	Inlet Velocity	m/s	0.52	0.52
	Volumetric Flow Rate	m^3/s, CFM	0.152,322.7	0.152,322.8
Capacity	Refrigerant-Side Capacity	W	1280	1427
	Air-Side Capacity	W	1174	1326
	Energy Balance	%	-8.6	-7.4
	Average Capacity	W	1227	1376
Predicted	Predicted Capacity	W	1295	1465
	Predicted Air-Side Pressure Drop	Pa	2.40	2.40
	Predicted R410A Pressure Drop	kPa	2.04	2.50

The evaporating temperature was 13°C with R-410A mass flow rates 8.2 and 9.3 g/s. At least 10K superheat was achieved to ensure all the refrigerant evaporated at the heat exchanger outlet. An inlet R410A quality of 0.30 was reached for both points. The inlet air temperature and RH were approximately 25.5°C and 33%, respectively. The heat exchanger's capacity and air-side pressure

drop were predicted within 10% and 37%, respectively, of the experimental values. The refrigerant-side pressure drop indicated there were no major internal tube blockages. Air was leaking where the core was sticking out the side of the duct and was not possible to seal without damaging or modifying the bare tubes. This decreased the reliability of the air-side capacity and the air-side pressure drop readings. Thermal images of the heat exchanger were taken during evaporator testing. Due to space constraints, the pictures were taken at an angle from outside the duct. Figure 70 shows these thermal images. There are no indications from the images that there are any major blockages. All the visible tubes clearly have two-phase R-410A entering the bottom header, flowing up the tubes, and then increase in temperature as it reaches a superheated vapor. There was some minor R410A mass flow rate maldistribution.

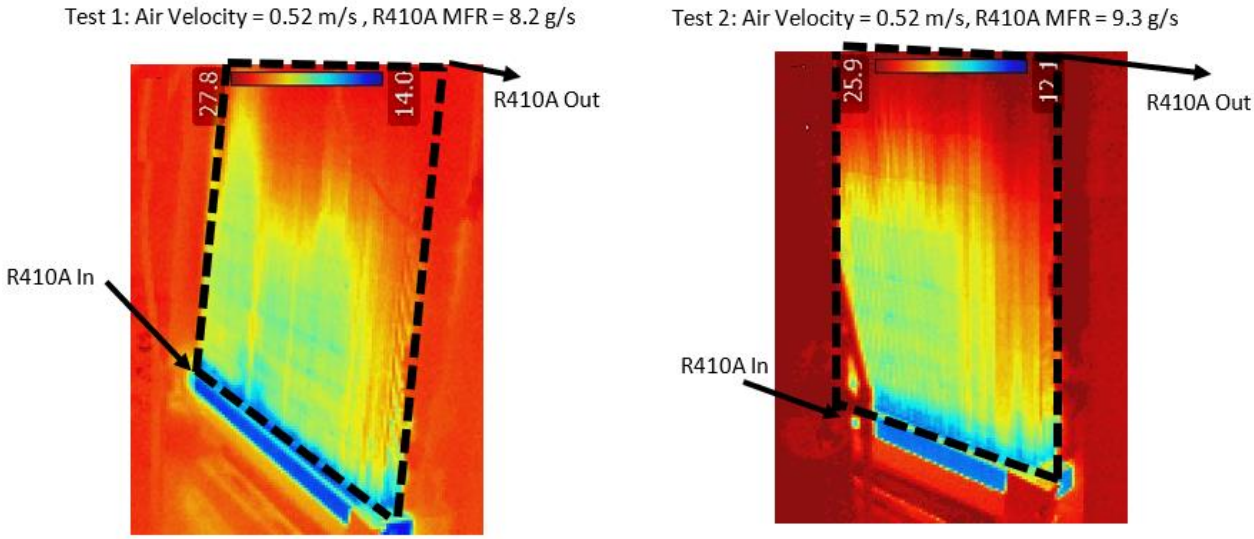

Figure 70: Thermal images of Full-Size Evaporator during dry evaporator testing w/ R-410A

These two steady state tests demonstrated that the heat exchanger performed as designed and is functional as an evaporator with R-410A. Even with the ambient air leakage around the core sticking outside the duct and higher than normal energy balance, the measured capacity, air-side

pressure drop, and the refrigerant-side pressure drop were predicted well. A larger number of data points were not recorded because CNTHX-FS was intended to be installed into a 7.03 kW residential air-conditioning unit. These tests provided a basic check of the functionality of the heat exchanger before it is installed into an actual residential air conditioning unit.

It is worth having a discussion on the reliability of CNTHX-FS. One of the biggest challenges with the NTHX heat exchangers is manufacturing. Specifically, for conventionally manufactured extruded tubes such as with CNTHX1 and CNTHX-FS, creating an assembly where all tubes are leak tight and successfully attached to the headers is very difficult and leaks at the connection between the header and tubes would form often. The prototype was successfully tested, but a more reliable way to attach the header to the extruded tubes is needed.

2.3.6 PNTHX Experimental Performance

PNTHX was designed and optimized by the Modeling and Optimization Consortium at CEEE as an automotive radiator to be printed in a polymer using stereolithography additive manufacturing. The entire heat exchanger is a single monolithic build with header manifolds. PNTHX is shown in Figure 71.

Figure 71: (Left) PNTHX Manufactured using SLA (Right) PNTHX Mounted in Wind Tunnel

Table 29 shows a summary of PNTHX's characteristics and physical properties. And Table 30 shows the testing summary.

Table 29: PNTHX Prototype Summary

Parameter	Units	Value(s)
Core Dimensions (LxWxD)	[mm]	208 x 107 x 33
Envelope Volume (w/ headers)	[cm^2]	2684
Frontal Area	[m^2]	0.0223
Weight	[kg]	0.837
Material	-	Accura Xtreme
Manufacturing Process	-	SLA
No. Fluid Passes	-	1
No. Tubes	-	180
No. Banks	-	9
Tube Hydraulic Diameter (Air-Side)	[mm]	4-5

Table 30: PNTHX Radiator Experimental Testing Summary

Parameter		Units	Value(s)
Water-Side	Mass Flow Rate	[g/s]	20 – 40
	Inlet Temperature	[°C]	50.0
Air-Side	Inlet Temperature	[°C]	25.0
	Inlet Velocity	[m/s]	3.5 – 8.5
	Inlet RH	[%]	< 20
	VFR	[m^3/s CFM]	0.063 – 0.153, 133 – 324
Measured Performance	Air-Side Pressure Drop	[Pa]	75 – 341
	Water-Side Pressure Drop	[kPa]	382 – 741
	Nominal Capacity	[W]	393 – 598
	Energy balance	[%]	-2.6 – 4.4

PNTHX provides an interesting case study as an additively manufactured heat exchanger as it was found that after the manufacturing process a large percentage of the tubes had internal blockages. The internal blockages are shown in Figure 72.

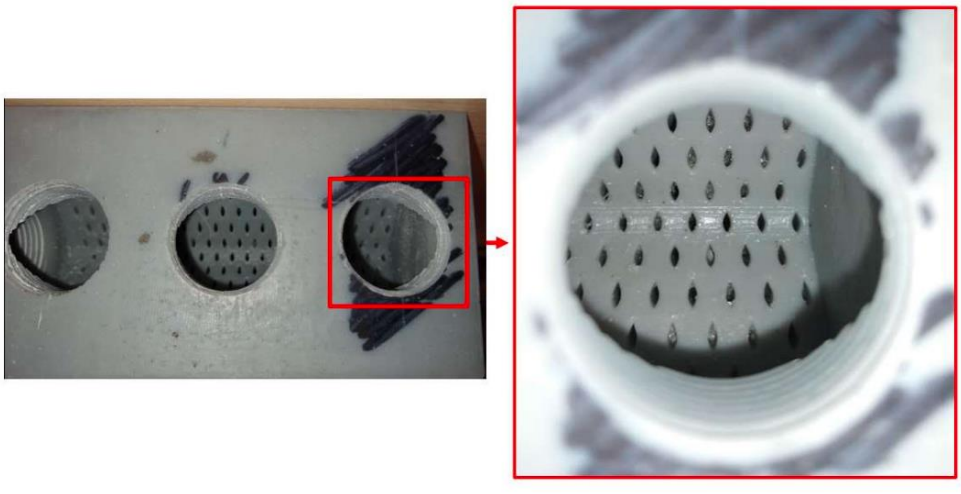

Figure 72: PNTHX1's Internal Tube Blockages with Support Material

It was estimated that approximately 50% of the total tubes were at least partially blocked with support material. Nonetheless, radiator testing was still conducted, but with the expectation that the heat transfer capacity would be greatly reduced and water-side pressure drop would be

significantly larger than predicted. A total of 18 steady state test points were measured. The energy balance is shown in Figure 73. The heat transfer capacity and air-side pressure drop are shown in Figure 74 and Figure 75, respectively. Lastly, the water-side pressure drop is shown in Figure 75.

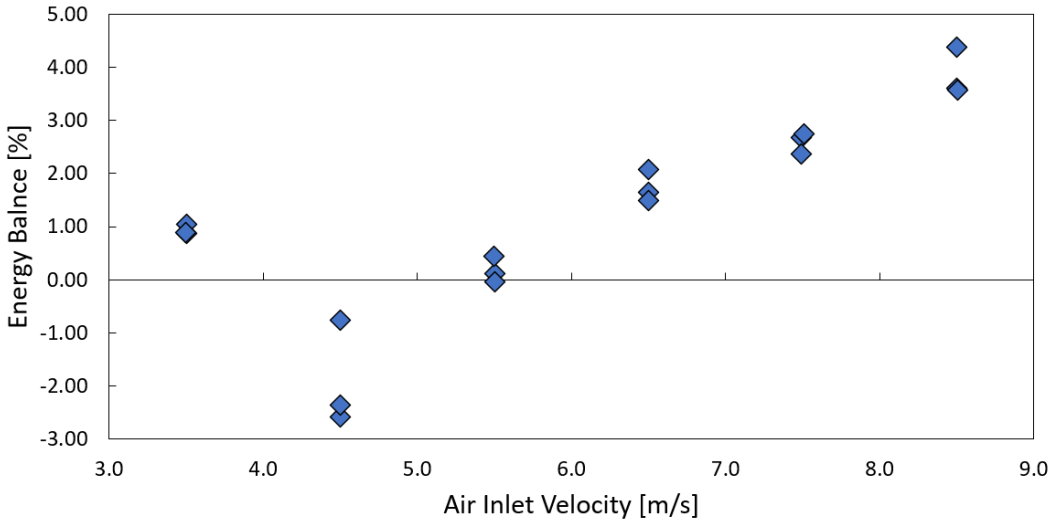

Figure 73: PNTHX Radiator Energy Balance

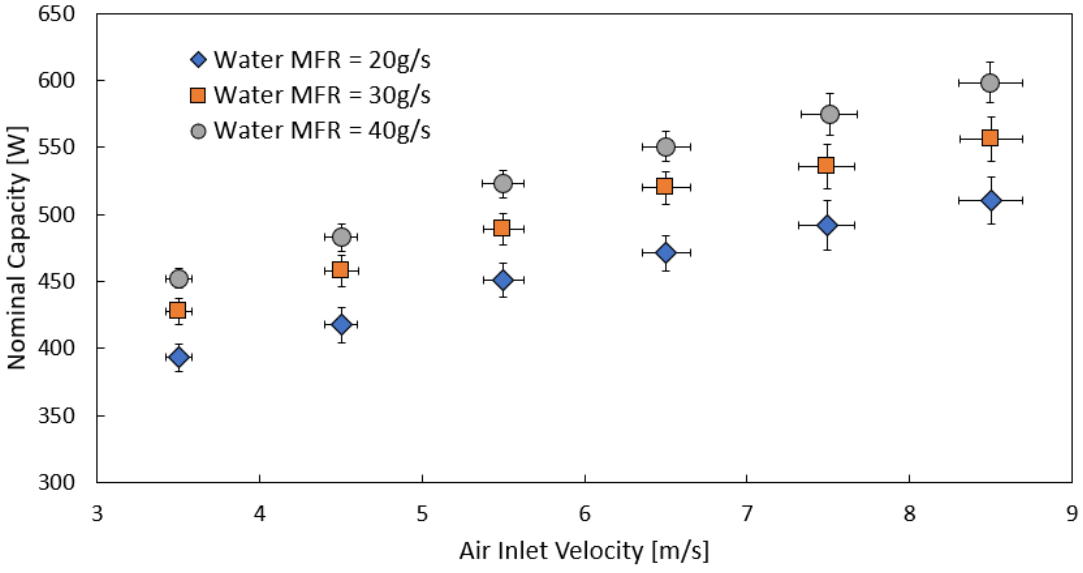

Figure 74: PNTHX Heat Transfer Capacity versus Inlet Air Velocity

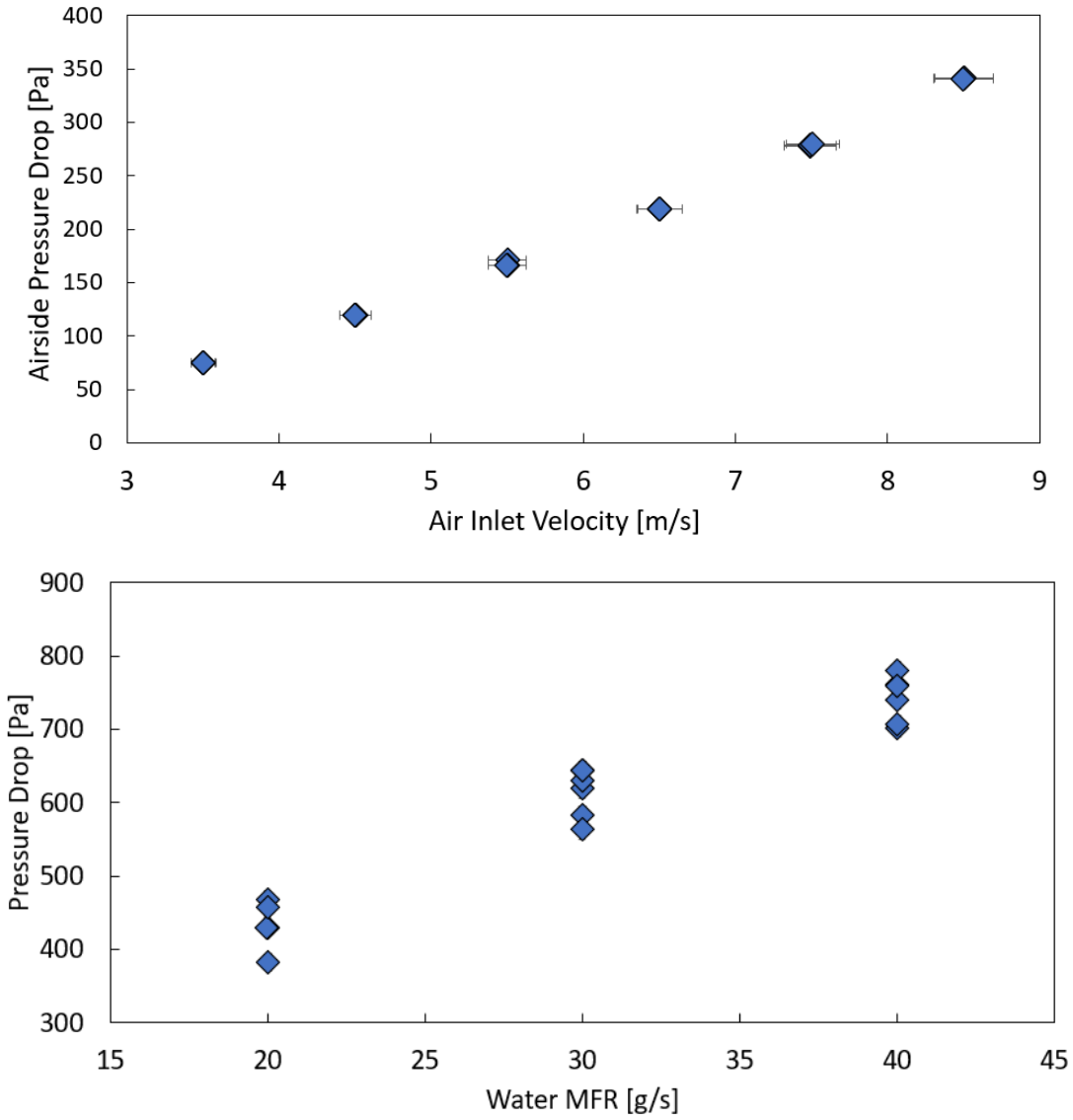

Figure 75: (Top) PNTHX Measured Air-Side Pressure Drop (Bottom) PNTHX Water-Side Pressure Drop versus Inlet Air Velocity

PNTHX was successfully tested as a radiator, but the experimental heat transfer capacity was greatly reduced due to the blocked water-side tubes. The internal blockages of PNTHX show that caution should be exercised when creating 3D printed heat exchangers. Especially with small diameter tubes (<6mm), there is a chance that the tubes will be significantly blocked during the

printing process. If this is the case, then the performance of the heat exchanger will be greatly reduced.

2.3.7 NTHX Experimental Testing Summary

A total of five heat exchangers were experimentally tested under a variety of different conditions. These conditions include radiator, condenser, and evaporator (wet and dry). Additionally, two different refrigerants were used R410A and R134a. All heat exchangers have similar shaped cross sectional shaped tubes as shown in Figure 21. Table 31 shows a summary of all the heat exchangers tested excluding PTNHX due to its blocked tubing. Figure 76 and Figure 77 shows the predicted versus measured heat transfer capacity and air-side pressure drop, respectively. Again, all predicted air-side pressure drop values and average air-side heat transfer coefficient values are using CFD results during the optimization and design of the heat exchanger (Bacellar, Aute, Huang, et al., 2016b; Bacellar et al., 2017; Tancabel et al., 2022).

Table 31: NTHX Prototypes Experimental Testing Summary

Heat Exchanger	Picture	Testing Condition	Max Percent Deviation from Predicted	Avg. Percent Deviation from Predicted
NURBS Tube Heat Exchanger (NTHX1)	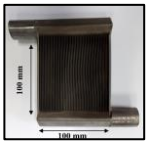	Radiator	Air-Side Pressure Drop: 4.45% Total Nominal Capacity: 9.40%	Air-Side Pressure Drop: 2.13% Total Nominal Capacity: 4.60%
		Condenser (R134a)	Air-Side Pressure Drop: 0.70% Total Nominal Capacity: 14.54%	Air-Side Pressure Drop: 0.47% Total Nominal Capacity: 8.48%
		Dry Evaporator (R410A)	Air-Side Pressure Drop: 13.05% Total Nominal Capacity: 2.05%	Air-Side Pressure Drop: 4.54% Total Nominal Capacity: 0.95%
Expanded NURBS Tube Heat Exchanger (ENTHX1)	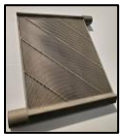	Radiator	Air-Side Pressure Drop: 24.56% Total Nominal Capacity: 10.25%	Air-Side Pressure Drop: 17.37% Total Nominal Capacity: 4.90%
Copper NURBS Tube Heat Exchanger (CNTHX1)	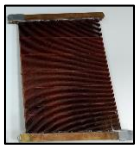	Dry Evaporator (R410A)	Air-Side Pressure Drop: 32.17% Total Nominal Capacity: 5.59%	Air-Side Pressure Drop: 20.26% Total Nominal Capacity: 2.71%
		Wet Evaporator (R410A)	Total Nominal Capacity: 4.27%	Total Nominal Capacity: 2.22%
Copper NURBS Tube Heat Exchanger-Full Size (CNTHX-FS)		Dry Evaporator (R410A)	Air-Side Pressure Drop: 37.14% Total Nominal Capacity: 6.47%	Air-Side Pressure Drop: 37.1% Total Nominal Capacity: 6.0%

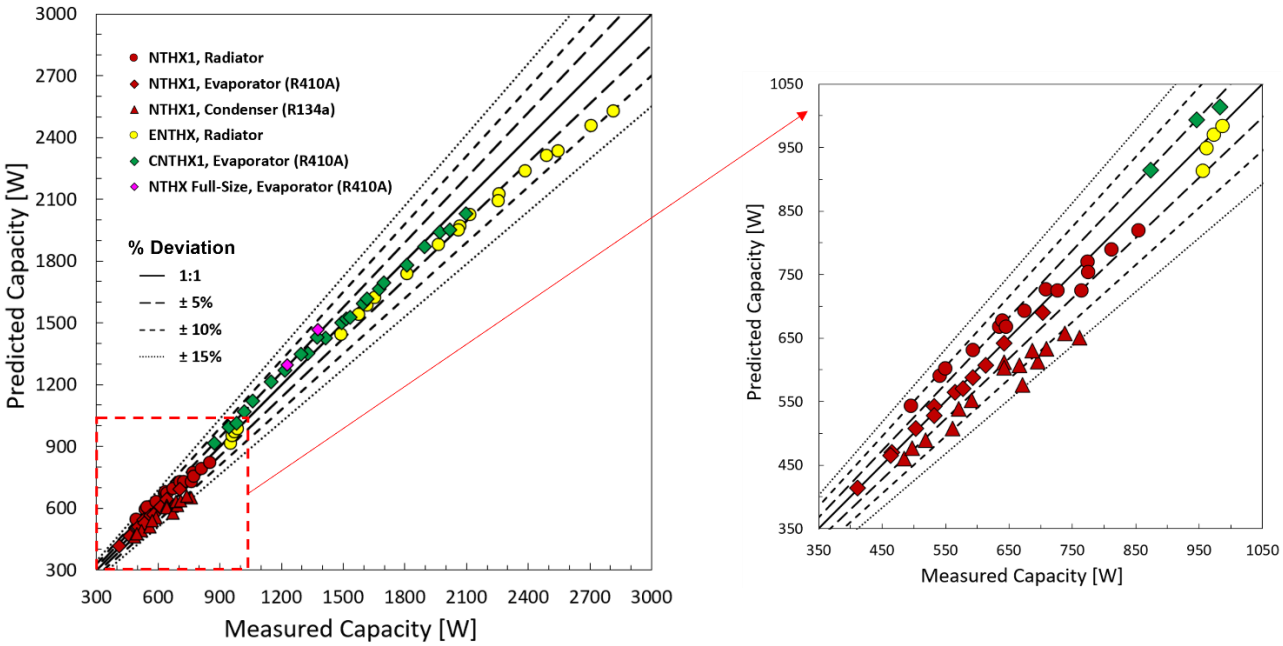

Figure 76: NTHX Predicted versus Measured Total Nominal Capacity for All NTHX Prototypes

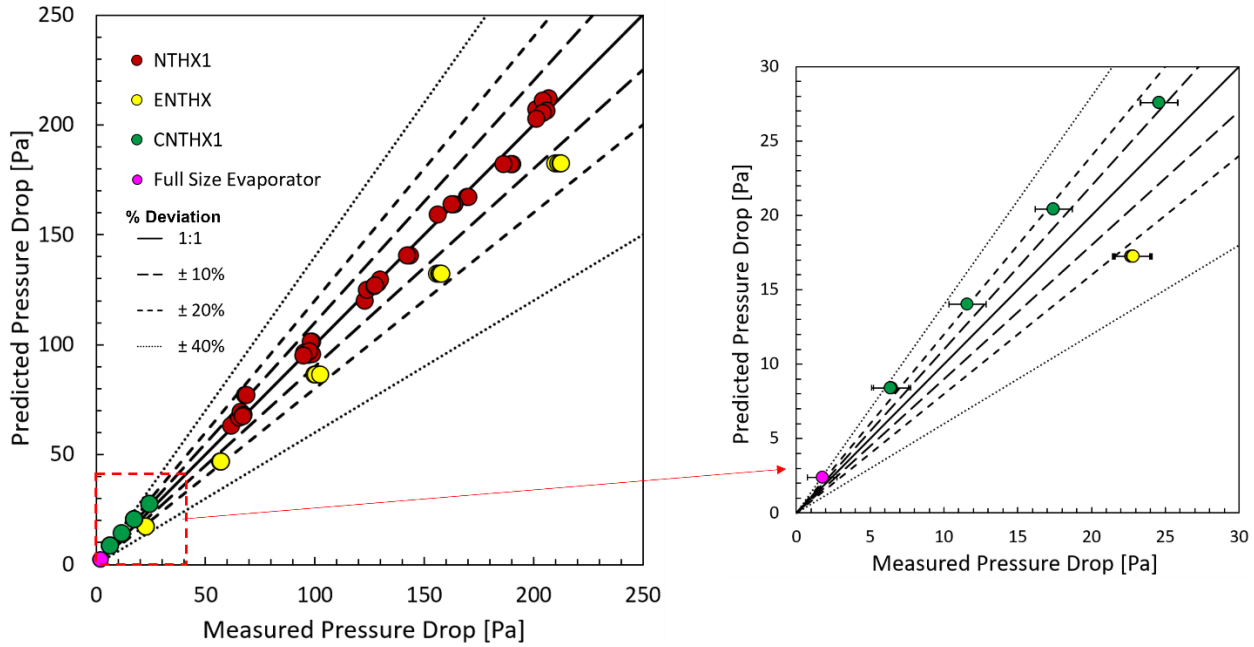

Figure 77: NTHX predicted versus Measured Air-Side Pressure Drop for All NTHX Prototypes (Excluding Wet Evaporator Conditions)

Table 32 shows a summary of the predicted versus measured performance of all heat exchangers' capacity and air-side pressure drop.

Table 32: NTHX Experimental Testing Data Summary

Total Data Points	87
Total Nominal Capacity	
Avg. Absolute % Deviation	4.3%
Max % Deviation	14.5%
Within 5% Deviation	62.1%
Within 10% Deviation	93.1%
Within 15% Deviation	100%
Air-Side Pressure Drop	
Avg. Absolute % Deviation	9.3%
Max % Deviation	37.1%
Within 10% Deviation	54.8%
Within 20% Deviation	87.7%
Within 30% Deviation	95.9%
Within 40% Deviation	100%

Overall, there was excellent agreement between the predicted and measured performance of all heat exchangers tested over these typical HVAC&R testing conditions. Heat transfer capacity and air-side pressure drop were predicted within 15% and 37.1% for all data points, respectively. Heat transfer capacity is predicted with higher accuracy than air-side pressure drop. The highest deviation in air-side pressure drop occurs where experimental uncertainty is highest proportionally (experimental uncertainty is ~68% of measured pressure drop) with CNTHX-FS. Note that where there is the highest percent deviation, with CNTHX-FS and CNTHX1, air-side pressure drop is over-predicted. Indicating, the hydraulic performance of these heat exchangers is better than expected while the thermal performance is performing as predicted. Additionally, it is worth noting the trend of surface roughness versus pressure drop prediction. The heat exchangers are listed below in order of highest to lowest surface roughness.

- ENTHX – Highest surface roughness, ~ 6.35 - 10.2 μm (Sintavia LLC, 2019). Air-side pressure drop was consistently under-predicted.
- NTHX1 – Middle surface roughness, ~3.8 - 6.1 μm (Sintavia LLC, 2019). No clear trend of over or under prediction of air-side pressure drop. Overall, the lowest average percent deviation from predicted air-side pressure drop of the NTHX prototypes tested. i.e., best overall predicted air-side pressure drop of the prototypes.
- CNTHX1 and CNTHX-FS – Lowest surface roughness, ~0.8 - 2.0 μm (Pohanish et al., 2016). Air-side pressure drop consistently over-predicted.

Surface roughness appears to be a significant factor as to whether the air-side pressure drop is under or over predicted. There have been other experimental investigations have also reported an increase in air-side pressure drop for additively manufactured cross-flow heat exchangers (Saltzman et al., 2018).

With regards to heat transfer capacity, below approximately 1000W, there is no clear prediction trend. Between a capacity of 1000 – 1500W, the capacity shows a trend of being overpredicted. Above a capacity of 1500W the capacity shows a trend of being underpredicted.

Other sources deviation from the predicted include the experimental inlet air velocity profile will not be uniform as is assumed in the CFD simulations. The exact geometry of the bare tube (shape and pitch) will inevitably vary slightly from that was designed. Additionally, with CNTHX1, CNTHX-FS, and ENTHX1 there are supports/spacers in the heat exchanger core which will affect the thermal-hydraulic performance as well.

These experimental results provide strong evidence this new class of compact finless heat exchangers are performing as intended under typical HVAC&R application conditions.

Additionally, it provides evidence the shape and topology optimization framework used to develop these heat exchangers (Bacellar et al., 2017; Tancabel et al., 2022) can accurately predict the air-side thermal-hydraulic performance of these novel non-round bare tube compact heat exchangers.

Chapter 3: Packaged Air Conditioning Unit Experimental Testing

Chapter 2 presented multiple NTHX heat exchanger prototypes that were individually tested under radiator, condenser, and evaporator conditions exchanger. The prototypes' thermal-hydraulic performances were experimentally validated on a component level. The next step is to determine how these non-round bare tube heat exchangers affect the system level performance of an actual air conditioning system.

First, a test facility was designed and constructed to evaluate the system level performance of a 2.0-2.5 RT (7.03 – 8.79 kW) packaged air conditioning unit at AHRI 210/240 test conditions (AHRI, 2023). Both the air-side and refrigerant-side were instrumented. The evaporator capacity energy balance between the refrigerant and air-side is evaluated and the condenser capacity is evaluated only on the refrigerant side. The power consumption of the compressor, evaporator fan, condenser fan, and overall unit were also measured to evaluate the power consumption of the unit and the COP could consequently be measured. The largest modification to the refrigerant-side when compared to the out of box unit is that in place of the fixed orifice expansion device a thermostatic expansion valve (TXV) was installed so refrigerant charge optimizations did not need to be conducted between heat exchanger retrofits.

The following sections first detail the design and construction of the packaged unit test facility and then show the data reduction methodology. Air-side mass flow rate calibrations were conducted to determine the evaporator air-side mass flow rate. Testing was then conducted on the baseline unit based at AHRI 210/240 testing conditions (AHRI, 2023) with the traditional tube-fin heat exchanger. The performance of the unit under these conditions is presented and compared to the predicted performance. Then, the tube-fin evaporator was replaced with the shape and topology

optimized CNTHX-FS evaporator. The same test conditions were repeated, and the unit's performance results are presented and discussed.

3.1 Packaged A/C Unit Test Facility

A test facility was constructed to evaluate the system level performance of an Amana 7.03-8.79 kW (2.0-2.5 RT) packaged air conditioning unit.

3.1.1 Test Facility Design and Construction

The specifications of this packaged air conditioning unit can be found in Table 33 and a picture of the unit is shown in Figure 78.

Table 33: Packaged Air-Conditioning Unit Specifications

Parameter		Units	Value
Overall System	Model No.	-	APG1430060M41AC
	Nominal Capacity	kW	8.38
	Rated Efficiency (SEER)	-	14
	Refrigerant	-	R-410A
	Refrigerant Factory Charge	kg	2.21
Evaporator Coil	Face Area	m^2	0.4
	No. Banks	-	3
	Fin Spacing	fins/cm, fins/in	5.5, 14
Condenser Coil	Face Area	m^2	1.14
	No. Banks	-	1
	Fin Spacing	fins/cm, fins/in	9.4, 24
Compressor	Type	-	Scroll
	Stage	-	1
	Quantity	-	1
Electrical	Voltage-Phase	V	208/230
	Phase	-	1

Figure 78: 7.03-8.79 kW (2.0-2.5 RT) Packaged Air-Conditioning Unit (APG14)

This air conditioning unit is termed a “packaged unit” because it contains both the evaporator and condenser in one single unit. I.e., there is not a separate indoor and outdoor unit. A top view of the unit is shown in Figure 79 with the top cover removed. The evaporator has a return and supply air duct opening. The condenser fan pulls in air from the side through the condenser and heated air leaves through the top condenser fan.

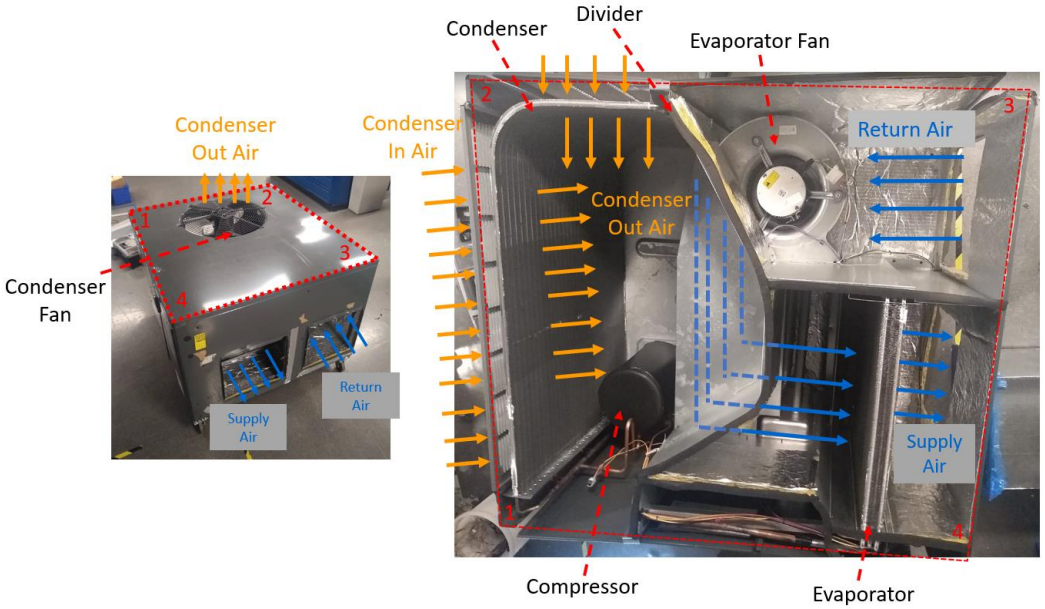

Figure 79: Top-View Packaged Air-Conditioning Unit with Cover Removed

A closed evaporator loop was constructed using 0.4 x 0.4 m (16”x16”) cross-section ducting. Figure 80 shows a general schematic of the designed closed loop.

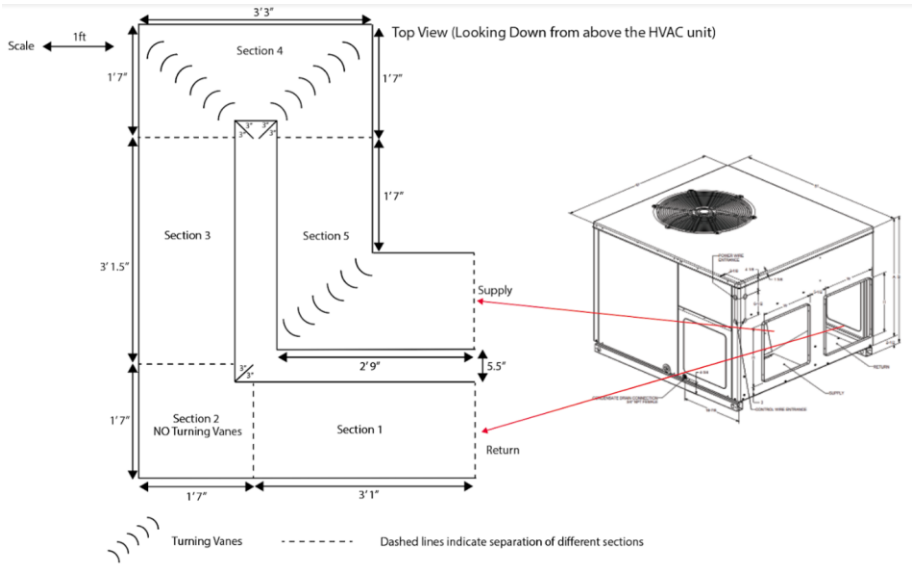

Figure 80: Evaporator Closed Loop Schematic and Connection to Packaged Unit

There are five major duct sections and were assembled and placed on mobile aluminum frame carts. Figure 81 shows the assembled closed loop and Figure 82 shows the closed loop’s schematic with full instrumentation.

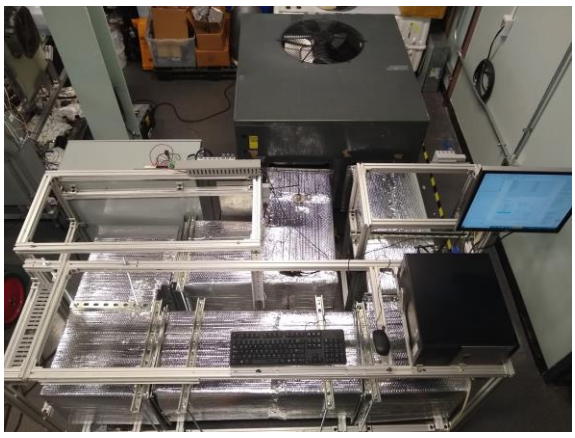

Figure 81: Assembled Evaporator Closed Loop Connected to Packaged Unit

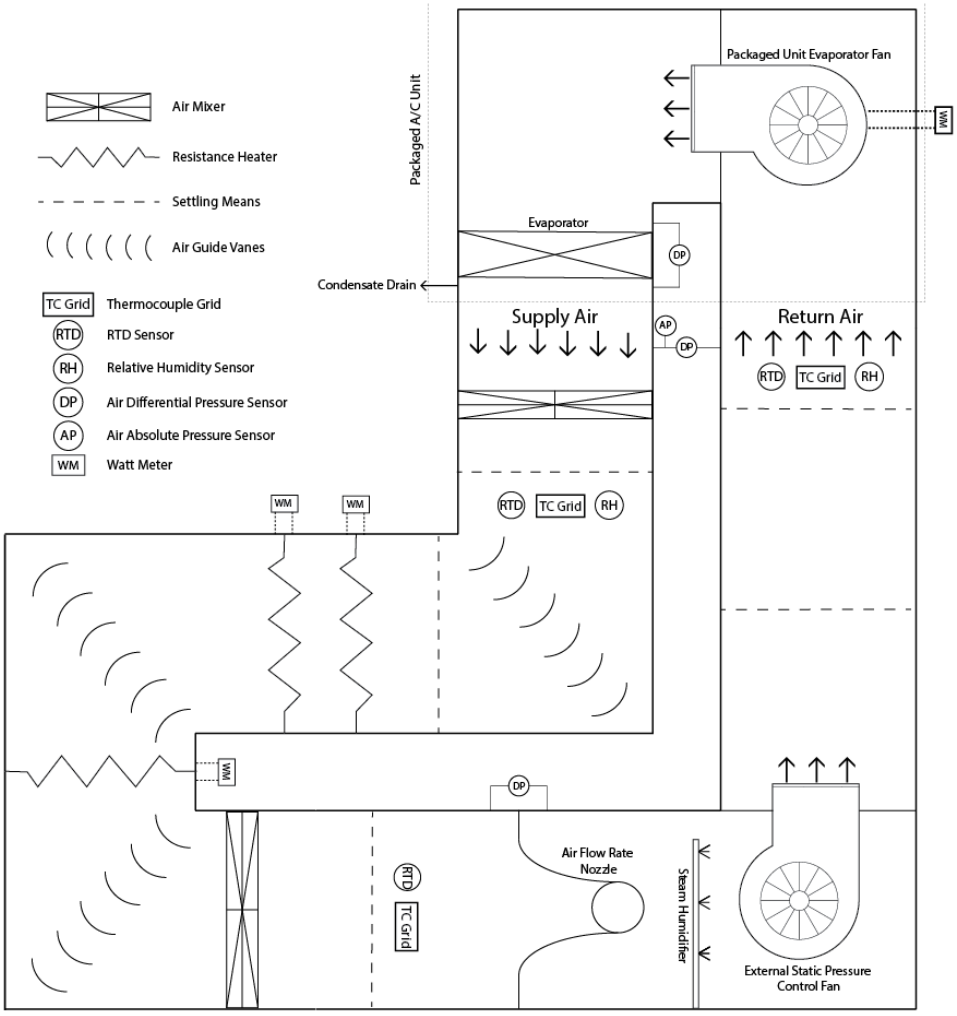

Figure 82: Evaporator Closed Loop Schematic with Instrumentation

Beginning with the chilled and de-humidified supply air from the packaged unit's evaporator into the ducted loop. Two mixers from Blender Products Inc. are used to ensure the air at the outlet of the evaporator is well mixed at the downstream measuring plane. The mixers' specifications are shown in Table 34 and are shown in Figure 83.

Table 34: Supply Air Mixer Specifications

Parameter	**Units**	**Value**
Model No.	-	AB8
Quantity	-	2
Pressure drop at 0.472 m^3/s	Pa, in.H_2O	62.2 , 0.25

Figure 83: Air Mixers Installed at Air Supply Side

The measuring plane downstream of the mixers is shown in Figure 84. It has eight thermocouples and an RTD to measure dry bulb temperature and a relative humidity sensor to measure humidity. The thermocouples are spaced evenly into four rows of two, and the RTD and relative humidity sensor is placed directly in the center of the duct. Settling means were installed upstream of the measuring plane to ensure uniform flow. Additionally, reflective insulation was added behind each thermocouple, RTD, and relative humidity sensor. The reflective insulation ensures that the irradiation from these heaters does not interfere with the airside measurements at this measuring plane. Downstream of this measuring plane are two resistance heaters used to recondition the air to the desired temperature as shown in Figure 85.

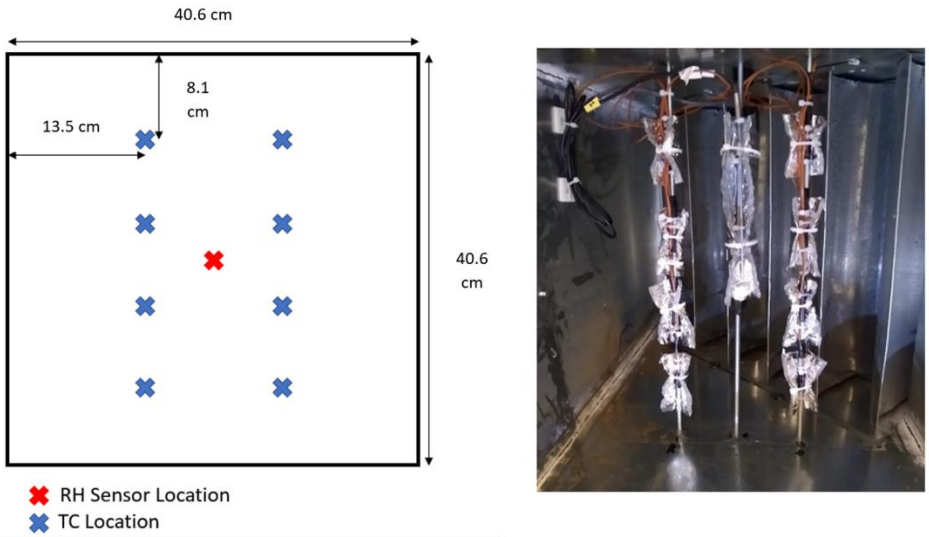

Figure 84: Instrumented Measuring Plane at Supply Side of Packaged Unit

Figure 85: Two 4 kW Resistance Heaters Installed in Ducted Closed Loop

The resistance heaters will have a total power output of approximately 8.0 kW when fully powered. A silicone controlled rectifier (SCR) controller was used to modulate the power to ensure the air at the return side of the packaged unit is at the desired temperature. A safety system is in place to ensure there is no risk of overheating. Multiple temeprature switches and a pressure switch (ensures there is airflow over the heaters) were installed. The heaters can only be energized when the all measured airside temperatures via the DAQ are below a certain threshold temperature and

the temperature and pressure switches are not triggered. A custom electrical distribution system was constructed to facilitate the power distribution for the heaters. Appendix D contains the wiring schematic. Evaporator fan, condenser fan, compressor, and overall unit total power consumption are all measued using watt-meters.

After being heated to the desired temperature there is an air mixer followed by settling means and a measuring plane. The air mixer's specifications are shown in Table 35 and the mixer is shown in Figure 86.

Table 35: Air Mixer after Heaters Specifications

Parameter	**Units**	**Value**
Model No.	-	AB12
Quantity	-	1
Pressure Drop at 0.472 m^3/s	Pa, in.H_2O	47.3, 0.19

Figure 86: Air Mixer Installed Downstream of Heaters

The measuring plane downstream of the mixer is shown in Figure 87. It has eight thermocouples and an RTD to measure dry bulb. The thermocouples are spaced evenly into four rows of two, and the RTD is placed directly in the center of the duct. Settling means were installed upstream of the

measuring plane to ensure uniform flow. The air temperatures before and after the heaters plus the heater's power dissipation will be used to calculate the airside mass flow rate.

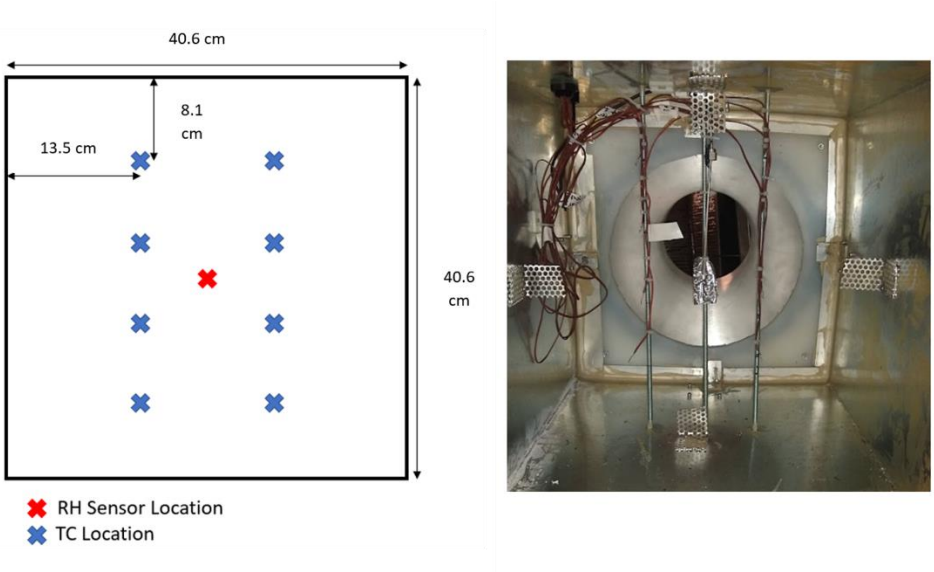

Figure 87: Instrumented Measuring Plane Downstream of Heaters

Downstream of this measuring plane is a 17.8 cm (7in) circular nozzle as shown in Figure 88. Pressure taps are used to measure the static pressure drop across the nozzle. This static pressure drop was correlated to the airside volumetric flow rate calculated from the resistance heaters.

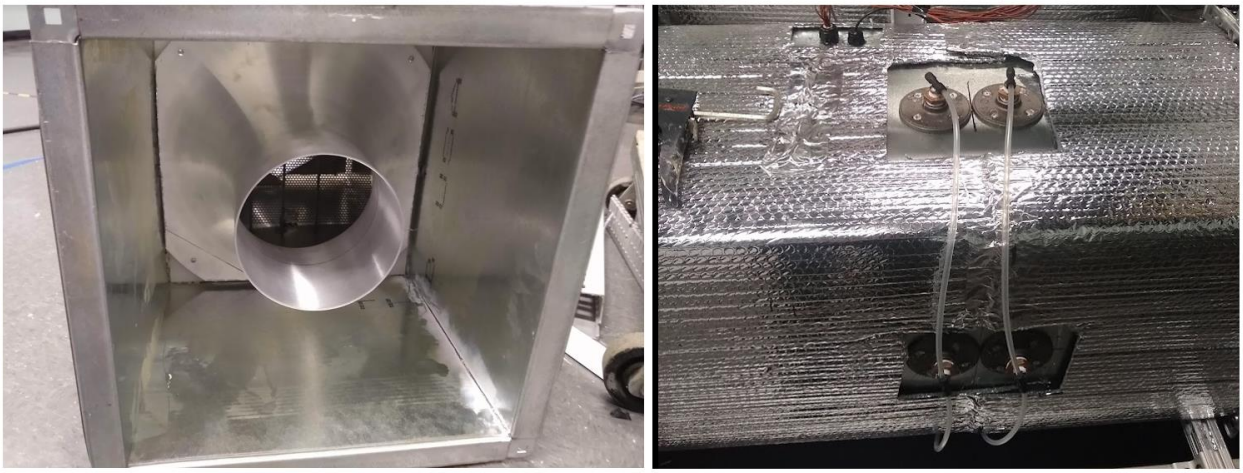

Figure 88: (Left) 17.8 cm (7”) Nozzle for Air VFR measurement (Right) Pressure Taps to Measure Static Pressure Drop across Nozzle

After the nozzle is the addition of steam to re-humidify the air to the desired inlet relative humidity at the return side of the packaged unit. Figure 89 shows the installed 4kW humidifier. Electrical heaters are used to generate steam and the amount of steam produced is controlled via a SCR controller.

Figure 89: 4kW Steam Humidifier Installed onto Evaporator Loop.

Next, downstream of the nozzle and steam addition is a variable speed centrifugal fan as shown in Figure 90. Its specifications are shown in Table 36. The fan was used to control the external static pressure (ESP) across the supply and return of the packaged unit. It is important to keep the external static pressure equal when testing the packaged unit with its original evaporator versus the packaged unit with the new CNTHX-FS prototype installed. Equal external static pressure before and after the NTHX evaporator retrofit allows for a fair comparison.

Figure 90: (Left) Centrifugal Fan Inlet (Right) Centrifugal Fan Outlet

Table 36. Centrifugal Fan Specifications

Parameter	**Units**	**Value**
Model No.	-	R3G280-RR03-H8
Manufacturer	-	ebm-Papst
Max VFR	m^3/s	0.944
Max Pressure Lift	Pa, in.H_2O	870.9, 3.5

Downstream of the centrifugal fan and directly before the return side of the packaged unit is one last set of settling means and a measuring plane as shown in Figure 91. The measuring plane has eight thermocouples and a relative humidity sensor. The thermocouples are spaced evenly into four rows of two, and the relative humidity sensor is placed directly in the center of the duct. Settling means were installed upstream of the measuring plane to ensure uniform flow. The upstream

variable speed centrifugal fan provides ample mixing before this measuring plane, so air mixers were not needed.

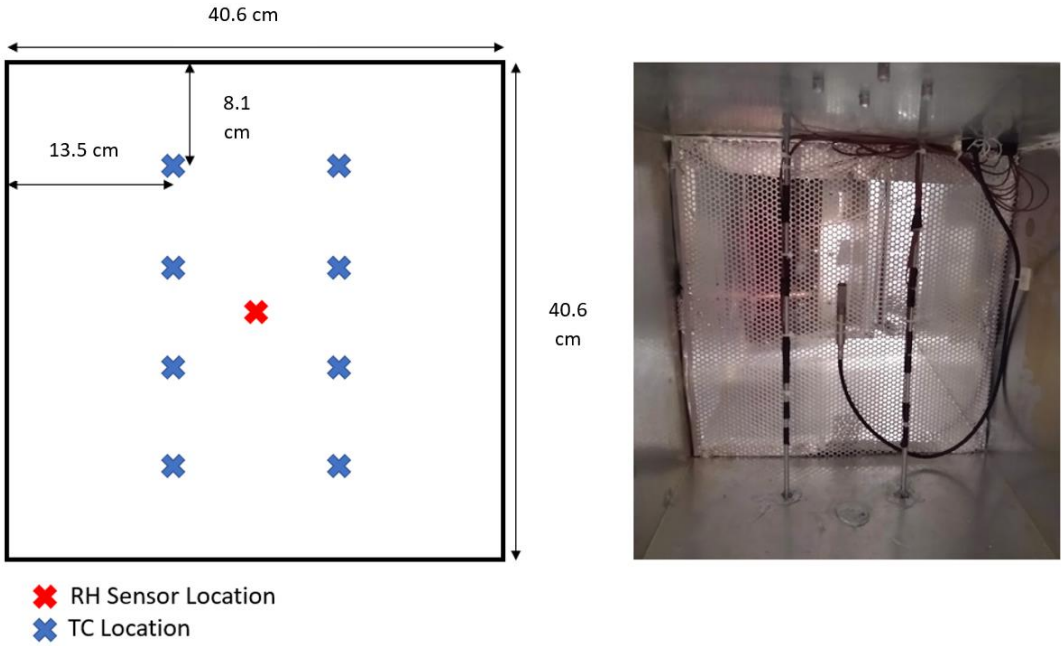

Figure 91: Instrumented Measuring Plane Inlet of Supply Air to Packaged Unit

Static pressure taps were installed at the supply and return of the ducted loop as shown in Figure 92. These were used to measure the external static pressure experienced by the packaged unit. Additionally, one of these pressure taps was used to measure the absolute air pressure in the ducted loop for airside properties calculations. Lastly, static pressure taps were installed across the evaporator to measure the air-side pressure drop across the evaporator.

Appendix C shows evaporator fan repairs. It was found the evaporator's fan motor's end cap control panel was not functioning "out-of-box" upon initial power-up of the unit.

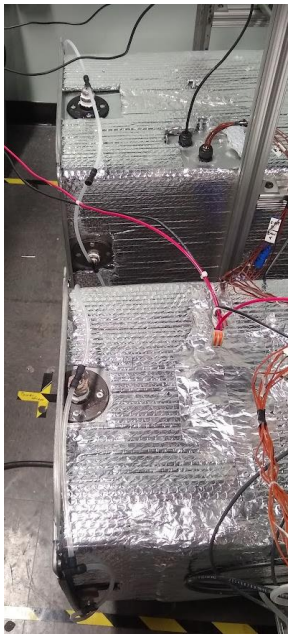

Figure 92: Pressure Taps to Measure External Static Pressure across Supply and Return

The unit's condenser air-side was also instrumented with thermocouples, a relative humidity sensor, and absolute pressure transducer. Condenser capacity was measured on the refrigerant-side. Condenser inlet temperature was required to be controlled. Figure 93 shows a schematic of the condenser's air-side instrumentation. Ten thermocouples are equally spaced across the inlet of the condenser's air-side and eight evenly spaced at the outlet of the condenser fan as shown in Figure 94.

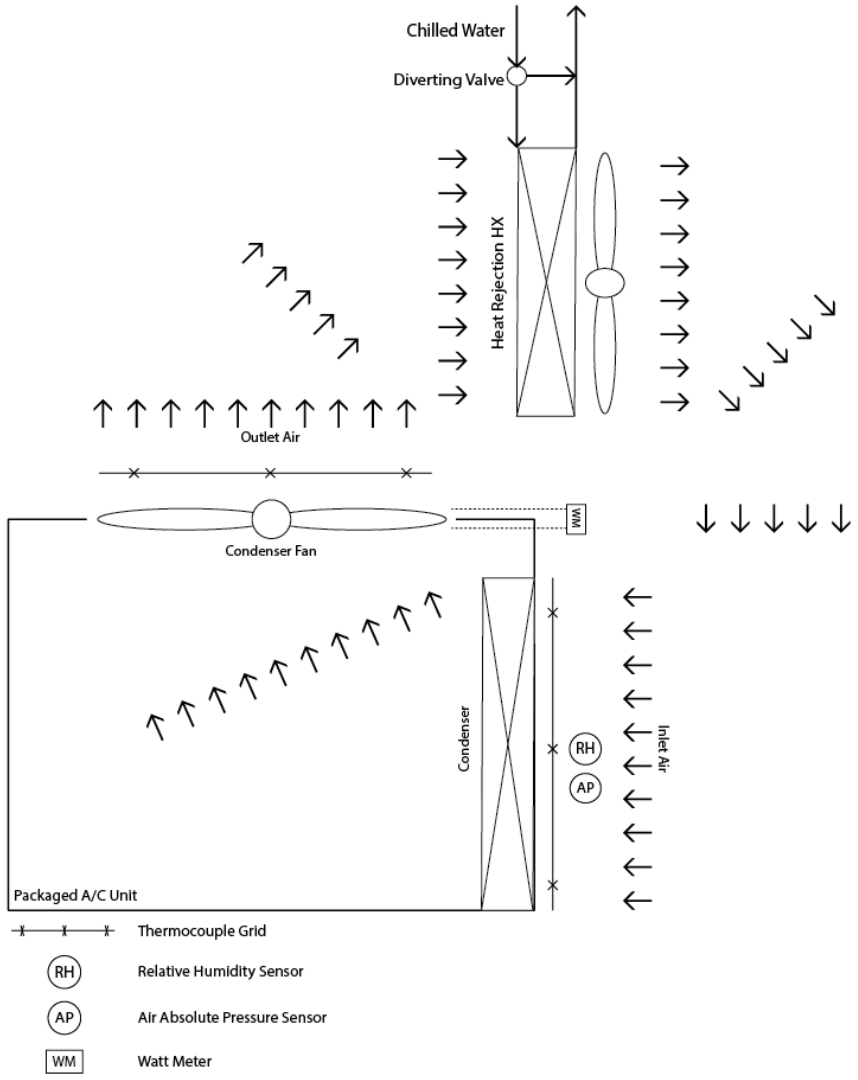

Figure 93: Condenser Air-Side Set-up and Instrumentation Schematic

Next, the installed heat rejection heat exchanger is shown in Figure 94. The outlet air from the condenser enters the air-to-water heat exchanger and is cooled with chilled water. Enough cooling was provided to achieve the desired inlet air condenser dry bulb temperature. A diverting valve was used to control the water mass flow rate into the heat exchanger which controls the amount of cooling provided.

Figure 94: Heat Rejection Heat Exchanger Installed on Packaged Unit.

The refrigerant-side was also instrumented. The instrumentation schematic is shown in Figure 95. The refrigerant piping in the packaged unit is shown in the side view in Figure 96. Absolute pressure transducers are installed at the outlet of the condenser and inlet of the compressor. A differential pressure transducer was installed across the inlet and outlet of the condenser. A separate differential pressure transducer was installed across the inlet of the evaporator distributor and the inlet of the compressor (measuring the pressure drop across the distributor + evaporator + suction line). A Coriolis mass flow meter was installed at the inlet of the TXV (liquid line). Two surface mount thermocouples were installed at the condenser inlet and outlet, and evaporator inlet and outlet. A single surface mount thermocouple was installed at the TXV inlet and compressor inlet as well. The same DAQ set-up as discussed Chapter 2 was used. Note, when the CNTHX-FS prototype evaporator was installed, the distributor was removed.

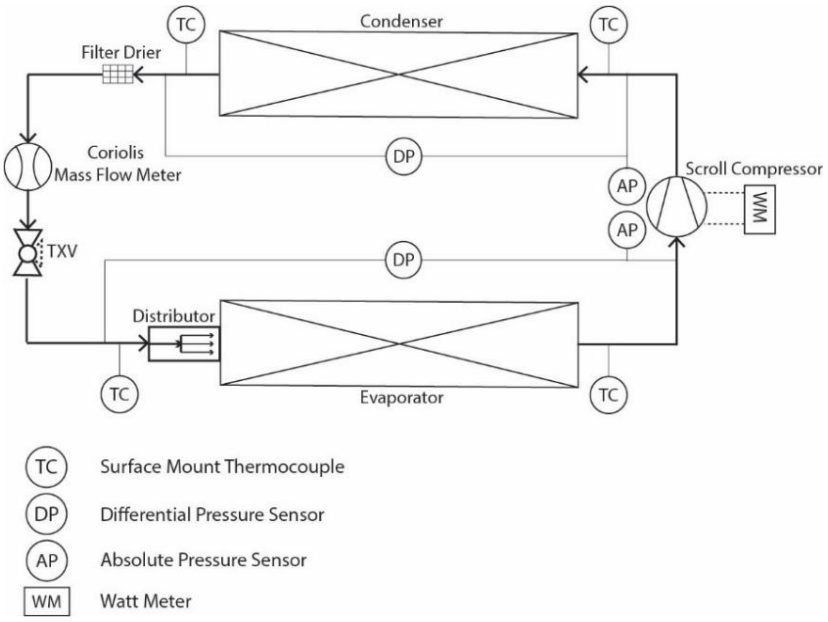

Figure 95: Packaged Unit Refrigerant-Side Set-up and Instrumentation Schematic

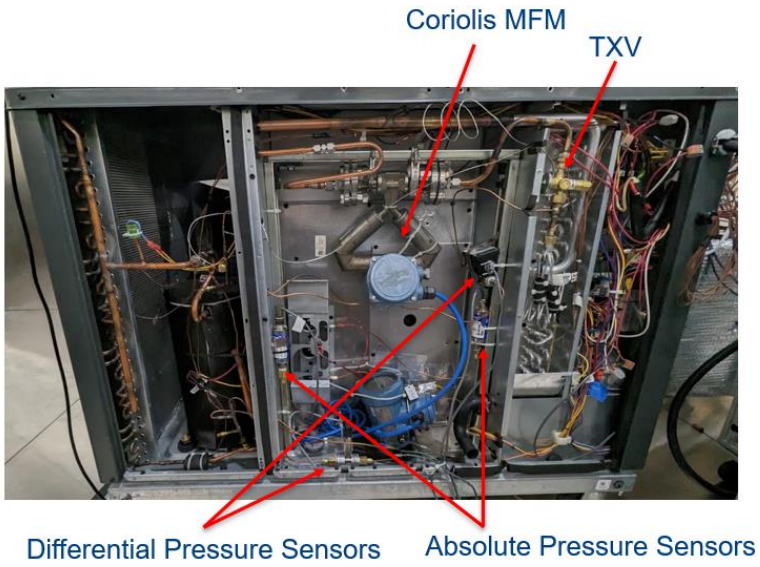

Figure 96: Packaged Unit Refrigerant Instrumentation

The finalized test facility set-up in an environmental chamber is shown in Figure 97. The environmental chamber does not provide any active cooling or de-humidification, but provides

an enclosed space for the air-to-water heat ejection heat exchanger to properly control the inlet air temperature of the condenser. Table 37 shows a summary of the test facility's instrumentation uncertainty.

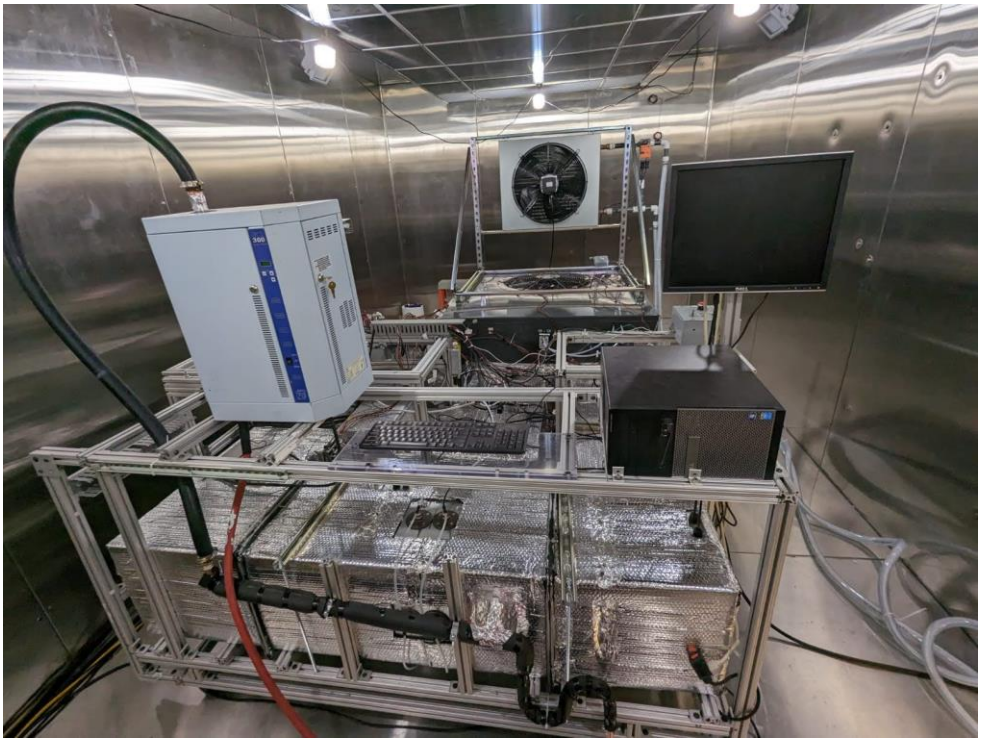

Figure 97: Packaged Unit Test Facility in Environmental Chamber

Table 37: Packaged Unit Testing Instrumentation and Uncertainty

Category	Measurement	Type	Range	Systematic Uncertainty
Air-Side	Temperature	Thermocouple, Type T	-250 to 350 °C	± 0.5 °C
		1/10 DIN RTD	-200 to 800 °C	± 0.03 to 0.07 °C
	Barometric Pressure	Strain	80 to 110 kPa	± 60 Pa
	ESP and Evaporator Differential Pressure	Strain	0 to 248.8 Pa	± 1.00 Pa
	Nozzle Differential Pressure	Strain	0 to 622.1 Pa	± 2.49 Pa
	Relative Humidity	Thin Film Capacitance	0 to 100 %	± 1.0 %
Refrigerant-Side	Mass Flow Meter	Coriolis	0 to 606 g/s	± 0.1% of reading
	Temperature	Thermocouple, Type T	-250 to 350 °C	± 0.5 °C
	Absolute Pressure	Strain	0 to 3447.4 kPa	± 1.72 kPa
	Differential Pressure	Strain	0 to 68.95 kPa	± 0.17 kPa
Electrical	Total Unit Watt-Meter	Hall Effect	0-20 kW	± 0.5% of reading
	Evap. Fan, Cond. Fan, Compressor, Resistance Heater Watt-Meters	Hall Effect	0-4 kW	± 20 W

3.1.2 Packaged Unit Data Reduction Methodology

The controlled air-side test conditions are shown in Table 38.

Table 38 Packaged Air-Conditioning Unit AHRI 210/240 Testing Conditions (AHRI, 2023)

	Baseline Unit w/ Tube-Fin Evaporator		Unit Retrofitted w/ CNTHX-FS Evaporator	
AHRI 210/240 Test Type	A_{full}	B_{full}	A_{full}	B_{full}
Evaporator Fan Speed	Full	Full	Full	Full
External Static Pressure [Pa , in H_2O]	124.4, 0.5	124.4, 0.5	124.4 0.5	124.4, 0.5
Evaporator Loop Air Return Temp. (Dry Bulb/Wet Bulb) [°C]	26.7/19.4	26.7/19.4	26.7/19.4	26.7/19.4
Condenser Air Inlet Temp. (Dry Bulb/Wet Bulb) [°C]	35/23.9	27.8/18.3	35/23.9	27.8/18.3
Compressor Speed	Full	Full	Full	Full

For all thermodynamic property evaluations, the commercial software XProps was used (Optimized Thermal Systems, 2023). Eq. 34 through Eq. 37 calculate the evaporator's calculated total, sensible, latent air-side loads, and SHR.

$$Q_{e,a,t} = \dot{m}_a\left(h_{a,in} - h_{a,out}\right) + P_{e,fan} \quad \text{Eq. 34}$$

$$Q_{e,a,s} = \dot{m}_a c_{p,avg}(T_{a,in} - T_{a,out}) + P_{e,fan} \quad \text{Eq. 35}$$

$$Q_{e,a,l} = \dot{m}_a h_{w,fg}(w_{a,i} - w_{a,o}) \quad \text{Eq. 36}$$

$$SHR = \frac{Q_{e,s}}{Q_{e,t}} \quad \text{Eq. 37}$$

Eq. 38 calculates the evaporator's refrigerant-side capacity. Isenthalpic expansion is assumed across the TXV to determine the evaporator's inlet specific enthalpy. Temperature and absolute pressure are used to determine the refrigerant's specific enthalpy values at all other points.

$$Q_{e,r} = \dot{m}_r(h_o - h_i) \quad \text{Eq. 38}$$

Eq. 39 shows the evaporator's energy balance. Ideally, this should stay between -5 to 5 %.

$$EB_e = 2 * 100 * \frac{(Q_{e,r} - Q_{e,a,t})}{(Q_{e,r} + Q_{e,a,t})} \quad \text{Eq. 39}$$

Eq. 40 through Eq. 41 calculate the condenser's refrigerant-side capacity and air-side mass flow rate.

$$Q_{c,r} = \dot{m}_r(h_i - h_o) \quad \text{Eq. 40}$$

$$\dot{m}_{c,a} = \frac{Q_{c,r} + P_{c,fan}}{Cp_{c,a,avg}(T_{c,a,o} - T_{c,a,i})} \quad \text{Eq. 41}$$

The evaporator's average total capacity is calculated as the average between the refrigerant-side and air-side capacity.

$$Q_{e,avg} = \frac{(Q_{e,r} + Q_{e,a,t})}{2} \quad \text{Eq. 42}$$

Lastly, the system level COP is calculated in Eq. 43.

$$COP = \frac{Q_{e,avg}}{P_{unit,total}} \quad \text{Eq. 43}$$

3.1.3 Evaporator Closed Loop Air Mass Flow Rate Calibration

Before testing was conducted the air-side mass flow rate was calibrated in the evaporator closed loop. The same testing procedure as Figure 10 is used to calibrate the air-side mass flow rate. Except, the resistance heaters in Figure 85 are used. Eq. 5 was used to calculate the mass flow rate. The packaged unit was powered on and provided active cooling. The pressure drop across the nozzle was correlated to the VFR calculated using the resistance heaters. Volumetric flow rate using the equations in (Bohanon, 1975) was also calculated as back-up check. The variable speed centrifugal fan Figure 90 is used to vary the ESP from 99.5 to 149.3 Pa (0.4 to 0.6 in. H2O).

Volumetric flow rate was measured to be between 0.425-0.484 m^3/s (900-1025CFM). The volumetric flow rate calculated using the resistance heaters and using (Bohanon, 1975) were within 3% of one another indicating excellent agreement between the two methods and giving high confidence in the accuracy of the measured air mass flow rate. Eq. 44 shows the correlated nozzle pressure drop [Pa] versus air VFR [m^3/s] through the nozzle to be used during the packaged unit testing for an applicable VFR of 0.425-0.484 m^3/s (900-1025CFM).

$$VFR_{Nozzle} = 0.001285 DP_{Nozzle} + 0.197 \ [m^3/s] \qquad \text{Eq. 44}$$

3.1.4 Packaged A/C Unit Baseline Testing

The packaged A/C unit was first tested at the AHRI 210/240 conditions given in Table 38 with the baseline tube-fin evaporator and condenser. The experimental performance was compared with the simulated predicted performance.

Packaged Unit Baseline Experimental Testing

Two steady state points were measured, each lasting one hour long, one for A_{full} condition and one for B_{full} condition. The method for determining the amount of R-410A charged into the system is described. The amount of R410A charge is an important performance parameter before and after the CNTHX-FS heat exchanger retrofit. This unit's refrigerant line was retrofitted with a TXV (replacing its fixed orifice expansion device). Based on AHRI standard 210/240 (AHRI, 2023) the following testing procedure was used to determine the amount of refrigerant in this system when a TXV is used.

- Charge system with initial target amount of refrigerant (for baseline system this is the factory rated charge, 2.21 kg).
- Achieve steady state AHRI A_{full} testing conditions with initial charge amount.

- Increase charge until at least 5.6K subcooling is achieved at condenser outlet.
- Adjust TXV control knob until greater than 4K superheat is achieved.
- Once desired subcooling and superheat is reached, conduct one-hour steady state test under A_{full} conditions.
- Next, conduct one-hour steady state test under B_{full} conditions without changing refrigerant charge.

Table 39 shows the experimental data summary for both A_{full} and B_{full} tests with the baseline unit. Table 40 shows a summary of the air-side thermodynamic states. Table 41 shows a summary of all refrigerant-side thermodynamic states.

Table 39: Packaged Unit Baseline Experimental Testing Data Summary.

				AHRI B_{full} Test		AHRI A_{full} Test	
		Measured Quantity	Units	Values	Uncertainty (+/-)	Values	Uncertainty (+/-)
Air-Side	Evaporator	Evaporator Supply Temp	[C]	13.57	0.31	14.24	0.31
		Evaporator Return Temp	[C]	26.68	0.35	26.70	0.35
		Evaporator Return RH	[%]	50.71	2.00	50.72	2.00
		Evaporator MFR	[kg/s]	0.548	0.020	0.548	0.020
		Evaporator VFR	[m^3/s,CFM]	0.468,990.80	0.02,35.66	0.467,988.67	0.02,35.60
		Inlet Velocity	[m/s]	1.17	0.04	1.17	0.04
		External Static Pressure	[Pa , in.H2O]	0.50	0.01	0.50	0.01
		Sensible Capacity	[kW]	7.49	0.38	7.13	0.37
		Latent Capacity	[kW]	2.72	0.95	1.72	0.95
		Total Evaporator Capacity	[kW]	10.38	1.14	9.00	1.12
		Evaporator Pressure Drop	[Pa]	30.18	1.24	29.48	1.24
	Condenser	Condenser Inlet Temperature	[C]	27.80	0.32	35.09	0.32
		Condenser Outlet Temperature	[C]	34.74	0.35	42.10	0.35
		Condenser MFR	[kg/s]	1.57	0.11	1.50	0.10
		Condenser VFR	[m^3/s,CFM]	1.38,2928.08	0.10,203.80	1.35,2860.73	0.10,197.56
R410A	Evaporator	Low-Side Pressure (Evaporator Outlet)	[KPa]	1070.87	17.24	1097.82	17.24
		Evaporator+Distributor+Suction Line R410A Pressure Drop	[kPa]	63.83	0.86	74.97	0.86
		Superheat	[K]	6.04	0.89	5.48	0.89
		Evaporator Capacity	[kW]	9.93	1.14	9.24	1.12
	Condenser	High-Side Pressure (Condenser Outlet)	[kPa]	2340.77	17.24	2785.63	17.24
		Condenser R410 Pressure Drop	[kPa]	32.20	0.17	31.91	0.17
		Subcooling	[K]	7.84	0.77	7.55	0.75
		Condenser Capacity	[kW]	11.38	0.09	10.98	0.09
	Overall	R410A MFR	[g/s]	54.69	0.11	54.96	0.11
Power Consumption		Evaporator Fan	[W]	227.64	0.93	225.68	0.92
		Condenser Fan	[W]	277.48	1.11	271.87	1.09
		Compressor	[kW]	1.68	0.01	2.01	0.01
		Total System	[kW]	2.20	0.02	2.53	0.03
System Level		Evaporator Average Total Capacity	[kW]	10.15	0.57	9.12	0.56
		Evaporator Energy Balance	[%]	-4.47	10.94	2.63	12.44
		COP	[-]	4.62	0.27	3.60	0.23
		SHR	[-]	0.74	0.04	0.78	0.04
		Refrigerant Charge	[kg]	2.36	0.11	2.36	0.11

Table 40: Packaged Unit Baseline Experimental Testing: Air-Side Thermodynamic State Summary.

				AHRI Bfull Test		AHRI Afull Test	
Location		Measureand	Units	Value	Uncertainty (+/-)	Value	Uncertainty (+/-)
Evaporator	Supply Air	DB Temperature	[C]	13.57	0.31	14.24	0.31
		RH	[%]	94.16	2.00	97.30	2.00
		Abs. Pressure	[kPa]	100.36	0.12	100.67	0.12
	Return Air	DB Temperature	[C]	26.68	0.35	26.70	0.35
		RH	[%]	50.71	2.00	50.72	2.00
		Abs. Pressure	[kPa]	100.24	0.12	100.54	0.12
Condenser	Inlet Air	DB Temperature	[C]	27.80	0.32	35.09	0.32
		RH	[%]	28.17	4.00	16.63	4.00
		Abs. Pressure	[kPa]	100.36	0.12	100.60	0.12
	Outlet Air	DB Temperature	[C]	34.74	0.35	42.10	0.35
		RH	[%]	18.98	4.00	16.64	4.00
		Abs. Pressure	[kPa]	100.36	0.12	100.60	0.12

Table 41: Packaged Unit Baseline Experimental Testing: R410A Thermodynamic State Summary.

			AHRI B_{full} Test		AHRI A_{full} Test	
Location	Measureand	Units	Values	Uncertainty (+/-)	Values	Uncertainty (+/-)
Compressor Inlet	Enthalpy	[kJ/kg]	432.09	0.93	431.68	0.95
	Temperature	[C]	15.49	0.71	15.77	0.71
	Pressure	[kPa]	1070.87	17.24	1097.82	17.24
Compressor Outlet	Enthalpy	[kJ/kg]	459.81	1.31	464.98	1.35
	Temperature	[C]	61.97	1.00	72.01	1.00
	Pressure	[kPa]	2372.97	17.24	2817.54	17.24
Condenser Inlet	Enthalpy	[kJ/kg]	458.58	0.96	463.51	0.99
	Temperature	[C]	61.00	0.71	70.90	0.71
	Pressure	[kPa]	2372.97	17.24	2817.54	17.24
Condenser Outlet	Enthalpy	[kJ/kg]	250.53	1.24	263.80	1.32
	Temperature	[C]	30.69	0.71	38.25	0.71
	Pressure	[kPa]	2340.77	17.24	2785.63	17.24
TXV Inlet	Enthalpy	[kJ/kg]	250.55	1.76	263.56	1.86
	Temperature	[C]	30.71	1.00	38.13	1.00
	Pressure	[kPa]	2340.77	17.24	2785.63	17.24
TXV Outlet	Enthalpy	[kJ/kg]	250.55	1.76	263.56	1.86
	Temperature	[C]	11.32	0.71	12.39	0.71
	Pressure	[kPa]	1134.70	17.26	1172.79	17.26
Evaporator Outlet	Enthalpy	[kJ/kg]	432.09	1.24	431.68	1.32
	Temperature	[C]	15.49	0.71	15.77	0.71
	Pressure	[kPa]	1070.87	17.24	1097.82	17.24

The evaporator energy balance for both the A_{full} and B_{full} test are within ±5%, indicating excellent agreement between the air-side and R410A calculated capacity. The evaporator delivered between 7.13-7.49 kW (2.03-2.13 Tons of Refrigeration) of sensible cooling. The rated packaged unit is rated for 2-2.5 tons of refrigeration indicating the unit is operating as intended. COP for the A_{full} and B_{full} tests were 3.60 and 4.62, respectively. As expected, the COP decreased as the condenser air inlet temperature increased causing the compressor power to increase. Both COP values are within the expected range for the unit. The SHR was 0.78 and 0.74 for A_{full} and B_{full} tests, respectively, and are within reasonable range for this unit. There was greater than 7K subcooling

and 5.5K superheat for both tests satisfying AHRI 210/240 testing standard for packaged unit with a TXV. A total of 2.36kg (83.2oz) of R410A was added to the system which is 6.7% higher than the rated factory charge of 2.21kg (78oz). There are multiple reasons for the increased charge needed for the system. Additional tubing, equipment, and sensors (pressure transducers, Coriolis mass flow meter, and TXV) increased the internal volume of the system. Charge was added to the system until at least 5.6K of subcooling was achieved at the outlet of the condenser to adhere to AHRI 210/240 standard.

The constructed test facility was able to successfully measure the packaged unit's performance and control the intended air-side parameters; inlet evaporator DB/WB temperatures, condenser inlet DB temperature, and external static pressure across the supply and return. All parameters measured for the baseline A_{full} and B_{full} tests were within the expected range. The packaged unit delivered the intended amount of cooling.

Packaged Unit Baseline Simulation Comparison

System level simulations were conducted by the Modeling and Optimization Consortium (MOC) group at CEEE using the software VapCyc to evaluate how well the baseline unit with the tube-fin heat exchanger is agreeing with the predicted performance (Winkler et al., 2007). To match the experimental conditions as close as possible, first, the A_{full} conditions were simulated with the convergence criteria being the measured experimental superheat and subcooling Then, the B_{full} condition was simulated using the resulting system refrigerant charge from the A_{full} simulation and the measured experimental superheat as convergence criteria. For both A_{full} and B_{full} simulations the measured experimental inlet air conditions for the evaporator and condenser were used. Figure 98 shows the comparison of the simulated versus experimental cycle simulation. Table 42 shows a detailed comparison of the critical system performance parameters.

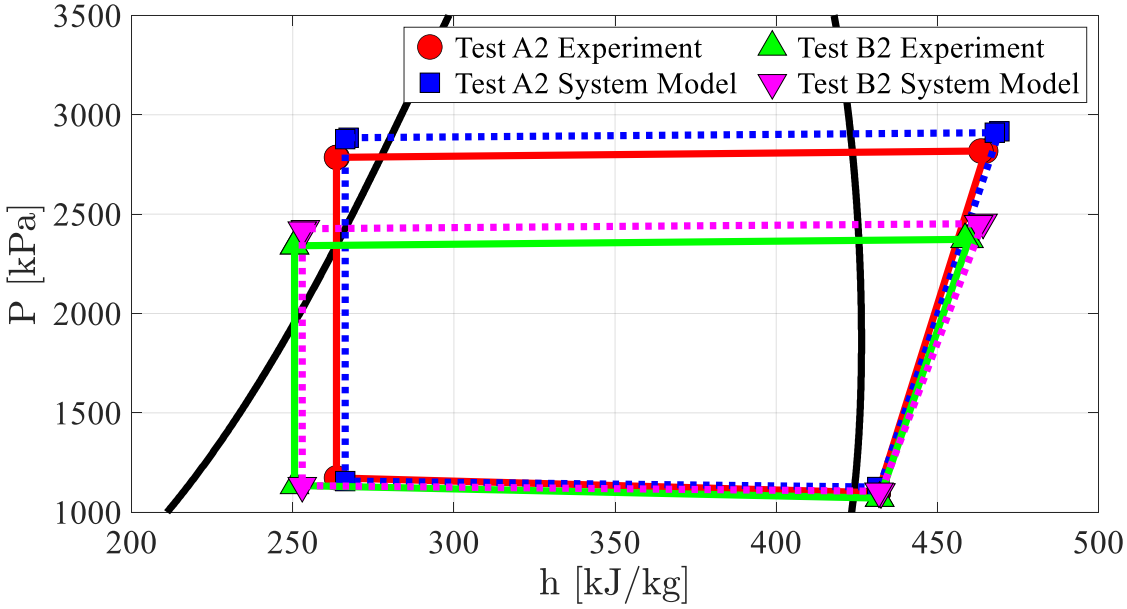

Figure 98: Packaged Unit Simulation versus Experimental Cycle Performance Comparison at AHRI 210/240 Conditions

Table 42: Packaged Unit Baseline Experimental Testing: Predicted versus Measured Summary

AHRI 210/240 Test Condition	AHRI A_{Full}			AHRI B_{Full}		
Category	Experimental	Simulation	Percent Difference	Experimental	Simulation	Percent Difference
Total Capacity [W]	9,108	9,371	2.89%	10,141	10,001	-1.38%
SHR [-]	0.78	0.76	-2.56%	0.74	0.73	-1.35%
Total Power Consumption [W]	2,531	2,472	-2.33%	2,196	2,131	-2.95%
COP [-]	3.60	3.72	3.14%	4.62	4.61	-0.37%
R410A Charge [kg]	2.36	1.57	-33.36%	2.36	1.57	-33.36% (Convergence Criteria)
Evaporator Air Outlet DB Temp. [C]	14.24	13.90	-2.39%	13.57	13.51	-0.44%
Evaporator Air Outlet WB Temp. [C]	13.98	13.41	-4.08%	13.02	12.95	-0.54%
R410A MFR [g/s]	55.0	56.5	2.87%	54.7	55.7	1.83%
Superheat [K]	5.48	5.48	0% (Convergence Criteria)	7.84	7.80	-0.51% (Convergence Criteria)
Subcooling [K]	7.55	7.55	0% (Convergence Criteria)	6.04	6.04	0%

Total cooling capacity, COP, and SHR were predicted within 2.9%, 3.1%, and 2.6%, respectively; indicating excellent agreement between simulation and experimental results. Refrigerant charge was underpredicted by 33.4%.

3.1.5 Packaged A/C Unit Testing w/ CNTHX-FS

A comparison between CNTHX-FS and the packaged unit's original tube-fin heat exchanger is shown in Figure 95 and Table 43. CNTHX-FS was tested on a component level as a dry evaporator in Chapter 2. The baseline fin-tube evaporator was replaced with the non-round bare tube shape and topology optimized CNTHX-FS evaporator.

Figure 99: (Left) Baseline Fin-Tube Evaporator (Right) CNTHX-FS Prototype Evaporator (not to scale)

Table 43: Baseline Fin-Tube Evaporator versus CNTHX-FS Comparison

	Baseline Tube-Fin Evaporator	CNTHX-FS Evaporator	Percent Difference from Baseline
Material	Aluminum	Copper	n/a
Core Dimensions (LxWxD) [mm]	660 x 603 x 57	564 x 580 x 29	n/a
Core Envelope Volume [cm^3]	22,684	9,486	-58.1%
Envelope Volume with headers [cm^3]	n/a	19,404	n/a
Face Area [m^2]	0.397	0.327	-17.6%
Core Weight [kg]	8.1	16.4	+100.6%
Active Air-Side Surface Area [m^2]	Unable to report values due to propriety restrictions. Percent differences reported.		-75.1%
Core Internal Volume [cm^3]			-78.9%
Internal Volume Including CNTHX-FS Headers [cm^3]			-55.2%
Core Material Volume [cm^3]			-43.0%

Note, if the tubes were instead made of Aluminum, CNTHX-FS's core would weigh 4.90 kg. The tube-fin heat exchanger and distributor were removed from the packaged unit and CNTHX-FS was installed in the same location Figure 100 .

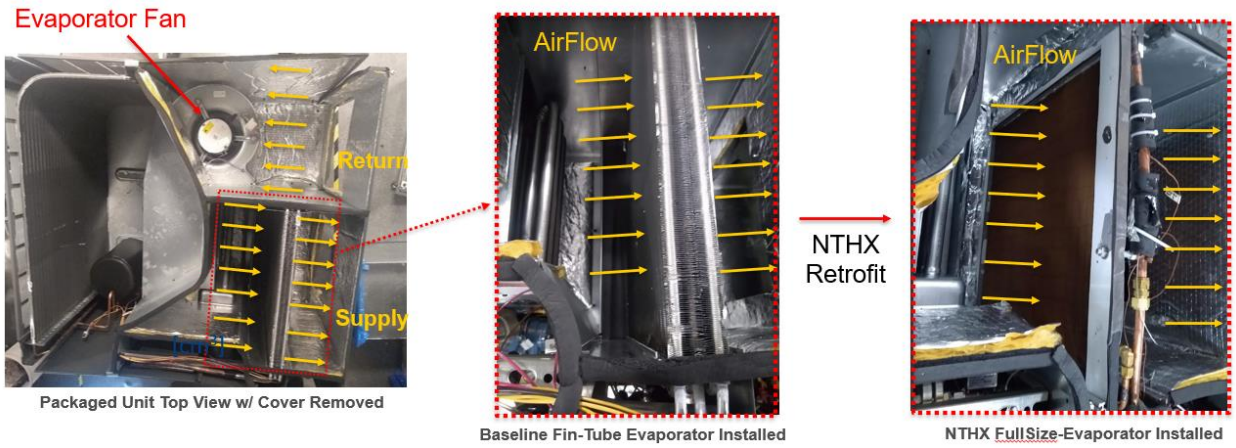

Figure 100: Installation Location of CNTHX-FS into Packaged Unit

Figure 101 shows the orientation of CNTHX-FS with respect to gravity and inlet/outlet ports. Two-phase refrigerant enters at the top left header and flows horizontally through the bare tubes. The heat exchanger is a single pass. Superheated vapor accumulates in the right header and exits the top right header.

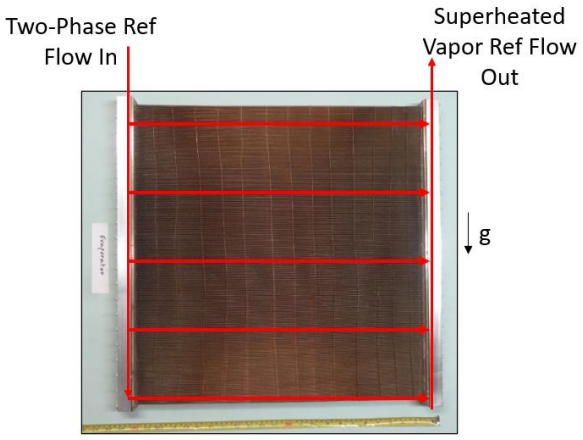

Figure 101: Installation and Port Orientation CNTX-FS

AHRI A_{Full} test was conducted with CNTHX-FS installed. This is the same test condition conducted for the baseline testing. Based on AHRI standard 210/240 the following testing procedure is used to determine the amount of refrigerant in this system

- Charge system with an initial target amount of R410A refrigerant, 1.77kg (75% of refrigerant charge compared to baseline testing).
- Achieve steady state AHRI A_{Full} testing conditions with initial charge amount.
- Increase charge until at least 5.6K subcooling is achieved at condenser outlet.
- Adjust TXV control knob until greater than 4K superheat is achieved.
- Once desired subcooling and superheat is reached, conduct one-hour steady state test under A_{Full} conditions.

An hour-long steady state test was conducted at A_{Full} test conditions. Table 39 shows the experimental data summary of the A_{full} test with CNTHX-FS and the A_{full} test from the baseline as well for comparison. Table 45 shows a comparison between experimental and simulation predicted performance of the packaged unit performance with CNTHX-FS. Simulation was conducted by CEEE Modeling and Optimization Consortium (Tancabel et al., 2022).

Table 44: Packaged Unit Performance Baseline Fin-Tube Evaporator versus CNTHX-FS

		Measured Quantity	Units	CNTHX-FS A_{full} Test	Baseline Tube-Fin A_{full} Test	Percent Diff. w/ Baseline
Air-side	Evaporator	Evaporator Supply Temp	[C]	20.57	14.24	44.45
		Evaporator Return Temp	[C]	26.68	26.70	-0.07
		Evaporator Return RH	[%]	50.68	50.72	-0.08
		Evaporator MFR	[kg/s]	0.57	0.55	3.64
		Evaporator VFR	[m^3/s , CFM]	0.492,1042.04	0.467,988.67	5.40
		Inlet Velocity	[m/s]	1.51	1.17	29.06
		External Static Pressure	[Pa , in.H2O]	124.4,0.50	124.4,0.50	0.00
		Sensible Capacity	[kW]	4.49	7.13	-37.03
		Latent Capacity	[kW]	1.75	1.72	1.74
		Total Evaporator Capacity	[kW]	6.32	9.00	-29.78
		Evaporator Pressure Drop	[Pa]	21.29	29.48	-27.78
	Condenser	Condenser Inlet Temperature	[C]	34.97	35.09	-0.34
		Condenser Outlet Temperature	[C]	40.31	42.10	-4.25
		Condenser MFR	[kg/s]	1.46	1.50	-2.67
		Condenser VFR	[m^3/s , CFM]	1.30,2756.79	1.35,2860.73	-3.63
R410A	Evaporator	Low-Side Pressure (Evaporator Outlet)	[KPa]	808.44	1097.82	-26.36
		Evaporator R410A Pressure Drop	[kPa]	103.75	74.97	38.39
		Superheat	[K]	7.01	5.48	27.92
		Evaporator Capacity	[kW]	6.38	9.24	-30.95
	Condenser	High-Side Pressure (Condenser Outlet)	[kPa]	2662.37	2785.63	-4.42
		Condenser R410 Pressure Drop	[kPa]	21.90	31.91	-31.37
		Subcooling	[K]	7.35	7.55	-2.65
		Condenser Capacity	[kW]	8.21	10.98	-25.23
	Overall	R410A MFR	[g/s]	37.58	54.96	-31.62
Power Consumption		Evaporator Fan	[W]	221.9	225.68	-1.67
		Condenser Fan	[W]	272.4	271.87	0.19
		Compressor	[kW]	1.99	2.01	-1.00
		Total System	[kW]	2.50	2.53	-1.19
System Level		Evaporator Average Total Capacity	[kW]	6.35	9.12	-30.37
		Evaporator Energy Balance	[%]	-0.94	2.63	n/a
		COP	[-]	2.54	3.60	-29.44
		SHR	[-]	0.71	0.78	-8.97
		Refrigerant Charge	kg	2.08	2.36	-11.86

Table 45: Packaged Unit with CNTHX-FS Evaporator Experimental Testing: Predicted versus Measured Summary

AHRI 210/240 Test Condition	AHRI A_{Full}		
Category	Experimental	Simulation	Percent Difference
Total Capacity [W]	6.35	9.27	46.0%
SHR [-]	0.71	0.73	2.8%
Total Power Consumption [W]	2.50	2.47	-1.2%
COP [-]	2.54	3.68	44.9%
R410A Charge [kg]	2.08	1.30	-37.5%
Evaporator Air Outlet DB Temp. [C]	20.6	15.2	-26.2%
R410A MFR [g/s]	37.6	55.4	473.%
Superheat [K]	7.0	7.0	0% (Convergence Criteria)
Subcooling [K]	7.4	7.4	0% (Convergence Criteria)

AHRI 210/240 B_{full} testing was attempted, however the TXV was unable to control the amount of superheat and subcooling. Testing was stopped and a leak was found at the CNTHX-FS gasket to be the cause and testing could not be continued.

The packaged unit's total evaporator capacity, COP, and SHR changed by -30.4%, -29.44%, and -9.0%, respectively, compared to the performance with the baseline tube-fin evaporator. The outlet refrigerant pressure of the evaporator decreased by 26.3%, indicating a significantly lower

evaporation pressure. Sub-cooling was approximately equal and there was 1.5 K more superheat with CNTHX-FS.

Air-side evaporator pressure drop decreased by 27.8% with CNTHX-FS at a higher VFR (5.4%). This translated to a decrease in evaporator fan power consumption by 1.7%. There were not more power savings because the ESP across the supply and return was kept constant at 0.5 in.H2O (124.4 Pa). Hence, the air-side pressure drop of the evaporator only makes up 15-20% of the total pressure lift the evaporator fan must provide.

There are three major reasons that CNTHX-FS is underperforming with regard to cooling capacity and COP when compared to the baseline tube-fin heat exchanger. First, is that the installation orientation and inlet/outlet port orientation was causing more severe refrigerant maldistribution than anticipated. Multiple studies have shown that maldistribution can cause as much as 35% capacity performance degradation for evaporators in air conditioning applications (both tube-fin and microchannel with vertical oriented headers) (Choi et al., 2003; Zou et al., 2014).

Second, the horizontal orientation of the tubing caused severe water condensate build up in the core of the heat exchanger. The tubes are compact enough that water bridging (adhesion) to the tubes restricted water drainage. The restricted drainage of water condensate also potentially led to a decrease in total evaporator capacity and decreased the sensible heat ratio. Lastly, the outlet port of CNTHX-FS is a 6.35mm (¼") NPT female fitting. The outlet port of the original tube-fin base line evaporator has 15.88mm (5/8") OD tubing at the outlet. The internal open area of CNTHX-FS's 6.35mm (¼") NPT fitting for the superheated vapor to pass through is approximately 20-30% when compared to the tube-fin's 15.88mm (5/8") OD tubing. Consequently, the pressure drop across the CNTHX-FS and the suction line was 104 kPa at a refrigerant mass flow rate of 37.6 g/s versus the pressure drop across the tube-fin evaporator, its distributor, and suction line, 75 kPa at

a refrigerant mass flow rate of 55.0 g/s. Even though CNTHX-FS's refrigerant mass flow rate is 32% lower, the pressure drop is 39% higher than the baseline. The pressure drop across the core of the CNTHX-FS was predicted to be less than 1kPa, and the extremely high pressure drop is attributed to the small outlet port area. The high pressure drop reduces the suction line density and since the compressor is fixed single speed, decreased the overall refrigerant mass flow rate. Additionally, the restricted outlet flow may have caused additional refrigerant mass flow maldistribution. Due to severe refrigerant maldistribution and condensate bridging and build-up the total cooling provided and unit COP decreased compared to with the baseline fin-tube evaporator. The results indicated that the installation orientation, inlet/outlet port orientation and sizing, and manifold set-up for this class of non-round bare tube finless heat exchangers are critical for proper system level performance and further investigation is needed into the effect of these factors on the heat exchanger and system level performance.

Chapter 4: Adjoint Method Shape Optimized Bare Tube Heat Exchangers

Adjoint method is an optimization technique used to obtain shape sensitivities with respect to many design variables as a guide for gradient based optimization methods for little additional computational cost and can reveal unintuitive, organic, and potentially superior designs (Jameson, 2003). Recently with improvement in CFD solvers and in computer computational power, the discrete adjoint method has become used more frequently to perform optimization for heat transfer and fluid flow applications. Many of these studies focus on a very limited geometry or very specific case to optimize (Table 5). The objective of this chapter is to develop new shape optimized variable geometry compact bare tube heat exchangers using discrete adjoint method for typical HVAC&R applications. This chapter is broken down into the following sections.

- First, a discussion on the selection of adjoint solver to use for the multi-objective shape optimization of compact bare tube heat exchangers. The solver's adjoint method process and implementation are shown.
- The CFD domain set-up and data reduction methodology are presented. A comparison study was conducted with the CFD set-up and data reduction methodology and compared to correlations in literature.
- An ε-constraint and penalty method optimization scheme was implemented to use ANSYS Fluent's built-in adjoint solver and perform multi-objective shape optimizations. Critical solver/mesh set-up and settings to efficiently and robustly shape optimize the compact bare-tube geometries were identified and established. Tube shape geometry constraints are shown. A pipeline was then developed to extract the optimized tube geometry design and generate a CAD model to be additively manufactured.

- Multi-objective optimizations of a baseline 9.525 mm bare tube heat exchanger and single 9.525 mm bare tubes in cross flow are presented.
- Using the multi-objective optimization scheme and adjoint solver a parametric study was conducted to determine the potential improvement of finless bare tube heat exchangers with hydraulic diameters ranging from 0.5-5.0 mm, 2-4 tube banks, in staggered tube arrangement.
- A 500 W finless bare tube radiator was designed and shape optimized to be additively manufactured in polymer using Polyjet. The radiator prototype was successfully additively manufactured, and air-side thermal hydraulic performance experimentally evaluated in the heat exchanger testing facility presented in Chapter 2.
- Multi-objective optimizations were conducted on a previously shape and topology optimized NTHX1 design as the starting geometry instead of circular bare tubes. Optimizations indicate how much the air-side thermal hydraulic performance of an already shape and topology optimized bare tube heat exchanger can be improved using adjoint method shape optimization.
- Overall trends and findings of the shape optimized designs are discussed.

4.1 ANSYS Fluent Adjoint Solver

There are multiple options to implement adjoint based methods to optimize heat exchangers. One can create custom code/program to implement the design process. This would allow for the most amount of customization, but requires the most skill and time to develop. The other option is using commercial CFD software which have built-in adjoint solvers. One such example is the ANSYS

Fluent (ANSYS Inc., 2016) platform which features a built-in discrete adjoint solver. This option requires the least amount of time and mathematical skill to implement, but has much less customization possibility (ANSYS Inc., 2016). The user may not be able to constrain and set-up an optimization as desired. ANSYS Fluent's adjoint solver was selected since developing a custom in-house CFD solver with an adjoint optimization capability is out of the scope of this work. ANSYS Fluent applies the discrete adjoint approach due to its ability to provide more robust sensitivity information in cases with complex geometry. A converged adjoint solution provides shape sensitivities, identifying the areas where the domain should be modified to best improve the objective function.

ANSYS Fluent's adjoint solver workflow is described by the following process:

1. Using the starting geometry, Fluent solves the flow solution until the residuals converge to the desired levels or the maximum number of iterations is reached.
2. Next, the adjoint solver runs until the adjoint flow solution residuals converge to the desired levels or the maximum number of iterations is reached.
3. The resulting shape sensitivities are used as a guide to change the design using the appropriate mesh morphing method while obeying the prescribed geometry constraints and keeping the mesh above a minimum orthogonality. If the mesh orthogonality is too low the objective function improvement goal is reduced to reduce mesh distortion.
4. Fluent then solves the flow solution using the modified geometry and mesh. The new expected objective function based on the shape sensitivities and the actual objective function value from the new flow solution are compared. Steps 2-4 are then repeated until the objective function converges. I.e. the adjoint solver can no longer improve the objective

function above the convergence criteria while maintaining a minimum mesh orthogonality and staying within the provided geometry constraints.

ANSYS Fluent's mathematical implementation of its discrete adjoint-solver is discussed here. More details can be found in the ANSYS Fluent theory guide (ANSYS Inc., 2016). The goal of the solver is to find the sensitivities of an observable of interest, J, versus the control variables c. This is difficult since as the control variable changes, the flow solution, w, changes as well, which then affects the observables of interest. The adjoint method resolves this by eliminating the relationship between control variables and the flow solution. Eq. 45 through Eq. 48 show this process. Begin by defining observables of interest J and residuals of the Navier-Stokes equations R, and their relationship to the flow solution, w, and control variables, c.

$$J = J(w(c), c) \quad , \quad R = R(w(c), c) \qquad \text{Eq. 45}$$

Define the Lagrangian L with Lagrange Multipliers ψ and assume R=0 when flow solution converges.

$$L(w(c), c) = J + \psi^T R \quad \rightarrow \quad \frac{dJ}{dc} \equiv \frac{dL}{dc} = \frac{\partial J}{dw}\frac{dw}{dc} + \frac{\partial J}{\partial c} + \psi^T \left[\frac{\partial R}{\partial w}\frac{\partial w}{\partial c} + \frac{\partial R}{\partial c}\right] + \cancel{\frac{d\psi^T}{dc} R} \qquad \text{Eq. 46}$$

Choose ψ such that dependence on w is eliminated. This is considered the "extra adjoint equation" to be solved in addition to the typical Navier-Stokes flow equations, Eq. 47.

$$\frac{\partial J}{\partial w} + \psi^T \frac{\partial R}{\partial w} = 0 \quad \rightarrow \quad \psi^T \frac{\partial R}{\partial w} = -\frac{\partial J}{\partial w} \qquad \text{Eq. 47}$$

With the adjoint equation solved, the sensitivity of the observable of interest to the control variables is obtained independent of the flow solution.

$$\frac{dJ}{dc} = \frac{\partial J}{\partial c} + \psi^T \frac{\partial R}{\partial c} \qquad \text{Eq. 48}$$

For all 2D heat exchanger adjoint optimizations in this chapter:

- c is essentially the shape of the bare tubes. More technically c is the position of each discretized segment of the tube wall boundary in the computational domain. The tube segments' adjacent and surrounding mesh morphs to accommodate the segments' desired movement. Hence, these are considered shape optimizations. Note, technically the tubes' center can slightly move location and affect the effective tube pitch. However, this change in tube pitch is not significant enough to consider these optimizations a type of topology optimization.
- w is the flow solution (air-side). This is the resulting velocity, pressure, and temperature field after the discretized Navier-Stokes equations are solved in ANSYS Fluent.
- J is the observable of interest. For these optimizations this will be one of three different quantities. Mass weighted average of temperature at the outlet of the flow, difference between the inlet and outlet area weighted static pressure, or a formulated combination of the two. This will be discussed in more detail in later sections, but these serve as performance quantifiers for the heat exchangers of interest.

Theoretically, the adjoint sensitivity solution only requires slightly more computational cost when compared to the initial flow solution. Increasing the number of design/control variables does not increase the computational cost of solving for the sensitivities when compared to the regular flow solution with the same mesh size. This means the shape of the bare tubes can be divided into many segments and each segment can be moved individually. This allows for complex, organic, and often unintuitive designs. Additionally, one can increase the number of bare tubes themselves. This allows for large geometry domains.

Though, there are practical limitations, there is no guarantee that the adjoint solver will converge. Indeed, as the flow domain becomes larger and the geometry becomes significantly more complex, instabilities arise, and the adjoint solver may not achieve the required convergence. When this occurs, the sensitivities will not be an accurate guide for the shape change to realize an improved objective function. There are a variety of solver methods to deal with these instabilities, but this can drastically increase the computational cost and could even make the computation unreasonably time and resource intensive. Additionally, the quality of the mesh during the shape change process is of particular importance. Often, the flow solution or the adjoint solution will not converge due to worsening mesh quality. To counter this, there are some mesh improvement techniques implemented in Fluent to improve the orthogonality of the mesh each time the mesh is morphed and changed. Though, the mesh can only be improved slightly and sometimes the adjoint solver will decrease the objective goal (how much to improve the objective by) to ensure the mesh quality limit is not violated. This leads to premature completion of the shape optimization as the optimizer cannot continue only because the mesh quality will be too poor to achieve proper convergence.

4.2 CFD Domain and Data Reduction Methodology

The CFD domain set-up for all 2D bare tube heat exchanger optimizations and the data reduction methodology to evaluate the thermal-hydraulic performance are presented.

4.2.1 CFD Domain

Figure 102 shows the representative computational flow domain for air-flow over the bare tubes. Tube pitches, number of tube banks, tubes per bank are varied for different simulations but the following set-up, settings, and boundary conditions were used for all simulations. The simulation

domain is simplified as 2D flow. Symmetry is assumed at the top and bottom of the domain. Model boundary conditions include uniform airflow velocity and temperature at the inlet, gauge pressure at the outlet is 0 Pa, bare tubes' surface temperature is constant at 70 °C with zero slip walls, and inlet air temperature is 26.9 °C with uniform flow. The flow is assumed incompressible ideal gas. Variable air properties are used based on temperature. Realizable k-ε turbulence model with enhanced wall functions is applied with 2nd order upwind discretization scheme. Five to eight times the depth of the heat exchanger core was modeled for the exit flow to allow for the flow to resolve and prevent reversed flow at the outlet which can hinder the flow solution from converging. This is the distance between the trailing edge of the last tube bank and the outlet (0 Pa Gauge pressure boundary condition). Table 46 lists all relevant parameters and settings for the CFD simulation.

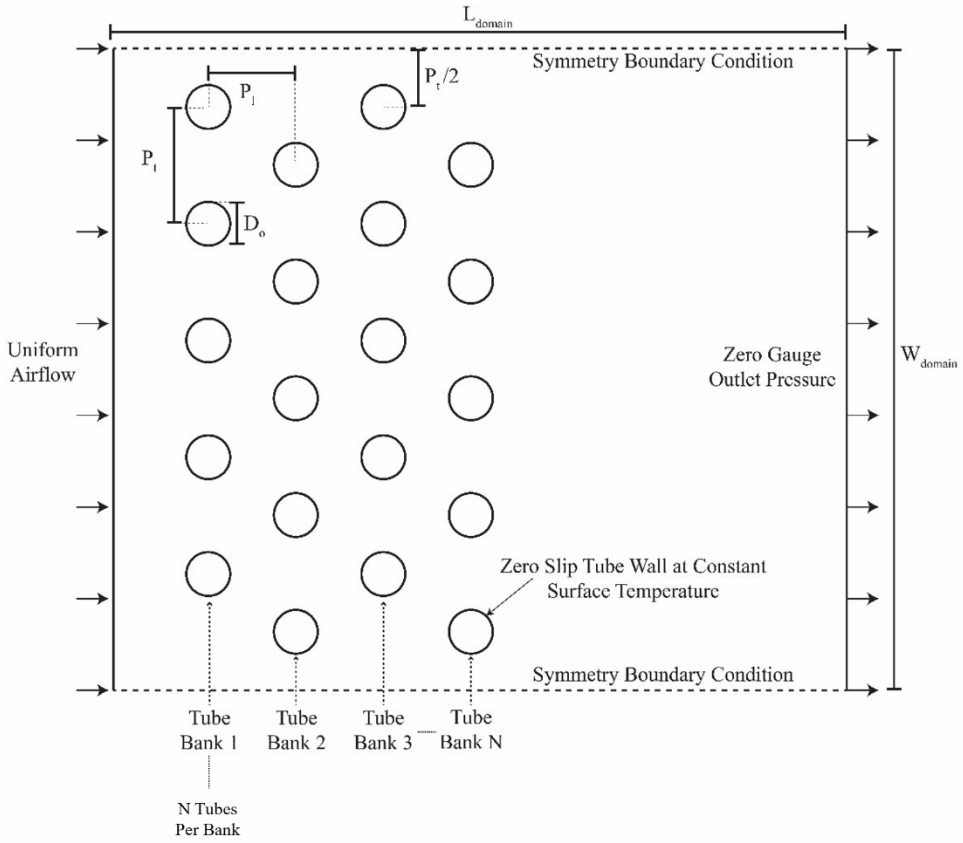

Figure 102: 2D Representative Computational Domain

Triangular mesh elements were used with smaller refined mesh around the bare tubes' core and coarser mesh at the inlet and outlet of the domain as shown in Figure 103 and Figure 104. Inflation layers were applied to the surface of the bare tubes' boundary wall.

Table 46: CFD Set-Up Parameters and Settings

Parameter		Value(s)
Fluid		Air
Properties	Density	Incompressible Ideal Gas
	Cp, k, μ	Variable with Temperature
Tube(s) Wall Surface	Temperature	Constant Temp. at 70°C
	Shear Conditions	Zero Slip Wall
Side Walls Boundary Condition		Symmetry
Flow Inlet	Distribution	Uniform Velocity
	Temperature	Uniform Temperature 26.9°C
Flow Outlet		0 Gauge Pressure
Turbulence Model		k-ε Realizable
Near Wall Treatment		Enhance Wall Treatment
Pressure-Velocity Coupling Scheme		Pressure Coupled
Spatial Discretization	Pressure	Second Order
	Momentum	Second Order Upwind
	Turbulent Kinetic Energy	Second Order Upwind
	Turbulent Dissipation	Second Order Upwind
	Energy	Second Order Upwind
	Pseudo Timestep	Global Time Step
Residuals	Continuity	1E-5
	x-velocity	1E-5
	y-velocity	1E-5
	energy	1E-6
	k	0.001
	ε	0.001

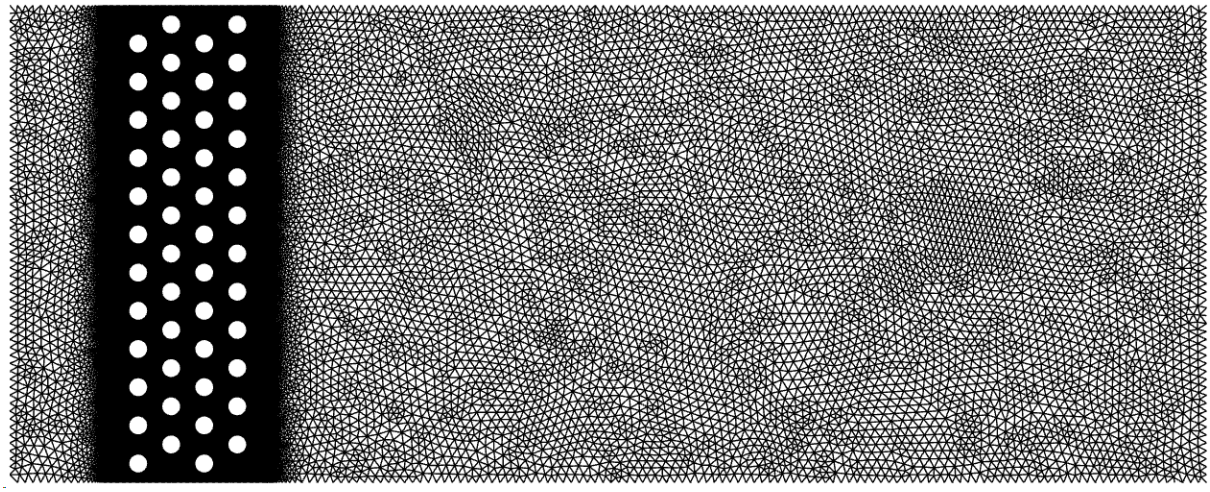

Figure 103: 2D Computational Mesh

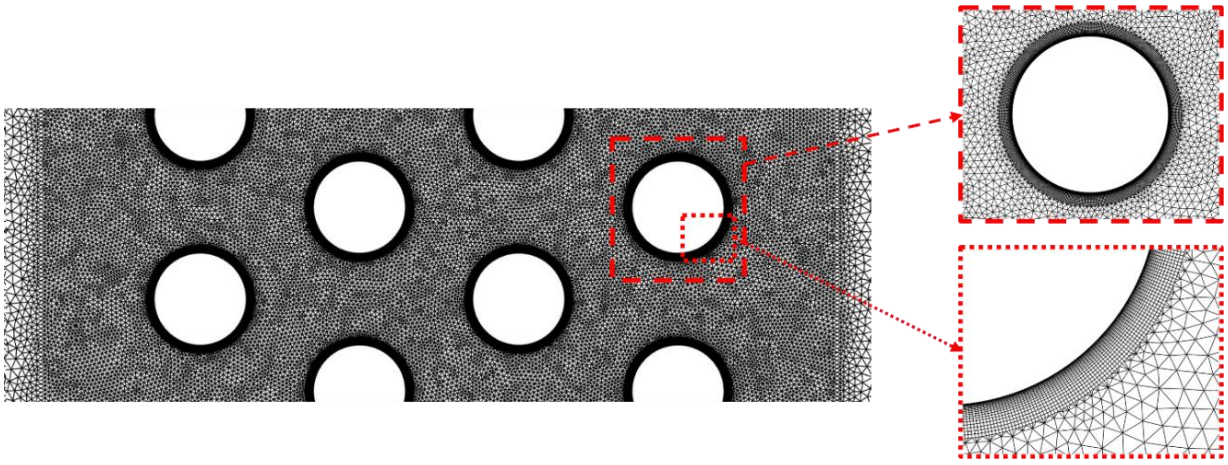

Figure 104: 2D Computational Mesh Zoomed In

4.2.2 Data Reduction Methodology

Eq. 49 through Eq. 51 calculate the airside heat transfer capacity. Note all flow domains are 2D, but assume a depth of 1 meter for calculations such as mass flow rate, tube surface area, etc. I.e. the bare tubes are assumed to be a meter in length. Mass-weighted average temperatures are calculated at the inlet and outlet and air-side mass flow is calculated at the inlet. The CFD model assumes constant tube wall temperature and only focuses on the air-side flow.

$$Q_{HX} = \dot{m}_{air} c_{p,air,m} (T_{air,out} - T_{air,in}) \quad \text{Eq. 49}$$

$$\mathrm{Q} = UA * LMTD \quad \text{Eq. 50}$$

$$LMTD = \frac{(T_w - T_{air,in}) - (T_w - T_{air,out})}{\ln\left(\frac{T_w - T_{air,in}}{T_w - T_{air,out}}\right)} \quad \text{Eq. 51}$$

Since the tube wall temperature is considered constant, the thermal resistance of tube wall conduction and refrigerant side convection are approximately zero. Also, A_o can be calculated via simulation data.

$$\mathrm{UA} = h_{air,avg} A_o \quad \text{Eq. 52}$$

Using the average air-side heat transfer coefficient, the Colburn j factor can be calculated. Additionally, friction factor (f) can be calculated. Note, for uniform geometry heat exchangers, the maximum velocity is calculated using tube pitch and outer diameter. However, since the final designs have irregular geometry, this could not be done. Maximum velocity was then estimated by locating the maximum velocity via completed simulation data and then taking an area-weighted average between the two tubes at that location's cross section.

$$j = \frac{h_{air,avg}}{\rho_m V_{max} c_{p,m}} Pr^{2/3} \quad \text{Eq. 53}$$

$$f = \frac{A_{min}}{A_o}\frac{\rho_m}{\rho_{in}}\left[\frac{2\Delta P \rho_{in}}{G_{max}{}^2} - (1+\sigma^2)\left(\frac{\rho_{in}}{\rho_{out}} - 1\right)\right] \quad \text{Eq. 54}$$

Here, σ is the contraction ratio, A_{min}/A_{in}, ratio of the minimum flow area to the frontal area and $V_{max} = V_{in}/\sigma$. A_{min} and A_o are the minimum-flow cross sectional area and total tube air-side surface area, respectively. G_{max} is the mass flux at the minimum flow area. ΔP is calculated as difference in area-weighted static pressure at the inlet and outlet of the flow domain. Overall surface efficiency of these bare tube heat exchangers, η, is unity since there are no extended surfaces.

Refrigerant-side cross sectional area calculations assume zero wall thickness unless otherwise specified.

4.2.3 Comparison with Literature Air-Side Heat Exchanger Correlations

CFD simulations were conducted using the described set-up and data reduction methodology. Inlet air velocity, tube pitches, number of tube banks, and tube outer diameter were varied, as shown in Table 47. The goal was to see how well the current CFD results align with the CFD based literature correlations for similar small diameter circular bare tube cross-flow heat exchangers. The air-side pressure drop and air-side average heat transfer coefficient were compared to Bacellar et al.'s correlations for staggered bare tubes with outer diameter ranging from 0.5 to 2.0 mm (Bacellar, Aute, Huang, et al., 2016a) and then 2.0 to 5.0 mm (Bacellar et al., 2014). The study was conducted for tube bank numbers of 2, 5, and 10. Figure 105 through Figure 107 show the comparison of the air-side pressure drop and air-side heat transfer coefficient for tube bank numbers of 2, 5, and 10.

Table 47: Parametric Study Matrix to Compare with Literature Correlations

Parameter	Units	Values
Inlet Air Velocity	m/s	0.5, 1, 3, 5, 7
Number of Tube Banks	[-]	2, 5, 10
[Horizontal and Vertical] Pitch Ratio* $\frac{D_o}{Pitch}$	[-]	[0.5,0.5]
Tube Outer Diameter	[mm]	1, 3, 5

*Horizontal and vertical pitch always equal

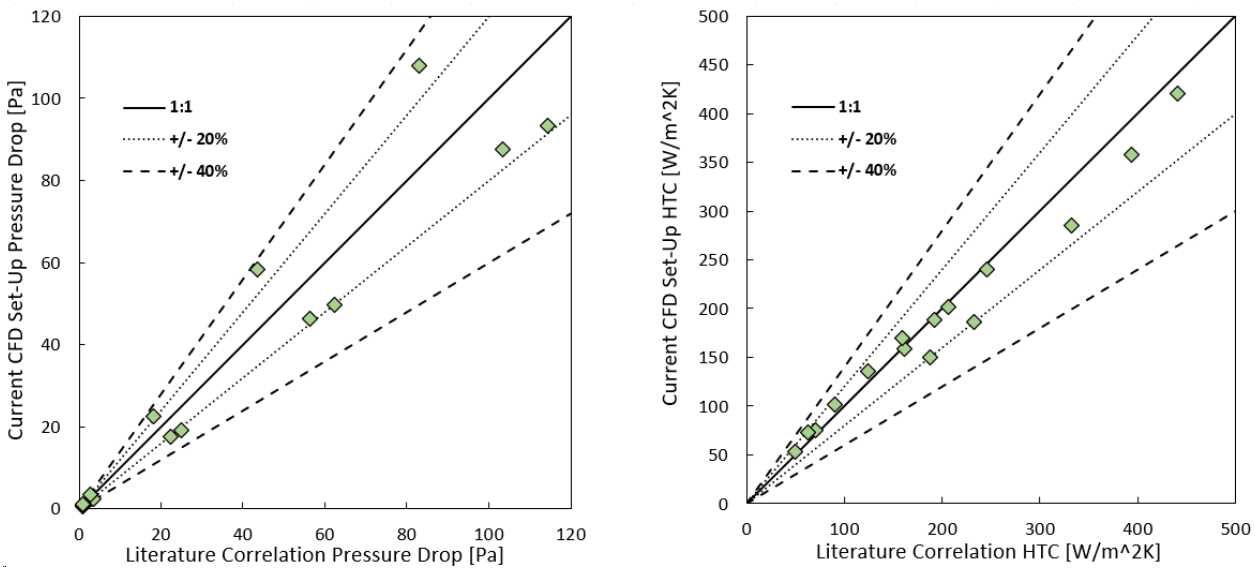

Figure 105: 2 Bank HX Correlation Comparison to CFD Set-Up (Left) Air-Side Pressure-Drop (Right) Average Air-Side HTC

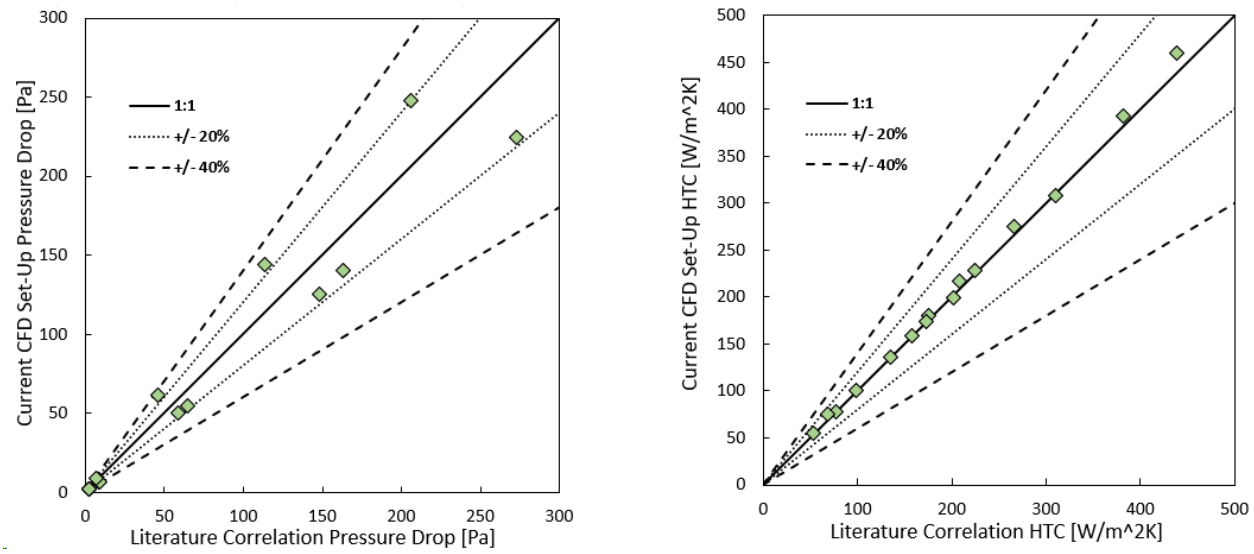

Figure 106: 5 Bank Correlation Comparison to CFD Set-Up (Left) Air-Side Pressure-Drop (Right) Average Air-Side HTC

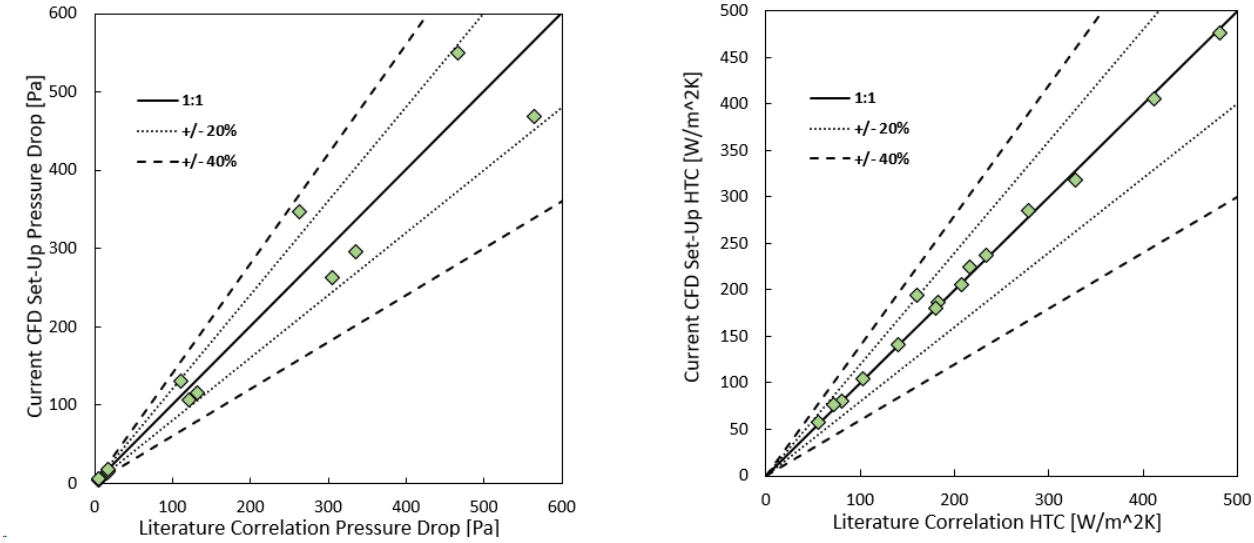

Figure 107: 10 Bank Correlation Comparison to CFD Set-Up (Left) Air-Side Pressure-Drop (Right) Average Air-Side HTC

Air-side pressure drop was predicted within 34% and air-side HTC was predicted within 20% for all points. The air-side pressure drop and air-side HTC agreed well enough with the literature CFD

correlations with bare tubes in this design space to continue forward with the current CFD set-up and data reduction methodology for the adjoint optimizations (Bacellar et al., 2014; Bacellar, Aute, Huang, et al., 2016a).

4.3 Multi-Objective Optimization Methodology

The following section details the optimization scheme developed and implemented to perform multi-objective shape optimizations of bare tube heat exchangers using ANSYS Fluent's adjoint solver. Tube shape geometry constraints are shown. Critical solver/mesh set-up and settings to efficiently and robustly shape optimize the 0.5-10.0 mm OD bare-tube geometries were identified and established.

4.3.1 ε-Constraint and Penalty Method Optimization Scheme

To achieve multi-objective optimizations, i.e. minimize the air-side pressure drop and maximize heat transfer capacity (air temperature change), an ε-constraint optimization framework (Aurora, 2012; Chircop & Zammit-Mangion, 2013) is implemented. First, two single objective optimization problems (SOOP) are conducted using Fluent's adjoint-solver.

$$minimize\ f(x_{tubes}) = \Delta P_{air} \quad \text{Eq. 55}$$

$$maximize\ f(x_{tubes}) = \Delta T_{air} \quad \text{Eq. 56}$$

These two designs act as the anchor points for the Pareto set to be generated and as reference points to normalize ΔP_{air} and ΔT_{air} from 0-1. These normalized parameters are referred to as $\Delta P_{air,norm}$ and $\Delta T_{air,norm}$. Using the anchor points the following constrained SOOP is created.

$$\begin{aligned} &maximize\ f(x_{tubes}) = \Delta T_{air,norm} \\ &s.t.\quad g(x_{tubes}):\ (\Delta P_{air,norm} - \varepsilon) \leq 0 \end{aligned} \qquad \text{Eq. 57}$$

A linear penalty method is utilized to transform the constrained SOOP to an unconstrained one. When the air-side pressure drop constraint is violated an artificial linear penalty is added (Aurora, 2012; Rao, 2009). The new final optimization problem is shown.

$$maximize\ f(x_{tubes}) = \Delta T_{air,norm} - C_{penalty} * \max\{(\Delta P_{air,norm} - \varepsilon), 0\} \qquad \text{Eq. 58}$$

For a given inlet air velocity, ε is varied N_{Pareto} number of times to generate a Pareto set of N_{Pareto} heat exchanger designs. This optimization scheme was used for all optimizations performed in this chapter (Ch. 4).

Note, the Fluent solver is limited to what can be calculated as an observable. It was desired to incorporate the average air-side heat transfer coefficient into the objective function. However, the surface area of the bare tubes was unable to be incorporated into the objective function due to limitations of Fluent's adjoint solver. This is a disadvantage of using a built-in adjoint solver tool as it can limit the user's capabilities. Hence, the average air-side heat transfer coefficient was not able to be calculated with Eq. 49 through Eq. 51. The change in air temperature across the tube bundle was used instead to measure heat transfer capacity across the heat exchanger since air-side mass flow rate stays constant during the design iterations. Figure 108 summarizes the optimization

formulation and Figure 109 shows a representative resulting Pareto set as the pressure drop constraint, ε , is varied.

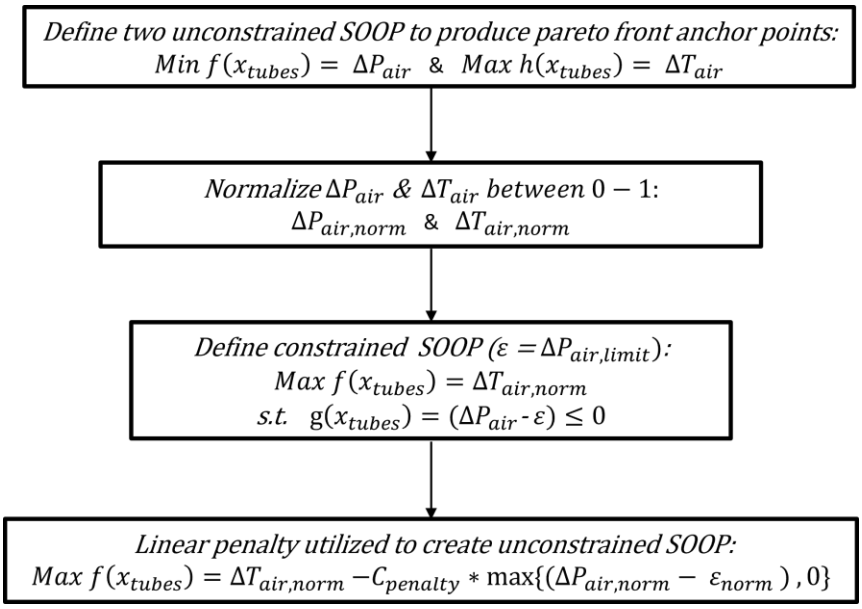

Figure 108: Multi-Objective Optimization Scheme Process

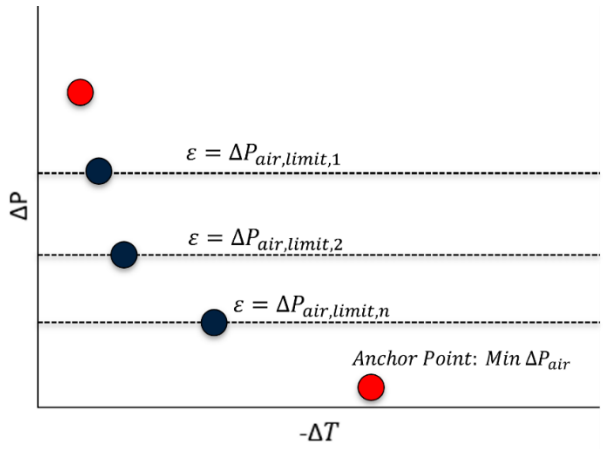

Figure 109: Representative Pareto set using Optimization Scheme

When the pressure drop constraint is violated, the optimization scheme decreases air-side pressure drop. Once the air-side pressure drop constraint limit is satisfied, typically the change in air-side temperature will begin to increase to improve the objective function while maintaining the air-side pressure drop below the constraint limit. An example of the change in pressure drop and outlet air temperature is shown in Figure 110 for the optimization of a sample 4-bank heat exchanger.

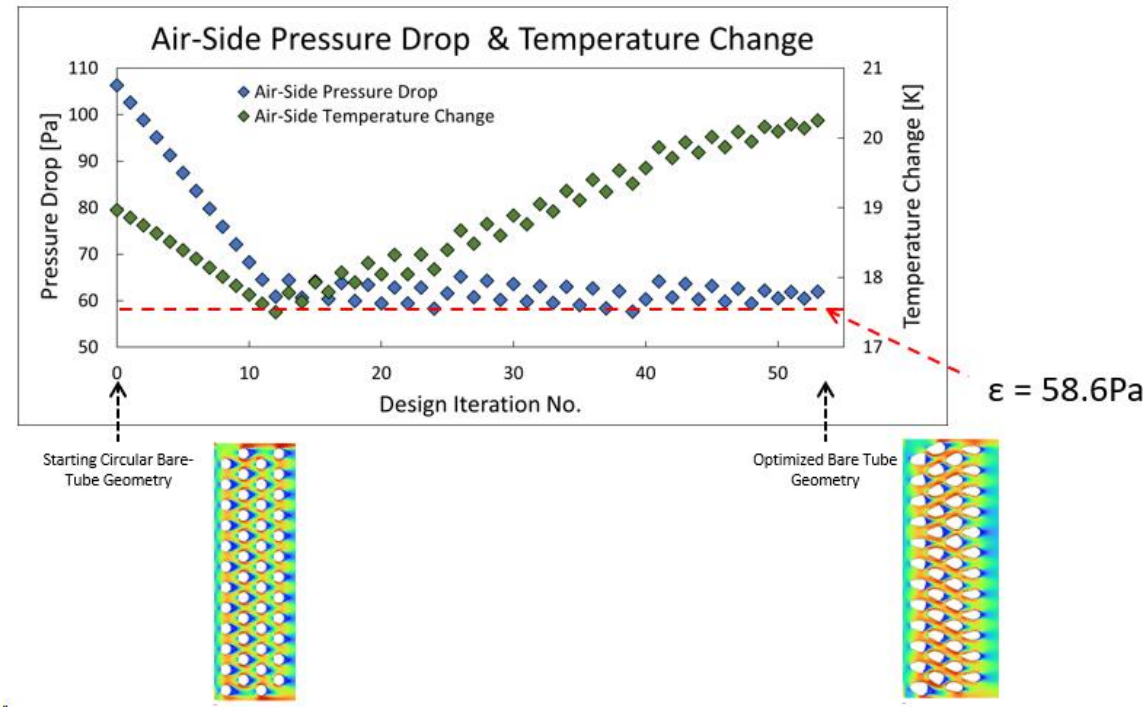

Figure 110: Change in Pressure Drop and Air Temperature Change over 54 Design Iterations using Optimization Scheme

Figure 111 shows the pipeline developed to set-up and perform the optimization and then generate a 3D CAD model to be 3D printed.

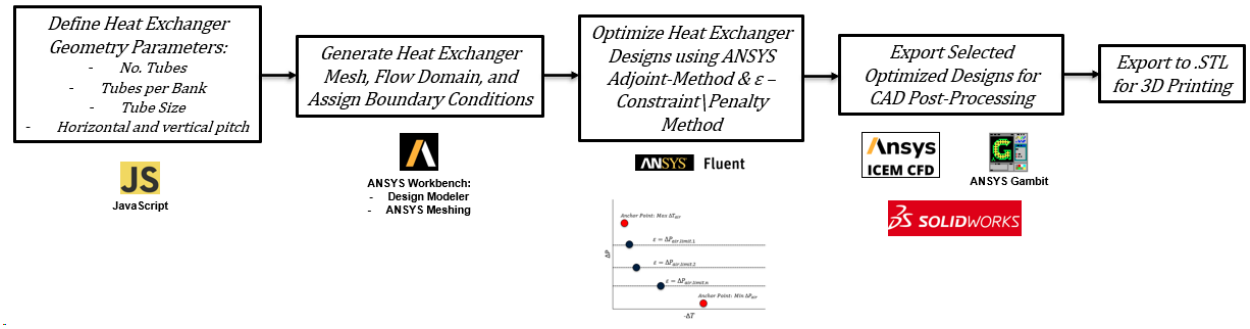

Figure 111: Developed Pipeline: From Domain Set-up to Additive Manufacturing

ANSYS Fluent supports the export of final adjoint optimized designs as a stereolithography (.STL) file with 3D geometry only. The final two steps in Figure 111 were developed because export of the final design is not directly supported for 2D geometry. A combination of ANSYS ICEM and ANSYS Gambit were used to go through the following conversion process.

- Save adjoint optimized design Fluent file as .CAS file type.
- Import .CAS into ANSYS ICEM.
- Export resulting mesh as an unstructured mesh file (.uns).
- Import unstructured mesh (.uns) into ANSYS Gambit and generate a 2D surface for all individual tube shapes in the heat exchanger core.
- Export 2D surfaces as a .IGES file type.
- Import .IGES into desired CAD software and use 2D shape geometry to construct 3D heat exchanger model for additive manufacturing (.STL). This includes
    - Creating tube walls
    - Extruding tubes to desired tube length
    - Designing headers/manifolds for tube core

4.3.2 Mesh and Adjoint Solver Set-up and Settings

The following section discusses the mesh sizing settings used and adjoint solver settings used to best optimize the bare tube geometries explored. Critical settings and sizing parameters are identified to provide insights for future researchers to help conduct adjoint optimization in similar design and air flow set-ups.

Mesh Set-Up and Sizing

Triangular mesh elements were used with smaller refined mesh around the bare tubes' core and coarser mesh at the inlet and outlet of the domain as shown in Figure 103 and Figure 104. Inflation layers were applied to the surface of the bare tubes' boundary wall. Additionally, the bare tube wall was discretized into 450 segments for each tube. The following mesh sizing rules were used when generating the mesh. Reasoning for each sizing rule is discussed.

- Mesh element size in core of heat exchanger - It was found that the mesh in this area needed to be very refined to allow for proper shape optimization of the bare tubes. As the tube shapes morph, the mesh morphs as well. The mesh in the core of the heat exchanger between the tubes experienced the largest amount of distortion and consequentially would have the lowest orthogonality value. A minimum orthogonality value was needed for the adjoint solver to continue and the solver would simply stop the optimization completely or reduce the objective function goal to reduce orthogonality degradation between design iterations and pre-maturely converge. The mesh orthogonality value distribution in the final core of a sample 4-bank optimized heat exchanger geometry is shown in Figure 112. Areas of blue indicate the lowest/worst orthogonality values. The triangular mesh sizing was based on the circular initial bare tube pitch. I.e. the distance between the bare tubes/available area for the

mesh to morph. This sizing was fine/small enough that it prevented significant orthogonality degradation for most optimization cases explored.

- Core Triangular Mesh Sizing: Mesh Size is 2-4% of initial circular bare tube pitch.

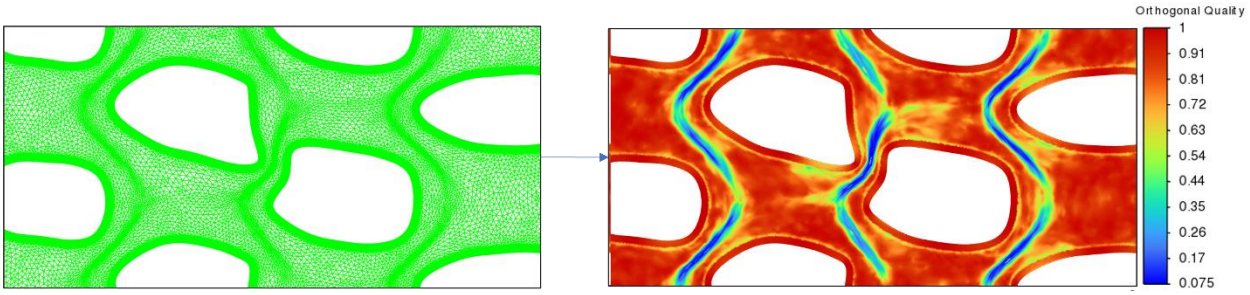

Figure 112: Mesh Orthogonality Map of Optimized Bare Tubes

- Tube Wall Inflation Layers – Inflation layers were applied to the zero slip tube walls. The settings in Table 48 were used. These inflation layer settings are included here because they had a significant effect on the adjoint optimizations.

Table 48: Bare Tube Inflation Layer Settings

Parameter	Units	Value(s)
First Inflation Layer Height	[mm]	0.09% of Circular Bare Tube D_o
Max. Number Inflation Layers	[-]	20
Inflation Rate	[-]	1.13-1.17

- Bare tube surface discretization – Each individual bare tube wall surface was discretized into 450 individual segments. The high number of segments allowed for more design flexibility and more complex designs. Additionally, it was found that below 300 segments, the adjoint solution would be less likely to converge.

ANSYS Fluent Adjoint Solver Settings and Set-Up

Table 49 shows a summary of all adjoint solver settings used during the multi-objective optimizations.

Table 49: Fluent Adjoint Solver Settings and Set-Up

Parameter		Value(s)
Adjoint Solver Methods	Pressure	Second Order
	Momentum	Second Order Upwind
	Energy	Second Order Upwind
Advancement Controls		Auto-Adjust
Stabilization Strategy		Blended (Dissipation+ Residual Minimization)
Dissipation	Damping Factor	1
	Damping Relaxation	0.9
	Damping Order	3
Residual Minimization	Number of Modes	400
	No. Recycled Modes	1
	AMG Iterations	10
Adjoint Residuals	Continuity	0.001
	Velocity	0.001
	Local Flow Rate	0.001
	Energy	0.001
Minimum Mesh Orthogonality		0.04
Objective Function Improvement Goal Per Design Iteration		0.015 – 0.035
Design Iteration Convergence Criteria		0.0001

The most crucial settings and set-up parameters for successful shape optimizations in this domain are discussed.

Adjoint Settings

With large computational domains and complex geometries (especially with sharp corners) the adjoint solver typically will not be able to converge within the required adjoint residual values without stabilization methods. The solver employs both dissipation and residual minimization stabilization schemes to help resolve instabilities and divergence behavior of the adjoint flow

solution. It was found the most effective stabilization method was using residual minimization scheme with a high number of modes (400). This drastically increases computational time when used. The minimization scheme increased the computational time of each design iteration ~20-30 times compared to without it. However, without it, the adjoint flow solution would not consistently converge. For a given flow domain, there is usually a threshold number of modes that will facilitate proper solution convergence. Any higher number of modes than this threshold and the solution will not converge faster but will require more computational time. It was found ~400 was the minimum needed number of modes for consistent solution convergence of the 2D bare tube geometries.

Bare-Tube Constraints

Figure 113 shows the morphing region constraints for each bare tube. A small gap (~0.05-0.1mm) was left between each diamond space surrounding the tube. The bare tube wall was restricted from moving outside its respective space. These constraints were added because there was no way to prevent the bare tube walls from colliding and merging; creating non-physical bare tube designs.

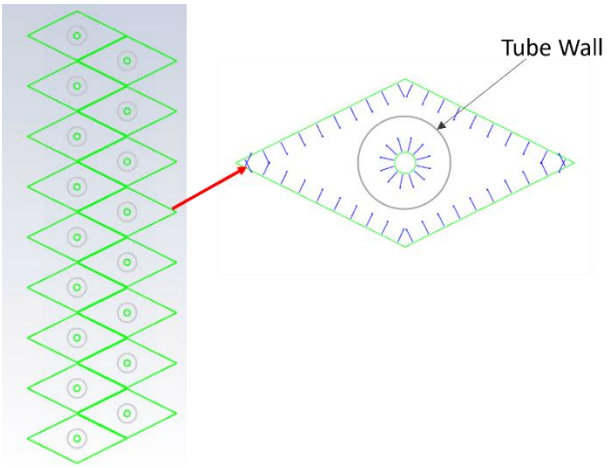

Figure 113: Tube Wall Constraint Area in Fluent

Mesh Morphing Method

ANSYS Fluent provides three different types of mesh morphing methods. A comparative study was performed on a simple two bank tube bundle to assess the differences between them and their respective advantages and disadvantages. Figure 114 shows a summary of the three mesh morphing methods offered and the final shape optimized tube designs for a two bank heat exchanger at an inlet velocity of 3 m/s with bare tubes of D_o=8 mm.

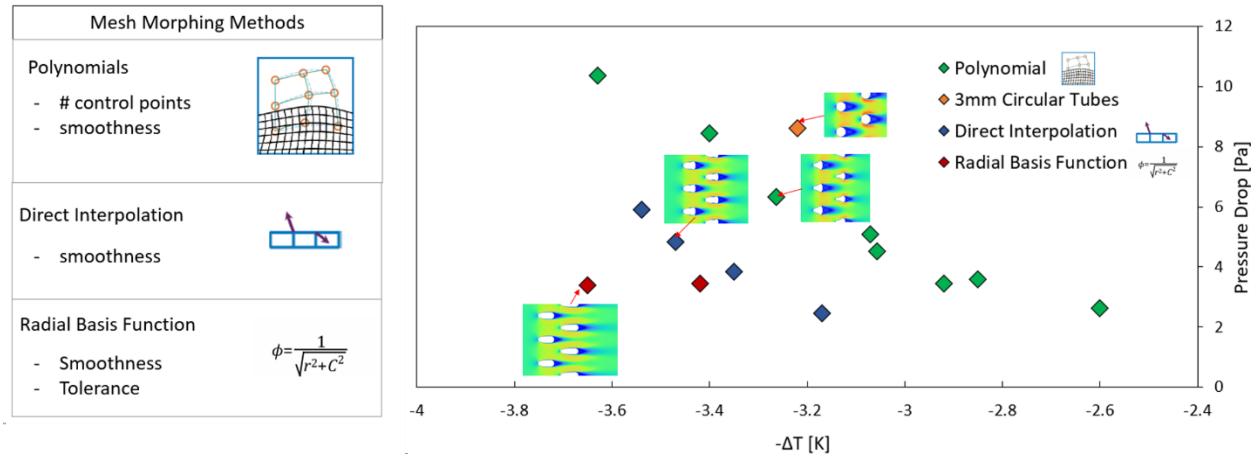

Figure 114: Mesh Morphing Method Comparison (ANSYS Inc., 2016)

Radial basis function was found to produce the best tube designs (lowest pressure drop and highest heat transfer capacity). However, the sides (symmetry boundary condition) of the computational domain were unintentionally being morphed. These sides should be fixed in location and not change in shape. Even though radial basis function provided the best tube designs for this particular study, the deformation of the symmetry boundary condition disqualified this mesh morphing method.

Polynomial mesh morphing method produced the worst performing designs with respect to air-side pressure drop and change in air temperature. Additionally, polynomial mesh morphing method used a significant amount of computational time using an iterative process to attempt to adhere the prescribed constraints on the tube wall. Even with this, it was not successful at adhering to the constraints at times.

Direct interpolation provided better tube designs than the polynomial mesh morphing method. It also has the advantage that it adheres to geometry boundary constraints well with minimal computational time and expense. Due to this, direct interpolation was selected as the mesh-morphing method to use for all optimizations.

Computational Domain Set-up Study

Before conducting final exchanger optimization, different flow domain set-ups were explored to reduce the computational expense as much as possible while still achieving optimal tube shapes. Since the adjoint solver finds the shape sensitivities for the entire flow domain (every element), changing the 2D flow domain boundary conditions will change the final optimized design. First it was attempted to use periodic boundary conditions, and then symmetric boundary conditions to reduce the computational expense of the optimizations.

Periodic boundary condition would significantly reduce the computational cost while providing an accurate representation of the actual flow domain of the heat exchanger center core. ANSYS Fluent supports the use of periodic boundary conditions with its adjoint solver. However, it was found using the periodic boundary conditions the flow solution did not converge to an acceptable level. The shape sensitivities at the periodic boundary were extremely large and were preventing the flow adjoint solution from converging. Consequentially, this prevented proper bare tube shape optimizations.

Next, symmetry at the intersection of the bare tubes was attempted to simplify the tube domain so only part of the full heat exchanger core would need to be modeled. However, it has a significant number of downfalls. The main one being that the intersection of the bare tube with the symmetry boundary condition is fixed and cannot be moved. This is shown in Figure 115.

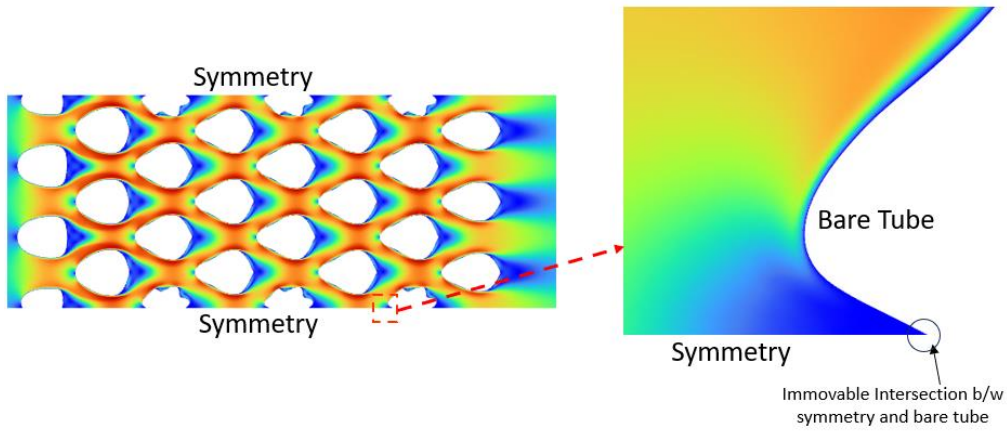

Figure 115: Symmetry Boundary Condition Simplified Flow Domain

ANSYS Fluent does not provide a way to allow this intersection to move and change freely. This limits the possible shapes the outer-most tube can achieve and consequently affects the rest of the flow domain as well. There is another disadvantage to using this symmetry boundary condition as

well. With this intersection of the tube and symmetry boundary condition fixed, the worst mesh quality occurred in this pinched area and caused pre-mature termination of the optimization. Due to this, cutting the domain using symmetry as shown in Figure 115 was deemed unacceptable for these optimizations. The full 2D heat exchanger core needed to be represented as shown in Figure 102. This requires significantly more computational power than using symmetry or periodic boundary conditions that cut the flow domain, but better represents the actual flow domain and allows for proper convergence of the adjoint flow solution.

4.4 9.525 mm Bare-Tube Baseline Optimizations

Two different geometries are optimized in this section. The first is optimization of a single bare tube in cross flow and the second is a 4-bank staggered configuration bare tube heat exchanger. Fin-tube heat exchangers with 9-10 mm outer diameter tubes are very common in typical HVAC&R application and products, hence, acts a good baseline geometry. Figure 116 and Figure 117 show the single tube and 4-bank heat exchanger flow domains.

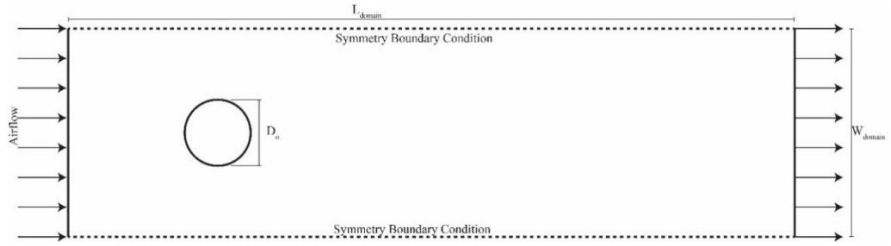

Figure 116: Single Bare Tube 2D Geometry and Flow Domain

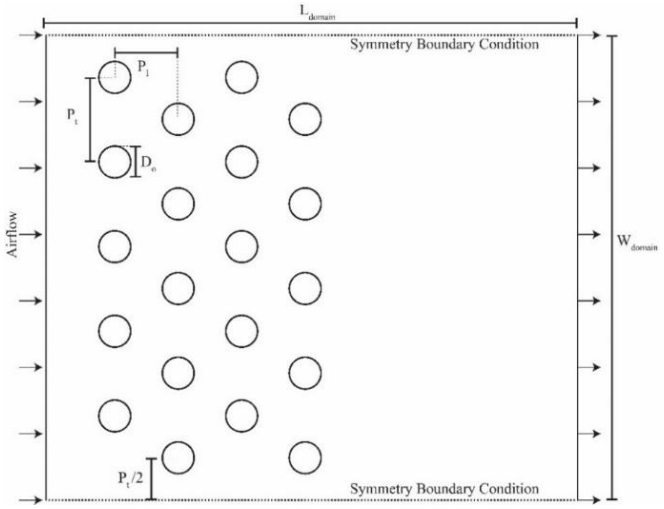

Figure 117: 4-Bank Bare Tube HX 2D Geometry and Flow Domain

Table 50: Bare Tube Geometry Parameter Summary

Parameter	Units	Single Tube	4-Bank Heat Exchanger
N_{tubes}	-	1	20
N_{banks}	-	1	4
D_o	mm	9.525	9.525
P_t	mm	-	25.40
P_l	mm	-	19.05
L_{domain}	mm	105	310
W_{domain}	mm	30	140

4.4.1 Single 9.525mm Bare Tube Optimizations

Shape optimizations were conducted for inlet air velocities of 1, 2, 3, 4, and 5 m/s for single bare tube. Figure 118 shows the optimization results and resulting j and f factors. The initial flow solution over single circular bare tube velocity contours are shown in Figure 118 at an air velocity of 3 m/s.

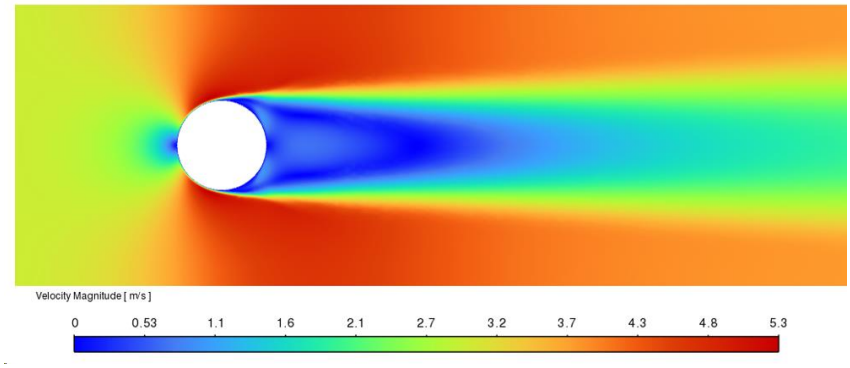

Figure 118: Air Velocity Contours over Circular 9.525mm Bare Tube

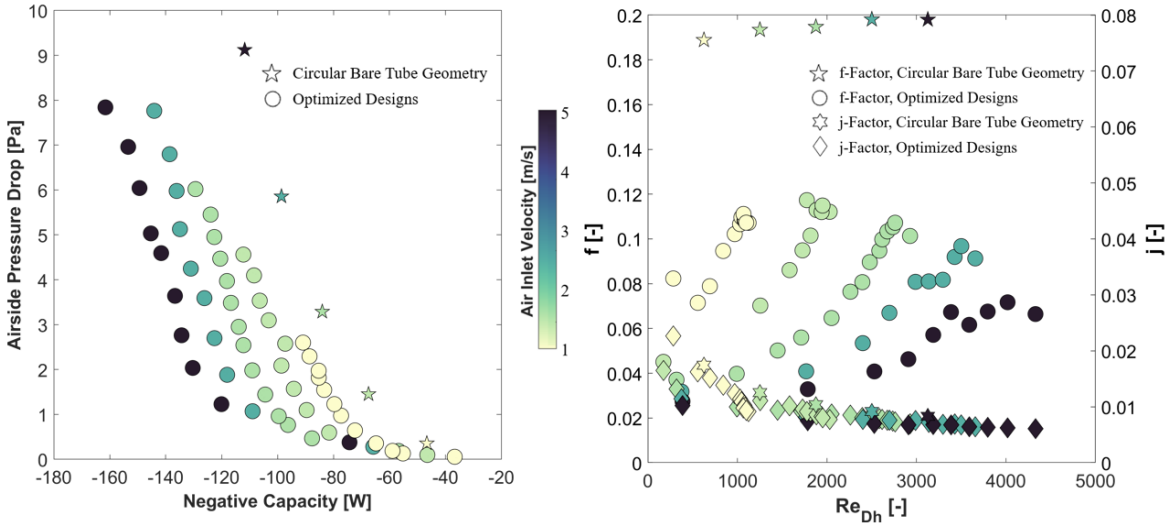

Figure 119: (Left) Air-Side Pressure Drop Optimized Single Bare Tube Designs (Right) f and j Factors for Optimized Single Bare Tube Designs.

Figure 120 shows five selected optimized tube geometries, one for each inlet air velocity used. Selection was based on having reduced air-side pressure drop and increased heat transfer capacity when compared to the starting circular bare tube geometry. Figure 119 shows a data summary of the selected designs.

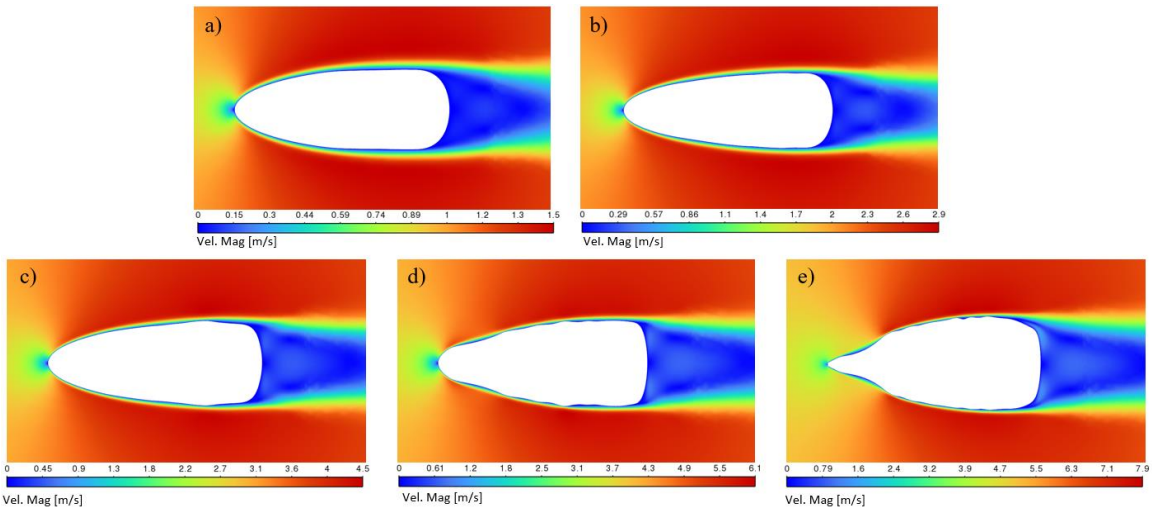

a) Inlet Velocity = 1 m/s , b) Inlet Velocity = 2 m/s, c) Inlet Velocity = 3 m/s, d) Inlet Velocity = 4 m/s, e) Inlet Velocity = 5 m/s

Figure 120: Optimized Single Bare Tube Design Velocity Contours

Table 51: Single Tube Optimization Data Summary

Design Case	Inlet Velocity [m/s]	Heat Transfer Capacity [W]	Pressure-Drop [Pa]	Average HTC [W/ m^2-K]	Total Surface Area [m^2]	j-Factor [-]	f-Factor [-]	j/f [-]	Ref-Side Area [cm^2]
a	1	58.9 (26.3%)	0.19 (-47.3%)	29.3 (-20.2%)	0.04755 (58.9%)	0.0152 (-12.9%)	0.0789 (-58.2%)	0.1925 (108.5%)	1.25 (75.8%)
b	2	81.6 (20.9%)	0.60 (-59.0%)	41.8 (-20.9%)	0.04585 (53.2%)	0.0111 (-11.6%)	0.0702 (-63.7%)	0.1578 (143.4%)	1.10 (53.8%)
c	3	104.4 (24.3%)	1.44 (-56.1%)	51.3 (-21.8%)	0.04768 (59.3%)	0.0087 (-16.1%)	0.0647 (66.8%)	0.1347 (152.6%)	1.24 (74.3%)
d	4	122.6 (24.3%)	2.70 (-53.9%)	60.0 (-22.1%)	0.04784 (59.9%)	0.0076 (-17.3%)	0.0670 (-66.2%)	0.1132 (144.6%)	1.23 (72.5%)
e	5	141.6 (26.7%)	4.59 (-49.6%)	69.0 (-20.9%)	0.04803 (60.5%)	0.0068 (-18.3%)	0.0673 (-66.0%)	0.1009 (140.4%)	1.24 (73.9%)

*(percentage is % change from starting circular bare tube geometry at same inlet air velocity)

When compared to the initial circular bare tube, selected optimized designs have 45-60% lower pressure drop with a 20-27% increase in heat transfer capacity. Interestingly, the average airside heat transfer coefficient decreased 20-22%, but this was compensated for with tube surface area

increasing ~50-60%. The ratio of the Colburn j factor to friction factor (j/f) increased between 108-153%.

Optimized design c from Figure 120 was investigated further by evaluating its air-side thermal hydraulic performance over a range of inlet air velocities, 0.5 – 6 m/s. Figure 121 shows the adjoint optimized thermal hydraulic performance over this inlet velocity range and is compared to the initial circular bare tube. The adjoint optimized design's thermal-hydraulic performance was improved over the circular bare tube design over all inlet air velocities. Over the circular bare tube design, the adjoint optimized design's heat transfer capacity, overall conductance, and j/f increased by 24.3-30.1%, 24.6-31.0%, and 87.8-194.0%, respectively. The air-side pressure drop and average heat transfer coefficient decreased by 37.3-61.9% and 17.8-20.5%, respectively.

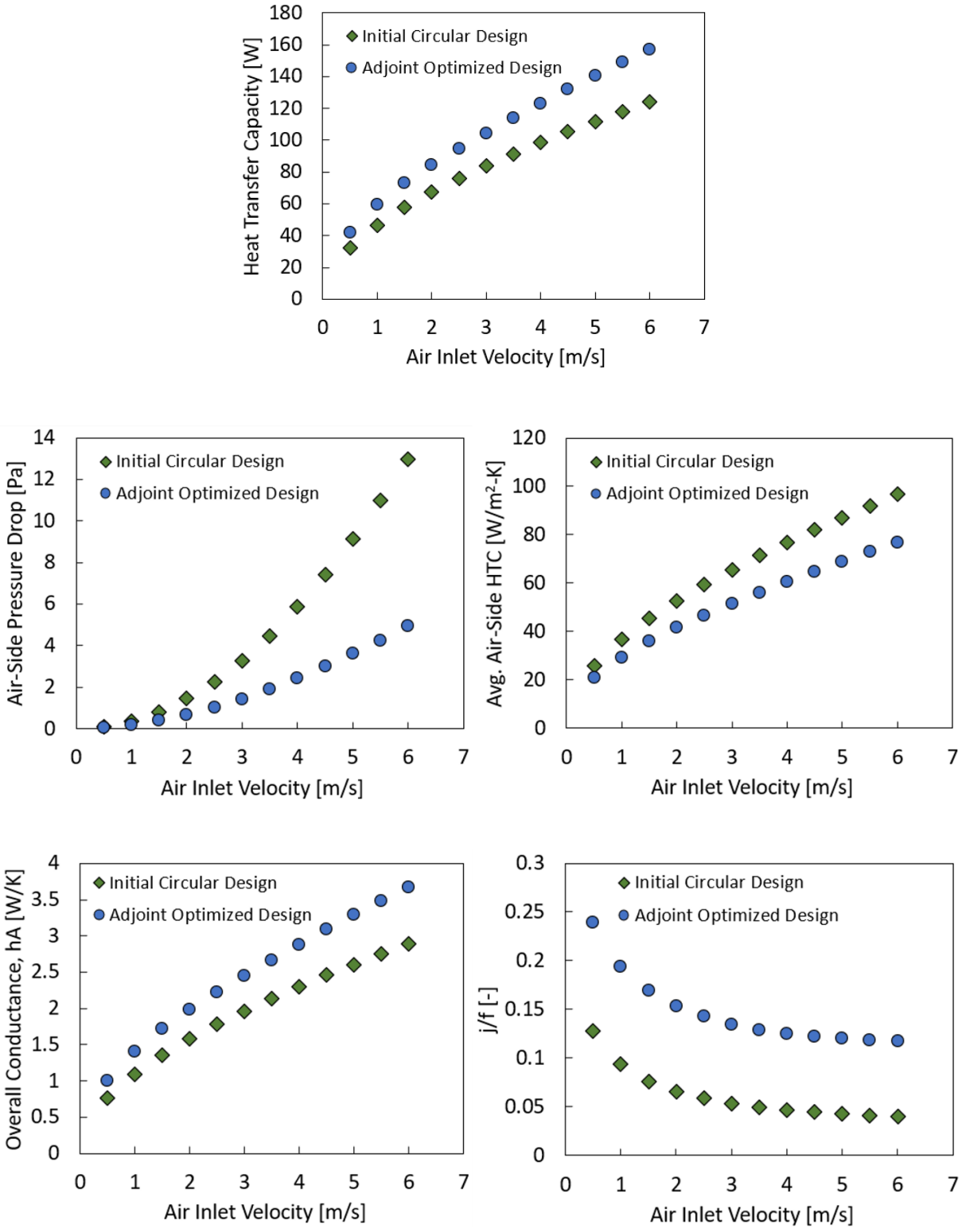

Figure 121: Thermal-Hydraulic Performance of Design c (Table 51) over Range of Inlet Air Velocities

4.4.2 4-Bank Staggered 9.525mm Bare Tube Optimizations

Next, optimizations were conducted for inlet air velocities of 1, 2, 3, 4, and 5 m/s for a 4-bank heat exchanger. Figure 122 shows the optimization results and resulting j and f factors. The initial flow solution's velocity contours are shown in Figure 122 at an air velocity of 3 m/s.

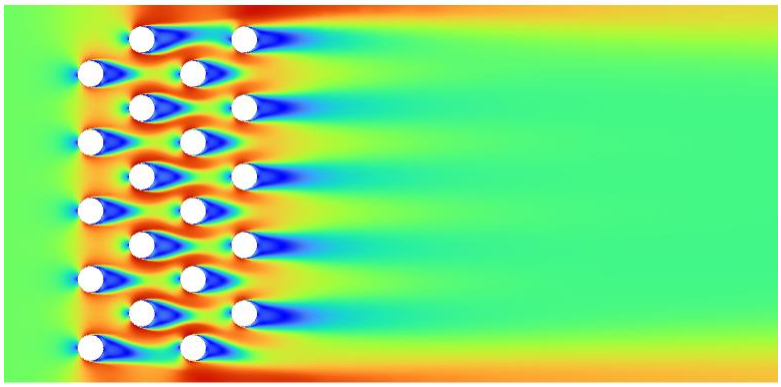

Figure 122: Air Velocity (3 m/s Inlet) Contours over 4-Bank Circular 9.525mm Bare Tube HX

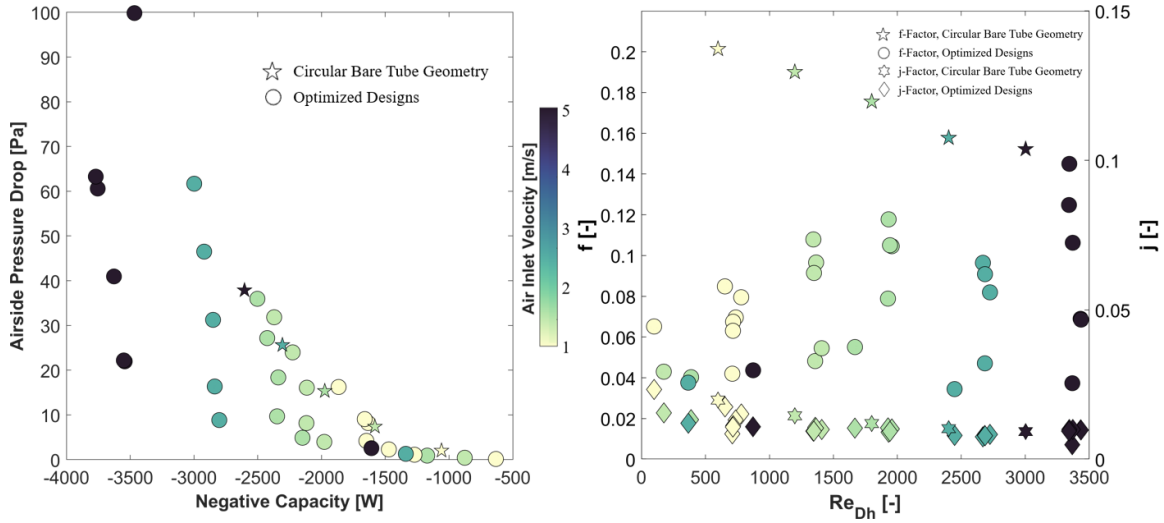

Figure 123: (Left) Optimized 4-bank bare tube HX designs, airside pressure drop versus negative heat transfer capacity for air inlet velocities 1-5 m/s (Right) f and j factors for optimized 4-bank bare tube HX designs.

Figure 124 shows five selected optimized tube geometries, one for each inlet air velocity used. Selection was based on having reduced air-side pressure drop and increased heat transfer capacity when compared to the starting circular bare tube geometry. Table 52 shows a data summary of the selected designs. Figure 123 shows a data summary of the selected designs.

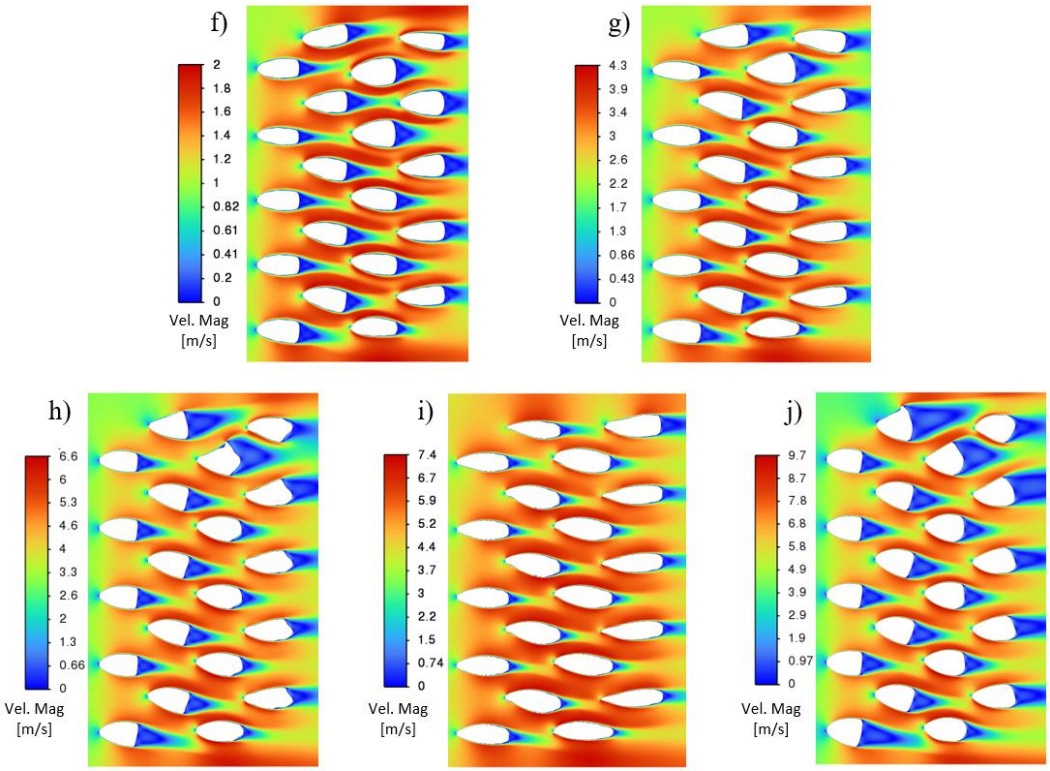

f) Inlet Velocity = 1 m/s , g) Inlet Velocity = 2 m/s, h) Inlet Velocity = 3 m/s, i) Inlet Velocity = 4 m/s, j) Inlet Velocity = 5 m/s.

Figure 124: Optimized 4-bank HX Design Velocity Contours

Table 52: 4-Bank Heat Exchanger Optimization Data Summary

Design Case	Inlet Velocity [m/s]	Heat Transfer Capacity [W]	Pressure-Drop [Pa]	Average HTC [W/ m^2-K]	Total Surface Area [m^2]	j-Factor [-]	f-Factor [-]	j/f [-]	Ref-Side Area [cm^2]
f	1	1271 (20.0%)	1.10 (-45.3%)	37.5 (-15.6%)	0.8654 (44.6%)	0.0175 (-11.6%)	0.085 (-57.9%)	0.206 (109.8%)	22.6 (57.6%)
g	2	1978 (25.1%)	3.97 (-46.2%)	52.0 (-19.8%)	0.9480 (58.4%)	0.0107 (-26.3%)	0.048 (-74.6%)	0.222 (190.4%)	25.7 (79.5%)
h	3	2348 (18.9%)	9.68 (-36.9%)	70.7 (-11.9%)	0.8152 (36.2%)	0.0105 (-12.2%)	0.079 (-55.1%)	0.1331 (95.4%)	20.9 (46.1%)
i	4	2801 (21.4%)	8.85 (-65.5%)	71.3 (-23.5%)	0.9587 (60.2%)	0.0080 (-22.1%)	0.034 (-78.2%)	0.232 (256.9%)	23.4 (63.1%)
j	5	3550 (36.4%)	22.19 (-41.4%)	109.2 (4.3%)	0.7930 (32.6%)	0.0098 (5.9%)	0.069 (-55%)	0.143 (135.2%)	21.7 (51.6%)

*(percentage is percent change from starting circular tube HX geometry at same inlet air velocity)

For the 4-bank bare tube heat exchanger, when compared to the initial circular bare tube design, selected optimized designs have 37-66% lower pressure drop with a 19-36% increase in heat transfer capacity over this range of inlet air velocities. The average airside heat transfer coefficient changed -24% to +4% and tube surface area increased 33-58%. The ratio of the Colburn j factor to friction factor (j/f) increased between 95-257%. Refrigerant-side cross sectional area increased between 22% to 84%. The refrigerant-side cross sectional area was not constrained or controlled during these optimizations. The increase in cross-sectional area indicates the refrigerant-side pressure drop will decrease for these designs.

Table 53 provides a comparison of the performance of a tube-fin heat exchanger with the exact same 4-bank circular tube arrangement as shown in Table 50, except 15 fins/inch are added. Air-side pressure drop and average heat transfer coefficient are calculated using the following correlations (C.-C. Wang et al., 2000).

Table 53: 4-Bank Heat Exchanger Adjoint Optimizations Compared to Traditional Tube-Fin HXs

Design Case (Figure 124)	Inlet Velocity [m/s]	Fins per Inch	Pressure-Drop [Pa]	Average HTC [W/ m^2-K]	Total Active Surface Area [m^2]
f	1	n/a	1.10	37.5	0.8654
Fin-tube HX		15	16	43.48	10.2
g	2	n/a	3.97	52.0	0.9480
Fin-tube HX		15	41.2	61.58	10.2
i	3	n/a	9.68	70.7	0.8152
Fin-tube HX		15	75.21	75.26	10.2
j	4	n/a	8.85	71.3	0.9587
Fin-tube HX		15	117.37	86.70	10.2
k	5	n/a	22.19	109.2	0.7930
Fin-tube HX		15	167.32	96.7	10.2

4.4.3 4-Bank Staggered 9.525 mm Bare Tube Manufacturability Study

The resulting designs from the adjoint optimization process show geometries where each individual bare tube has a unique shape. This higher degree of freedom is one of the advantages of the optimization process to potentially achieve higher performance. However, these adjoint optimized designs are typically only possible to be manufactured using additive manufacturing. To address this, it was investigated how using the single 9.525 mm bare tube optimizations in Figure 120 as the tube geometry throughout the 4-bank heat exchanger. This is shown in Figure 125. Design c in Figure 120 was selected at an inlet air velocity of 3 m/s (design velocity). The single bare tube design is feasible to manufacture using conventional extrusion based process similar to the copper NTHX heat exchangers in Chapter 2.

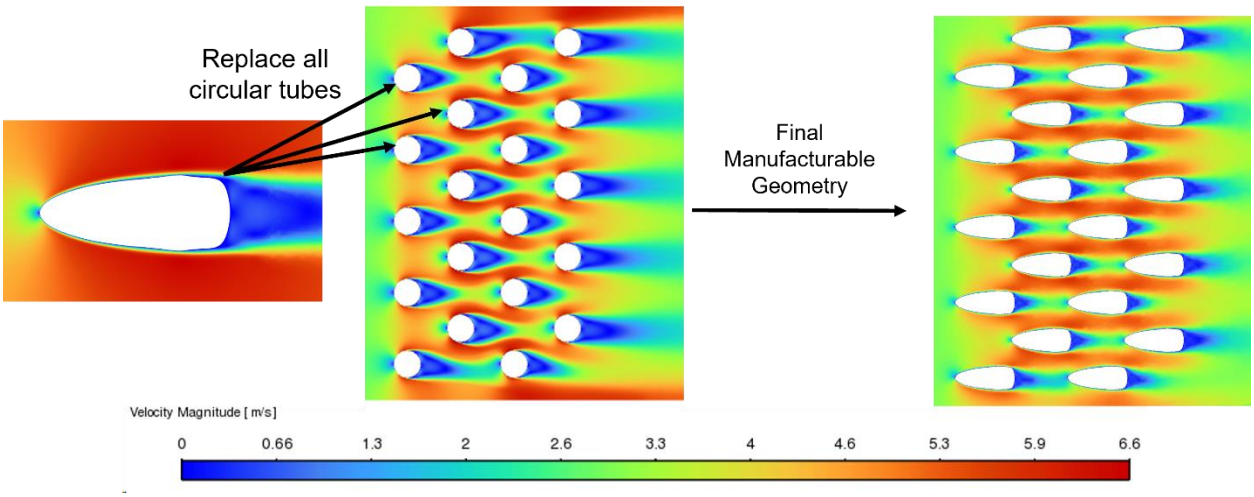

Figure 125: 4-Bank Heat Exchanger using Adjoint Optimized Single Bare Tube Design at Air Velocity of 3 m/s

Table 54 shows a comparison of new manufacturable design versus design h in Figure 124, which was also optimized at an inlet air velocity of 3 m/s. The manufacturable design has similar performance to the full adjoint optimized domain of design h, Figure 124, at inlet air velocity of 3 m/s. Higher heat transfer capacity than design h was reached due to the significantly larger amount of surface area. Air-side pressure drop and air-side HTC are both smaller than design h.

Table 54: 4-Bank Manufacturable Heat Exchanger Data Summary and Comparison

Design Case	Inlet Velocity [m/s]	Heat Transfer Capacity [W]	Pressure-Drop [Pa]	Average HTC [W/ m^2-K]	Total Surface Area [m^2]	Ref-Side Area [cm^2]
h (Figure 124)	3	2348	9.68	70.7	0.8152	20.9
New Manufacturable Design	3	2503	9.29	68.02	0.952	24.8

4.5 Bare-Tube Adjoint Optimization Parametric Study

A parametric study was conducted to determine the potential improvement of finless circular bare tube heat exchangers with hydraulic diameters ranging from 0.5-5.0 mm using adjoint method shape optimization. Figure 126 shows the 2D CFD design space. The design space was selected to cover a large range of common HVAC&R applications. The number of tubes per bank for all designs in this section is 12.

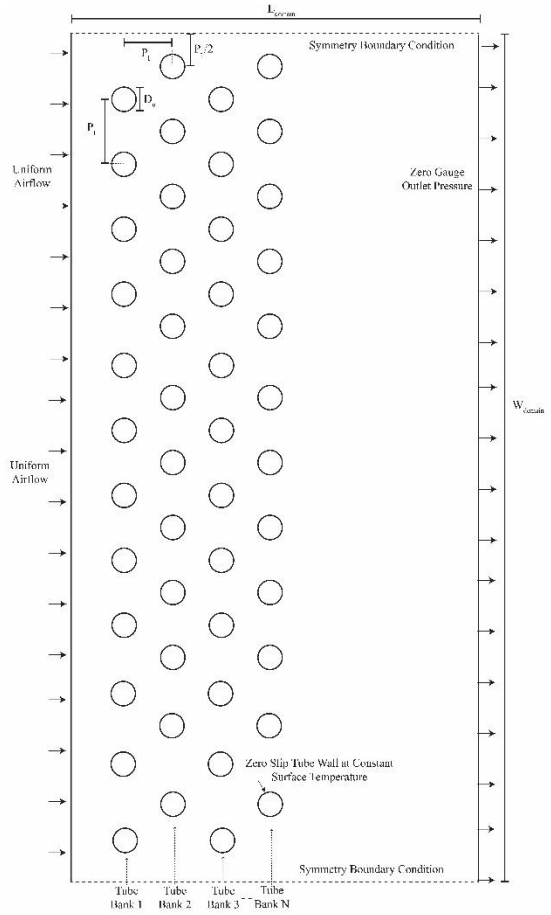

Figure 126: Parametric Study Design Space 2D CFD Set-Up

Table 55 shows all initial design points' bare tube parameters. The total number of tube banks, inlet air velocity, and horizontal/vertical pitch were varied. The ratio of vertical to horizontal pitch

was kept constant throughout. The initial circular bare tube outer diameter was always one half the vertical pitch for vertical pitch to outer diameter ratio (P_v/D_o) of two. For each starting design listed in this table, the optimization scheme in section 4.3 is utilized to produce four shape optimized designs by varying pressure drop constraint, ε, to be four values: 40%, 60%, 80%, and the same pressure drop as the initial circular bare tube starting design. This produced 18 Pareto sets with four designs per front. Resulting in a total of 72 optimized heat exchanger designs.

$$\begin{aligned} &maximize\ f(x_{tubes}) = \Delta T_{air} \\ &s.t.\quad g(x_{tubes}):\ (\Delta P_{air} - \varepsilon) \leq 0 \end{aligned} \qquad \text{Eq. 59}$$

A grid convergence index (GCI) study (ASME, 2009) was conducted for the 3 bank circular bare tube geometry at an inlet air velocity of 3 m/s and vertical pitch of 6 mm and 2 mm. Uncertainty was within 0.4% for Tout and 1.4% for pressure drop for both geometries. Table 55 shows the initial circular bare tube design parameters for all 18 Pareto sets. Table 56 and Table 57 show a summary of the optimized designs.

Table 55: Design Parameter Values for Shape Optimization of Bare Tube Heat Exchangers

Pareto set No.	No. Tube Banks	Air Inlet Velocity [m/s]	Vertical Pitch [mm]	Horizontal Pitch [mm]	Initial Bare Tube Outer Diameter [mm]
1	2	1	2	1.7	1
2			6	5.2	3
3		3	2	1.7	1
4			6	5.2	3
5		6	2	1.7	1
6			6	5.2	3
7	3	1	2	1.7	1
8			6	5.2	3
9		3	2	1.7	1
10			6	5.2	3
11		6	2	1.7	1
12			6	5.2	3
13	4	1	2	1.7	1
14			6	5.2	3
15		3	2	1.7	1
16			6	5.2	3
17		6	2	1.7	1
18			6	5.2	3

Table 56: Shape Optimization of Bare Tube Heat Exchangers Results*

Pareto set No.	Air-Side Pressure Drop [Pa]	Heat Transfer Capacity [kW]	Air-Side Surface Area [m^2]	Avg. Air-Side HTC [W/m^2-K]
1	1.28-3.19 (-59.9% to 0.0%)	0.48-0.58 (3.2% to 22.6%)	0.075-0.098 (17.7% to 30.2%)	161.5-183.6 (-11.6% to 0.5%)
2	1.15-2.32 (-50.4% to -2.8%)	0.80-1.02 (6.8% to 28.3%)	0.228-0.331 (9.6% to 45.5%)	76.7-91.1 (-15.8% to -1.7%)
3	8.71-20.50 (-57.5% to -0.4%)	0.79-1.02 (13.0% to 29.1%)	0.075-0.112 (17.8% to 48.5%)	224.4-272.9 (-17.8% to 2.5%)
4	8.37-18.03 (-53.6% to -3.8%)	1.40-1.92 (12.9% to 37.2%)	0.228-0.371 (37.9% to 63.2%)	124.8-151.6 (-17.7% to -13.8%)
5	31.7-75.0 (-57.4% to 0.8%)	1.12-1.54 (15.7% to 37.7%)	0.075-0.121 (45.3% to 60.5%)	300.4-372.4 (-19.3% to -11.4%)
6	27.44-66.73 (-58.9% to -0.6%)	2.03-2.60 (10.1% to 28.3%)	0.228-0.332 (41.8% to 45.7%)	168.9-216.4 (-22.0% to -10.1%)
7	1.96-4.88 (-59.6% to 0.7%)	0.65-0.77 (4.0% to 18.5%)	0.113-0.140 (12.9% to 24.1%)	170.6-194.6 (-8.2% to 4.7%)
8	1.39-3.39 (-59.1% to -0.77%)	1.11-1.47 (10.7% to 32.3%)	0.339-0.446 (17.0% to 31.5%)	86.5-96.2 (-3.4% to 7.4%)
9	12.63-30.53 (-58.6% to -0.4%)	1.11-1.47 (10.2% to 32.7%)	0.113-0.148 (14.7% to 30.8%)	262.2-289.9 (-1.9% to 8.4%)
10	12.74-28.24 (-54.9% to -2.2%)	2.12-2.64 (5.0% to 24.4%)	0.339-0.453 (21.0% to 33.6%)	139.9-160.3 (-12.7% to -4.3%)
11	47.6-118.7 (-59.9% to -0.3%)	1.68-2.22 (10.2% to 31.7%)	0.113-0.160 (28.2% to 41.7%)	339.7-389.7 (-12.8% to -2.5%)
12	40.77-101.89 (-60.0% to -2.2%)	3.15-3.97 (4.7% to 26.0%)	0.339-0.459 (31.2% to 35.4%)	185.4-231.7 (-20.0% to -5.0%)
13	2.64-6.52 (-59.5% to -0.1%)	0.78-0.86 (4.5% to 9.5%)	0.151-0.174 (11.8% to 15.3%)	174.6-195.2 (-6.5% to 4.5%)
14	1.91-4.64 (-58.6% to 0.2%)	1.44-1.71 (7.9% to 18.9%)	0.452-0.549 (14.8% to 21.4%)	88.9-98.8 (-3.8% to 6.9%)
15	17.2-41.5 (-58.5% to -1.2%)	1.44-1.77 (7.4% to 23.2%)	0.151-0.183 (12.9% to 21.6%)	268.5-299.7 (-2.9% to 8.4%)
16	15.69-40.9 (-60.0% to 4.1%)	2.81-3.52 (5.4% to 25.1%)	0.452-0.602 (26.9% to 33.0%)	138.4-165.2 (-16.2% to -0.6%)
17	66.52-164.68 (-59.6% to -0.5%)	2.21-2.70 (6.9% to 22.2%)	0.151-0.196 (21.4% to 29.7%)	357.8-407.9 (-10.7% to 1.8%)
18	74.86-142.46 (-47.0% to 0.8%)	4.22-5.33 (9.8% to 26.2%)	0.452-0.613 (31.3% to 35.6%)	202.1-239.1 (-15.5% to -4.1%)

*(percentages are percent change from starting circular tube heat exchanger geometry)

Table 57: Shape Optimization of Bare Tube Heat Exchangers Results Continued*

Pareto set No.	Overall Air-Side Conductance (hA) [W/m]	j/f [-]	Refrigerant Cross-Sectional Area [cm^2]
1	13.8-18.0 *(3.2% to 22.6%)*	0.334-0.433 *(10.4% to 29.7%)*	0.156-0.279 *(-17.1% to 47.8%)*
2	20.7-27.6 *(7.7% to 33.1%)*	0.228-0.337 *(10.8% to 48.0%)*	1.72-2.98 *(18.8% to 73.8%)*
3	20.6-27.6 *(14.9% to 34.1 %)*	0.225-0.336 *(14.9% to 49.7%)*	0.188-0.324 *(29.2% to 71.7 %)*
4	34.5-48.6 *(13.9% to 40.7%)*	0.143-0.237 *(29.9% to 66.5%)*	1.72-3.66 *(44.3% to 112.9%)*
5	28.1-39.9 *(17.3% to 42.3%)*	0.161-0.271 *(35.7% to 69.1%)*	0.188-0.395 *(43.9% to 109.6%)*
6	49.3-64.1 *(10.6% to 30.1%)*	0.106-0.218 *(38.5% to 106.7%)*	1.72-3.04 *(45.1% to 77.2%)*
7	21.0-27.3 *(6.0% to 30.0%)*	0.350-0.483 *(21.8% to 37.9%)*	0.222-0.398 *(-21.6% to 40.9%)*
8	30.4-42.9 *(13.0% to 41.3%)*	0.222-0.412 *(51.5% to 85.6%)*	2.52-3.90 *(-0.9% to 53.4%)*
9	30.2-42.9 *(12.5% to 41.8%)*	0.233-0.378 *(43.4% to 61.9%)*	0.276-0.434 *(-2.3% to53.6 %)*
10	54.4-69.5 *(5.6% to 27.9%)*	0.133-0.250 *(65.9% to 87.8%)*	2.54-3.99 *(21.1% to 56.6%)*
11	44.1-60.7 *(11.7% to 37.7%)*	0.162-0.300 *(54.8% to 85.6%)*	0.283-0.465 *(20.0% to 64.5%)*
12	78.6-101.1 *(5.0% to 28.6%)*	0.107-0.222 *(68.2% to 108.7%)*	2.54-3.89 *(33.3% to 53.0%)*
13	28.2-33.0 *(11.8% to 15.3%)*	0.347-0.477 *(27.9% to 37.5%)*	0.292-0.463 *(-22.5% to 22.9%)*
14	41.8-52.5 *(10.4% to 25.6%)*	0.224-0.446 *(51.3% to 99.0%)*	3.37-4.52 *(-0.6% to 33.1%)*
15	41.7-55.0 *(9.6% to 31.8%)*	0.234-0.416 *(30.6% to 78.4%)*	0.369-0.525 *(-2.0% to 39.3 %)*
16	74.8-97.3 *(6.3% to 30.2%)*	0.131-0.345 *(64.2% to 164.4%)*	3.39-5.12 *(26.3% to 50.8%)*
17	60.4-77.2 *(8.4% to 27.7%)*	0.160-0.399 *(57.5% to 149.5%)*	0.377-0.538 *(17.2% to 42.6%)*
18	108.2-140.6 *(11.0% to 29.9%)*	0.106-0.207 *(61.2% to 96.0%)*	3.39-5.62 *(42.8% to 65.8%)*

*(percentages are percent change from starting circular tube HX geometry at same inlet air velocity)

The shape optimizations were able to improve the thermal-hydraulic performance by keeping the air-side pressure drop below its defined constraint while maximizing the change in air temperature across the core. Total active surface area increased over all designs. Average air-side heat transfer coefficient generally decreased or remained constant across all shape optimizations. The solver produced designs that increased heat transfer by increasing the active air side heat transfer surface area while average heat transfer coefficient decreased slightly or remained constant. Refrigerant-side cross sectional area changed between -22.5% to 112.9% over all designs. Most of the designs' refrigerant-side cross sectional area increased. Refrigerant-side cross sectional area was not constrained or controlled during these optimizations. The increase in cross-sectional area indicates the refrigerant-side pressure drop will decrease for these designs.

Figure 127 shows the velocity contours of a single design from Pareto set number 15 for demonstration purposes. The design is termed adjoint optimized heat exchanger – design 15 (AOHX-D15). Air-side pressure drop was reduced by 40% and air-side heat transfer capacity increased by 14.2% at an inlet air velocity of 3 m/s. Table 58 shows the design change from the initial circular bare tube geometry.

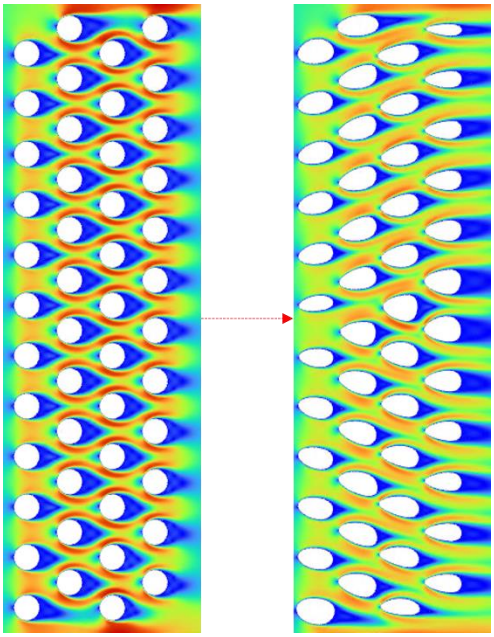

Figure 127: 2D Velocity Contours (Left)Starting Circular Geometry (Right)AOHX-D15

Table 58: AOHX-D15 Design Change Summary

Parameter	Unit(s)	Initial Circular Bare Tube Heat Exchanger	AOHX-D15	Percent Change
Pressure Drop	[Pa]	41.5	24.8	-40.2%
Air Temp. Change (ΔT_{air})	[K]	16.2	18.5	14.2%
Active Surface Area (A_o)	[m^2]	0.151	0.178	17.9%
Average Air Heat Transfer Coefficient ($h_{a,avg}$)	[W/m^2K]	276.2	279.0	1.0%
$h_{a,avg} A_o$	[W/m]	41.7	49.7	19.2%
f factor	[-]	0.1386	0.1064	-23.2%
Colburn j factor	[-]	0.0316	0.0369	16.8%
j/f	[-]	0.2278	0.3464	52.1%
Compactness	[m^2/m^3]	1048.6	1136.2	8.4%

4.6 Design and Radiator Testing of Additively Manufactured Adjoint Optimized Heat Exchanger (AOHX)

This section covers the design, additive manufacturing, and experimental validation of a single 500 W finless bare tube heat exchanger which was optimized using the developed multi-objective adjoint shape optimization scheme in section 4.3. The design and optimization of a 500 W bare tube radiator termed, adjoint optimized heat exchanger (AOHX), is presented. The design was additively manufactured out of polymer material and its experimental performance evaluated and compared to the predicted performance. Figure 128 shows the approach taken to design, optimize, additively manufacture, and experimentally test AOHX.

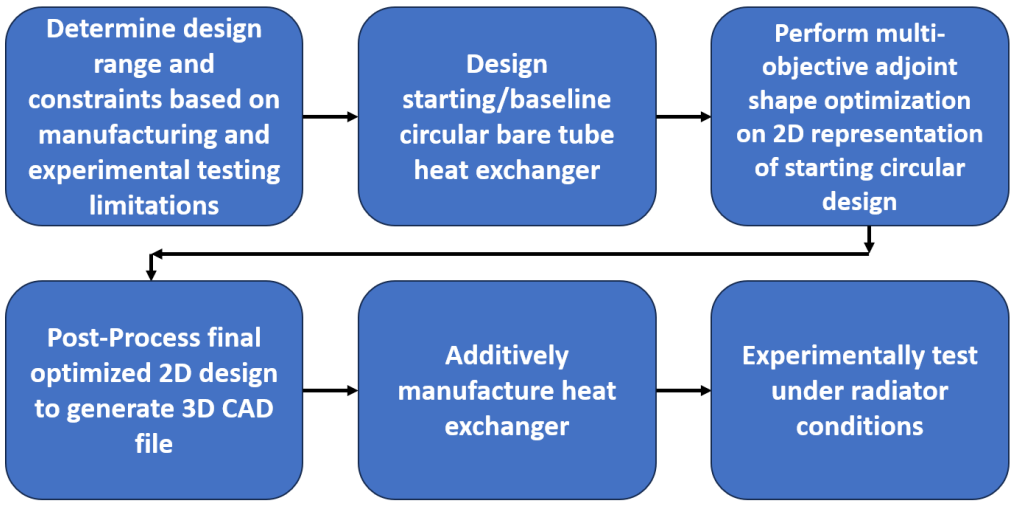

Figure 128: Outline of Process to Design, Manufacture, and Experimentally Test AOHX

4.6.1 AOHX Design and Optimization

Starting Circular Bare Tube Heat Exchanger Design

Table 59 shows the design criteria and constraints for the initial circular bare tube heat exchanger geometry to be shape optimized using the adjoint based multi-objective optimization scheme.

Table 59: Design Space and Constraints for Initial Circular Bare Tube Design

Parameter		Unit(s)	Value Range
Geometry	Tube Length	[mm]	100 - 180
	Width	[mm]	150 - 290
	Depth	[mm]	20 - 100
	No. Tube Banks	[mm]	4 - 10
	Tube Configuration	[-]	Staggered
	Tube Horizontal Pitch Ratio (P_h /D_o)	[-]	1.5 - 2.5
	Tube Vertical Pitch Ratio (P_v /D_o)	[-]	1.5 - 2.5
	Initial Circular Geometry Outer Diameter	[mm]	3.0 - 10.0
	Tube Wall Thickness	[mm]	1.0
	No. Fluid Passes	[-]	1
	Tube Material	[-]	Polymer
	Tube Material Thermal Conductivity	[W/m-K]	0.10 - 0.40
Experimental Conditions and Performance	Testing Condition	[-]	Radiator
	Inlet Air Velocity	[m/s]	0.5 - 6
	Tube Fluid Side	[-]	Water
	Water MFR	[g/s]	15 - 200
	Total Heat Transfer Capacity	[W]	>500
	Air-Side Pressure Drop	[Pa]	< 300
	Minimum ΔT_{air}	[K]	>2.5
	Minimum ΔT_{water}	[K]	>2.5
	T_{water}	[C]	20 - 45
	T_{air}	[C]	15 - 30

A Stratasys J850 Polyjet 3D printer was designated to be used to manufacture the final prototype through Stratasys Direct Manufacturing Services. The 3D printer's specifications are shown in Table 60. VeroClear is a transparent material similar to PMMA (polymethyl methacrylate), commonly known as acrylic. Its material properties are shown in Table 61.

Table 60: Stratasys J850 Polyjet 3D Printer Specifications (Stratasys, 2023a)

Parameter	Unit(s)	Value(s)
Additive Manufacturing Process	[-]	Polyjet
Material Type	[-]	Polymer
Build Volume	[mm]	490 x 390 x 200
Material	[-]	VeroClear
Accuracy		For structures under 100mm: ±100µm
		For structures over 100mm: ±200µm or ± 0.06% of part length, whichever is greater
Minimum Free-Standing Wall Thickness for Leak Free Tubes*	[mm]	1

*Based on private communication (StratasysDirectManufacturing, 2023)

Table 61: VeroClear Polymer Material Properties (Stratasys, 2023b)

Parameter	Unit(s)	Value(s)
Density	[g/cm^3]	1.18 - 1.19
Tensile Strength	[MPa]	50 - 65
Flexural Strength	[MPa]	75 - 110
Modulus of Elasticity	[MPa]	2000 - 3000
HDT @ 0.45MPa	[°C]	45 - 50
Thermal Conductivity @25°C	[W/m-K]	0.22*

*(Weiss et al., 2015)

The same heat exchanger test facility as in section 2.1 was designated to experimentally test the final optimized heat exchanger, AOHX. Table 62 shows the final design parameters for the initial circular bare tube heat exchanger. This design is the starting point for the adjoint optimization scheme. Figure 129 shows the design's 2D CFD velocity contours at an inlet air velocity of 3 m/s. Figure 130 shows the simulated air-side pressure drop and average air-side heat transfer coefficient versus an inlet air velocity of 0.5-7.0 m/s.

Table 62: Initial Starting Design Summary: Circular Bare Tube Heat Exchanger

Parameter	Unit(s)	Value(s)
Tube Length	[mm]	150
Width	[mm]	198.5
Core Depth	[mm]	78.4
No. Tube Banks	[-]	7
Tube Configuration	[-]	Staggered
Horizontal Pitch	[mm]	11.81
Vertical Pitch	[mm]	13.64
Outer Diameter	[mm]	7.50
Tube Wall Thickness	[mm]	1.0
No. Fluid Passes	[-]	1
Tube Material	[-]	VeroClear
Tube Material Thermal Conductivity	[W/m-K]	0.22

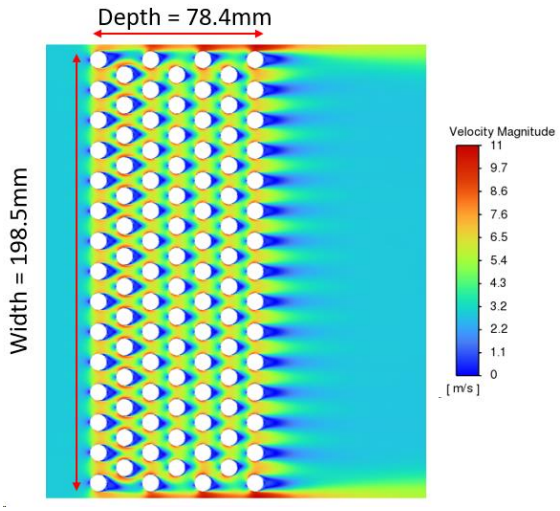

Figure 129: 2D CFD Velocity Contours of Initial Circular Bare Tube HX Design

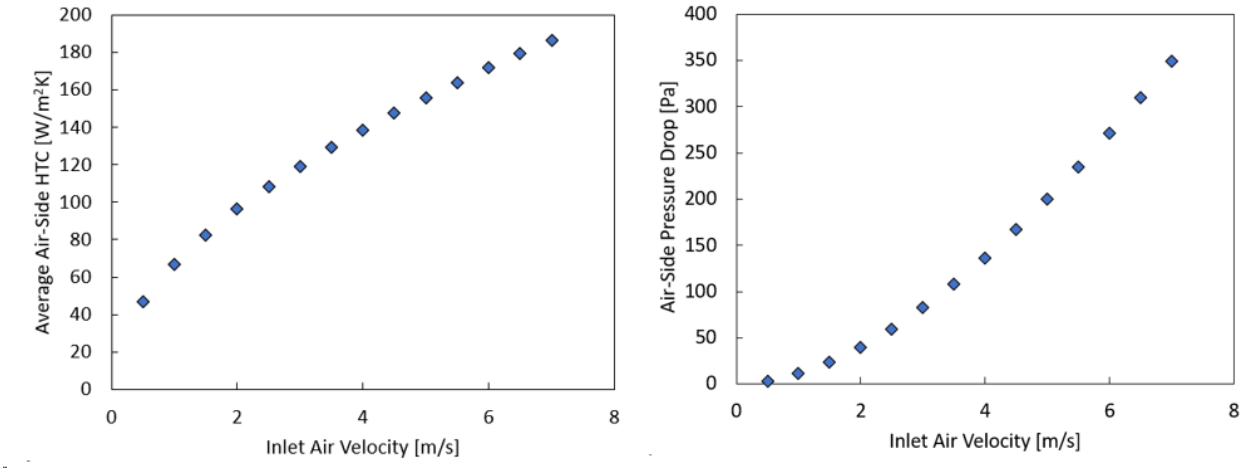

Figure 130: Initial Circular Bare Tube HX Predicted (Left) Average Air-Side HTC versus Inlet air Velocity (Right) Air-Side Pressure Drop versus Inlet Air Velocity

Using the air-side pressure drop and average heat transfer coefficients from Figure 130, and the parameters in Table 62, the heat exchanger's performance as a radiator was simulated at an inlet air velocity of 3 m/s using CoilDesigner®, which is a finite volume heat exchanger model utilizing ε-NTU solver (Jiang et al., 2006). Table 63 shows the simulated testing conditions and results.

Table 63: Simulated Radiator Performance of Initial Circular Bare Tube Design

	Parameter	Unit(s)	Value(s)
Air-Side Conditions	Inlet Temperature	[C]	15
	MFR	[g/s]	112.6
	VFR	[m^3/s, CFM]	0.0921,195
	Inlet Velocity	[m/s]	3.0
	RH	[%]	25
	Abs. Pressure	[kPa]	101.1
Water-Side Conditions	Inlet Temperature	[C]	43
	MFR	[g/s]	30
	Inlet Pressure	[kPa]	105
Predicted Results	Heat Transfer Capacity	[W]	513
	Air-Side Pressure Drop	[Pa]	82.7

The initial bare tube is predicted to provide 513 W of heating under the given experimental radiator conditions at an air-side pressure drop of 82.7 Pa. The heat transfer capacity, change in water temperature, and change in air temperature were all large enough to be experimentally measured with the heat exchanger test facility described in section 2.1. I.e. heat transfer capacity and air-side pressure drop measured within 5% experimental uncertainty with the test facility. The next step was to shape optimize the given circular bare tube geometry to improve the air-side thermal-hydraulic performance; reduce air-side pressure drop and increase heat transfer capacity (air-side temperature change).

AOHX Multi-Objective Shape Optimization

The multi-objective shape optimization process described in section 4.3 was used to shape optimize the baseline circular bare tube heat exchanger (Figure 129). The air-side pressure drop was constrained to be less than 45.7 Pa (45% reduction from starting design) while maximizing the change in air temperature across the heat exchanger (increase capacity).

$$\begin{gathered} maximize\ f(x_{tubes}) = \Delta T_{air} \\ s.t.\quad g(x_{tubes}):\ (\Delta P_{air} - \ \varepsilon) \leq 0 \\ \varepsilon = 45.7\ Pa \end{gathered} \qquad \text{Eq. 60}$$

Figure 131 shows the change in ΔT_{air}, ΔP_{air}, active tube surface area, and air-side average HTC. The amount of active surface area, average air-side HTC, and air temperature change decrease during the initial circular design to approximately design iteration 38 until the pressure drop constraint was reached. During design iterations 39-149:

- Pressure drop was maintained below the pressure drop constraint (45.7Pa) for the remainder of the design iterations.
- Active air-side surface area consistently increased.
- Air-side average HTC decreased.
- Air-side temperature change increased.

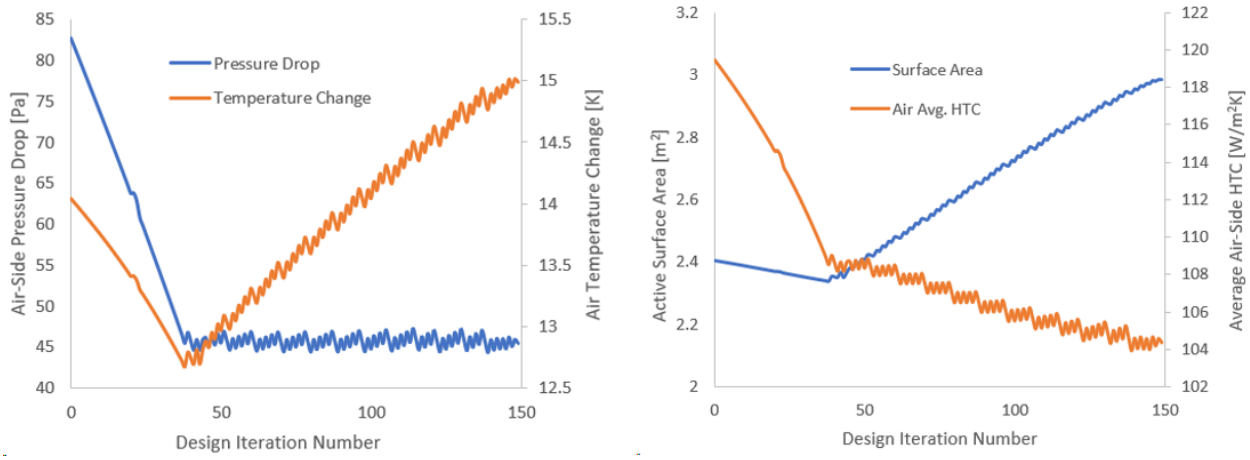

Figure 131: Change in HX Performance over 149 Design Iterations (Left) Pressure Drop and Temperature Change (Right) Surface Area and Average Air-side HTC

Figure 132 shows the final design's (Iteration 149) resulting 2D velocity contours. Figure 133 shows the temperature and pressure contours.

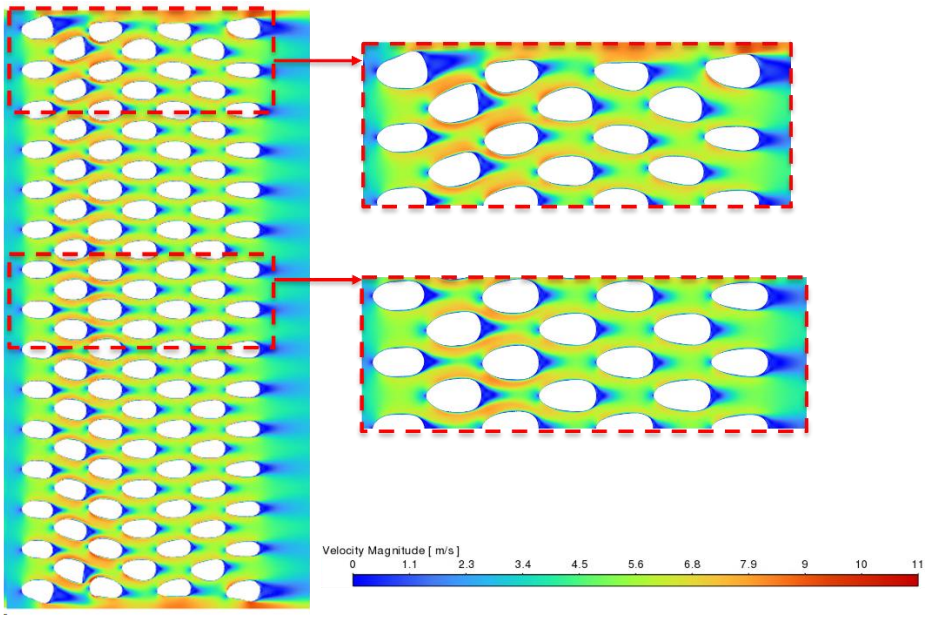

Figure 132: 2D Velocity Contours of Final Optimized Design (AOHX)

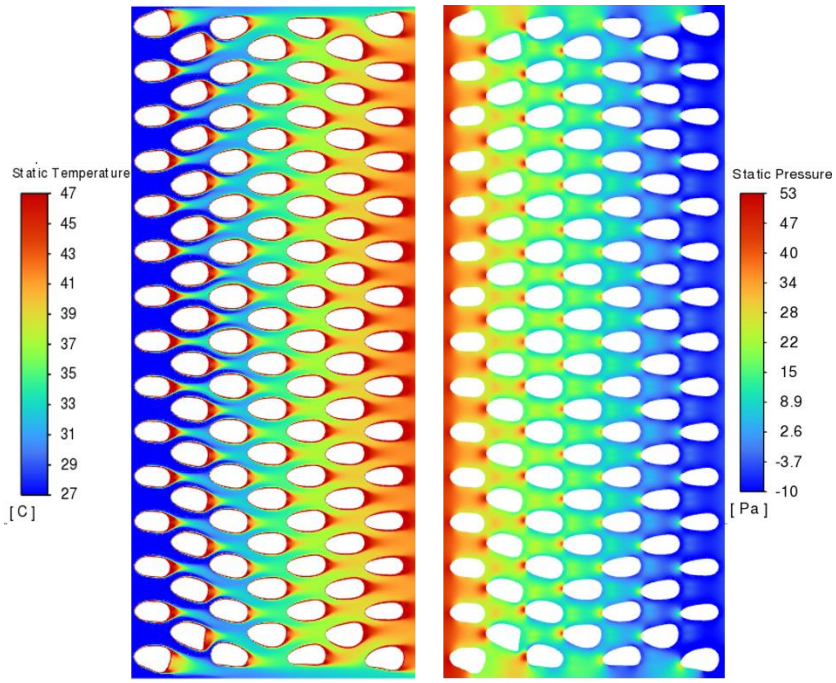

Figure 133: AOHX 2D Contours (Left) Temperature Contours (Right) Static Pressure Contours

Table 64 shows a comparison summary against the initial circular bare tube design at an air velocity of 3 m/s, including f and Colburn j factors.

Table 64: AOHX Design Change Summary

Parameter	Unit(s)	Initial Circular Bare Tube Heat Exchanger	Final AOHX	Percent Change
Pressure Drop	[Pa]	82.67	45.59	-44.9%
Air Temp. Change (ΔT_{air})	[K]	14.09	14.92	5.9%
Active Surface Area (A_o)	[m^2]	2.40	2.97	23.8%
Average Air Heat Transfer Coefficient ($h_{a,avg}$)	[W/m^2K]	119.05	103.96	-12.7%
$h_{a,avg}$ A_o	[W/m]	286.11	308.46	7.8%
f factor	[-]	0.1150	0.0605	-47.4%
Colburn j factor	[-]	0.0126	0.0117	-7.1%
j/f	[-]	0.1095	0.1928	76.1%
Water-Side Cross-Sectional Area*	[cm^2]	21.08	29.44	39.7%

*Wall thickness of 1mm

The optimization scheme was able to reduce the air-side pressure drop by 47.4% and improve the heat transfer capacity by 5.9%. The air-side average heat transfer coefficient decreased by 12.7%, while active air-side surface area increased by 23.8%. Resulting in $h_{a,avg}$ A_o increasing by 7.8%. The waterside cross sectional area increased by 39.7%. CFD inlet air velocity was varied between 0.5-7.0 m/s for AOHX. Figure 134 shows the resulting air-side pressure drop and average air-side heat transfer coefficient.

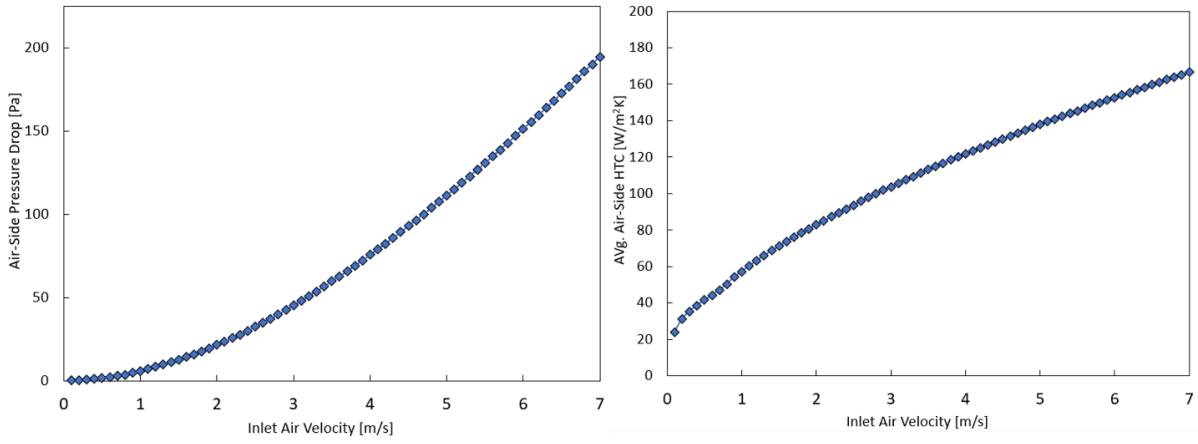

Figure 134: AOHX Predicted (Left) Average Air-Side HTC versus Inlet air Velocity (Right) Air-Side Pressure Drop versus Inlet Air Velocity

Table 65: AOHX Coil Geometry Summary for Radiator Simulation

Parameter	Unit(s)	Value(s)
Tube Length	[mm]	150
Width	[mm]	200.0
Core Depth	[mm]	80.4
Tube Wall Thickness	[mm]	1.0
No. Fluid Passes	[-]	1
Tube Material	[-]	VeroClear
Tube Material Thermal Conductivity	[W/m-K]	0.22

Using the simulated AOHX air-side pressure drop and average heat transfer coefficients from Figure 134 and the parameters shown in Table 65, AOHX's performance as a radiator was simulated at an inlet air velocity of 3 m/s using CoilDesigner®. Table 66 shows the simulated testing conditions and results.

Table 66: Simulated Radiator Performance of AOHX

Fluid	Parameter	Unit(s)	Value(s)
Air-Side	Inlet Temperature	[C]	15
	MFR	[g/s]	112.6
	VFR	[m^3/s, CFM]	0.0921,195
	Inlet Velocity	[m/s]	3.0
	RH	[%]	25
	Abs. Pressure	[kPa]	101.1
Water-Side	Inlet Temperature	[C]	43
	MFR	[g/s]	30
	Inlet Pressure	[kPa]	105
Predicted Results	Heat Transfer Capacity	[W]	562
	Air-Side Pressure Drop	[Pa]	45.2

The heat transfer capacity increased by 9.6% and air-side pressure drop decreased by 45% compared to the initial circular design (Table 63) and Table 67 breaks down the thermal resistances of the water-side convection (laminar flow), wall thermal conduction, and air-side convection.

Table 67: AOHX Radiator Thermal Resistance Composition

Thermal Resistance	Value [K/W]	Percentage of Total
Water-Side Convection (Laminar Flow)	0.00819	17.6%
Wall Conduction	0.01575	33.9%
Air-Side Convection	0.02247	48.5%

Air-side thermal resistance is the highest, but wall conduction is similar in magnitude due to the walls having low thermal conductivity and a thickness of 1 mm. Based on the simulation results, the final AOHX design meets all needs set in Table 59 to successfully manufacture and experimentally test AOHX as a radiator. The next step was to additively manufacture AOHX.

4.6.2 AOHX Additive Manufacturing

Stratasys J850 Polyjet 3D printer

A Stratasys J850 Polyjet 3D printer was to be used to manufacture the final prototype through Stratasys Direct Manufacturing Services. The 3D printer's specifications are shown in Table 60. VeroClear was used as the build material. VeroClear is a transparent material similar to PMMA (polymethyl methacrylate), commonly known as acrylic. Its material properties are shown in Table 61. Stratasys Direct Manufacturing conducted post-processing on AOHX (StratasysDirectManufacturing, 2023). The printer encases the entire 3D print VeroClear structure in a gel like material SUP705 for support. For post-processing, SUP705 can be chemically dissolved using a 2% solution of caustic soda (sodium hydroxide) and sodium metasilicate and or manually removed during post-processing. Additionally, a water pressure washer can be used to remove the material.

AOHX Small Sample Print

The last two steps in Figure 111 were used to extract the 2D bare tube shapes from ANSYS Fluent and generate an additively manufacturable 3D CAD Model.

Before additively manufacturing the full heat exchanger a small section (21 tubes) of AOHX's core was 3D printed with a tube length of 150 mm. The results are shown in Figure 135.

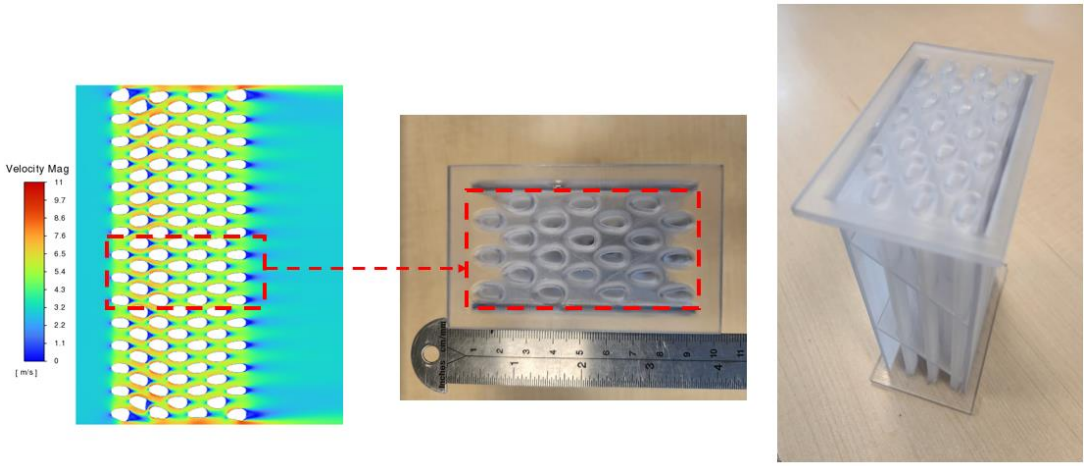

Figure 135: AOHX Small Test Print Section with Polyjet (Middle) Top View (Right) Overview

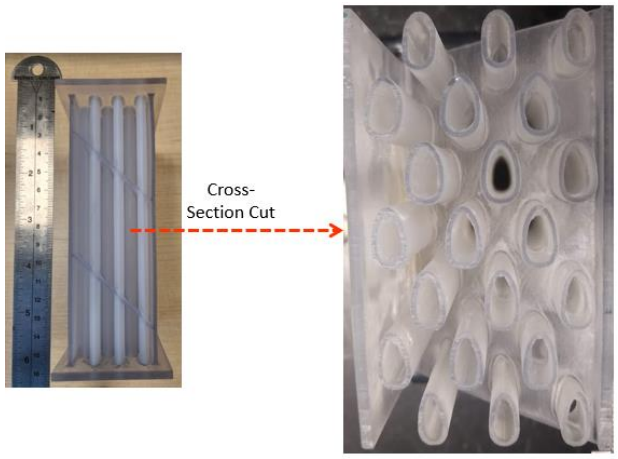

Figure 136: AOHX Cross-Sectional Cut of Small Test Print Section

Figure 136 shows the cut cross section of the sample. Note, tube walls are 1mm thick. The tubes were found to be clear of any blockage material, no defects, and held ~4psig pressure with no leakage.

Additive Manufacturing of Full AOHX

Based on this successful sample print with no tube blockages, the full AOHX was then additively manufactured using the same Stratasys J850 Polyjet 3D printer by Stratasys Direct Manufacturing. Figure 137 shows the generated CAD model with the 1mm wall thickness.

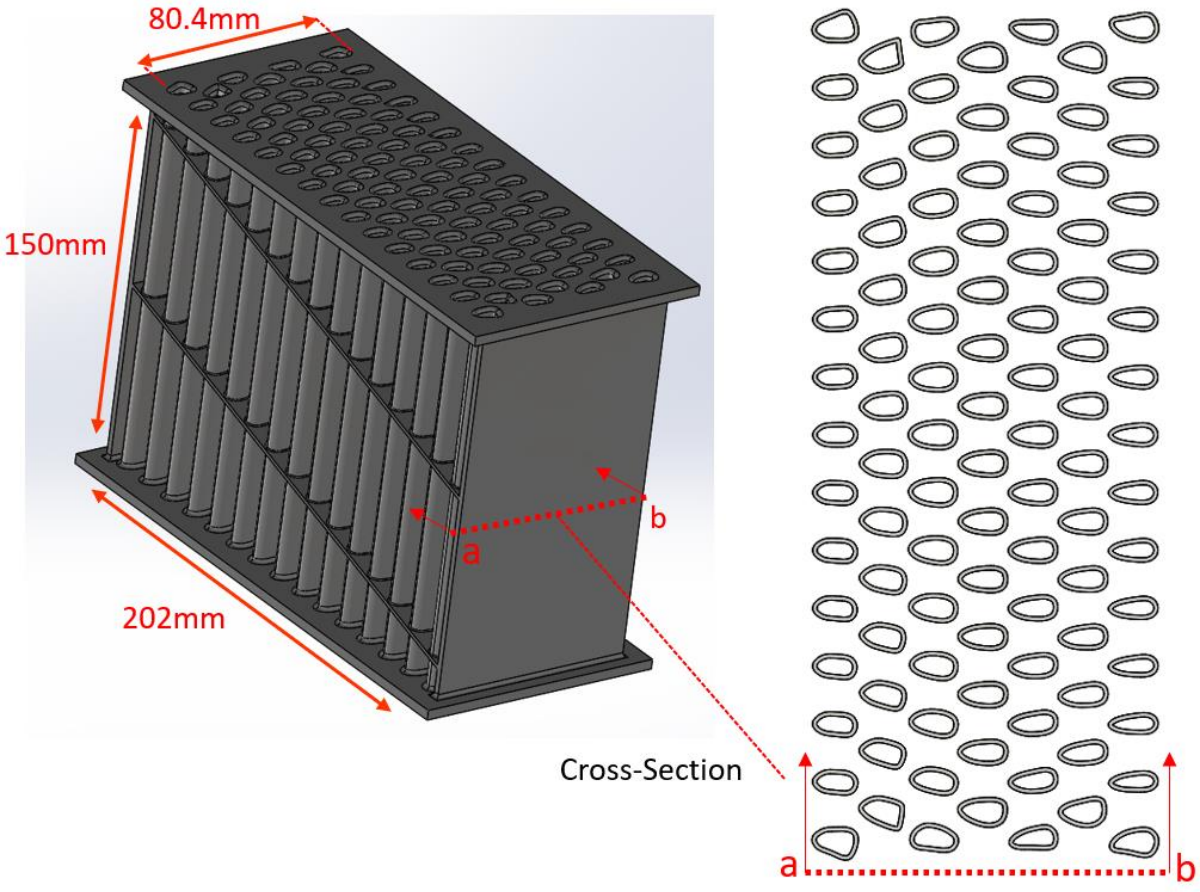

Figure 137: AOHX CAD Model with 2D Cross-Section

Diagonal supports were added to prevent tube warping during printing and increase the tubes' rigidity to prevent accidental breakage during handling. The core was manufactured without any type of headers because it was desired to visually confirm there was no blockages within the tubes after printing. As shown in section 2.3.6 tube blockages can be detrimental to heat exchanger performance. Figure 138 shows the additively manufactured final prototype, AOHX. Figure 139 shows AOHX's Side view and front view.

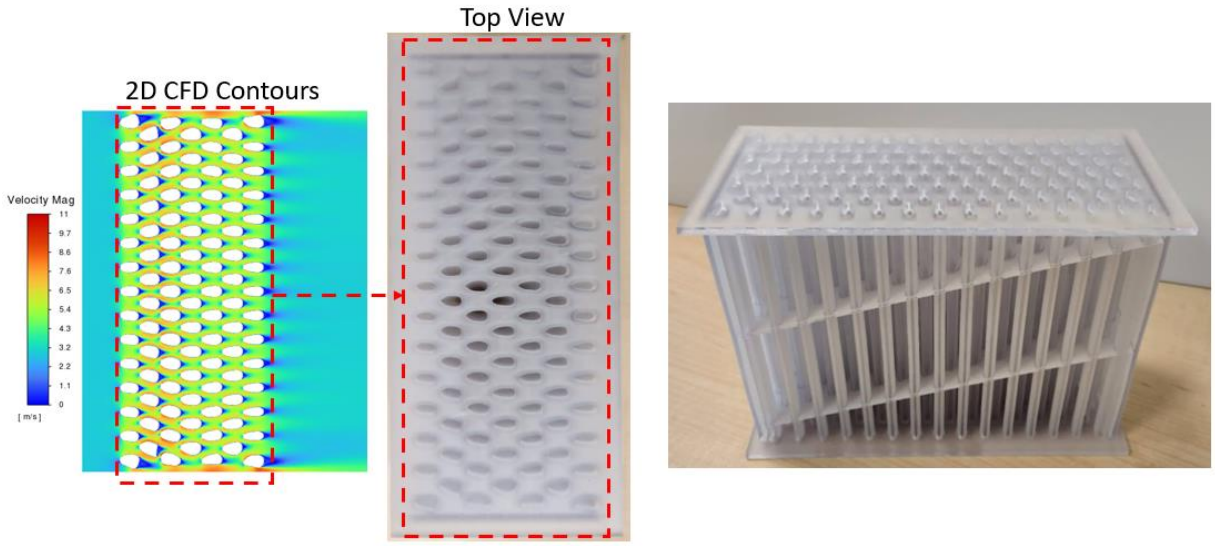

Figure 138: Polyjet Additively Manufactured AOHX Core

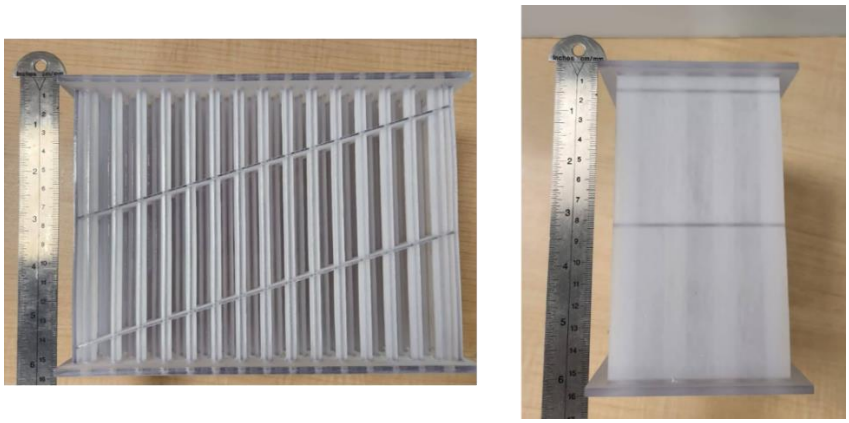

Figure 139: Polyjet Additively Manufactured AOHX Core (Left) Front View (Right) Side View

Two ABS headers were printed using a Fusion 3 F400 3D printer (FDM printing process) to be attached to AOHX's printed core. A thin layer of Acetone was applied to the entire surface of the headers. This dissolved the surface layer of ABS to create a waterproof seal. The processed headers were then epoxied onto the core of the AOHX using RELTEK LLC BONDiT^{TM} B-45TH Epoxy. Figure 140 shows the designed CAD exploded assembly view and the actual completed assembly.

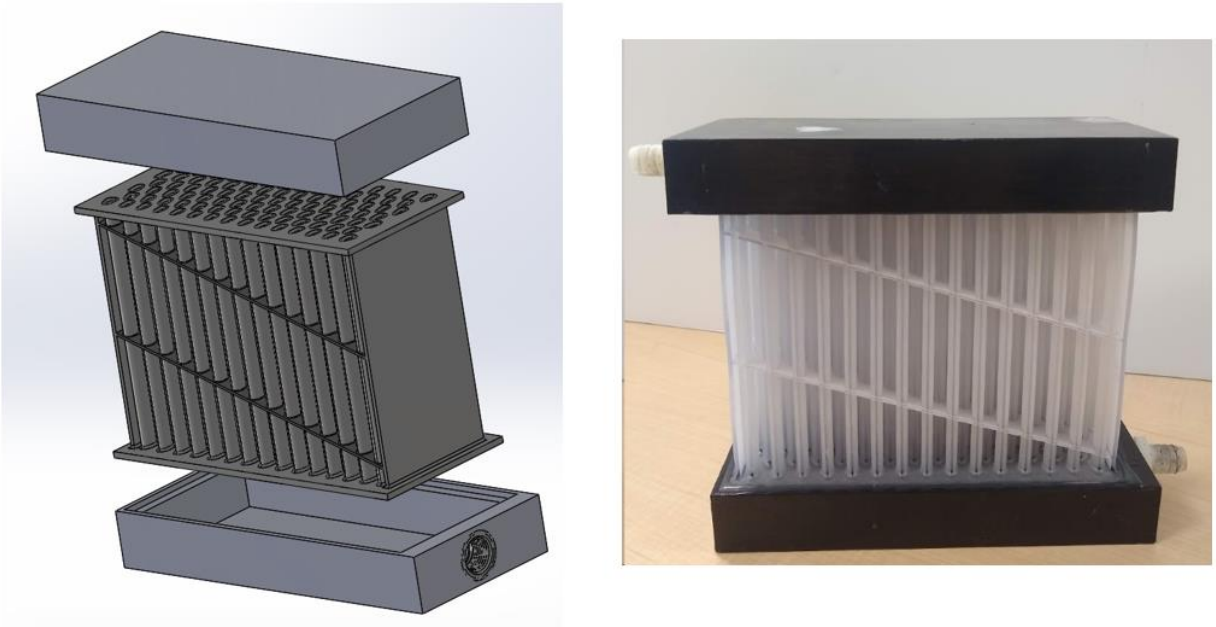

Figure 140: Assembled Additively Manufactured AOHX with ABS Headers

45°C water was flowed through the assembled AOHX at a pressure of 4psig for three hours. No leaks were detected and AOHX was deemed ready for radiator testing.

4.6.3 AOHX Experimental Radiator Testing

Figure 141 shows AOHX mounted in the closed loop wind tunnel section for radiator testing and Table 68 shows a summary of the AOHX prototype.

Table 68: AOHX Prototype Summary

Parameter	Units	Value
Core Dimensions (LxWxD)	[mm]	150 x 202 x 80.4
Core Volume (no headers)	[cm^2]	2,424
Frontal Area	[m^2]	0.0303
Weight without headers	[kg]	0.754
Wall Thickness	[mm]	1
Material	-	VeroClear , Polymer
Manufacturing Process	-	Additive Manufacturing, Polyjet
No. Fluid Passes	-	1
No. Tubes	-	102
No. Banks	-	7
Tube Hydraulic Diameter (Air-Side) Range*	[mm]	5-8

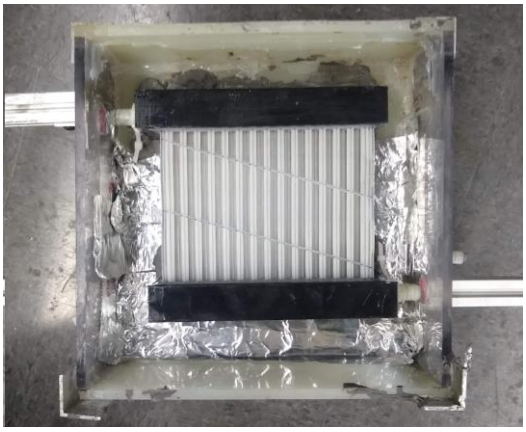

Figure 141: AOHX Mounted in Wind Tunnel Section for Radiator Testing (Air Inlet)

Hot water enters into the bottom right header and flows up against gravity and then cooled water exits out the top left header. The experimental facility is the same as 2.1 with the same data

reduction and uncertainty calculation methodology outline in section 2.2 and 2.1.5, respectively. Table 69 shows the radiator experimental testing summary.

Table 69: AOHX Radiator Experimental Testing Summary

	Parameter	Units	Value(s)
Water-Side	Mass Flow Rate	[g/s]	30 – 70
	Inlet Temperature	[°C]	42.0
	Absolute Pressure	[kPa]	102 – 106
Air-Side	Inlet Temperature	[°C]	15.0
	Inlet Velocity	[m/s]	1.0 – 5.0
	Inlet RH	[%]	< 20
	VFR	[CFM]	74 – 371
Measured Performance	Air-Side Pressure Drop	[Pa]	6.2 – 129.0
	Nominal Capacity	[W]	341 – 710
	Energy balance	[%]	1.0 – 5.6

15 steady state data points were measured; each being 25 minutes long. Figure 142 shows the measured energy balance for all points. The energy balance was below 6% for all 15 data points; indicating good agreement between the water-side and air-side capacity.

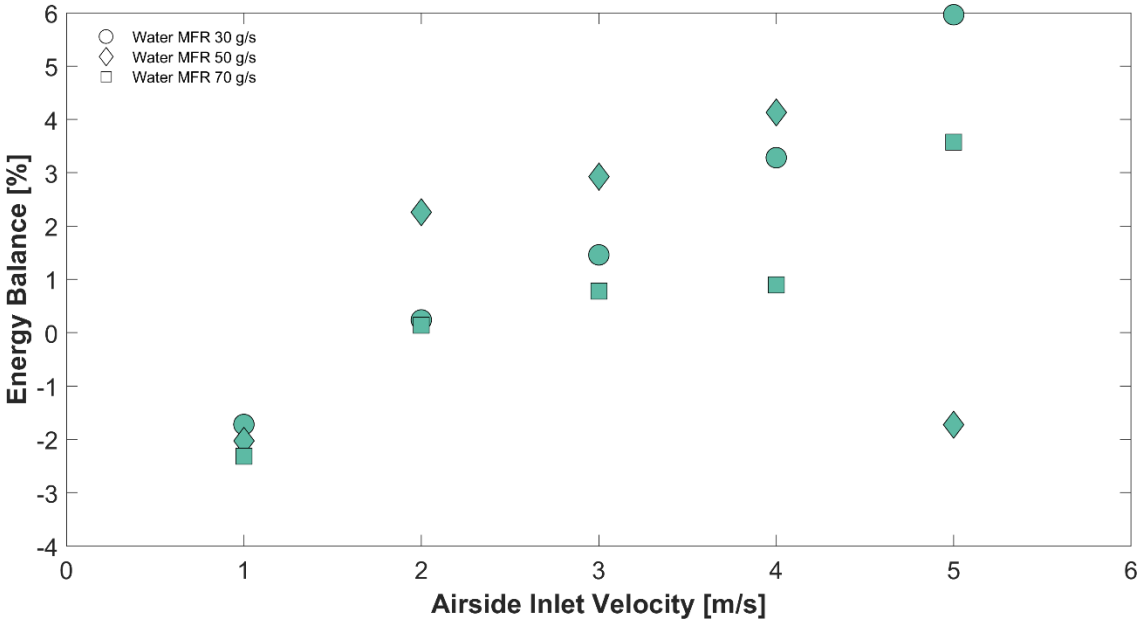

Figure 142: AOHX Radiator Experimental Energy Balance

Figure 143 shows the measured average nominal capacity as the air inlet velocity and water mass flow rate was varied. Figure 144 shows the air-side pressure drop as inlet air velocity was varied.

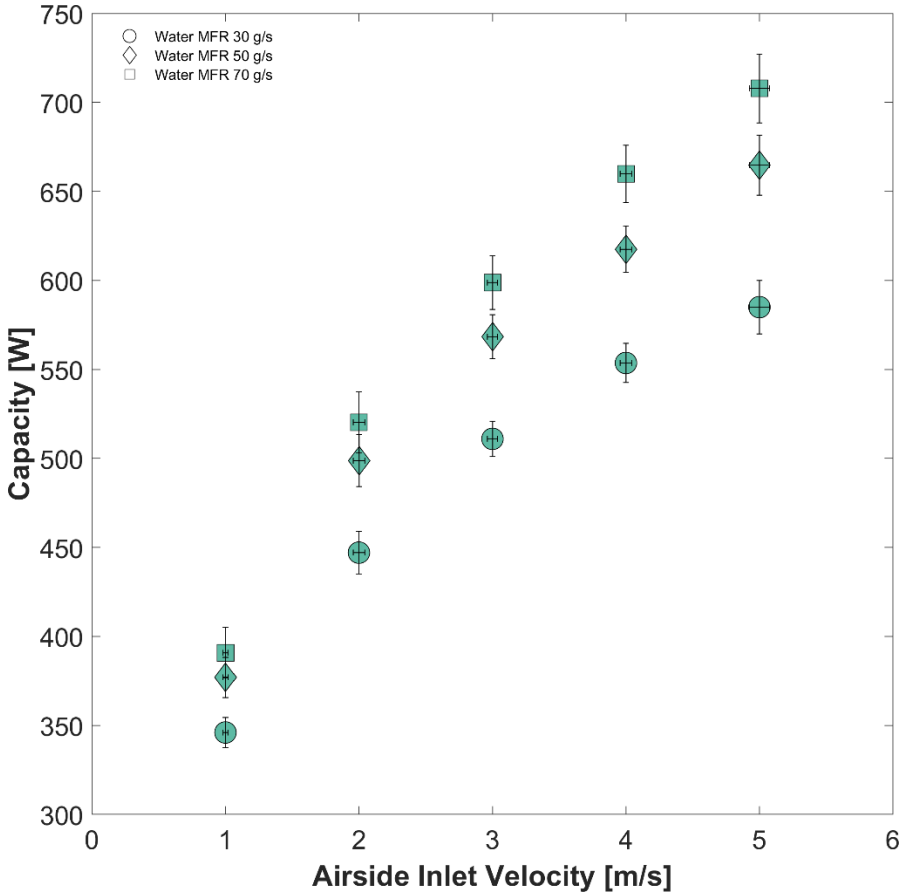

Figure 143: AOHX Radiator Nominal Capacity versus Inlet Air Velocity

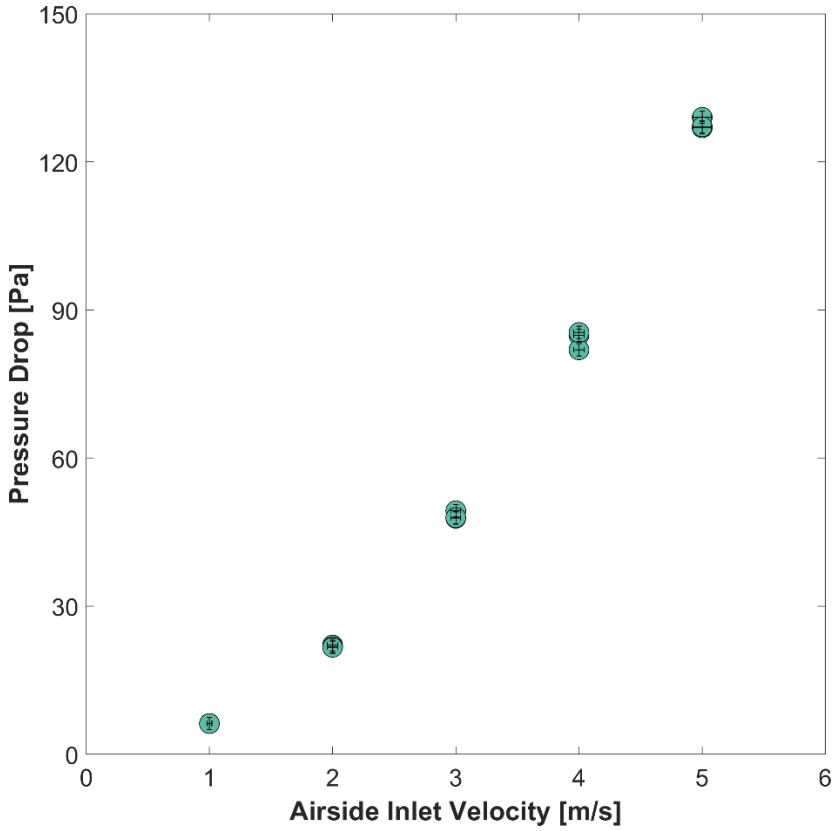

Figure 144: AOHX Radiator Air-Side Pressure Drop versus Inlet Air Velocity

Figure 145 shows the comparison between the simulated and experimental capacity and air-side pressure drop. The air-side pressure-drop and heat transfer coefficients used in this simulation are based on CFD based correlations (Figure 134).

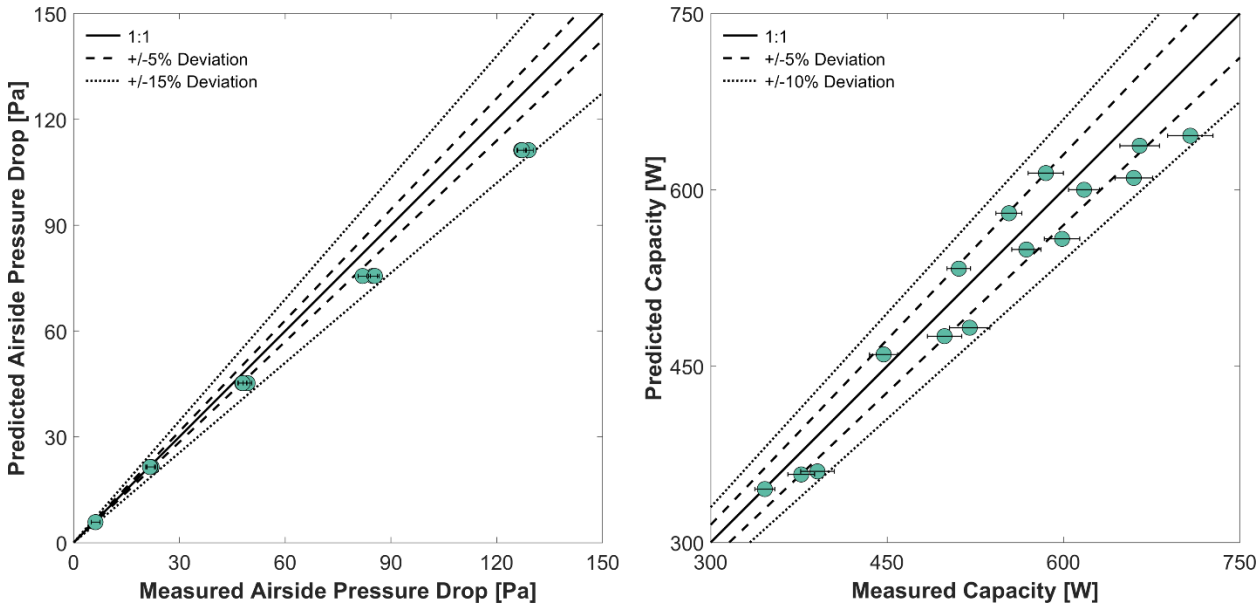

Figure 145: AOHX Radiator Testing Simulated versus Experimental (Left) Air-Side Pressure Drop (Right) Heat Transfer Capacity

Air-side pressure-drop and heat transfer capacity were predicted within 15% and 10%, respectively. Showing excellent agreement between the simulated and experimental results. Air-side pressure drop was consistently under-predicted with the highest percent deviation occurring at the highest inlet air velocity of 5 m/s. For the lowest water-side mass flow rate of 30 g/s, capacity was consistently over-predicted. For water mass flow rates of 50 and 70 g/s capacity was significantly under-predicted. Table 70 shows a performance prediction summary. The experimental performance confirms the shape optimized designs improve the thermal-hydraulic performance over the initial circular bare tube geometry. The experimental validation of this multi-objective optimized compact non-circular bare tube heat exchanger using adjoint methods adds to the limited experimental validation of adjoint optimized heat exchangers.

Table 70: AOHX Radiator Predicted versus Measured Performance Summary

Heat Exchanger	Picture	Testing Condition	Max Percent Deviation from Predicted	Avg. Percent Deviation from Predicted
Adjoint Optimized Heat Exchanger (AOHX)		Radiator	Air-Side Pressure Drop: 13.8% Total Nominal Capacity: 8.7%	Air-Side Pressure Drop: 7.6% Total Nominal Capacity: 5.0%

4.7 NTHX1 Adjoint Shape Optimization Case Study

A disadvantage of adjoint shape optimization is that it is unlikely for the optimization to reach a global optimum. All of the previous optimizations in this chapter started with a circular bare tube design. Different final optimized designs typically will be reached based on the initial geometry. Instead of starting with a circular bare tube design, it was desired to have the starting design as an already shape and topology optimized bare tube heat exchanger. This section is broken down as follows:

- Step 1 - A 7-bank circular bare tube geometry heat exchanger is used as the starting geometry for the adjoint shape optimization scheme at an inlet air velocity of 3 m/s. This initial design has similar horizontal and vertical pitch as NTHX1.
- Step 2 - Then NTHX1 (also 7-banks) is used as the starting geometry for the adjoint shape optimization scheme also at an inlet air velocity of 3 m/s. Details on the heat exchanger can be found in Chapter 2. The adjoint shape optimized designs are compared to the designs from step 1.

4.7.1 7-bank Circular Bare Tube Adjoint Optimization

Table 71 shows the details of the initial circular bare tube design.

Table 71: Initial 3 mm Bare Tube Geometry Parameter Summary

Parameter	Units	4-Bank Heat Exchanger
$N_{tubes,total}$	-	102
$N_{tubes\ per\ Bank}$	-	14/15
Starting Circular D_o	mm	3.0
P_t	mm	5.455
P_l	mm	4.724
$V_{a,in}$	m/s	3.0

The initial 2D velocity contours are shown in Figure 146. The multi-objective shape optimization process described in section 4.3 was used to shape optimize the baseline circular bare tube heat exchanger. The air-side pressure drop constraint (ε) was varied for three shape optimized designs (Eq. 61).

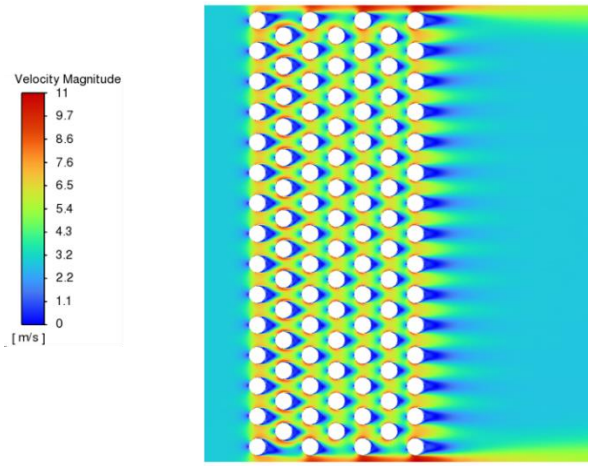

Figure 146: 2D CFD Velocity Contours of Initial 3 mm Circular Bare Tube Heat Exchanger

$$maximize\ f(x_{tubes}) = \Delta T_{air}$$
$$s.t.\quad g(x_{tubes}):\ (\Delta P_{air} - \varepsilon) \leq 0 \qquad \text{Eq. 61}$$
$$\varepsilon = 40.5\ Pa\ , 46.0\ Pa\ , 53.0\ Pa$$

Figure 147 shows the resulting velocity contours. Table 72 summarizes the design change from the initial circular design.

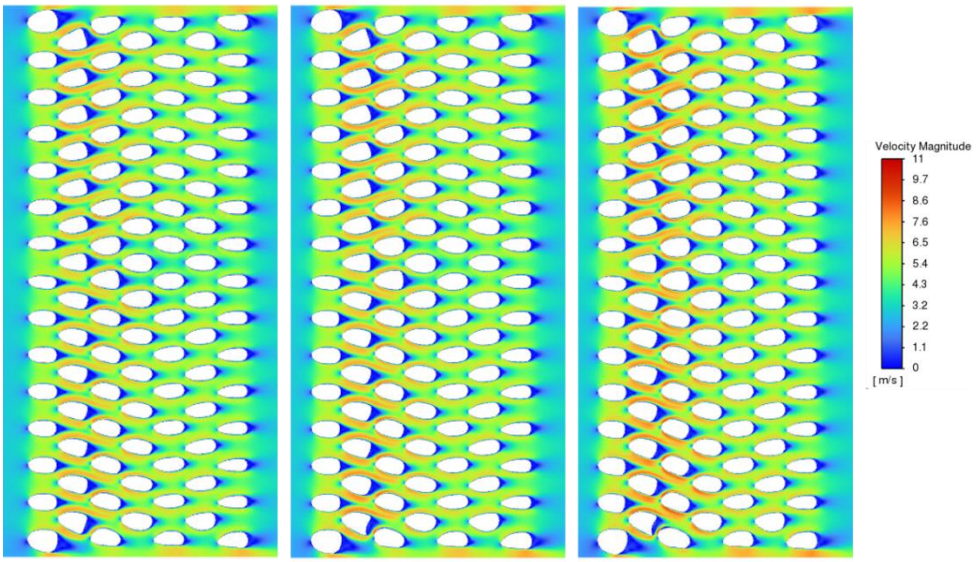

Figure 147: 2D Velocity Contours of Final Optimized Designs from 3 mm Circular Bare Tube Geometry

Table 72: Bare Tube Geometry Parameter Summary

	Starting 3 mm Circular	ε = 40.5 Pa	ε = 46.0 Pa	ε = 53.0 Pa
Inlet Velocity [m/s]	3	3	3	3
ΔT_{air} [K]	19.63	19.76	20.27	20.71
Pressure-Drop [Pa]	97.6	40.2	45.6	53.0
Average HTC [W/ m^2-K]	183.6	157.2	160.3	164.7
Total Surface Area [m^2]	0.96	1.13	1.15	1.15
j-Factor [-]	0.01943	0.0184	0.01874	0.0181
f-Factor [-]	0.131	0.0607	0.0678	0.0648
j/f [-]	0.1483	0.3031	0.2767	0.2787
Compactness [m^2/m^3]	386.3	440.6	448.0	449.1
Refrigerant-Side Cross Sectional Area [m^2]	0.0007164	0.000822818	0.000863127	0.000891057

4.7.2 NTHX1 Adjoint Shape Optimization

NTHX1's initial 2D velocity contours are shown in Figure 148. The multi-objective shape optimization process described in section 4.3 was used to shape optimize the baseline circular bare tube heat exchanger. The air-side pressure drop constraint (ε) was varied six times for six shape optimized designs (Eq. 62).

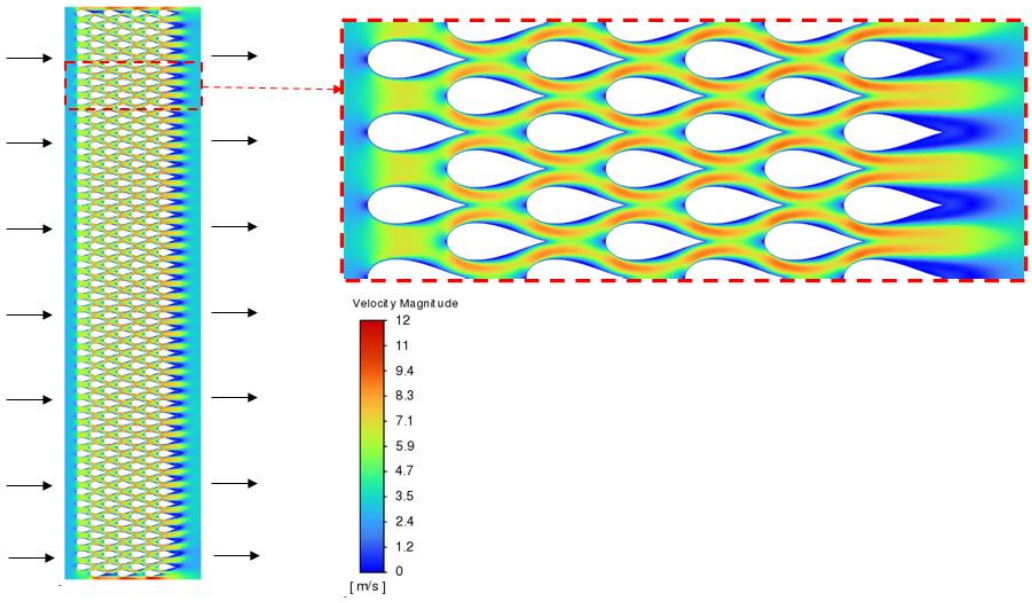

Figure 148: NTHX1 CFD 2D Velocity Contours at Inlet Air Velocity of 3 m/s

Figure 149 shows a close up of the core for all six optimized designs. Table 73 summarizes the final designs' performance and comparison with the initial NTHX1 design.

$$maximize\ f(x_{tubes}) = \Delta T_{air} \qquad \text{Eq. 62}$$
$$s.t.\quad g(x_{tubes}):\ (\Delta P_{air} - \varepsilon) \leq 0$$
$$\varepsilon = 35.5Pa\ ,41.5Pa\ ,48.4Pa\ ,56.5Pa\ ,64.3Pa\ ,70.5Pa$$

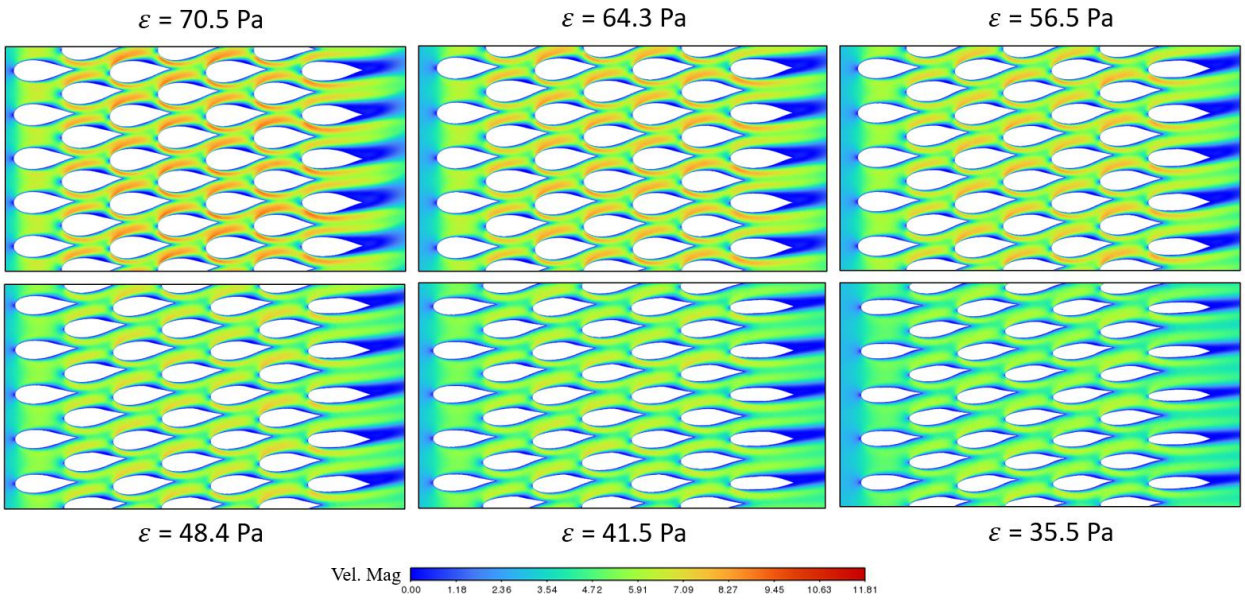

Figure 149: Adjoint Shape Optimized NTHX1 Designs at Inlet Air Velocity 3 m/s (Zoomed In Section)

Table 73: NTHX1 Adjoint Optimization Summary

	Starting NTHX	ε = 70.5 Pa	ε = 64.3 Pa	ε = 56.5 Pa	ε = 48.4 Pa	ε = 41.5 Pa	ε = 35.5 Pa
Inlet Velocity [m/s]	3	3	3	3	3	3	3
ΔT_{air} [K]	30.91	32.96	32.38	32.48	31.74	31.18	30.54
Pressure-Drop [Pa]	70.54	70.38	62.3	56.2	47.4	41.0	34.1
Average HTC [W/ m^2-K]	212.4	243.25	235.0	237.7	229.6	223.0	215.5
Total Surface Area [m^2]	2.11	2.11	2.10	2.10	2.06	2.05	2.03
j-Factor [-]	0.02418	0.02499	0.0271	0.0283	0.0293	0.0240	0.0308
f-Factor [-]	0.0601	0.0437	0.0554	0.0554	0.0574	0.0551	0.0587
j/f [-]	0.403	0.573	0.490	0.511	0.510	0.534	0.525
Compactness [m^2/m^3]	1253.8	1235.5	1229.7	1229.5	1206.3	1198.0	1188.7
Ref-Side Cross-Sectional Area [cm^2]	6.67	6.60	6.40	6.05	5.59	5.10	4.53

The multi-objective adjoint optimization scheme was able to successfully meet the pressure drop constraint for all designs and improve the performance of an already shape and topology optimized heat exchanger. This study indicates that previously shape and topology optimized bare tube heat exchanger designs have the potential to be further improved using adjoint based shape optimization. It also shows the determination of the initial starting geometry is of particular importance.

Refrigerant-side cross sectional area decreased between 1.0 to 32.1%. Refrigerant-side cross sectional area was not constrained or controlled during these optimizations. The decrease in cross-sectional area indicates the refrigerant-side pressure drop will increase for these shape optimized NTHX1 heat exchanger designs.

4.8 Adjoint Shape Optimizations Summary

The following provides a high-level summary on the shape optimized designs when compared to their respective initial starting design geometries for section 4.4 through 4.7.

Section 4.4, 9.525 mm Four-Bank Heat Exchanger Optimizations: Air-side pressure drop changed between -68.0 to 188.1%. Overall capacity increased between 8.9 to 56.8%. The air-side surface area increased between 17.2 to 60.2% while air-side heat transfer coefficient changed by -23.5 to 19.9%, with a majority showing a decrease in air-side heat transfer coefficient. Even though average air-side heat transfer coefficient decreased for many of the designs, the increase in surface area compensated for this decrease in average air-side heat transfer coefficient. Refrigerant-side cross sectional area increased between 22.0 to 83.8%.

Section 4.5, 1.0-3.0 mm Heat Exchanger Optimizations*:* Air-side pressure drop changed between -60 to 0.8%. Overall capacity changed between -3.2 to 37.7%. The air-side surface area increased between 9.6 to 63.2% while air-side heat transfer coefficient changed by -22.0 to 8.4%, with a majority showing a decrease in air-side heat transfer coefficient. Similar to the 9.525 mm four-bank heat exchangers, the average air-side heat transfer coefficient decreased for many of the designs, but the increase in surface area compensated for this decrease in average air-side heat transfer coefficient. Refrigerant-side cross sectional area changed between -22.0 to 112.9%.

Section 4.6, 7-Bank AOHX Optimization*:* Air-side pressure drop decreased 47% over initial circular design. Overall capacity increased by 6%. The average air-side heat transfer coefficient decreased by 13%, but the increase in surface area of 24% compensated for this decrease in average air-side heat transfer coefficient. Refrigerant-side cross sectional area increased by 40%.

Section 4.7, NTHX1 Optimizations: Air-side pressure drop changed between -50 to 0%. Overall capacity changed between -1.2 to 6.6%. The air-side surface area changed between -3.8 to 0% while air-side heat transfer coefficient changed by -1.5 to 14.5%, with a majority showing an increase in air-side heat transfer coefficient. This differs from the previous shape optimizations where the starting point was the circular bare tube design. In contrast to the previous designs, the optimizations increased the air-side heat transfer coefficient while decreasing or maintaining the amount of air-side surface area. The refrigerant-side cross section changed between -32.1 to -1.0 %.

It is valuable to have a discussion on why the shape optimized designs have improved thermal-hydraulic performance over the initial circular geometry. Figure 150 shows a close up the velocity, velocity angle, and turbulence intensity contours of heat exchanger design h in Figure 124. The

top contours show the initial circular bare tube design and the bottom contours show design's shape optimized design.

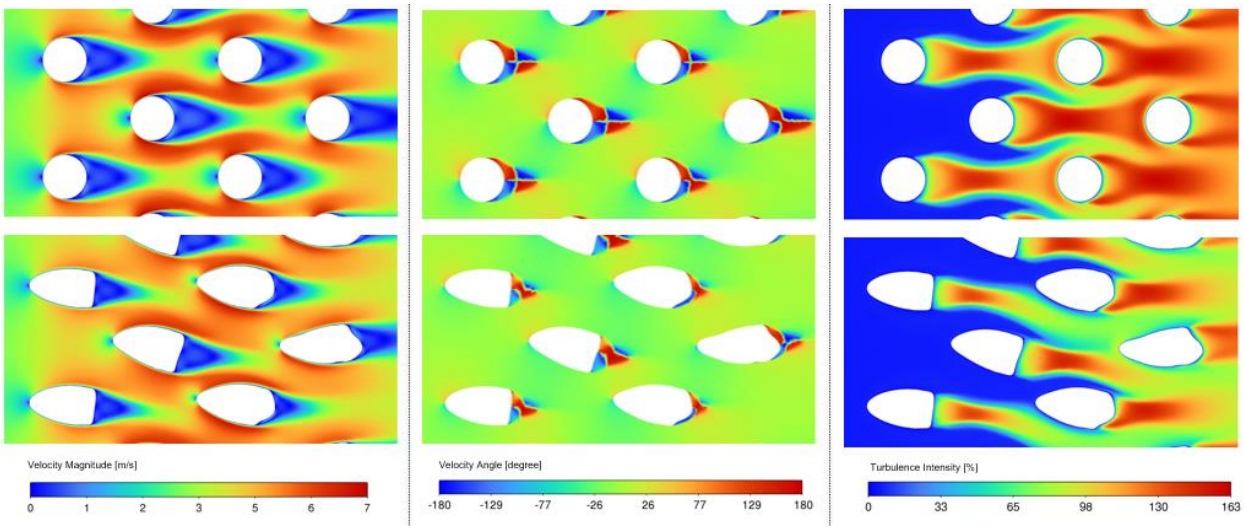

Figure 150: Adjoint Shape Optimized Design (Left) - Velocity Magnitude Contours (Middle) - Velocity Angle Contours (Right) - Turbulence Intensity Contours

The velocity contours show that the optimized designs are much more streamline and reduce the bare tubes' stagnation point. As the bare tubes become more streamlined, the tubes also elongate to increase active surface area and increase heat transfer capacity. The velocity angle contours show that the optimized designs' air-side separation point is shifted to the trailing edge of the bare tubes. This reduces the turbulence wake size and amount of vortex shedding as shown by the turbulence intensity contours. The combination of a more streamlined design with reduced stagnation point and less turbulence intensity reduced the air-side pressure drop while at the same time active air-side heat transfer area increased to increase heat transfer capacity.

Chapter 5: Conclusions

The objectives of this dissertation were to experimentally evaluate the performance of shape and topology optimized compact bare tube heat exchangers with non-round bare tubes on a 1) component level, and 2) system level integrated into an air conditioner. Plus, 3) develop new shape optimized variable geometry compact bare tube heat exchangers using discrete adjoint methods for typical HVAC&R applications. Conclusions of Chapter 2, 3, and 4 are as follows.

First, in Chapter 2, a comprehensive experimental investigation of four shape and topology optimized compact non-round 2-3 mm bare tube heat exchangers was conducted under wet and dry evaporator, condenser, and radiator conditions. R-410A and R-134a were both used as refrigerants. The heat exchangers' air-side thermal-hydraulic performance was measured. Air-side pressure drop (dry conditions) and heat transfer capacity were predicted within 37% and 15%, respectively, for all heat exchangers. These experimental results provide strong evidence this new class of compact finless heat exchangers are performing as intended under typical HVAC&R application conditions. Additionally, it provides evidence the shape and topology optimization framework used to develop these heat exchangers (Bacellar et al., 2017; Tancabel et al., 2022) can accurately predict the air-side thermal-hydraulic performance of these novel non-round bare tube compact heat exchangers.

During wet evaporator testing of the non-round bare tube heat exchanger, CNTHX1, more severe than anticipated condensate bridging between bare tubes and build-up in the core was observed. Under these wet evaporator conditions, air-side pressure drop increased 111-160% at the same inlet air velocity (1.0-2.5 m/s) when compared to dry evaporator conditions. CNTHX1's increase in air-side pressure drop under wet conditions is higher or roughly equal than plain fin-tube heat exchangers with a fin pitch of 1-2 mm (11-120% increase in hydraulic resistance over dry

conditions) reported in literature. The latent load and sensible heat ratio were both predicted within 20% and 5%, respectively. CNTHX1's sensible heat ratio was measured to be 0.70-0.74. The measured sensible heat ratio indicated this new type of compact heat exchanger is able to handle the latent load under these air-side conditions with approximately equal to 10% lower sensible heat ratio when compared to a plain fin-tube heat exchanger with a fin pitch of 1.8 mm tested under similar air-side conditions.

Next, an experimental test facility capable of evaluating the system level performance of a 7.03-8.79 kW (2.0-2.5 refrigeration ton (RT)) commercial packaged air conditioning unit was designed and constructed. The performance of the air conditioning unit was evaluated before and after its conventional plain fin-tube evaporator was replaced with one of the four experimentally tested finless non-round bare tube heat exchangers. The capacity, COP, and SHR of the packaged air conditioning unit with the baseline fin-tube evaporator were all predicted within 5% at AHRI 210/240 conditions. The fin-tube evaporator was then replaced with a finless non-round bare tube heat exchanger, CNTHX-FS. At the same AHRI experimental test conditions, the packaged unit's capacity and COP changed by -30.4% and -29.44%, respectively. The sensible heat ratio and R410A charge decreased by 9% and 12%, respectively. CNTHX-FS's total cooling capacity and COP were degraded due to more severe than anticipated refrigerant maldistribution and condensate bridging/retention. This was attributed to the installation orientation (horizontal bare tubes with respect to gravity), inlet/outlet port orientation and under-sizing, and manifold header set-up. The results indicated that the installation orientation, inlet/outlet port orientation and sizing, and manifold set-up for this class of non-round bare tube finless heat exchangers are critical for proper system level performance and further investigation is needed into the effect of these factors on the heat exchanger and system level performance.

Lastly, a discrete adjoint solver built into ANSYS Fluent CFD software was utilized to perform multi-objective shape optimizations of finless bare tube compact heat exchangers for typical HVAC&R applications. An ε-constraint and penalty method optimization scheme was utilized with Fluent's CFD adjoint solver tool to perform multi-objective shape optimizations of bare tube heat exchangers. Optimizations maximized air-side temperature change over the bare tube heat exchanger (heat transfer capacity) while satisfying the prescribed air-side pressure drop constraint. Critical solver and mesh set-up to best optimize the bare-tube geometry were identified and established. Using the optimization scheme and Fluent's adjoint solver, approximately 100 shape optimized bare tube heat exchanger designs were reached to determine the potential improvement of finless circular bare tube heat exchangers with hydraulic diameters ranging from 0.5-10.0 mm, 2-4 tube banks, in staggered tube arrangement. Optimized designs can achieve a 40-50% reduction in air-side pressure drop with equal to 20% increase in heat transfer capacity compared to the initial circular bare tube geometry. The designs achieved this by increasing the air-side surface area with an equal or lower average air-side heat transfer coefficient. Simultaneously, air-side pressure drop was reduced below the air-side pressure drop constraint. Most of the designs observed an increase in refrigerant-side cross sectional area, with the largest cross-sectional decrease being -22% over the initial circular bare tube design. These adjoint based shape optimizations demonstrate superior air-side thermal-hydraulic performance over the initial circular bare tube geometries. However, disadvantages of adjoint shape optimization include it is very unlikely to find a global optimum and is limited by the initial starting circular geometry, quality of the computational mesh, and definition of the objective function.

Optimizations were then conducted where the initial starting design was not a circular design, but instead a previously shape and topology optimized bare tube heat exchanger. The previously shape

and topology optimized NTHX1 prototype (Bacellar et al., 2017) was used as the starting geometry for the adjoint shape optimization scheme. The multi-objective adjoint solver was able to reduce air-side pressure drop by 40-50% while maintaining the same heat transfer capacity. The optimizations increased the air-side heat transfer coefficient while decreasing or maintaining the amount of air-side surface area. The refrigerant-side cross section was reduced by 1.0 to 32.1 % when compared to the initial NTHX1 design. The optimizations indicate that previously shape and topology optimized bare tube heat exchanger designs have the potential to be further improved using adjoint based shape optimization. The adjoint solver's practical infinite degrees of freedom to define the bare tubes' shapes can improve the previously shape and topology optimized design.

Lastly, a 7-bank 500 W circular finless bare tube radiator (AOHX) was shape optimized to be additively manufactured in polymer and experimentally evaluated to measure the performance of one of these novel variable geometry adjoint optimized bare tube heat exchangers. AOHX's air-side pressure drop decreased by 47.4% and increased heat transfer capacity by 5.9% over the initial circular bare tube design. The air-side average heat transfer coefficient decreased by 12.7%, while active air-side surface area increased by 23.8%. A pipeline was then developed to extract the 2D optimized tube geometry design from ANSYS Fluent and generate a CAD model to be additively manufactured. AOHX was successfully additively manufactured in a polymer material with 1 mm thick walls, and the air-side thermal-hydraulic performance experimentally evaluated under radiator conditions. AOHX's air-side pressure drop and heat transfer capacity were measured to be 6.2-127.1 Pa and 340-720 W, respectively. The air-side pressure drop and heat transfer capacity were predicted within 15% and 10%, respectively. The experimental performance confirms the shape optimized design's improved thermal-hydraulic performance over the initial circular bare tube geometry.

5.1 Contributions

The contributions of this dissertation are broken down into three main sections.

First, a comprehensive experimental investigation of four shape-and-topology optimized compact non-round 2-3 mm bare tube heat exchangers was conducted under dry and wet evaporator, condenser, and radiator conditions. This body of work adds to the experimental performance evaluation of finless non-circular bare tube heat exchangers (hydraulic diameter less than 6 mm). Results add experimental evidence that these novel shape and topology optimized non-round bare tube compact heat exchangers have the potential to out-perform their finned counterparts with their improve air-side thermal-hydraulic performance. Included in this body of work is wet evaporator (R-410A) testing. Condensate bridging and condensate retention in the core of the heat exchanger was identified as a potential issue for high humidity conditions as it dramatically increased air-side pressure drop over dry conditions.

Next, an experimental test facility capable of evaluating the system level performance of a commercial packaged air conditioning unit was designed and constructed. The performance of the air conditioning unit was evaluated before and after its conventional tube-fin evaporator was replaced with a shape and topology optimized non-round bare tube evaporator. To the author's knowledge, this is the first known experimental evaluation of an air conditioning system with a shape and topology optimized small diameter non-round bare tube evaporator. Results revealed the refrigerant maldistribution and condensate bridging was more severe than anticipated and consequentially the packaged air conditioning unit's capacity and COP changed by -30.4% and -29.4%, respectively. It was identified that further investigation is needed into mitigating the refrigerant maldistribution and condensate bridging issues for this novel type of non-round bare

tube compact heat exchanger to be successfully integrated into an air conditioning system with the desired COP and cooling capacity benefits.

Lastly, a discrete adjoint solver built into ANSYS Fluent CFD software was used to perform shape optimizations of bare tube heat exchangers under typical HVAC&R conditions. Critical solver and mesh set-up to best optimize compact 0.5-10.0 mm bare-tube heat exchanger geometry were identified and established. A parametric study utilizing the optimization scheme and adjoint solver identified the scope and of potential thermal-hydraulic improvement of non-uniform shape optimized bare-tube heat exchangers for typical HVAC&R applications in this tube size range. A 500 W bare tube radiator was designed, and shape optimized using discrete adjoint method. The thermal-hydraulic performance was experimentally validated. The experimental validation of this multi-objective optimized compact non-circular bare tube heat exchanger using adjoint methods adds to the limited experimental validation of adjoint optimized heat exchangers. Additionally, this experimental evaluation adds to the body of work of additively manufactured heat exchangers.

5.2 Future Work

Chapter 2 showed experimental evidence that shape and topology optimized non-round bare tube compact heat exchangers have the potential to out-perform their finned counterparts with their improved air-side thermal-hydraulic performance. It is recommended to better quantify the effects of surface roughness on the air-side thermal hydraulic performance of compact bare tube heat exchangers. It is also recommended to investigate the performance of these compact non-circular bare tube heat exchangers under wet evaporator conditions and further quantify fundamental heat and mass transfer principles under de-humidifying conditions. This could be quantified by Lewis number correlations.

Chapter 3 showed the refrigerant maldistribution and condensate bridging was more severe than anticipated with the new compact non-round bare tube heat exchanger as an evaporator. In the future, CNTHX-FS should be reinstalled into the packaged air conditioning unit with different installation orientations and manifold port locations and sizes to reduce refrigerant maldistribution, pressure drop, and increase the condensate drainage rate. Additionally, retrofitting the initial packaged unit's plain fin-tube condenser with a shape and topology optimized non-round bare tube condenser would further confirm the ability for these heat exchangers to improve the system level performance of air-conditioning systems and decrease refrigerant charge.

With regards to the developed multi-objective optimization scheme developed in Chapter 4, it is recommended to additively manufacture one of the smaller hydraulic diameter designs (1-3 mm hydraulic diameter) in metal. The adjoint shape optimizations of the NTHX1 heat exchanger are some of the most promising designs for this. Then experimentally evaluate this metal heat exchanger under evaporator and/or condenser conditions. Additionally, it is recommended to constrain the refrigerant-side cross sectional area to achieve designs that do not increase refrigerant-side pressure drop.

5.3 Publications

- Conferences In print (3)
    - **Klein, E.,** Hwang, Y., Aute, V., and Radermacher, R. A Review of Recent Advances in Additively Manufactured Heat Exchangers, *17th International Refrigeration and Air Conditioning Conference*, West Lafayette, Indiana, USA, July 9-12, 2018.
    - **Klein, E.,** Muehlbauer, J., Hwang, Y., and Aute, V. Experimental Study of a Novel Shape-Optimized Air-to-Refrigerant Heat Exchanger. *2nd Pacific Rim Thermal Engineering Conference*, Maui, Hawaii, USA, December 13-17, 2019.
    - **Klein, E**., Muehlbauer, J., Ling, J., Shabtay, Y., Aute, V., Hwang Y., and Tancabel, J. Experimental Study of a Novel Shape-Optimized Air-to-Refrigerant Heat Exchanger under Evaporator Conditions. Manuscript accepted to the *18th International Refrigeration and Air Conditioning Conference*, West Lafayette, Indiana, USA, May 24-28, 2021.
- Journals in Print (1: 3rd Author)
    - Tancabel, J., Aute, V., **Klein, E.,** Hwang, Y., Ling, J., Muehlbauer, J., and Radermacher, R. "Design Optimization and Experimental Validation of Heat Exchangers Utilizing High Performance, Non-round Tubes". Manuscript submitted to the *15th International Conference on Heat Transfer, Fluid Mechanics and Thermodynamics (HEFAT 2020)*, Amsterdam, The Netherlands, July 20-22, 2020.
- Planned Journal Manuscripts (2)
    - **Klein, E.,** Aute, V., Hwang, Y. (2023). Design and Experimental Investigation of an Additively Manufactured Adjoint Shape Optimized Variable Geometry Bare Tube Heat Exchanger, Intended Journal: International Journal of Heat and Mass Transfer
    - **Klein, E.,** Aute, V., Hwang, Y. (2023). Discrete Adjoint Method Shape Optimizations of Bare Tube Heat Exchangers for HVAC&R Applications, Intended Journal: Structural and Multidisciplinary Optimization
- Planned Conference Manuscripts (1)
    - **Klein, E.,** Tancabel, J., Aute, V., Muehlbauer, J., Hwang, Y., Radermacher, R. (2023). Retrofit and Experimental Validation of a Packaged Air-Conditioning Unit with Heat Exchangers Utilizing Shape-and Topology-Optimized Tube Bundles. Planned Conference Proceedings: 2024 ASHRAE Winter Conference

Appendix

6.1 Appendix A: Pumped Refrigerant Loop Electrical Schematics

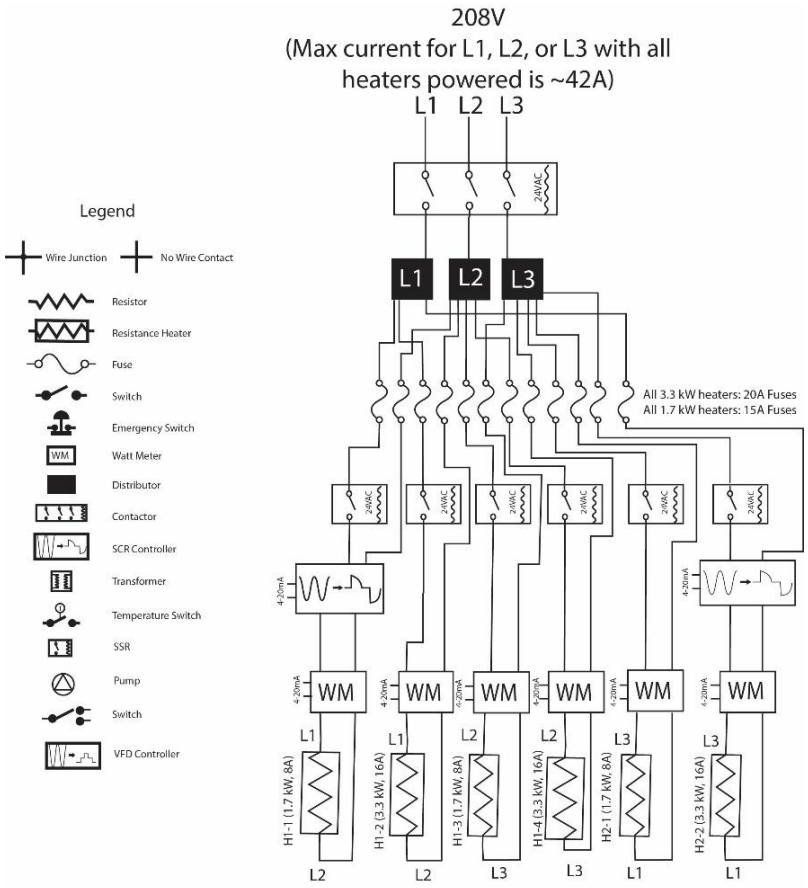

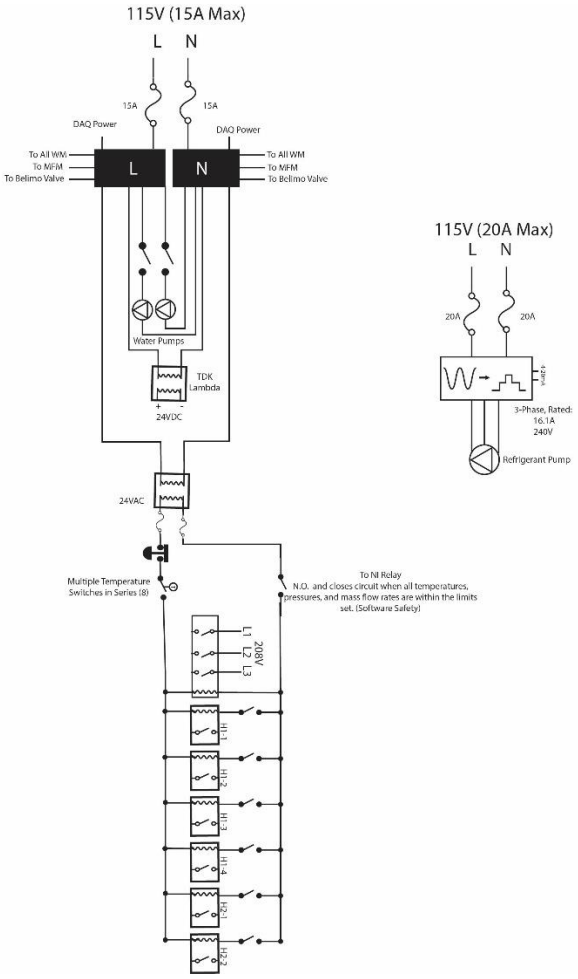
115V (15A Max)
L N
15A
15A
DAQ Power
DAQ Power
To All WM
To MFM
To Belimo Valve
To All WM
To MFM
To Belimo Valve
L
N
Water Pumps
TDK
Lambda
+ -
24VDC
24VAC
115V (20A Max)
L N
20A
20A
3-Phase, Rated:
16.1A
240V
Refrigerant Pump
Multiple Temperature
Switches in Series (8)
To NI Relay
N.O. and closes circuit when all temperatures,
pressures, and mass flow rates are within the limits
set. (Software Safety)
L1
L2
L3
208V
H1-1
H1-2
H1-3
H1-4
H2-1
H2-2

6.2 Appendix B: Uncertainty Propagation Example

The following shows an example of error propagation of the sensible capacity of a heat exchanger based on sample data. Assume constant C_p of 1 kJ/kg-K.

Sample No.	Inlet Temperature [C]	Outlet Temperature [C]	Mass flow rate [kg/s]	Capacity [kW]
1	26.72	30.15	.0461	0.158
2	26.68	30.12	.0462	0.159
3	26.78	30.04	.0459	0.150
4	26.61	30.12	.0461	0.162
5	26.60	30.2	.0462	0.166
Avg.	26.68	30.13	.0461	0.159
Reported Systematic Uncertainty	.07	.07	.001	

Heat exchanger capacity is defined as. $Q = \dot{m}c_p(T_{out} - T_{in})$. Sensitivities and systematic uncertainty of the capacity is calculated as.

$$\theta_{T_{out}} = \frac{\partial Q}{\partial T_{out}} = \dot{m}c_p = 0.0461\ ,\ \theta_{T_{in}} = \frac{\partial Q}{\partial T_{out}} = -\dot{m}c_p = -0.0461\ ,\ \theta_{\dot{m}} = \frac{\partial Q}{\partial \dot{m}} = (T_{out} - T_{in}) = 3.45$$

$$b_Q = \sqrt{(0.0461 * 0.07)^2 + (-0.0461 * 0.07)^2 + (3.45 * .001)^2} = .00572\ kW$$

The random standard uncertainty of the capacity is calculated as.

$$s_{\bar{X}} = \frac{\sqrt{\frac{(0.158 - .159)^2 + (0.158 - .159)^2 + (0.158 - .159)^2 + (0.158 - .159)^2 + (0.158 - .159)^2}{5 - 1}}}{\sqrt{5}} = 0.003\ kW$$

The expanded uncertainty of the capacity Q at approximately 95% confidence is then given by.

$$U_{\bar{Q}} = 2\sqrt{.00572^2 + 0.003^2} = 0.012\ kW$$

6.3 Appendix C: NTHX1 Leak Repairs and Blockage Test

NTHX1 Leak Repairs

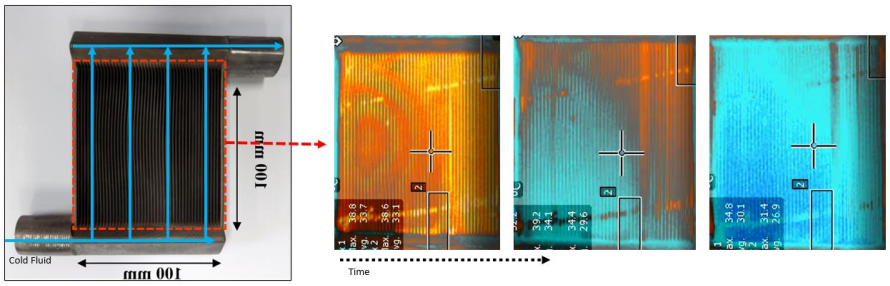

NTHX1 Thermal Imaging Blockage Test

6.4 Appendix D: Packaged Unit Electrical Schematics

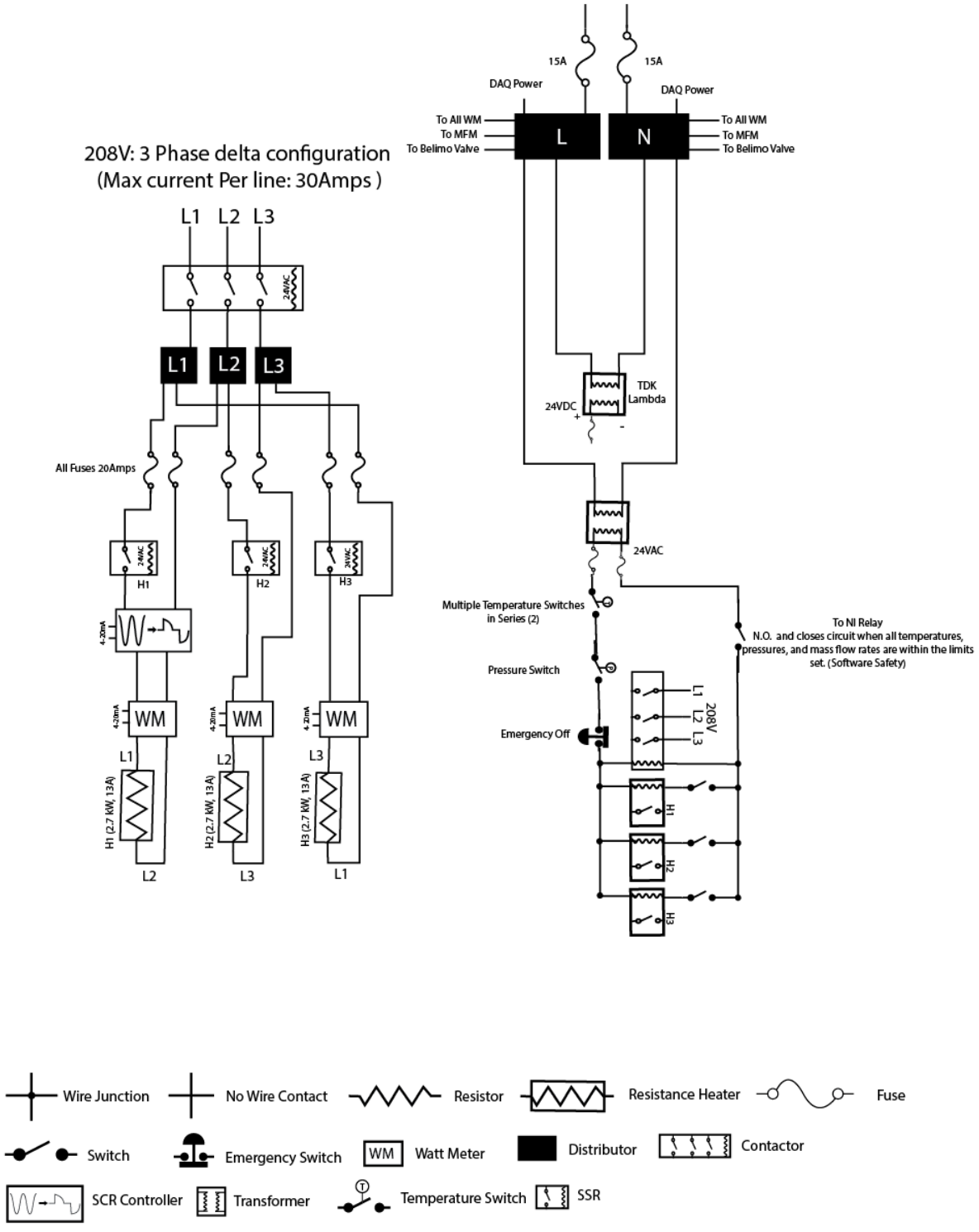

6.5 Appendix C: Packaged Unit Evaporator Fan Motor Repairs

Upon initial packaged unit start-up for shakedown testing, the compressor and condenser fan energized. However, the evaporator fan was not functioning. After troubleshooting, it was determined that the evaporator fan motor's "end cap control panel" was not functioning and needed to be replaced. The evaporator fan and malfunctioning end cap control panel are shown in. A proper replacement had to be found and shipped to UMD. After replacing the end cap control panel, the evaporator fan began functioning properly.

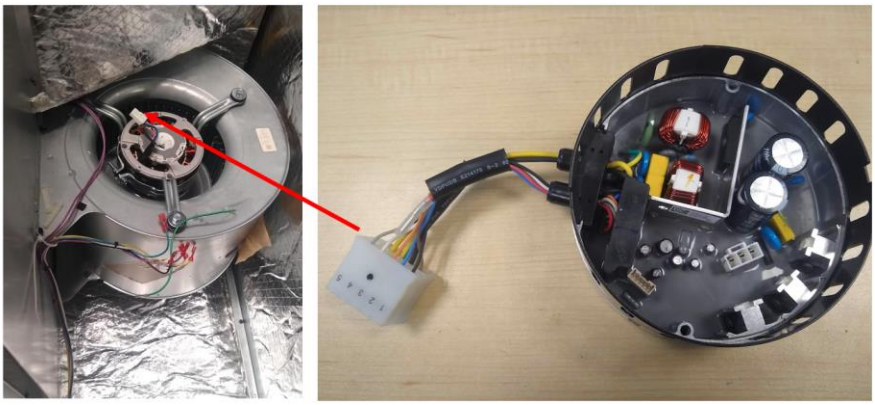

References

Abdelaziz, O. (2009). *Development of multi-scale, multi-physics, analysis capability and its applications to novel heat exchanger design and optimization* (Thesis). University of Maryland.

Abdelaziz, O., Aute, V., Azarm, S., & Radermacher, R. (2010). Approximation-assisted optimization for novel compact heat exchanger designs. *HVAC&R Research*, *16*(5), 707–728.

Achenbach, E. (1977). The effect of surface roughness on the heat transfer from a circular cylinder to the cross flow of air. *International Journal of Heat and Mass Transfer*, *20*(4), 359–369.

AHRI. (2023). AHRI Standard 210/240 Performance rating of unitary air-conditioning & air-source heat pump equipment. *AHRI Standard*.

Alam, T., & Kim, M. H. (2018). A comprehensive review on single phase heat transfer enhancement techniques in heat exchanger applications. *Renewable and Sustainable Energy Reviews*, *81*, 813–839.

Alnakeeb, M. A., Saad, M. A., & Hassab, M. A. (2021). Numerical investigation of thermal and hydraulic performance of fin and flat tube heat exchanger with various aspect ratios. *Alexandria Engineering Journal*, *60*(5), 4255–4265. https://doi.org/10.1016/j.aej.2021.03.036

ANSYS Inc. (2016). *ANSYS FLUENT 12.0 User's Guide*.

Aqida, S. N., Ghazali, M. I., & Hashim, J. (2004). Effect of Porosity on Mechanical Properties of Metal Matrix Composite: An Overview. *Jurnal Teknologi*, *40A*, 17–32.

Arie, M. A., Shooshtari, A. H., & Ohadi, M. M. (2018). Experimental characterization of an additively manufactured heat exchanger for dry cooling of power plants. *Applied Thermal Engineering*, *129*, 187–198. https://doi.org/10.1016/j.applthermaleng.2017.09.140

Arie, M. A., Shooshtari, A. H., Rao, V. V., Dessiatoun, S. V., & Ohadi, M. M. (2016). Air-Side Heat Transfer Enhancement Utilizing Design Optimization and an Additive Manufacturing Technique. *Journal of Heat Transfer*, *139*(3). https://doi.org/10.1115/1.4035068

Arie, M. A., Shooshtari, A. H., Tiwari, R., Dessiatoun, S. V., Ohadi, M. M., & Pearce, J. M. (2017). Experimental characterization of heat transfer in an additively manufactured polymer heat exchanger. *Applied Thermal Engineering*, *113*, 575–584. http://dx.doi.org/10.1016/j.applthermaleng.2016.11.030

Arie, M., Shooshtari, A., Dessiatoun, S., & Ohadi, M. (2016). Performance Characterization of an Additively Manufactured Titanium (Ti64) Heat Exchanger for an Air-water Cooling Application. *ASME 2016 Heat Transfer Summer Conference*, 1–13.

ASHRAE. (1987). *ANSI/ASHRAE standard 41.2-1987, standard methods for laboratory airflow measurement*.

ASHRAE. (2000). *ASHRAE standard 33-2000, method of testing forced circulation air cooling and air heating coil*.

ASME. (2009). Standard for Verification and Validation in Computational Fluid Dynamics and Heat Transfer. *ASME V&V Standard*.

ASME. (2013). *Test Uncertainty - ASME Performance Test Codes 19.1*.

Aurora, J. (2012). *Introduction to Optimum Design* (3rd ed.). Academic Press.

Aute, V., Saleh, K., Abdelaziz, O., Azarm, S., & Radermacher, R. (2013). Cross-validation based

single response adaptive design of experiments for Kriging metamodeling of deterministic computer simulations. *Structural and Multidisciplinary Optimization*, *48*, 581–605.
Awais, M., & Bhuiyan, A. A. (2018). Heat and mass transfer for compact heat exchanger (CHXs) design: A state-of-the-art review. *International Journal of Heat and Mass Transfer*, *127*, 359–380. https://doi.org/10.1016/j.ijheatmasstransfer.2018.08.026
Ayad, F., Benelmir, R., & Idris, M. (2021). Thermal-hydraulic experimental study of louvered fin-and-flat-tube heat exchanger under wet conditions with variation of inlet humidity ratio. *Applied Thermal Engineering*, *183*.
Bacellar, D., Aute, V., Huang, Z., & Radermacher, R. (2016a). Airside friction and heat transfer characteristics for staggered tube bundle in crossflow configuration with diameters from 0.5 mm to 2.0 mm. *International Journal of Heat and Mass Transfer*, *98*, 448–454. https://doi.org/10.1016/j.ijheatmasstransfer.2016.02.072
Bacellar, D., Aute, V., Huang, Z., & Radermacher, R. (2016b). Novel Airside Heat Transfer Surface Designs Using an Integrated Multi-Scale Analysis with Topology and Shape Optimization. *16th International Refrigeration and Air Conditioning Conference*.
Bacellar, D., Aute, V., Huang, Z., & Radermacher, R. (2017). Design optimization and validation of high-performance heat exchangers using approximation assisted optimization and additive manufacturing. *Science and Technology for the Built Environment*, *23*(6), 896–911.
Bacellar, D., Aute, V., & Radermacher, R. (2014). CFD-Based Correlation Development For Air Side Performance Of Finned And Finless Tube Heat Exchangers With Small Diameter Tubes. *15th International Refrigeration and Air Conditioning Conference*.
Bacellar, D., Aute, V., & Radermacher, R. (2016). CFD-Based Correlation Development for Air Side Performance of Wavy Fin Tube Heat Exchangers using Small Diameter Tubes. *16th International Refrigeration and Air Conditioning Conference*.
Baehr, H. D., & Stephan, K. (2006). *Heat Transfer* (2nd ed.). Springer.
Bauereiß, A., Scharowsky, T., & Körner, C. (2014). Defect generation and propagation mechanism during additive manufacturing by selective beam melting. *Journal of Materials Processing Technology*, *214*, 2522–2528.
Bernardin, J., Ferguson, K., Sattler, D., & Kim, S. (2017). The Design, Analysis, and Fabrication of an Additively Manufactured Twisted Tube Heat Exchagner. *ASME 2016 Heat Transfer Summer Conference*.
Beshr, M., Aute, V., & Radermacher, R. (2016). Optimization of a Residential Air Source Heat Pump using Heat Exchangers with Small Diameter Tubes. *16th International Refrigeration and Air Conditioning Conference at Purdue*.
Bohanon, H. (1975). Fan test chamber – nozzle coefficients. *ASHRAE Transactions*, *82*, 104–122.
Bowman, R. A., Mueller, A. C., & Nagle, W. M. (1940). Mean Temperature Difference In Design. *Transactions of ASME*, *62*(4), 283–294.
Čarija, Z., Franković, B., Perčić, M., & Čavrak, M. (2014). Heat transfer analysis of fin-and-tube heat exchangers with flat and louvered fin geometries. *Energy Economics*, *45*, 160–167.
Cevallos, J. (2014). *Thermal and Manufacturing Design of Polymer Composite Heat Exchagners*. University of Maryland, College Park.
Chang, Y. J., & Wang, C. C. (1997). A generalized heat transfer correlation for louver fin geometry. *International Journal of Heat and Mass Transfer*, *40*(3), 533–544.
Chaudhari, S. S., Bhambere, M. B., & Fulzele, P. (2022). Comparative Review On Conventional

And Recently Developed Perforated Fins For Heat Transfer Enhancement. *International Conference on Product Design, Development, and Deployment*.
Chircop, K., & Zammit-Mangion, D. (2013). On Epsilon-Constraint Based Methods for the Generation of Pareto Frontiers. *Journal of Mechanics Engineering and Automation*, *3*, 279–289.
Choi, J. M., Payne, W. V., & Domanski, P. A. (2003). Effects of Non-Uniform Refrigerant and Air Flow Distributions on Finned- Tube Evaporator Performance. *International Congress of Refrigeration*.
COMSOL. (2022). *COMSOL Multiphysics®*. www.comsol.com
Cormier, Y., Dupuis, P., Farjam, A., Corbeil, A., & Jodoin, B. (2014). Additive manufacturing of pyramidal pin fins: Height and fin density effects under forced convection. *International Journal of Heat and Mass Transfer*, *75*, 235–244.
Cormier, Y., Dupuis, P., Jodoin, B., & Corbeil, A. (2013). Net shape fins for compact heat exchanger produced by cold spray. *Journal of Thermal Spray Technology*, *22*, 1210–1221.
Cormier, Y., Dupuis, P., Jodoin, B., & Corbeil, A. (2016). Pyramidal Fin Arrays Performance Using Streamwise Anisotropic Materials by Cold Spray Additive Manufacturing. *Journal of Thermal Spray Technology*, *25*((1-2)), 170–182.
Czerwiński, G., & Wołoszyn, J. (2021). Optimization of air cooling system using adjoint solver technique. *Energies*, *14*, 3753.
Deb, K. (2001). *Multi-objective optimisation using evolutionary algorithms*. John Wiley and Sons.
Deisenroth, D. C., Arie, M., Dessiatoun, S., Shooshtari, A., Ohadi, M., & Bar-cohen, A. (2016). Review of Most Recent Progress on Development of Polymer Heat. *ASME 2015 International Technical Conference and Exhibition on Packaging and Integration of Electronic and Photonic Microsystems*.
Dupuis, P., Cormier, Y., Farjam, A., Jodoin, B., & Corbeil, A. (2014). Performance evaluation of near-net pyramidal shaped fin arrays manufactured by cold spray. *International Journal of Heat and Mass Transfer*, *69*, 34–43.
Dupuis, P., Cormier, Y., Fenech, M., Corbeil, A., & Jodoin, B. (2016). Flow structure identification and analysis in fin arrays produced by cold spray additive manufacturing. *International Journal of Heat and Mass Transfer*, *93*, 301–313. https://doi.org/10.1016/j.ijheatmasstransfer.2015.10.019
Dupuis, P., Cormier, Y., Fenech, M., & Jodoin, B. (2016). Heat transfer and flow structure characterization for pin fins produced by cold spray additive manufacturing. *International Journal of Heat and Mass Transfer*, *98*, 650–661.
EIA. (2012). *Energy Information Administration (EIA)- Commercial Buildings Energy Consumption Survey (CBECS) Data*. https://www.eia.gov/consumption/commercial/data/2012/
EIA. (2018). *Energy Information Administration (EIA)- Commercial Buildings Energy Consumption Survey (CBECS) Data*. https://www.eia.gov/consumption/commercial/data/2018/
EIA. (2019a). EIA energy outlook 2020. *EIA*. www.eia.gov/aeo
EIA. (2019b). *U.S. Energy Information Administration - EIA - Independent Statistics and Analysis*. https://www.eia.gov/todayinenergy/detail.php?id=40232#
EIA. (2022). *Consumption & Efficiency - U.S. Energy Information Administration (EIA)*. https://www.eia.gov/consumption/

Farjam, A., Cormier, Y., Dupuis, P., Jodoin, B., & Corbeil, A. (2015). Influence of Alumina Addition to Aluminum Fins for Compact Heat Exchangers Produced by Cold Spray Additive Manufacturing. *Journal of Thermal Spray Technology*, *24*(7), 1256–1268.

Felber, R. A., Nellis, G., & Rudolph, N. (2016). Design and modeling of 3D-printed air-cooled heat exchangers. *16th International Refrigeration and Air Conditioning Conference*.

Fugmann, H., Laurenz, E., & Schnabel, L. (2019). Multi-dimensional performance evaluation of heat exchanger surface enhancements. *Energies*, *12*.

Galanos, N., Papoutsis-Kiachagias, E. M., Giannakoglou, K. C., Kondo, Y., & Tanimoto, K. (2022). Synergistic use of adjoint-based topology and shape optimization for the design of Bi-fluid heat exchangers. *Structural and Multidisciplinary Optimization*, *65*.

Garde, K. (2017). *Design and Manufacture of an Oil Cooler By Additive Manufacturing*. Univeristy of Minnesota.

Gerstler, W., & Erno, D. (2017). Introduction of an Additively Manufactured Multi-Furcating Heat Exchanger. *16th IEEE InterSociety Conference on Thermal Phenomena in Electronic Systems*.

Gharbi, N. El, Kheiri, A., Ganaoui, M. El, & Blanchard, R. (2015). Numerical optimization of heat exchangers with circular and non-circular shapes. *Case Studies in Thermal Engineering*, *6*, 194–203.

Ghasemi, A., & Elham, A. (2021). Multi-objective topology optimization of pin-fin heat exchangers using spectral and finite-element methods. *Structural and Multidisciplinary Optimization*, *64*, 2075–2095.

Goetzler, W., Guernsey, M., Young, J., Fuhrman, J., & Abdelaziz, O. (2016). The Future of Air Conditioning for Buildings. *Department of Energy Office of Energy Efficiency and Renewable Energy, Building Technologies Office*, *July*. www.osti.gov/home/

Harris, C., Despa, M., & Kelly, K. (2000). Design and fabrication of a cross flow micro heat exchanger. *Journal of Microelectromechanical Systems*, *9*(4), 502–508.

Hassan, I., Phutthavong, P., & Abdelgawad, M. (2004). Microchannel heat sinks: An overview of the state-of-the-art. *Microscale Thermophysical Engineering*, *8*, 183–205.

Hathaway, B. J., Garde, K., Mantell, S. C., & Davidson, J. H. (2018). Design and characterization of an additive manufactured hydraulic oil cooler. *International Journal of Heat and Mass Transfer*, *117*, 188–200. https://doi.org/10.1016/j.ijheatmasstransfer.2017.10.013

Hilbert, R., Janiga, G., Baron, R., & Thévenin, D. (2006). Multi-objective shape optimization of a heat exchanger using parallel genetic algorithms. *International Journal of Heat and Mass Transfer*, *49*, 2567–2577.

Høghøj, L. C., Nørhave, D. R., Alexandersen, J., Sigmund, O., & Andreasen, C. S. (2020). Topology optimization of two fluid heat exchangers. *International Journal of Heat and Mass Transfer*, *163*.

Huang, L., Aute, V., & Radermacher, R. (2015). A Survey of Optimization Formulations and Techniques for the Design of Heat Exchangers Using Lower GWP Refrigerants. *ASHRAE Winter Conference*.

Huang, Y., Leu, M. C., Mazumder, J., & Donmez, A. (2015). Additive manufacturing: Current state, future potential, gaps and needs, and recommendations. *Journal of Manufacturing Science and Engineering, Transactions of the ASME*, *137*.

Huang, Z. (2017). *DEVELOPMENT OF A COMPACT HEAT EXCHANGER WITH BIFURCATED BARE TUBES*. University of Maryland.

Huang, Z., Huang, R., Ling, J., Aute, V., & Hwang, Y. (2018). Application of A Bifurcated Bare-tube Heat Exchanger in Water-based Hybrid VRF System. *17th International Refrigeration and Air Conditioning Conference*.

Huang, Z., Ling, J., Bacellar, D., Hwang, Y., Aute, V., & Radermacher, R. (2020). Airside thermal and hydraulic characteristics of compact bare tube heat exchanger under dry and wet conditions. *International Journal of Refrigeration*, *110*, 295–307.

Ibrahim, O. T., Monroe, J. G., Thompson, S. M., Shamsaei, N., Bilheux, H., Elwany, A., & Bian, L. (2017). An investigation of a multi-layered oscillating heat pipe additively manufactured from Ti-6Al-4V powder. *International Journal of Heat and Mass Transfer*, *108*, 1036–1047.

Jameson, A. (1988). Aerodynamic design via control theory. *Journal of Scientific Computing*, *3*(3), 233–260. https://doi.org/10.1007/BF01061285

Jameson, A. (2003). A Crash-Course on the Adjoint Method for Aerodynamic Shape Optimization. *Lectures at Von Karman Institute*, 1–29. http://citeseerx.ist.psu.edu/viewdoc/summary?doi=10.1.1.13.6065

Jameson, A., Alonso, J., Reuther, J., Martinelli, L., & Vassberg, J. (1998). Aerodynamic shape optimization techniques based on control theory. *American Institute of Aeronautics and Astronautics*. https://doi.org/10.2514/6.1998-2538

Jarny, Y., Ozisik, M. N., & Bardon, J. P. (1991). A general optimization method using adjoint equation for solving multidimensional inverse heat conduction. *International Journal of Heat and Mass Transfer*, *34*(11), 2911–2919.

Jazi, H. R. S., Mostaghimi, J., Chandra, S., Pershni, L., & Coyle, T. (2009). Spray-formed, metal-foam heat exchangers for high temperature applications. *Journal of Thermal Science and Engineering Applications*, *1*.

Jiang, H., Aute, V., & Radermacher, R. (2006). CoilDesigner: a general-purpose simulation and design tool for air-to-refrigerant heat exchangers. *International Journal of Refrigeration*, *29*, 601–610.

Jones, D. R., Schonlau, M., & Welch, W. J. (1998). Efficient Global Optimization of Expensive Black-Box Functions. *Journal of Global Optimization*, *13*, 455–492.

Kametani, Y., Fukuda, Y., Osawa, T., & Hasegawa, Y. (2020). A new framework for design and validation of complex heat transfer surfaces based on adjoint optimization and rapid prototyping technologies. *Journal of Thermal Science and Technology*, *15*(2), 1–15.

Kang, H., Han, U., Lim, H., Lee, H., & Hwang, Y. (2021). Numerical investigation and design optimization of a novel polymer heat exchanger with ogive sinusoidal wavy tube. *International Journal of Heat and Mass Transfer*, *166*.

Kays, W. M., & London, A. L. (1984). *Compact Heat Exchangers* (3rd ed.). McGraw-Hill.

Kim, C. S., Kim, C., & Rho, O. H. (2001). Sensitivity analysis for the Navier-Stokes equations with two-equation turbulence models. *AIAA Journal*, *39*(5), 838–845.

Kim, M. H., & Bullard, C. W. (2002a). Air-side performance of brazed aluminum heat exchangers under dehumidifying conditions. *International Journal of Refrigeration*, *25*, 924–934.

Kim, M. H., & Bullard, C. W. (2002b). Air-side thermal hydraulic performance of multi-louvered fin aluminum heat exchangers. *International Journal of Refrigeration*, *25*.

Kim, N. H., & Youn, B. (1999). Air-Side Heat Transfer and Friction Correlations for Plain Fin-and-Tube Heat Exchangers with Staggered Tube Arrangements. *Journal of Heat Transfer*, *121*(3).

Kirsch, K. L., & Thole, K. A. (2017). Heat transfer and pressure loss measurements in additively manufactured wavy microchannels. *Journal of Turbomachinery*, *139*(1). https://doi.org/10.1115/1.4034342

Klein, E., Ling, J., Aute, V., Hwang, Y., & Radermacher, R. (2018). A Review of Recent Advances in Additively Manufactured Heat Exchangers. *17th International Refrigeration and Air Conditioning Conference*. https://docs.lib.purdue.edu/iracc%0Ahttps://docs.lib.purdue.edu/iracc/1983

Kong, Y. Q., Yang, L. J., Du, X. Z., & Yang, Y. P. (2016). Air-side flow and heat transfer characteristics of flat and slotted finned tube bundles with various tube pitches. *International Journal of Heat and Mass Transfer*, *99*, 357–371.

Korinko, P., Bobbit, J., McKee, H., List III, F., & Carver, K. (2017). Characterization of Additively Manufactured Heat Exchanger Tubing. *ASME 2017 Pressure Vessels and Piping Conference*, 1–7.

Korte, C. M., & Jacobi, A. M. (1997). Condensate Retention and Shedding Effects on Air-Side Heat Exchanger Performance. In *Air Conditioning and Refrigeration Center*.

Kumar, A., Joshi, J. B., Nayak, A. K., & Vijayan, P. K. (2015). A review on the thermal hydraulic characteristics of the air-cooled heat exchangers in forced convection. *Indian Academy of Sciences*, *40*, 673–755.

Kumbhar, N. N., & Mulay, A. V. (2018). Post Processing Methods used to Improve Surface Finish of Products which are Manufactured by Additive Manufacturing Technologies: A Review. *Journal of The Institution of Engineers (India): Series C*, *99*(4), 481–487.

Lee, G., Lee, I., & Kim, S. J. (2021). Topology optimization of a heat sink with an axially uniform cross-section cooled by forced convection. *International Journal of Heat and Mass Transfer*, *168*, 120732.

Li, H., Ding, X., Meng, F., Jing, D., & Xiong, M. (2019a). Optimal design and thermal modelling for liquid-cooled heat sink based on multi-objective topology optimization: An experimental and numerical study. *International Journal of Heat and Mass Transfer*, *144*, 118638.

Li, X., Zhu, D., Yin, Y., Tu, A., & Liu, S. (2019). Parametric study on heat transfer and pressure drop of twisted oval tube bundle with in line layout. *International Journal of Heat and Mass Transfer*, *135*, 860–872.

Lim, H., Han, U., & Lee, H. (2020). Design optimization of bare tube heat exchanger for the application to mobile air conditioning systems. *Applied Thermal Engineering*, *165*. https://doi.org/10.1016/j.applthermaleng.2019.114609

Liu, X., Yu, J., & Yan, G. (2020). An experimental study on the air side heat transfer performance of the perforated fin-tube heat exchangers under the frosting conditions. *Applied Thermal Engineering*, *166*.

LLNL. (2021). *2021 US Energy Flowchart*. https://flowcharts.llnl.gov/

Maji, A., & Choubey, G. (2020). Improvement of heat transfer through fins: A brief review of recent developments. *Heat Transfer*, *49*, 1658–1685.

MathWorks. (2022). *MATLAB*. The MathWorks Inc.

Menéndez Pérez, A., Fernández-Aballí Altamirano, C., & Borrajo Pérez, R. (2022). Parametric analysis of the influence of geometric variables of vortex generators on compact louver fin heat exchangers. *Thermal Science and Engineering Progress*, *27*.

Mirabdolah Lavasani, A., & Bayat, H. (2016). Numerical study of pressure drop and heat transfer from circular and cam-shaped tube bank in cross-flow of nanofluid. *Energy*

Conversion and Management, *129*, 319–328.
Morimoto, K., Suzuki, Y., & Kasagi, N. (2010). Optimal shape design of compact heat exchangers based on adjoint analysis of momentum and heat transfer. *Journal of Thermal Science and Technology*, *5*(1), 24–35.
NationalInstruments. (2023). *Autotuning PID Controllers (PID and Fuzzy Logic)*. https://www.ni.com/docs/en-US/bundle/labview/page/lvpidmain/tuning_pid.html
Optimized Thermal Systems. (2023). *XProps®*.
Pakkanen, J., Calignano, F., Trevisan, F., Lorusso, M., Ambrosio, E. P., Manfredi, D., & Fino, P. (2016). Study of Internal Channel Surface Roughnesses Manufactured by Selective Laser Melting in Aluminum and Titanium Alloys. *Metallurgical and Materials Transactions A: Physical Metallurgy and Materials Science*, *47*, 3837–3844.
Papoutsis-Kiachagias, E. M., & Giannakoglou, K. C. (2016). Continuous Adjoint Methods for Turbulent Flows, Applied to Shape and Topology Optimization: Industrial Applications. *Archives of Computational Methods in Engineering*, *23*, 255–299.
Pironneau, O. (1974). On optimum design in fluid mechanics. *Journal of Fluid Mechanics*, *64*, 97–110.
Pohanish, R., MCCAULEY, C., & HUSSAIN, M. (2016). Surface Texture. In *Machinery's Handbook Pocket Companion* (p. 278). INDUSTRIAL PRESS, INC.
Radermacher, R., Bacellar, D., Aute, V., Huang, Z., Hwang, Y., Muehlbauer, J., Tancabel, J., Abdelaziz, O., & Zhang, M. (2017). Miniaturized Air-to-Refrigerant Heat Exchangers Final Report. *DOE*, 1–80.
Ranut, P., Janiga, G., Nobile, E., & Thévenin, D. (2014). Multi-objective shape optimization of a tube bundle in cross-flow. *International Journal of Heat and Mass Transfer*, *68*, 585–598.
Rao, S. (2009). *Engineering Optimization Theory and Practice* (fourth). John Wiley and Sons.
Rua, Y., Muren, R., & Reckinger, S. (2015). Limitations of additive manufacturing on microfluidic heat exchanger components. *Journal of Manufacturing Science and Engineering, Transactions of the ASME*, *137*(3), 1–5.
Ryu, K., & Lee, K. S. (2015). Generalized heat-transfer and fluid-flow correlations for corrugated louvered fins. *International Journal of Heat and Mass Transfer*, *83*, 604–612.
Saini, P., Dhar, A., & Powar, S. (2023). Performance enhancement of fin and tube heat exchanger employing curved trapezoidal winglet vortex generator with circular punched holes. *International Journal of Heat and Mass Transfer*, *209*, 124142. https://doi.org/10.1016/j.ijheatmasstransfer.2023.124142
Saleh, K., Aute, V. C., Azarm, S., & Radermacher, R. (2010). Online Approximation Assisted Multiobjective Optimization with Space Filling, Variance and Pareto Measures. *13th AIAA/ISSMO Multidisciplinary Analysis Optimization Conference*.
Saltzman, D., Bichnevicius, M., Lynch, S., Simpson, T. W., Reutzel, E. W., Dickman, C., & Martukanitz, R. (2018). Design and evaluation of an additively manufactured aircraft heat exchanger. *Applied Thermal Engineering*, *138*(November 2017), 254–263. https://doi.org/10.1016/j.applthermaleng.2018.04.032
Sarpotdar, S., Nasuta, D., & Aute, V. (2016). CFD-Based Airside Heat Transfer and Pressure Drop Correlation Development for Small Diameter (3 mm to 5 mm) Louver Fin Heat Exchangers. *16th International Compressor Engineering, Refrigeration and Air Conditioning, and High Performance Buildings Conferences*.
Scheithauer, U., Schwarzer, E., Moritz, T., & Michaelis, A. (2018). Additive Manufacturing of Ceramic Heat Exchanger: Opportunities and Limits of the Lithography-Based Ceramic

Manufacturing (LCM). *Journal of Materials Engineering and Performance*, *27*(1), 14–20. https://doi.org/z

Schwarzer, E., Götz, M., Markova, D., Stafford, D., Scheithauer, U., & Moritz, T. (2017). Lithography-based ceramic manufacturing (LCM) – Viscosity and cleaning as two quality influencing steps in the process chain of printing green parts. *Journal of the European Ceramic Society*, *37*, 5329–5338. http://dx.doi.org/10.1016/j.jeurceramsoc.2017.05.046

Shah, R. K., & Sekulic, D. P. (2003). Classification of Heat Exchangers. In *Fundamentals of Heat Exchanger Design* (pp. 1–77). John Wiley and Sons.

Shah, R., & Sekulic, D. (2003). Surface Basic Heat Transfer and flow Friction Characteristics. In *Fundamentals of Heat Exchanger Design* (pp. 425–562). John Wiley and Sons.

Shikazono, N., Okawa, D., Kobayashi, M., Kasagi, N., Waki, T., Kandori, I., & Hataya, S. (2007). Research and development of high-performance compact finless heat exchanger. *6th Int. Conf. on Enhanced, Compact and Ultra-Compact Heat Exchangers: Science, Engineering and Technology*.

Shulman, H., & Nicole, R. (2015). Additive Manufacturing for Cost Efficient Production of Compact Ceramic Heat Exchangers and Recuperators. *NETL Cross-Cutting Research Conference*.

Simpson, T. W., Peplinski, J. D., Koch, P. N., & Allen, J. K. (2001). Metamodels for computer-based engineering design: Survey and recommendations. *Engineering with Computers*, *17*, 129–150.

Sinha, A., Chattopadhyay, H., Iyengar, A. K., & Biswas, G. (2016). Enhancement of heat transfer in a fin-tube heat exchanger using rectangular winglet type vortex generators. *International Journal of Heat and Mass Transfer*, *101*, 667–681.

Sintavia LLC. (2019). *Private Communications*.

Sintavia LLC. (2023). *Sintavia*. https://sintavia.com/

Snyder, J. C., Stimpson, C. K., Thole, K. A., & Mongillo, D. (2016). Build direction effects on additively manufactured channels. *Journal of Turbomachinery*, *138*(5), 1–8.

Stimpson, C. K., Snyder, J. C., Thole, K. A., & Mongillo, D. (2016). Roughness effects on flow and heat transfer for additively manufactured channels. *Journal of Turbomachinery*, *138*(5), 1–10.

Stimpson, C. K., Snyder, J. C., Thole, K. A., & Mongillo, D. (2017). Scaling roughness effects on pressure loss and heat transfer of additively manufactured channels. *Journal of Turbomachinery*, *139*(2).

Stratasys. (2023a). *J850™ Digital Anatomy™ 3D Printer*. https://www.stratasys.com/en/3d-printers/printer-catalog/polyjet/j850-digital-anatomy/

Stratasys. (2023b). *VeroClear*. https://www.stratasys.com/en/materials/materials-catalog/polyjet-materials/veroclear/

StratasysDirectManufacturing. (2023). *Private Communications*.

Strobel, M., & Mortean, M. V. V. (2022). Pressure drop and fluid maldistribution analysis of a compact heat exchanger manufactured by 3D printing. *International Journal of Thermal Sciences*, *172*(PB), 107331. https://doi.org/10.1016/j.ijthermalsci.2021.107331

Subasi, M. (2002). Optimal Control of Heat Source in a Heat Conductivity Problem. *Optimization Methods and Software*, *17*(2), 239–250.

Subramaniam, V., Dbouk, T., & Harion, J. L. (2018). Topology optimization of conductive heat transfer devices: An experimental investigation. *Applied Thermal Engineering*, *131*, 390–411.

Sun, S., Liebersbach, P., & Qian, X. (2020). 3D topology optimization of heat sinks for liquid cooling. *Applied Thermal Engineering*, *178*, 115540.

Syaiful, Wahyuni, T., Yunianto, B., & Sinaga, N. (2021). Evaluation of vortex generators in the heat transfer improvement of airflow through an in-line heated tube arrangement. *Fluids*, *6*.

Tancabel, J., Aute, V., Klein, E., Lee, C. Y., Hwang, Y., Ling, J., Muehlbauer, J., & Radermacher, R. (2022). Multi-scale and multi-physics analysis, design optimization, and experimental validation of heat exchangers utilizing high performance, non-round tubes. *Applied Thermal Engineering*, *216*, 118965.

Tancabel, J., Aute, V., & Radermacher, R. (2018). Review of shape and topology optimization for design of air-to-refrigerant heat exchangers. *17th International Refrigeration & Air Conditioning Conference*.

Tang, T. L. E., Xia, S., Rop, P., De Wispelaere, S., Subramanian, R., & Koos, B. (2021). Multi-physics topology optimization for thermal-flow problems applied to additively manufactured heat exchangers. *ASME Turbo Expo*.

Tapia, G., Elwany, A. H., & Sang, H. (2016). Prediction of porosity in metal-based additive manufacturing using spatial Gaussian process models. *Additive Manufacturing*, *12*, 282–290. https://doi.org/10.1016/j.addma.2016.05.009

Tsopanos, S., Wong, M., Owen, I., & Sutcliffe, C. J. (2006). Manufacturing Novel Heat Transfer Devices By Selective Laser Melting. *13th International Heat Transfer Conference*.

Ventola, L., Robotti, F., Dialameh, M., Calignano, F., Manfredi, D., Chiavazzo, E., & Asinari, P. (2014). Rough surfaces with enhanced heat transfer for electronics cooling by direct metal laser sintering. *International Journal of Heat and Mass Transfer*, *75*, 58–74.

Vidya, M. C., Beishuizen, N. A., Kleine, D. De, & Meer, T. H. Van Der. (2019). Three-Dimensional Multi-Objective Shape Optimization of a Cylinder in a Cross-Flow Using Discrete Adjoint Method. *Second Pacific Rim Thermal Engineering Conference*.

Vidya, M. C., Hannink, M. J. M., Beishuizen, N. A., De Kleine, D., & Van Der Meer, T. H. (2018). Multi-objective optimization of a heat exchanger using the discrete adjoint method. *16th International Heat Transfer Conference*.

Wang, C.-C., Chi, K.-Y., & Chang, C.-J. (2000). Heat transfer and friction characteristics of plain fin-and-tube heat exchangers, part II: Correlation. *International Journal of Heat and Mass Transfer*, *43*(15), 2693–2700.

Wang, C. C., Lee, C. J., Chang, C. T., & Lin, S. P. (1999). Heat transfer and friction correlation for compact louvered fin-and-tube heat exchangers. *International Journal of Heat and Mass Transfer*, *42*, 1945–1956.

Wang, C., Montanari, F., & Hill, D. C. (2015). Application of Adjoint Solver to Optimization of Fin Heat Exchagner. *ASME Turbo Expo 2015: Turbine Technical Conference and Exposition*.

Wang, Chi Chuan, Chen, K. Y., Liaw, J. S., & Tseng, C. Y. (2015). An experimental study of the air-side performance of fin-and-tube heat exchangers having plain, louver, and semi-dimple vortex generator configuration. *International Journal of Heat and Mass Transfer*, *80*, 281–287.

Wang, Chi Chuan, Hsieh, Y. C., & Lin, Y. T. (1997). Performance of plate finned tube heat exchangers under dehumidifying conditions. *Journal of Heat Transfer*, *119*, 109–117.

Wang, Chi Chuan, Hwang, Y. M., & Lin, Y. T. (2002). Empirical correlations for heat transfer and flow friction characteristics of herringbone wavy fin-and-tube heat exchangers. *International Journal of Refrigeration*, *25*, 673–680.

Wang, Chi Chuan, Lee, W. S., & Sheu, W. J. (2001). A comparative study of compact enhanced fin-and-tube heat exchangers. *International Journal of Heat and Mass Transfer*, *44*, 3565–3573.

Wang, Chi Chuan, Tsai, Y. M., & Lu, D. C. (1998). Comprehensive study of convex-louver and wavy fin-and-tube heat exchangers. *Journal of Thermophysics and Heat Transfer*, *12*(3), 423–430.

Weiss, K. P., Bagrets, N., Lange, C., Goldacker, W., & Wohlgemuth, J. (2015). Thermal and mechanical properties of selected 3D printed thermoplastics in the cryogenic temperature regime. *IOP Conference Series: Materials Science and Engineering*, *102*.

Westphalen, D., Roth, K. W., & Brodrick, J. (2006). Heat transfer enhancement. *ASHRAE Journal*, *48*(4), 68–71.

Winkler, J., Aute, V., & Radermacher, R. (2007). Comprehensive investigation of numerical methods in simulating a steady-state vapor compression system. *International Journal of Refrigeration*, *31*.

Wong, M., Owen, I., Sutcliffe, C. J., & Puri, A. (2009a). Convective heat transfer and pressure losses across novel heat sinks fabricated by Selective Laser Melting. *International Journal of Heat and Mass Transfer*, *52*, 281–288.

Wong, Matthew, Owen, I., & Sutcliffe, C. (2009). Pressure loss and heat transfer through heat sinks produced by selective laser melting. *Heat Transfer Engineering*, *30*(13), 1068–1076.

Wong, Matthew, Tsopanos, S., Sutcliffe, C. J., & Owen, I. (2007). Selective laser melting of heat transfer devices. *Rapid Prototyping Journal*, *13*(5), 291–297.

Yadav, A., & Singh, Y. (2023). A review on microchannel heat exchanger and the effects of various parameters. *Advances in Manufacturing Technology and Application of Artificial Intelligence AIP Conf.*

Yan, C., Hao, L., Hussein, A., Bubb, S. L., Young, P., & Raymont, D. (2014). Evaluation of light-weight AlSi10Mg periodic cellular lattice structures fabricated via direct metal laser sintering. *Journal of Materials Processing Technology*, *214*(4), 856–864.

Yin, J., & Jacobi, A. M. (2000). Condensate Retention Effects on the Air-Side Heat Transfer Performance of Plain and Wavy-Louvered Heat Exchangers. In *Air Conditioning and Refrigeration Center*.

Yun, R., Kim, Y., & Kim, Y. (2009). Air side heat transfer characteristics of plate finned tube heat exchangers with slit fin configuration under wet conditions. *Applied Thermal Engineering*, *29*, 3014–3020.

Zhang, M., Sun, C. N., Zhang, X., Goh, P. C., Wei, J., Li, H., & Hardacre, D. (2020). Competing influence of porosity and microstructure on the fatigue property of laser powder bed fusion stainless steel 316L. *Solid Freeform Fabrication 2017: Proceedings of the 28th Annual International Solid Freeform Fabrication Symposium - An Additive Manufacturing Conference, SFF 2017*, 365–376.

Zhao, J., Zhang, M., Zhu, Y., Cheng, R., & Wang, L. (2021). Topology optimization of turbulent forced convective heat sinks using a multi-layer thermofluid model. *Structural and Multidisciplinary Optimization*, *64*, 3835–3859.

Zhou, J., Lu, M., Zhao, Q., Hu, D., Qin, H., & Chen, X. (2022). Thermal design of microchannel heat sinks using a contour extraction based on topology optimization (CEBTO) method. *International Journal of Heat and Mass Transfer*, *189*, 122703.

Zou, Y., Tuo, H., & Hrnjak, P. (2014). R-410A Maldistribution Impact on the Performance of Microchannel Evaporator. *ASHRAE Transactions*.